



**HAL**  
open science

# STUDY OF NOVEL ELECTRONIC CONDUCTORS: The case of BaVS<sub>3</sub>

Neven Barisic

► **To cite this version:**

Neven Barisic. STUDY OF NOVEL ELECTRONIC CONDUCTORS: The case of BaVS<sub>3</sub>. Condensed Matter [cond-mat]. Ecole Polytechnique Fédérale de Lausanne (EPFL), 2004. English. NNT: . tel-00011952

**HAL Id: tel-00011952**

**<https://theses.hal.science/tel-00011952>**

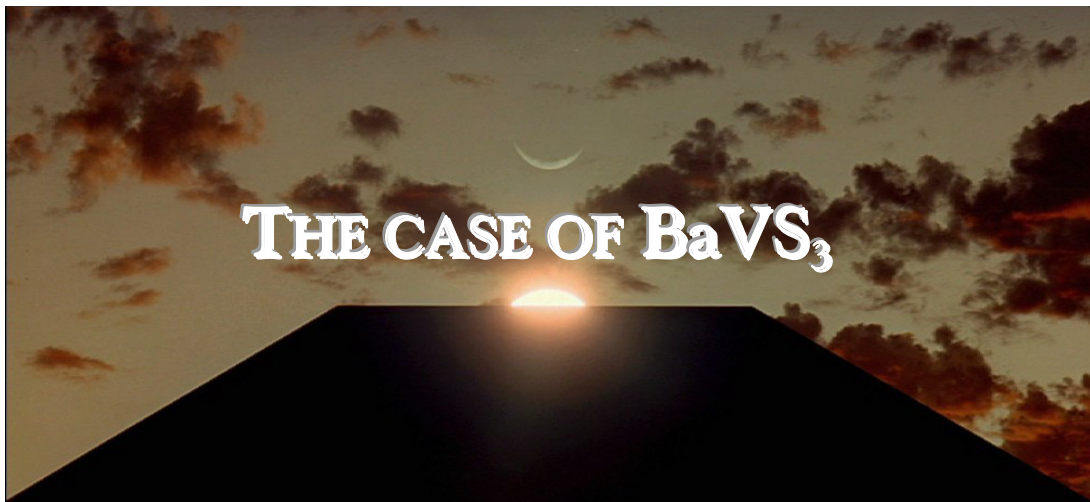
Submitted on 15 Mar 2006

**HAL** is a multi-disciplinary open access archive for the deposit and dissemination of scientific research documents, whether they are published or not. The documents may come from teaching and research institutions in France or abroad, or from public or private research centers.

L'archive ouverte pluridisciplinaire **HAL**, est destinée au dépôt et à la diffusion de documents scientifiques de niveau recherche, publiés ou non, émanant des établissements d'enseignement et de recherche français ou étrangers, des laboratoires publics ou privés.

FACULTE DES SCIENCES DE BASE  
INSTITUT DE PHYSIQUE DE LA MATIÈRE COMPLEXE

**STUDY OF NOVEL ELECTRONIC  
CONDUCTORS:**



POUR L'OBTENTION DU GRADE DE DOCTEUR ÈS SCIENCES  
PAR

**Neven BARIŠIĆ**

Directeur de thèse: Prof. László FORRÓ

Lausanne, EPFL

2004



**STUDY OF NOVEL ELECTRONIC CONDUCTORS:  
The case of BaVS<sub>3</sub>**

THESE N° 3162 (2004)

PRESENTÉE A LA FACULTE DES SCIENCES DE BASE

Institut de physique de la matière complexe

SECTION DE PHYSIQUE

ECOLE POLYTECHNIQUE FEDERALE DE LAUSANNE

POUR L'OBTENTION DU GRADE DE DOCTEUR ES SCIENCES

PAR

**Neven BARIŠIĆ**

Physicien diplômé de l'Université de Zagreb, Croatie  
et de nationalité Croate

acceptée sur proposition du jury:

Prof. L. Forró, directeur de thèse  
Prof. P. Fazekas, rapporteur  
Prof. J. Floquet, rapporteur  
Prof. A. Georges, rapporteur  
Prof. F. Mila, rapporteur  
Prof. H. Brune, rapporteur

Lausanne, EPFL  
2004





## *Abstract*

This thesis presents the results of a concerted effort to understand the complex array of physical properties exhibited by the BaVS<sub>3</sub> family of materials. As a  $3d^1$  system, BaVS<sub>3</sub> displays a unique collection of correlation-driven phenomena, including a metal-insulator transition driven by spin-density waves and or charge-density waves as well as a pressure-dependent crossover between the non-Fermi-liquid and Fermi-liquid behaviors. In an attempt to better understand these and many other properties, we have undertaken a systematic experimental study of BaVS<sub>3</sub> and related compounds.

The primary measurements carried out were those of the transport properties, resistivity and thermoelectric power (TEP). Through the construction of specialized measuring apparatuses, we were able to measure simultaneously these transport properties under conditions of variable temperature (from 2 to 600 K), pressure (up to 3 GPa) and magnetic field (up to 12 T).

At ambient pressure and in the range of 250 to 600K, BaVS<sub>3</sub> shows nearly isotropic but poor metallic behavior with linear temperature dependences of resistivity and TEP and a Curie-like magnetic susceptibility. The nearly isotropic conductivity contrasts with the 1D  $2k_F$  fluctuations observed by lowering the temperature below 250 K (at which the first Jahn-Teller structural phase transition occurs) deep in the metallic phase. The fluctuations reveal the 1D aspects of the electronic character, originating from the chain like structure of the material. The salient feature of BaVS<sub>3</sub> at ambient pressure is the second order metal-to-insulator (MI) transition at  $T_{MI} = 69$  K, accompanied by the tetramerization (doubling of the 2V unit cell in the chain direction). In addition to the transport measurements, the strong changes in the electrical and magnetic properties of the system around  $T_{MI}$  were followed by magnetic susceptibility, angle-resolved photoelectron spectroscopy and frequency-dependent conductivity.

By increasing the pressure, the three-dimensionality of BaVS<sub>3</sub> is enhanced and the MI phase transition is suppressed to lower temperatures. TEP and magneto TEP measurements in this pressure range revealed the existence of polarons and of spin fluctuations in the metallic phase. The latter can be identified as precursors to the MI transition. Around 1.8 GPa, where  $T_{MI} \sim 15$  K, the system enters a strongly fluctuating regime, highly sensitive to the magnetic field, the amplitude and the frequency of the measuring current and to a further increase of the pressure. Closely related to these features, the phase boundary collapses and a hysteretic behavior appears in the transport properties and their magnetic-field-dependent counterparts. At a critical pressure of  $\sim 2$  GPa, a non-Fermi liquid (NFL) state arises (with  $n \sim 1.5$  in the  $T^n$  resistivity law between 1 and 15 K) in relation to the proximate Quantum Critical Point. The  $p$ - $H$ - $T$  phase diagram of BaVS<sub>3</sub> in this region has been explored in some detail with particular

emphasis placed upon the relevance of the spin degrees of freedom (on the insulator side) and the role of quantum fluctuations above the critical pressure. Finally, as the pressure is increased further, the conventional Fermi-liquid exponent of  $n = 2$  is obtained.

In order to delve further into the subtleties of the MI transition and the NFL behavior, a comparative study was carried out on the sister compounds  $\text{Ba}_{x-1}\text{Sr}_x\text{VS}_3$  and  $\text{BaVSe}_3$  and on sulfur-deficient  $\text{BaVS}_3$ . From this study it became apparent that the imposed chemical substitution manifests itself as an additional effective pressure. The inherent disorder of these samples was observed to affect the NFL behavior by reducing the exponent  $n$  towards a value of 1, while the apparent ferromagnetic order below 15 K was seemingly independent of pressure.

All the observed features are consistent with a relatively simple two-band tight-binding, vanadium-based, model consisting of a wide quasi one-dimensional band hybridized with a rather isotropic narrow band. Within this context, it is concluded that the MI transition is controlled by the Coulomb-interacting electrons of the wide quasi one-dimensional band. Based on this model a new description of the NFL regime has been proposed.

## *Version abrégée*

Cette thèse présente les résultats d'une étude approfondie des propriétés complexes des matériaux dérivés du  $\text{BaVS}_3$ , système  $3d^1$  qui présente une collection unique de phénomènes liés aux corrélations. Celle-ci inclue une transition métal-isolant (MI) induite par des corrélations type onde de densité de spin, onde de densité de charge, et un passage à haute pression d'un Non Liquides de Fermi (NLF) à un liquide Fermi. Afin de comprendre nombre de ces propriétés, une étude expérimentale systématique de  $\text{BaVS}_3$  et de certains de ses dérivés a été entreprise.

L'étude est basée sur les mesures de propriétés de transport, résistivité et pouvoir thermoélectrique (PTE). La construction d'un appareillage spécialisé a permis de caractériser simultanément les effets de température (de 2 à 300 K), de pression (jusqu'à 3 GPa) et du champ magnétique (jusqu'à 12 T) sur les propriétés de transport.

A pression atmosphérique et pour des températures comprises entre 250 et 600 K,  $\text{BaVS}_3$  présente un comportement de mauvais métal, quasi isotrope avec une résistivité et un PTE linéaires en fonction de la température, ainsi qu'une susceptibilité magnétique de Curie. La conductivité quasi isotrope contraste avec des fluctuations 1D à  $2k_F$ , observées en-dessous de 250 K (température où une première transition structurelle de Jahn – Teller se produit) profondément dans l'état métallique. Ceci révèle les aspects 1D du caractère électronique, trouvant son origine dans la structure cristalline en chaînes. La principale propriété de  $\text{BaVS}_3$  est la transition MI de second ordre à 69K à pression atmosphérique, qui s'accompagne d'une tétramérisation (dimérisation de la cellule élémentaire ayant 2V le long des chaînes). S'ajoutant aux mesures de transport, des variations importantes des propriétés électriques et magnétiques du système au voisinage de  $T_{MI}$  ont été observées à l'aide de mesures de susceptibilité magnétique, d'ARPES et de dépendance en fréquence de la conductivité.

Par une augmentation de la pression,  $\text{BaVS}_3$  devient plus tridimensionnel et la température de transition MI diminue. Les mesures de PTE, dans cet intervalle de pressions et en fonction du champ magnétique, ont montré l'existence de polarons et de fluctuations de spin dans la phase métallique. Ces dernières sont liées aux effets pré-transitoires de la transition MI. Pour une pression proche de 1.8 GPa, où la température de transition MI est d'environ 15K, le système entre dans un régime de fluctuations fortes qui est très sensible au champ magnétique, à l'amplitude et à la fréquence du courant de mesure, ainsi qu'à une augmentation supplémentaire de la pression. La ligne de transition s'effondre, aussi accompagnée de comportements d'hystérésis de toutes les propriétés mesurées, c'est à dire la résistivité, la magnétorésistivité, le PTE et le magnéto-PTE. A une pression critique d'environ 2GPa, un état de Non Liquides de Fermi (avec  $n \approx 1.5$  dans la loi en  $T^n$  pour la résistivité), lié

au Point Quantique Critique (PQC), est présent entre 1 à 15 K. L'ensemble du diagramme p-H-T de BaVS<sub>3</sub> a été étudié en détail au voisinage de cette pression critique. Deux aspects importants sont surtout considérés: les degrés de liberté de spin du côté isolant de la transition MI et le rôle des fluctuations quantiques au-dessus de la pression critique. Enfin, on retrouve pour des pressions supérieures (2.7 GPa) l'exposant conventionnel n=2 d'un liquide de Fermi.

Une étude comparative a été effectuée pour les composés apparentés Ba<sub>1-x</sub>Sr<sub>x</sub>VS<sub>3</sub>, BaVSe<sub>3</sub>, et BaVS<sub>3-δ</sub> déficient en soufre. Cette étude a révélé que la substitution chimique peut être considérée comme un effet de pression additionnel. L'effet de désordre sur le comportement LNF, fait diminuer n vers 1. De plus, l'existence d'un ordre ferro-magnétique, présent en-dessous de 15K et indépendant de la pression, est proposée.

Toutes les propriétés observées sont interprétées à partir d'un modèle de liaisons fortes à deux bandes basées sur le vanadium, qui fait intervenir une bande large quasi 1D en hybridation avec une bande étroite et quasi isotrope. En conclusion, la transition MI est contrôlée par les électrons de la bande large quasi 1D, soumis à l'interaction coulombienne. Une nouvelle description de LNF, basée sur ce modèle, est avancée.

---

# Table of Contents

<b>CHAPTER 1: MATERIALS WITH NOVEL ELECTRONIC PROPERTIES</b>	<b>5</b>
<b>CHAPTER 2: ODYSSEY BaVS<sub>3</sub></b>	<b>11</b>
2.1 THE DAWN OF BaVS <sub>3</sub>	12
2.2 BEGINNING TO UNDERSTAND BaVS <sub>3</sub>	14
2.2.1 MAGNETIC PROPERTIES AND THEIR IMPLICATIONS	15
2.3 LAUSANNE IN SIGHT	19
2.3.1 HIGH-QUALITY SINGLE CRYSTALS	19
2.3.2 THE IMPORTANCE OF HIGH PRESSURE	21
2.4 REFERENCES	23
<b>CHAPTER 3: CRYSTAL SYMMETRY ANALYSIS &amp; ELECTRONIC BAND STRUCTURE</b>	<b>27</b>
3.1 CRYSTAL FIELD SPLITTING	28
3.2 SYMMETRY ANALYSIS	33
3.3 LOCALIZED LIMIT	38
3.3.1 CONSTRUCTION OF THE MODEL	38
3.3.2 TESTING AND INTERPRETATION OF THE MODEL	40
3.4 ITINERANT LIMIT	43
3.4.1 AB INITIO CALCULATION OF THE BAND STRUCTURE	43
3.4.2 THE TIGHT BINDING APPROXIMATION	46
3.4.3 ARPES AND TIGHT BINDING: A SYNERGISTIC COOPERATION	55
3.5 CONCLUDING REMARKS	59
3.6 REFERENCES	60
<b>CHAPTER 4: FOLLOWING THE MI PHASE BOUNDARY BY RESISTIVITY</b>	<b>63</b>
4.1 AMBIENT PRESSURE	64
4.1.1 SAMPLE CHARACTERIZATION	66
4.2 INTERMEDIATE PRESSURES (1BAR < $p$ < 1.7GPa)	68
4.3 MAGNETORESISTIVITY (1BAR < $p$ < 1.7GPa)	70
4.4 CONCLUDING REMARKS	75
4.5 REFERENCES	76
<b>CHAPTER 5: CROSSOVER FROM THE NON-FERMI LIQUID TO THE FERMI LIQUID</b>	<b>79</b>

---

---

---

<b>5.1</b>	<b>COLLAPSE OF THE INSULATING PHASE</b>	<b>81</b>
<b>5.2</b>	<b>QUANTUM CRITICAL POINT (QCP)</b>	<b>83</b>
<b>5.3</b>	<b>FERMI LIQUID VERSUS NON-FERMI LIQUID BEHAVIOR</b>	<b>91</b>
5.3.1	DISORDER AND THE QCP	94
5.3.2	MAGNETIC FIELD AND THE QCP	97
5.3.3	CLEAN BaVS <sub>3</sub> AND THE QCP	101
<b>5.4</b>	<b>NEW FEATURES IN THE VICINITY OF <math>p_{cr}</math></b>	<b>106</b>
5.4.1	HYSTERESIS, RELAXATION TIMES AND NON-LINEAR TRANSPORT	108
<b>5.5</b>	<b>FERROMAGNETIC VERSUS INTERCHAIN-COMPENSATED-FERRO-MAGNETIC INSTABILITIES AT LOW <math>T</math>/HIGH <math>P</math></b>	<b>120</b>
<b>5.6</b>	<b>SUMMARY OF THE PHYSICS OF BaVS<sub>3</sub></b>	<b>123</b>
<b>5.7</b>	<b>REFERENCES</b>	<b>129</b>

---

**CHAPTER 6: CHEMICAL PRESSURE** **137**

<b>6.1</b>	<b>CHEMICAL PRESSURE: THE CONCEPT</b>	<b>138</b>
<b>6.2</b>	<b>Ba-Sr ISOVALENT SUBSTITUTION</b>	<b>140</b>
6.2.1	RESISTIVITY UNDER PRESSURE	141
6.2.2	MAGNETIC PROPERTIES	144
6.2.3	IMPLICATIONS	146
<b>6.3</b>	<b>S-Se ISOVALENT SUBSTITUTION</b>	<b>148</b>
6.3.1	PREVIOUS STUDIES	148
6.3.2	TRANSPORT PROPERTIES OF BaVSe <sub>3</sub>	149
<b>6.4</b>	<b>CONCLUDING REMARKS</b>	<b>151</b>
<b>6.5</b>	<b>REFERENCES</b>	<b>152</b>

---

**CHAPTER 7: THERMOELECTRIC POWER OF BaVS<sub>3</sub> UNDER PRESSURE** **155**

<b>7.1</b>	<b>THERMOELECTRIC POWER</b>	<b>156</b>
<b>7.2</b>	<b>THE CASE OF BaVS<sub>3</sub></b>	<b>158</b>
7.2.1	MAIN FEATURES OF TEP BELOW $p_{cr}$ AND ABOVE $T_{MI}$	159
7.2.2	FINE FEATURES OF TEP - MAGNETO-TEP	161
7.2.3	MAIN FEATURES OF TEP ABOVE $p_{cr}$	165
<b>7.3</b>	<b>CONCLUDING REMARKS</b>	<b>167</b>
<b>7.4</b>	<b>REFERENCES</b>	<b>169</b>

---

**CHAPTER 8: OPTICAL CONDUCTIVITY OF BaVS<sub>3</sub> IN THE INFRARED REGION** **171**

---

---

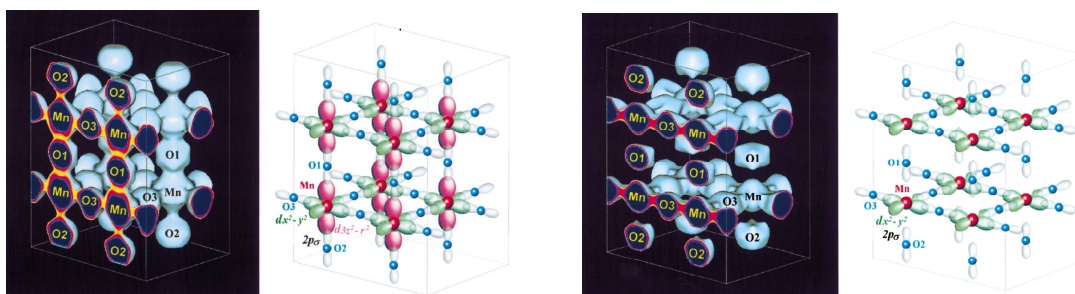
<b>8.1</b>	<b>INTRODUCTION TO OPTICAL MEASUREMENTS</b>	<b>172</b>
<b>8.2</b>	<b>AMBIENT PRESSURE MEASUREMENTS</b>	<b>173</b>
<b>8.3</b>	<b>PRESSURE DEPENDENT OPTICAL CONDUCTIVITY MEASUREMENTS</b>	<b>176</b>
<b>8.4</b>	<b>CONCLUDING REMARKS</b>	<b>178</b>
<b>8.5</b>	<b>REFERENCES</b>	<b>179</b>
<b>CHAPTER 9: CONCLUSIONS</b>		<b>181</b>
<hr/>		
<b>9.1</b>	<b>THE JOURNEY: FROM THE BEGINNING TO THE END</b>	<b>182</b>
<b>9.2</b>	<b>FUTURE PERSPECTIVES</b>	<b>187</b>
<b>APPENDIX A: HOW TO MEASURE</b>		<b>189</b>
<hr/>		
<b>APPENDIX B: CATALOG OF SAMPLES</b>		<b>203</b>
<hr/>		





## Chapter 1

# MATERIALS WITH NOVEL ELECTRONIC PROPERTIES





An obvious question for a non-specialist reader to pose in the context of this thesis is: “Why would one study novel electronic materials in the 21st century, which seems to be dominated by the biological sciences?” Indeed, as more and more researchers from outside of biology turn towards the study of living matter, addressing questions such as DNA-conduction, oxidative stress, and neural networks (just to name a few), it is a very pertinent question. The physicist may well respond by pointing out that many of the aforementioned topics are studied with devices that owe their origin to solid state physics. As such, the responsibility for the improvement of such devices still rests heavily upon the solid state physicist, and will continue to do so for the foreseeable future. That said, it is important to point out that physics is much more than a mere service science for biology. Fundamental research in physics may be justifiably called the birthplace of development.

But even insiders, who are well aware of the above arguments, may still ask the question: “What this study is good for?” Most of the materials we need, such as metals and semiconductors, are already well-understood. It is true that metals like copper, niobium, iron etc. are established materials in applications such as electric transport, superconducting magnets for magnetic resonance imaging, and magnetic bearings and their study is not the focus of fundamental research. A similar view can be taken for semiconductors like silicon which, through the MOSFET (metal-oxide semiconductor field-effect transistor) technology, gave us processors, very fast computers, light emitting diodes, powerful lasers etc. What else do we need?

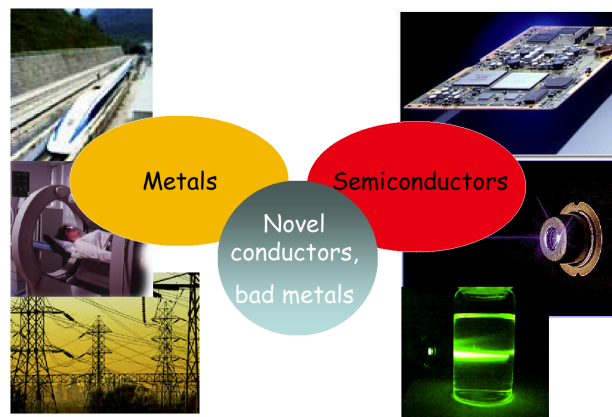


**Figure 1.1:** Schematic representation of two separate (as distinguished by an energy gap) classes of materials, metals and semiconductors with chosen examples of their applications. In the broad region in between these two classes, there is a variety of materials called novel conductors displaying a rich physics which is craving to be both understood and applied.

Actually, despite some belief to the contrary, there is still a pressing need for better and faster devices. One promising direction for research in this area started a few decades ago amongst materials with properties in between those of conventional metals and semiconductors. The materials from this class, including low-dimensional organic conductors, conducting polymers, manganites, charge density wave systems, heavy fermions, cuprates, fullerides and lately carbon nanotubes, were often named “bad metals”. In our vocabulary, we prefer to call them novel conductors (Fig. 1.1), a few representative structures of which can be found in Fig. 1.2.

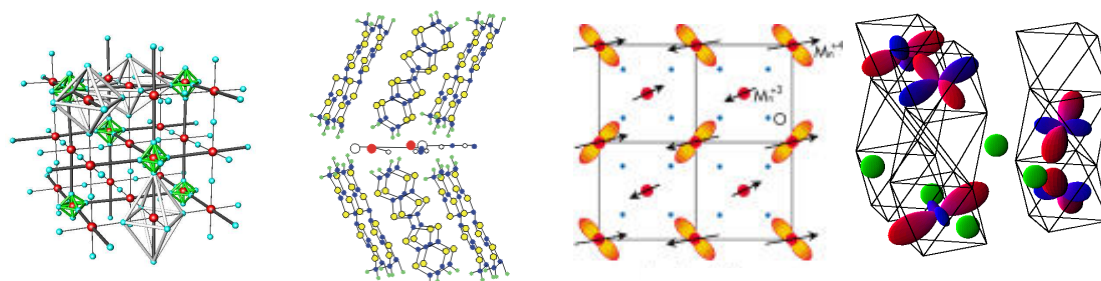


**Figure 1.2:** A few representative structures of materials with novel electronic properties: superconductor (cuprate), organic conductor ((BEDT-TTF)<sub>2</sub>I<sub>3</sub>), manganites (La<sub>0.5</sub>S<sub>1.5</sub>MnO<sub>4</sub>) and the material which is the subject of my thesis, BaVS<sub>3</sub>.

It is generally believed among the specialists that by simply modulating the charge distribution in, for example MOSFETs, one can neither reduce the size nor increase the speed of the processors. In order to do so, one needs to modulate other degrees of freedom, like spins and orbitals. The manipulation of spin through spin valves and spin-dependent transport is already known to the market as spintronics. In terms of controlling the electronic orbitals, however, we are just in the learning phase and it is the aim of the present study to further our knowledge in this direction. There are many d-shell conductors where this phenomenon could be studied. Our choice of material is BaVS<sub>3</sub> which, besides the orbital ordering, offers the following array of very rich physics:

*Bad metallicity*

*Metal Insulator transition*

*Orbital order*

*Charge order, CDW*

*Spin order, SDW*

*Frustrations*

*Jahn-Teller distortion*

*Non Fermi Liquid & Quantum Critical Point*

*Magnetic ordering*

*Role of disorder*

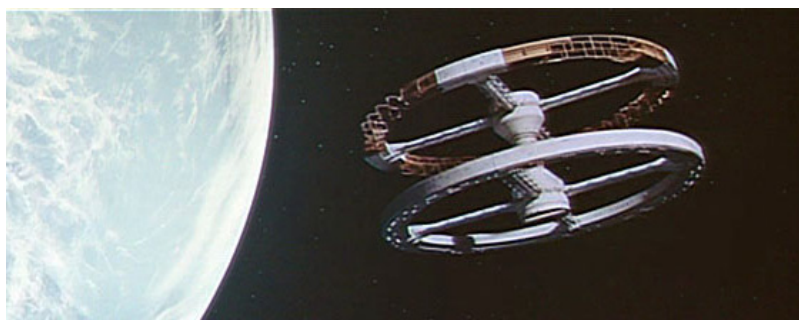
All of these issues will be addressed in my dissertation. In our opinion, if we understand the main parameters which control the interplay between lattice, charge, orbital, and spin interactions, we can start to manipulate them and engineer materials suitable for devices. Nevertheless, one may still say that the topics listed above belong to fundamental physics, without any possibility of application. From our point of view, however, every seriously executed piece of basic research will find application; the only question is the timescale.



---

## Chapter 2

# ODYSSEY $\text{BaVS}_3$



<b>2.1</b>	<b>THE DAWN OF <math>\text{BaVS}_3</math></b>	<b>12</b>
<b>2.2</b>	<b>BEGINNING TO UNDERSTAND <math>\text{BaVS}_3</math></b>	<b>14</b>
2.2.1	MAGNETIC PROPERTIES AND THEIR IMPLICATIONS	15
<b>2.3</b>	<b>LAUSANNE IN SIGHT</b>	<b>19</b>
2.3.1	HIGH-QUALITY SINGLE CRYSTALS	19
2.3.2	THE IMPORTANCE OF HIGH PRESSURE	21
<b>2.4</b>	<b>REFERENCES</b>	<b>23</b>

In this chapter we will present the state of the art in the research of  $\text{BaVS}_3$ , indicate the main achievements thus far and present the problems identified in previous works.

---



## 2.1 The dawn of *BaVS<sub>3</sub>*

The odyssey *BaVS<sub>3</sub>* started several years before my birth. To be more modest and not to relate the beginning of time to my own coordinate system, in fact it started much earlier. As is already well known, in the beginning God created the heavens and the earth, and probably some atoms of barium, vanadium, and sulfur too. Even if there is no direct proof, since it was too dark to see, we believe that it is a sound assumption supported by the early mention of sulfur (brimstone) in the Book of Genesis, 19:24. In the interests of simplicity, let me skip several millennia (barium was discovered in 1808 by Sir Humphrey Davy, England, and vanadium in 1801 by Adres Manuel del Rio, Mexico, and Nils Safstöm, Sweden) and return to my epoch, to the year 1968 when Gardner and co-workers announced, during the 70<sup>th</sup> annual meeting of the American ceramic society the synthesis of a new material, namely *BaVS<sub>3</sub>* (Gardner *et al.*, 1968).

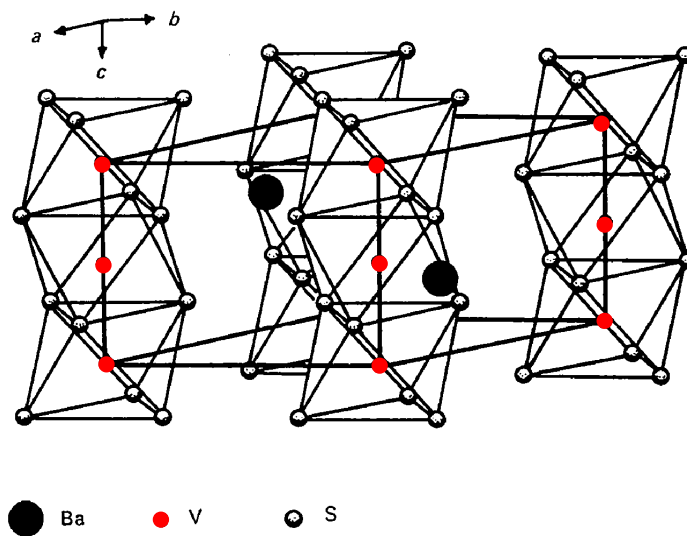


**Figure 2.1:** The structure of *BaVS<sub>3</sub>* showing chains of face-sharing sulfur octahedra. The hexagonal unit cell is outlined with bold lines. Picture adopted from Gardner *et al.* (1969).

Shortly afterwards, in 1969, they published their results (Gardner *et al.*, 1969). From the single-crystal analysis, they were able to refine the room temperature crystal structure of *BaVS<sub>3</sub>*, which consists of linear chains of vanadium atoms, surrounded by face-sharing sulfur octahedra, running parallel to the *c* – axis. Barium ions serve as spacers, separating the chains (Fig. 2.1). The room temperature *space group is P6<sub>3</sub>/mmc with two formula units per cell*. At lower temperatures (below 183 K) a transition from a hexagonal to an orthorhombic cell was observed. The separation

between the two nearest neighboring vanadium ions on the same chain at room temperature is 2.805 Å, which is close to the atomic distance (2.624 Å) in pure metallic ( $\rho = 20 \mu\Omega \text{ cm}$ ) BCC vanadium. The much larger distance between the chains, 6.73 Å, suggests a quasi-one-dimensionality of the compound. As the electrical properties in the monocrystals were observed to be strongly affected by impurity content, the electrical resistivity, as a function of temperature from 80 to 350 K, was determined on well-characterized sintered bars. It was also noted that BaVS<sub>3</sub> begins to lose sulfur at approximately 370 K under vacuum. The measurement of resistivity revealed a metallic behavior at high temperatures with an associated change of slope at approximately 130 K. This change was (incorrectly) assigned to be a transition from the metallic to the insulating (MI) state.

---

---

## 2.2 Beginning to understand *BaVS<sub>3</sub>*

Ten years later, provoked by the magnetic susceptibility measurement of Takano and his coworkers (Takano *et al.*, 1977), the compound began to receive heightened attention. In particular, these authors found a Curie-like (paramagnetic) susceptibility in the metallic phase, and a sharp peak around  $T_{MI} = 70$  K, below which the susceptibility decreases with decreasing temperature. This is accompanied by a sharp increase of resistivity, suggesting an antiferromagnetic (AFM) order of the localized spins. The structural change from hexagonal to orthorhombic was confirmed. It was found that the structural transition is of the second order, setting in at  $T_S = 250$  K. The temperature dependence of the cell dimensions was determined and showed a sharp change at  $T_{MI}$ . These results were confirmed later by Sayetat *et al.* (1982), and are presented in Fig. 2.2.

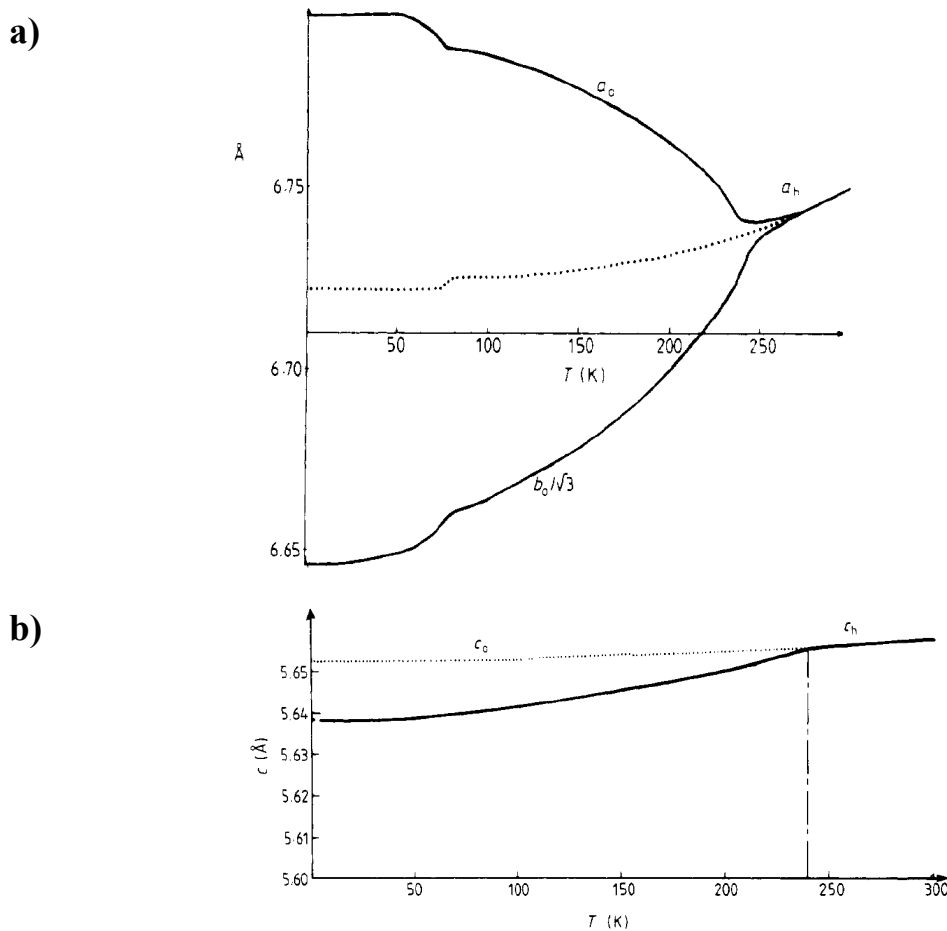


**Figure 2.2:** The thermal variation of unit cell parameters. The orthorhombic distortion appears at  $T_S = 250$  K, and increases by cooling as seen from the different change of lattice parameters. Those in the  $a$ - $b$  plane (a) show a sharp change at  $T_{MI}$ . On the contrary, the change of the  $c$ -axis lattice parameter (b) is moderate. Picture adopted from Sayetat *et al.* (1982).

By the end of the 70ies it was clear that pure BaVS<sub>3</sub> undergoes (at least) three successive phase transitions as the temperature is decreased from 300 to 5 K. The 240 K transition seems to be well understood; it corresponds to a change in the crystal structure and, as it will be shown later concerning the electrical properties of the system, it is accompanied by only a weak change in the slope of the resistivity. On the other hand, the origin of the two other transitions remained elusive and they remain a subject of discussion to this very day.

### 2.2.1 *Magnetic properties and their implications*

The first attempt to reconcile the high temperature paramagnetic behavior in the metallic phase and the vanishing susceptibility in the insulating phase, below  $T_{MI}$ , came from the already mentioned work of Massnet en co-workers (Massnet *et al.*,1979). A two-band model, shown in Fig. 2.3 was proposed. In the octahedral environment, the fundamental d wave functions belong to the  $t_{2g}$  triplet which, due to the non-perfect octahedral symmetry of the V site, is split into a fundamental  $e(t_{2g})$  doublet, corresponding to two orbitals extending principally in the  $x$ - $y$  plane, and a higher energy singlet  $d_z^2$  pointing along the chain direction (this is discussed in more detail in Chapter 3).

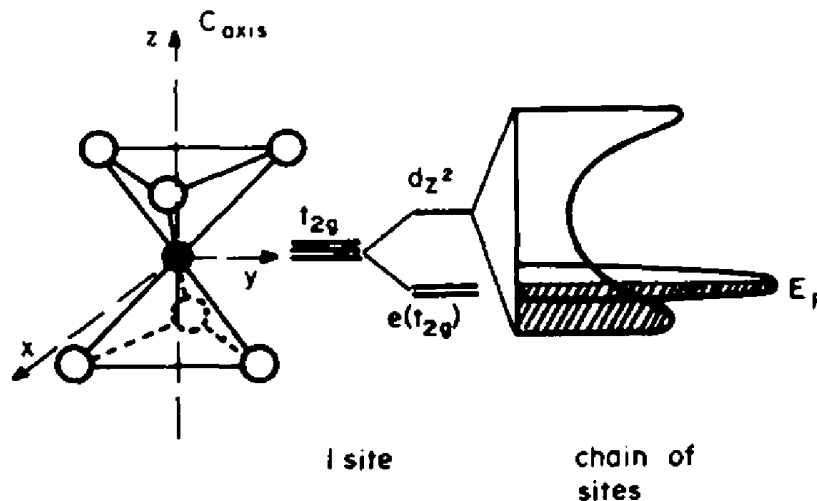


**Figure 2.3:** Left part of the figure shows the nearest neighbor sulfur (○) environment at the vanadium (●) site. In the middle part, a possible  $d$ -electron level diagram for one vanadium site is shown with the consequential density of the states for the chain of vanadium sites, in the right part of the figure. Picture originates from Massenet *et al.* (1979).

The short distance separating nearest neighbor vanadium atoms along a single chain leads to a large overlap of the  $d_z^2$  orbitals. Consequently, in the actual crystal, the  $d_z^2$  states should form a broad band. The  $e(t_{2g})$  orbitals which are actually tilted with respect to the  $x$ - $y$  plane also overlap with the nearest neighbor  $e(t_{2g})$  orbitals, but to a lesser extent, and should form a narrow band with a high density of states. The essentially delocalized electrons in the broad, partially filled,  $d_z^2$  band, which were supposed to be at the origin of the quasi-metallic behavior of BaVS<sub>3</sub> at room temperature, contribute very little to the magnetic susceptibility.

The magnetic properties were attributed mainly to the more localized, and hence magnetic, electrons in states of  $e(t_{2g})$  symmetry. The rapid increase of the resistivity was attributed to the AFM ordering at 70 K, being explained on the basis of a model (Slater, 1951). Shortly thereafter, in 1980, Massenet *et al.* (1980) proposed another scenario at the MI phase transition. They suggested that the break in the magnetic susceptibility detected at this transition is not related to an antiferromagnetic order but results instead from a progressive transfer of electrons from localized magnetic states to a non-magnetic band. The magnetic and the diamagnetic states would be separated by a small energy gap. Therefore, at the MI transition, BaVS<sub>3</sub>, goes from a Curie-Weiss paramagnetic metallic state to a diamagnetic non-metallic state.

In 1980, Heidemann and Takano (1980) published the results of inelastic neutron scattering experiments performed at low temperature on stoichiometric BaVS<sub>3</sub>. These authors measured the hyperfine interaction at the V sites by means of high-resolution inelastic spin-flip scattering of neutrons. The V nuclei have a large spin-incoherent neutron scattering cross section and are, therefore, ideal probes for the detection of hyperfine fields with neutrons. By analyzing the energy spectra of neutrons scattered in BaVS<sub>3</sub> at 10 and 40 K, Heidemann and Takano were able to conclude that a third phase transition must take place in this temperature range since magnetic order was found at 10 K. From the ratio of the total integrated inelastic intensity and under the assumption that the observed scattered intensity is only due to the spin-incoherent scattering from the V nuclei, they estimated that the ***fraction of V sites with an internal magnetic field of 75 kOe is ~ 45%***. This indicates the ***coexistence of non-magnetic and magnetic V sites in a magnetically ordered phase***. The temperature of the magnetic phase transition was determined by measuring the total scattered intensity at energy transfer  $\hbar\omega = 0$ , as a function of temperature. The value of  $31 \pm 1$  K was obtained. Heidemann and Takano stated that from their measurements no information could be obtained about the nature of the magnetic order existing below 31 K.

---

---

In 1981 Nishihara and Takano (1981) reported the results of pulsed Nuclear Magnetic Resonance (NMR) experiments at low and high frequencies carried out between room temperature and 1.3 K on polycrystalline samples of BaVS<sub>3</sub>. ***A weak single paramagnetic signal*** was observed from room temperature ***down to 229 K*** with no pronounced anomaly at the 240 K transition. The temperature dependence of the line shift, the line width and the decay time as deduced from spin-echo spectra of the <sup>51</sup>V nuclei taken below 80 K, ***confirmed the existence of the 31 K*** transition. Furthermore, Nishihara and Takano argued that based on their data, the 70 K transition involved a gradual pairing of the vanadium atoms in linear chains as to form covalent non-magnetic bonds with decreasing temperature. This gradual pairing would take place for only 81% of the vanadium atoms, while the remaining 19% would remain localized V<sup>4+</sup> cations, which would not contribute to the NMR signal. These latter cations would order magnetically at the 31 K transition.

Nishihara and Takano (1981) provided also a spin-echo spectrum at high frequencies. It was taken without an external field at 1.3 K by the use of a phase-incoherent pulsed NMR spectrometer, and revealed two resonance frequencies (106.0 MHz and 101.4 MHz) which originated from the <sup>51</sup>V nuclei. The magnitude of the fields at 1.3 K were determined to be 94.7 and 90.6 kOe, which are somewhat larger than the unresolved value of 75 kOe at 10 K determined by inelastic neutron scattering. This would indicate that at 1.3 K ***two independent magnetic sites for the V cations exist*** in the structure of BaVS<sub>3</sub>. The field dependence of the echo spectra at 1.3 K and the corresponding frequency-field diagrams show that the ***spin structure is antiferromagnetic***. Complex spin structures such as helical structures are possible; however, Nishihara and Takano concluded that the observation of the modulation of the spin-echo decay envelope indicates that the spin structure should be commensurate with that of the crystal. No discontinuities in the specific heat (Massenet *et al.*, 1980) and in the lattice parameters (Sayetat *et al.*, 1982) were observed at 31 K.

In 1991, Matsuura and his coworkers reported the first measurements of the magnetic and transport properties of BaVS<sub>3</sub> (Matsuura *et al.* 1991). A few years later the first band calculations, carried out by Solovyev *et al.* (1994), showed that the Fermi level in BaVS<sub>3</sub> lies at the narrow peak in the density of states, which indicates that the system is potentially sensitive to pressure changes. The band calculations were soon accompanied by the photoemission spectroscopy study of Nakamura *et al.* (1994). The strong suppression of  $T_M$  by increasing pressure was revealed in the work of Graf *et al.* (1995).

---

---

All of these aforementioned results will be completed by our much more detailed studies performed on high quality single crystals which will be presented and discussed in following chapters. But, to have a complete overview of the important events and ideas in the history of BaVS<sub>3</sub>, I will continue the presentation the model of Nakamura *et al.* (1994) in which the  $e(t_{2g})$  doublet lies lower in energy than the  $d_z^2$  orbital. It was proposed that the gradual orthorhombic distortion of the Jahn-Teller type below  $T_S$  lowers one of the  $e(t_{2g})$  levels and that below  $T_{MI}$ , electrons are fully transferred to the lowest energy level making it half-filled, and resulting in the opening of a Mott-Hubbard gap (Mott, 1974). The authors argued that the effects of large fluctuations as a consequence of the one dimensionality of the system prevent the long-range magnetic order. Finally the suppression of the magnetic susceptibility below  $T_{MI}$  was attributed to the growth of the antiferromagnetic spin correlation resulting with the magnetic order below  $T_x$ . If the proposed scenario is correct, the orbital degeneracy is quenched at the MI transition which inhibits the possibility of orbital order at lower temperatures. This is in contradiction with the Nuclear Quadruple Resonance (NQR) measurements by Nakamura *et al.* (1997), where a ***large electrical field gradient is observed below  $T_x$ .***

---

---

## 2.3 *Lausanne in sight*

In the 90ies, several important things happened which decided my future and lead me towards Lausanne and BaVS<sub>3</sub>. Besides the fact that these were the years when I entered the world of physics and significant progress was achieved in investigating BaVS<sub>3</sub>, as presented above, these were also the years when the research on the compound started in Lausanne. New questions arising from the work of my future group in Lausanne and its collaborators placed the material under a new spotlight of interest, uncovering even more intriguing physical properties of the material.

### 2.3.1 *High-quality single crystals*

The first step of this kind happened in 1995 when the Fukuoka-Lausanne collaboration (Kuriyaki *et al.*, 1995) resulted in the new method of synthesis; single crystal growth of BaVS<sub>3</sub> in melted tellurium as flux. The crystals were obtained in the form of large needles with typical dimensions of about 10 mm in length and 1 mm in width. For the first time it was found that a change in the slope of the temperature-dependent resistivity occurs at  $T_S$ , which indicated that the synthesized crystals were of high quality. Several further years passed until a breath of fresh air was given to these samples by taking them out of a drawer and into the daylight. In 2000, Mihály *et al.* (2000) published the direction-dependent conductivity and susceptibility measurements performed on the single crystals. The conduction anisotropy (shown in Fig. 2.4), defined as the ratio of the conductivities measured along and perpendicular to the chain direction, is surprisingly low above  $T_{MI}$ ,  $\sigma_c/\sigma_a \approx 3$ , putting a question-mark on the one-dimensional character of the system.

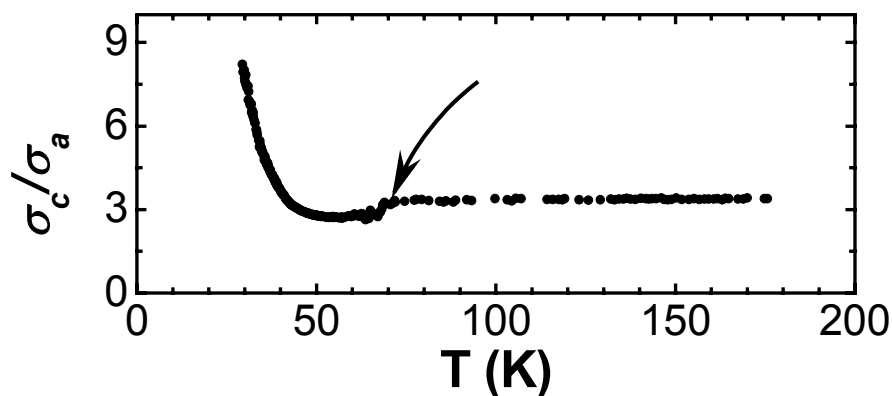


**Figure 2.4:** Temperature dependence of the conduction anisotropy  $\sigma_c / \sigma_{ab}$  in BaVS<sub>3</sub>. The arrow indicates the MI transition temperature. Picture from Mihály *et al.* (2000).



The anisotropy is temperature independent in the metallic phase and there is only a small jump at the MI transition. Below  $T_{MI}$ , the anisotropy has the same small value over a broad temperature range down to about 30-40 K. Note that in this range of  $T$ , the resistivity increases by about six orders of magnitude in both directions. The low-temperature upturn below  $T_{MI}$  in Fig. 2.4 was attributed to the impurities. The  $d_z^2$  orbitals have large overlap along the chain directions and, taking into account the wide separation of the vanadium chains, it is reasonable to expect a high anisotropy in electrical properties of the system. Since this is not the case, it was proposed that the hopping along more isotropic channels, resulting from the weak indirect overlaps of two  $e(t_{2g})$  orbitals, is the origin of electron propagation.

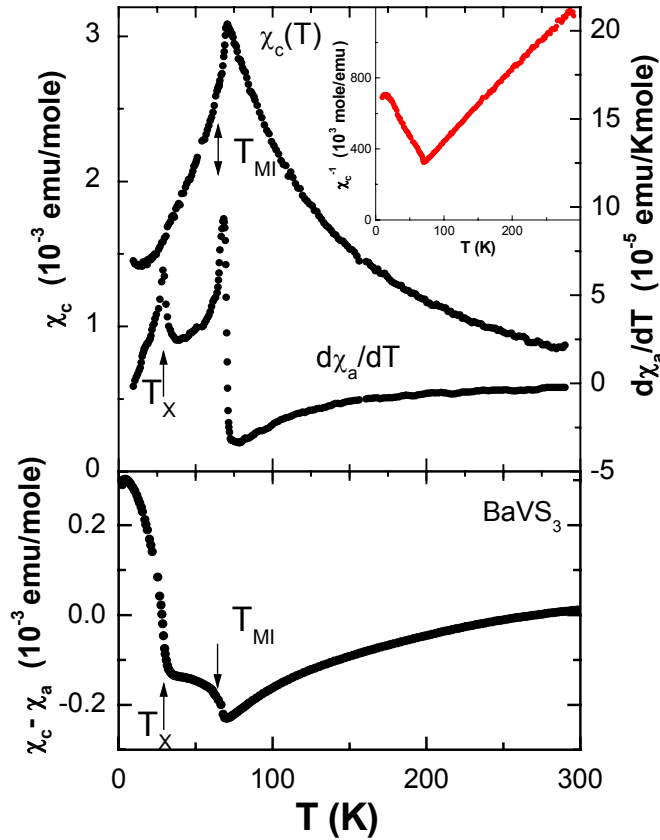


**Figure 2.5:** Temperature dependence of the  $c$ -axis magnetic susceptibility ( $\chi_c$ ), the derivative of the  $a$ -axis susceptibility ( $d\chi_a/dT$ ), and susceptibility anisotropy ( $\chi_c - \chi_a$ ). The inset clearly reveals the Curie susceptibility above  $T_{MI}$ . Data from Mihály *et al.* (2000).

The magnetic susceptibility measurement (results summarized in Fig. 2.5) confirmed the previous data on the stoichiometric samples: the Curie-Weiss behavior in the metallic phase is followed by the steep decrease at  $T_{MI}$  showing that the number of polarizable moments drops drastically upon entering the insulating phase. In Fig. 2.5,

$\chi_c$  and  $\chi_a$  look very similar, and are both fairly smooth at  $T_x$ . However, a sharp peak in the temperature derivative of the a-axis susceptibility  $d\chi_a / dT$ , and **a sudden break in the anisotropy  $\chi_c - \chi_a$  at  $T_x \approx 30$  K** was found, giving another piece of evidence for the phase transition within the insulating phase.

It was proposed that the MI transition involves both the spin and the orbital degrees of freedom in a similar manner as for  $V_2O_3$ , where the onset of orbital order leads to an insulating state whose magnetic ordering pattern cannot be anticipated from the short-range order found in either of neighboring phases (Paolasini *et al.*, 1999). Since, in  $BaVS_3$ , the V chains form a triangular array, it was suggested that the frustration results in the intermediate ( $T_x < T < T_{MI}$ ) unordered magnetic phase. Instead, in this temperature range, the system has an overall nonmagnetic state with peculiar spin and orbital short-range order. Finally, by decreasing the temperature well below the MI transition, at  $T_x$ , a long-range order is established.

### 2.3.2 *The importance of high pressure*

Shortly afterwards, further exciting results from the work of Forró *et al.* (2000) made the material even more appealing. The phase diagram of  $BaVS_3$  was studied under hydrostatic pressure, up to 2.2 GPa, by resistivity measurements. As in the work of Graf *et al.* (1995), the **suppression of the MI transition** with temperature was observed. On this occasion, however, the observation was made on single crystals. In addition, it was found that at high enough pressure, the MI transition vanishes and the behavior is metallic in the whole of the measured temperature region (1.5 to 300 K). Interestingly, the low temperature behavior of the resistivity (over several decades of Kelvins) showed a **power law** temperature dependence of the form:  $\Delta\rho = \rho - \rho_0 \sim T^n$ , **with  $1 \leq n < 2$** , (where  $\rho_0$  is the residual resistivity), differing from the  $n = 2$  Fermi liquid law. The interpretation of this behavior usually invokes nearness to a quantum critical point (QCP). The critical pressure  $p_{cr}$  was estimated to be 2 GPa and, for  $p < p_{cr}$ , the resistivity in the metallic phase has a marked minimum which has been identified as an extended precursor regime to the insulating phase. As the overall result of the resistivity measurements under pressure, the  $p$ - $T$  phase diagram, shown in Fig. 2.6, was proposed.

On the eve of December 1<sup>st</sup> 2000, I came to Switzerland (not Lugano but Lausanne) overwhelmed by the colors of early autumn, and joined The Glass Beads Game (Hesse, 1945). My first task was to develop a self-clamped pressure cell with the possibility of simultaneous measuring of thermoelectric power (TEP), resistivity and

---

pressure. A year and several months were needed to solve related technical problems. The simultaneous measurement meant that the number of electric leads, passing from ambient pressure into the pressure cell, was supposed to be considerably augmented in comparison with the self-standing resistivity measurement.

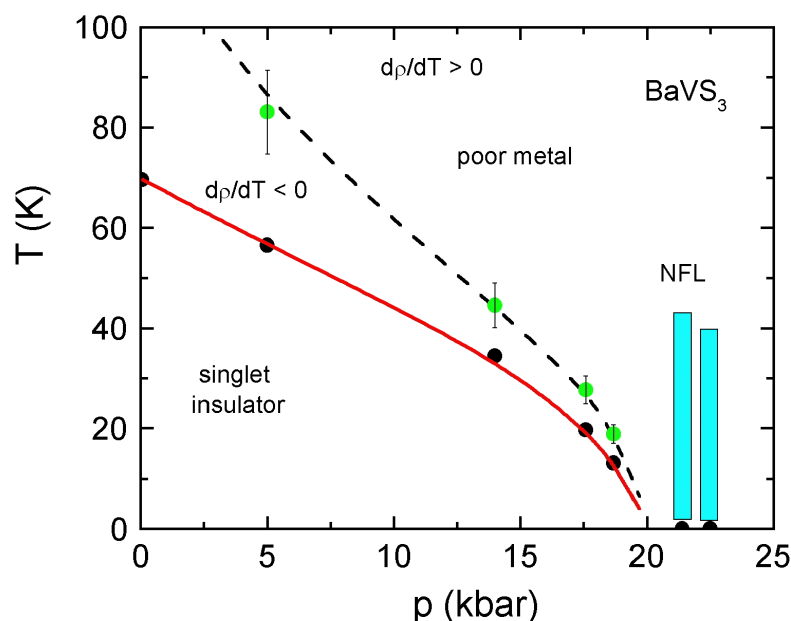


**Figure 2.6:** The  $p$ - $T$  phase diagram of  $\text{BaVS}_3$ , based on the early resistivity measurements. The solid red line indicates the MI phase boundary, by the dashed black line the precursor region is marked, and the blue columns indicate the region of  $\Delta\rho \sim T^n$  ( $1 \leq n < 2$ ) non-Fermi-liquid behavior. Picture from Kézsmárki, (2003).

The biggest problem and the first step was mastering of feed-through production (Appendix 1). This is a wire passage which allows the change of pressure from the ambient pressure to several GPa without cutting the wires. The next step was to learn how to drive the wires in the cell. At high pressure, the liquid in the cell freezes and thereby breaks the wires. Finally, a homemade sample holder was designed, which fits in the pressure cell, enabling the measurement of TEP in the pressure medium. By solving the principal technical problems, the time came to deal with  $\text{BaVS}_3$ .

To return to the point and close the circle without taking a space ship to Saturn, as I was heading home for the Christmas and New Year break in 2001 with the sounds of An der schönen, blauen Donau, by J. Strauss II filling my car, I reflected. The experiment was ready. Those monocrystals of  $\text{BaVS}_3$  I was about to measure bore a strange resemblance to a monolith, and April 1968 was not only the premier month for  $\text{BaVS}_3$ , but also for Kubrick's film 2001: A space Odyssey. What sort of a journey was I embarking upon?

## 2.4 References

- Forró L., R. Gaál, H. Berger, P. Fazekas, K. Penc, I. Kézsmárki, G. Mihály. 2000. Pressure induced quantum critical point and non-Fermi-liquid behavior in BaVS<sub>3</sub>. *Phys. Rev Lett.*, **85**(9), 1938.
- Gardner R. A., M. Vlasse, and A. Wold. 1968. Crystal structure and electrical properties of barium vanadium sulfide. *Am. Ceram. Soc. Bull.* **47**(4), 383.
- Gardner R. A., M. Vlasse, and A. Wold. 1969. Preparation, properties and crystal structure of barium vanadium sulfide. *Acta Crys. B*, **25**, 781.
- Graf T., D. Mandrus, J. M. Lawrence, J. D. Thompson, P. C. Canfield, S. W. Cheong, and L. W. Rupp. 1995. Suppression of the metal-to-insulator transition in BaVS<sub>3</sub> with pressure. Jr., *Phys. Rev B*, **51**(4), 2037.
- Heidemann A, and M. Takano.1980. Hyperfine interaction and magnetic phase transition of BaVS<sub>3</sub> observed by inelastic spin-flip scattering of neutrons. *Phys. Stat. Sol. B*, **100**(1), 343.
- Hesse H., The glass bead game (Magister Ludi), Vintage Classics. UK.
- Kézsmarki I. 2003. Phase diagram of a Correlated d-electron System: Experimental Study of BaVS<sub>3</sub>. *PhD thesis*. Ecole Polytechnique Fédérale de Lausanne. Lausanne. Swiss.
- Kuriyaki H., H. Berger, S. Hishioka, H. Kawakami, K. Hirakawa, and F. A. Levy, *Synthetic Metals*, **71**(1-3), 2049 (1995), Synthesis and characterization of BaVS<sub>3</sub> single crystal grown in melted Te
- Landau L. D. and E. M. Lifshitz. 1959. Statistical Physics. London, Pergamon Press. UK.
- Massenet O., M. Avignon, B. K. Chakraverty, and J. Marcus. 1980. *1980 Ann. Condensed Matter Div. EPS Meeting, 9 - 11 April*.
- Massenet O., R. Buder, J. J. Since, C. Schlenker, J. Mercier, J. Kelber, and D. G.
- 
-

Stucky. 1978. BaVS<sub>3</sub>, a quasi one dimensional ferromagnet of antiferromagnet depending on stoichiometry. *Mat. Res. Bull.*, **13**(3), 187.

Massenet O., J. J. Since, J. Mercier, M. Avignon, R. Buder, V. D. Nguyen, and J. Kelber. 1979. Magnetic and electrical properties of BaVS<sub>3</sub> and BaV<sub>x</sub>Ti<sub>1-x</sub>S<sub>3</sub>. *J. Phys. Chem. Solids*, **40**(8), 573.

Matsuura K., T. Wada, T. Nakamizo, H. Yamauchi, and S. Tanaka. 1991. Magnetic and transport properties of BaV<sub>1-x</sub>Ti<sub>x</sub>S<sub>3</sub> ( $0 \leq x \leq 0.2$ ). *Phys. Rev B*, **43**(16), 13118.

Mihály G., I. Kézsmárki, F. Zámorszky, M. Miljak, K. Penc, P. Fazekas, H. Berger, and L. Forró. 2000. Orbitally driven spin pairing in the three-dimensional nonmagnetic Mott insulator BaVS<sub>3</sub>: Evidence from single-crystal studies. *Phys. Rev B*, **61**(12), R7831.

Mott N. F. 1974. *Metal-Insulator Transitions*. London, Taylor and Francis.

Nakamura H., H. Imai, and M. Shiga. 1997. Possible orbital ordering in a spin-singlet ground state: <sup>51</sup>V NMR and NQR study of BaVS<sub>3</sub>. *Phys. Rev Lett.*, **79**(19), 3779.

Nakamura M., A. Sekiyama, H. Namatame, A. Fujimori, H. Yoshihara, T. Ohtani, A. Misu, and M. Takano. 1994. Metal-semiconductor transition and Luttinger-liquid behavior in quasi-one-dimensional BaVS<sub>3</sub> studied by photoemission spectroscopy. *Phys. Rev B*, **49**(23), 16191.

Nishihara H., and M. Takano. 1981. NMR study of the metal-insulator-magnetic transitions in BaVS<sub>3</sub>. *J. Phys. Soc. Japan*, **50**(2), 426.

Paolasini L., C. Vettier, F. de Bergevin, F. Yakhou, D. Mannix, A. Stunault, W. Neubeck, M. Altarelli, M. Fabrizio, P. A. Metcalf, and J. Honig. 1999. Orbital Occupancy Order in V<sub>2</sub>O<sub>3</sub>: Resonant X – Ray Scattering Results. *Phys. Rev Lett.*, **82**(23), 4719.

Sayetat F., M. Ghedira, J. Chenavas, and M. Marezio. 1982. Correlations between crystallographic data and physical properties at the 240K and 80K phase transitions in

---

---

stoichiometric BaVS<sub>3</sub>. *J. Phys. C: Solid State Phys.*, **15**(8), 1627.

Slater J. C. 1951. Magnetic Effects and Hartree - Fock Equation. *Phys. Rev.*, **82**(4), 538.

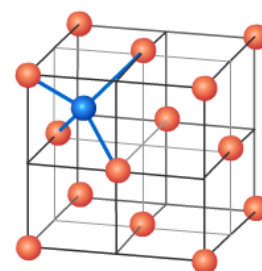
Solovyev I. V., V. I. Anisimov, and E. Z. Kurmaev. 1994. LMTO-ASA Band Structure Calculations of BaVS<sub>3</sub>, BaTiS<sub>3</sub> and their solid solutions. *Physica Scripta.*, **50**(1), 90.

Takano M., H- Kosugi, N. Nakanishi, M. Shimasa, T. Wada, and M. Noizumi. 1977. Electrical, magnetic and structural transitions of BaVS<sub>3</sub>. *J. Phys. Soc. Japan*, **43**(3), 1101.



## Chapter 3

# CRYSTAL SYMMETRY ANALYSIS AND ELECTRONIC BAND STRUCTURE



<b>3.1</b>	<b>CRYSTAL FIELD SPLITTING</b>	<b>28</b>
<b>3.2</b>	<b>SYMMETRY ANALYSIS</b>	<b>33</b>
<b>3.3</b>	<b>LOCALIZED LIMIT</b>	<b>38</b>
3.3.1	CONSTRUCTION OF THE MODEL	38
3.3.2	TESTING AND INTERPRETATION OF THE MODEL	40
<b>3.4</b>	<b>ITINERANT LIMIT</b>	<b>43</b>
3.4.1	AB INITIO CALCULATION OF THE BAND STRUCTURE	43
3.4.2	THE TIGHT BINDING APPROXIMATION	46
3.4.2.1	Analysis of the three-band model	49
3.4.2.2	The influence of sulfur and the four band model	53
3.4.3	ARPES AND TIGHT BINDING: A SYNERGISTIC COOPERATION	55
<b>3.5</b>	<b>CONCLUDING REMARKS</b>	<b>59</b>
<b>3.6</b>	<b>REFERENCES</b>	<b>60</b>

In this chapter we will discuss what one can learn about the electronic structure of  $\text{BaVS}_3$  from the crystal symmetry and its lowering due to structural phase transitions. Crystal symmetry is an important factor in band structure calculations which will be reviewed and compared to recent angle resolved photoemission measurements.

---



### 3.1 Crystal field splitting

The Coulomb interaction between an electron of charge  $-e$  and a nucleus of charge  $+Ze$  is described with the attractive potential  $V(r) = -Ze^2 / r$ . Solving the appropriate spherically symmetric atomic Hamiltonian  $H_{at}$ , neglecting spin-orbit coupling,  $2l + 1$  ( $l = 2$  for  $d$ - electrons) degenerate eigenvalues and eigenstates can be found. The degeneracy of the state is determined by the dimension of the irreducible representations of the 3D rotation group. On the other hand, an ion in a crystal is always surrounded by other ions which lead to a crystalline electric field,  $H_{cf}$  perturbing the atomic states. The new Hamiltonian is:

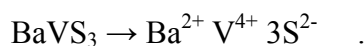
$$H = H_{at} + H_{cf}.$$

Assuming that the crystal field is purely electrostatic the surrounding ions can be replaced by charge distributions giving the potential at the lattice site  $\mathbf{r}$  expressed through the crystal field Hamiltonian:

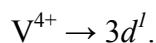
$$H_{cf} = \sum_j V(\mathbf{r} - \mathbf{R}_j),$$

where the  $\mathbf{R}_j$ -s represent the positions of the ions. The above Hamiltonian has, as its important feature, a symmetry which is imposed by the crystal. As this symmetry is necessarily lower than the isolated atomic system, the degeneracy of the atomic states is lifted. The splitting scheme is characteristic of a given symmetry of a crystal field, and can be determined by the standard methods explained elsewhere (Abragam and Bleaney, 1970). In the present discussion, however, we will focus only on those aspects that are relevant for the case of  $\text{BaVS}_3$  (Ballhausen, 1962). The whole approach is meaningful as long as the local states, in the metallic state in particular, are well described by the atomic wave-functions and to the extent that the tight-binding approximation is applicable. We will argue that both of these conditions are satisfied for  $\text{BaVS}_3$ . However it should be kept in mind that while symmetry analysis through group theory is a tool that can qualitatively reveal how a given set of states will be split in a given environment, it cannot predict the quantitative energy and sequence of the resulting levels. Such a prediction requires much more detailed model calculations.

Using the stoichiometric formula of  $\text{BaVS}_3$ , and supposing a complete charge transfer it follows that



Barium and sulfur ions have full electron shells while one electron remains in the vanadium  $3d$  levels. It is this electron that is primarily responsible for the electronic properties of the compound,



At room temperature, the vanadium site in  $\text{BaVS}_3$  feels a hexagonal rather than cubic crystal field because the surrounding sulfur octahedron is stretched along the  $c$  direction. The symmetry at the vanadium site is lowered to orthorhombic at  $T_S$  through a second order phase transition (Takano *et al.*, 1977). Let us examine how this affects the  $3d$  levels:

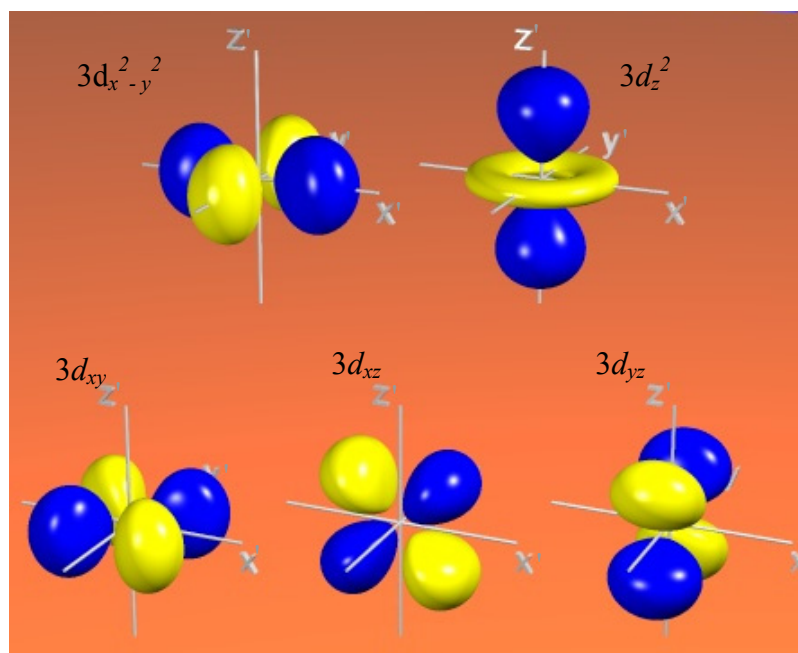


**Figure 3.1:** The shape of the five-fold degenerate  $3d$  orbitals. For each, the yellow zones signify regions in which the wave functions have negative values whereas the blue zones denote positive values. Picture from: <http://www.shef.ac.uk/chemistry/orbitron/AOs/3d/wave-fn.html>.

In an isotropic environment, the  $3d$  subshell is 5-fold degenerate (Fig. 3.1) with the standard  $3d_{xy}$ ,  $3d_{xz}$ ,  $3d_{yz}$ ,  $3d_{x^2-y^2}$  and  $3d_z^2$  labels employed to distinguish the different eigenstates. Four of these functions have the same shape but are aligned differently in space. The fifth function ( $3d_z^2$ ) has a different shape. Each of the  $3d_{xy}$ ,  $3d_{xz}$ ,  $3d_{yz}$ , and  $3d_{x^2-y^2}$  orbitals has four lobes. There are two planar nodes normal to the axis of the orbital (for instance, the  $3d_{xy}$  orbital has a node when either  $x = 0$  or  $y = 0$ ). The  $3d_z^2$

orbital is different and has two conical nodes.

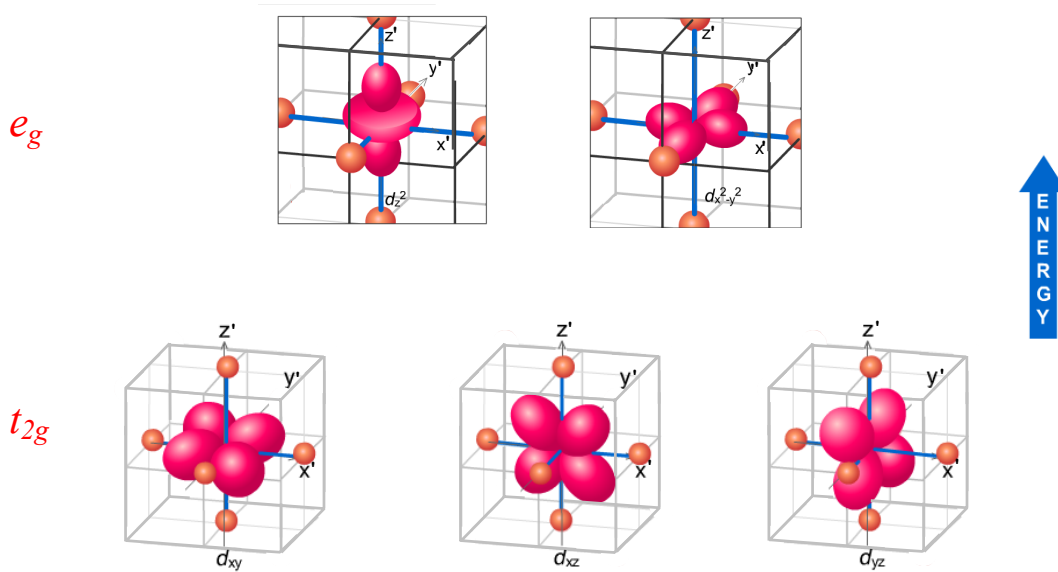


**Figure 3.2:** Directions in space of  $d$  orbitals of an atom in an octahedral site. The arrow signifies the difference in energy between the low lying 3-fold degenerate  $d_{xy}$ ,  $d_{xz}$ ,  $d_{yz}$ , (pointing in between ligands) and higher-energy doubly-degenerate orbitals  $d_{yz}$ , and  $d_{x^2-y^2}$  (pointing towards ligands).

Through an "octahedral crystal field" the six sulphur atoms, on either side of all three octahedral axes ( $x', y', z'$ ) shown in Fig. 3.2, repel the electron in the  $d$  orbitals that lie on the axes ( $d_{yz}$ , and  $d_{x^2-y^2}$ ) and lift the 5-fold degeneracy. The law of conservation of energy says that if these orbitals are destabilized (higher in energy), the other orbitals ( $d_{xy}$ ,  $d_{xz}$ ,  $d_{yz}$ ) must be stabilized (lower in energy) so that the net effect is no change in energy. The energy difference between the 3-fold degenerate  $t_{2g}$  level and the 2-fold degenerate  $e_g$  level is the crystal field splitting energy. The magnitude of the splitting depends on the type of ion whose levels are being split and the type of ion which produces the splitting.

Further lowering of the crystal symmetry, from the octahedral to trigonal (hexagonal) has the effect of splitting the 3-fold degenerate  $t_{2g}$  level while preserving the degeneracy of the higher-energy  $e_g$  level. In order to see this, it is convenient to use a coordinate system ( $x, y, z$ ) parallel to the ( $a, b, c$ ) axes of the crystalline Bravais lattice of the crystal (Fig. 3.3). In this coordinate system the three, presumably lowest energy, orbitals can be chosen as:

$$d_z^2 = \frac{3z^2 - r^2}{\sqrt{12}}, \quad d_{ex} = \frac{x^2 - y^2}{\sqrt{6}} - \frac{xz}{\sqrt{3}}, \quad d_{ey} = \frac{xy}{\sqrt{3/2}} + \frac{yz}{\sqrt{3}}.$$

These orbitals are linear combinations of the three orbitals which are degenerate in the octahedral environment, i.e. the forms of  $d_{ex}$  and  $d_{ey}$  are obtained under the assumption that the octahedral splitting is large. Their directions with respect to crystal lattice are shown in Fig. 3.3. It is noteworthy that, in the trigonal lattice,  $d_z^2$  optimizes the overlap between V – ions along the chain. The fact that the V – S octahedra form a chain affects the site energy of the  $d_z^2$  orbital (looking along the chains) in a manner different than that of the  $d_{ex}$ ,  $d_{ey}$  (with  $e_g$  symmetry) manifests itself by causing the splitting of the  $t_{2g}$  level into a single  $d_z^2$  level and a doubly-degenerate  $e(t_{2g})$  level. Finally, sliding the  $xy$  planes of the crystal decreases the symmetry to orthorhombic, completely lifting the degeneracy of the  $d$  levels.

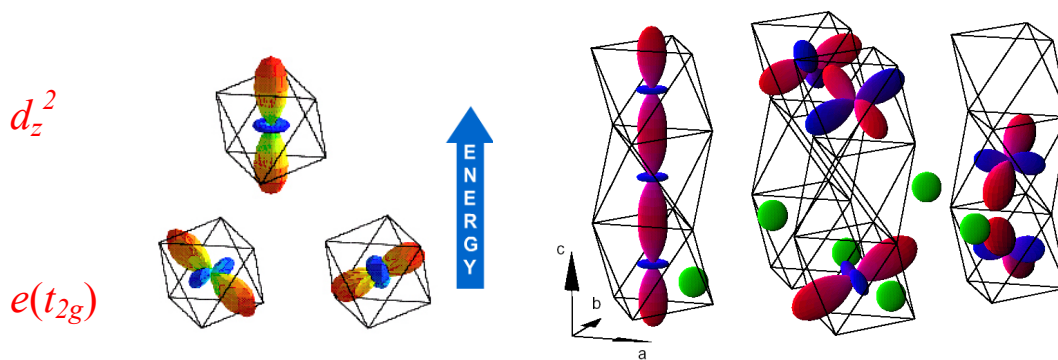


**Figure 3.3:** Orientation of three lowest lying orbitals with respect to the principal crystallographic axes.

The sequence and the magnitude of the splitting between the  $d_z^2$  level and the doubly-degenerate  $e(t_{2g})$  level in  $\text{BaVS}_3$  are still subject to discussion. One possible splitting scheme is presented in Fig. 3.4. It is based on the fact that the measured electrical conductivity along and perpendicular to the chains shows a low anisotropy,  $\sigma_c/\sigma_{ab} = 3.4$  (Mihály *et al.*, 2000). As the  $d_z^2$  orbital is highly anisotropic with large overlap only along the V - V chains, the electrical conductivity ratio suggests that the electron transport along the  $a$  and  $b$  axes comes mainly from the two other orbitals. Since the conduction electrons sit at the Fermi level, the assumption is that at least one of those two orbitals is present at the Fermi level, in addition to  $d_z^2$ . This picture is supported by the latest angle resolved photoemission spectroscopy (ARPES) experiments (*vide infra*) that clearly demonstrate the existence of the  $d_z^2$  band below the Fermi level.

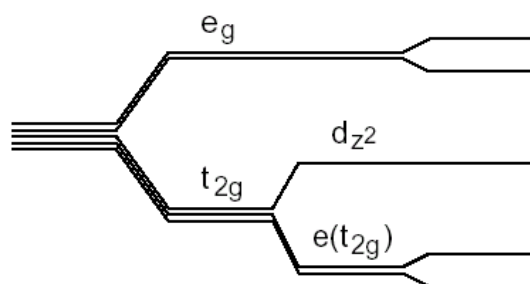
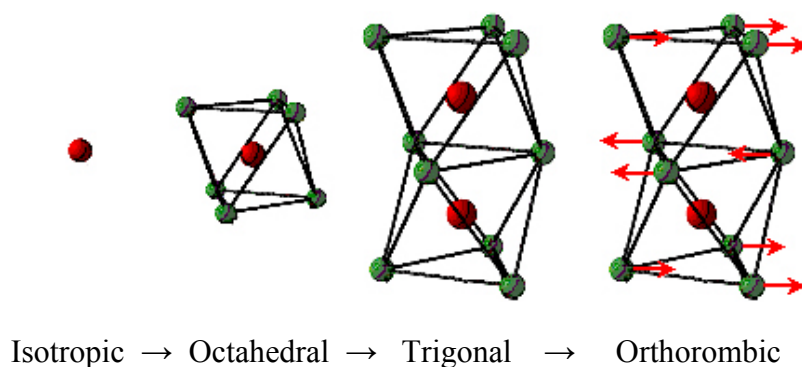


**Figure 3.4:** Possible energy scheme of the  $3d$  orbitals as the symmetry of the vanadium site is reduced from isotropic to orthorhombic.

After discussing the basic crystallographic data and considering the dominant crystal field effects, two different paths could be followed. The first one is the localized limit, handy for interpretation of the insulating phase, in which all intra-ionic interaction terms are taken into account through Hund's rules. The band effects are considered only in the sense that they mediate the inter-site couplings of the local variables. The second limit is the itinerant limit in which the influence of the crystal field is taken into account in the calculation of the tight-binding electronic bands. Once the bands are obtained, the interactions (particularly the intra – atomic interactions in the  $d$  levels) are treated explicitly. When small in magnitude compared to the band energies, these processes (centered about the Fermi level and thereby determining the properties of the system) can be treated perturbatively in the corresponding calculations.

### 3.2 Symmetry analysis

At ambient pressure,  $\text{BaVS}_3$  undergoes two successive second-order phase transitions. Landau proposed a phenomenological theory for describing such phase transitions introducing the concept of the order parameters (Landau, 1980). He used the fact that the system has a higher symmetry at high temperatures than it does at low temperatures. At the phase transition, the symmetry is thus lowered. The symmetry of the crystal, at a certain temperature, is described by a set of symmetry group generators. In the case of a second order phase transition, this set is decreased by only one symmetry group generator. This is reflected through the appearance of a non-zero order parameter at the transition. In order to determine a suitable order parameter, associated with the correct symmetry breaking, it is necessary to find the symmetries of the crystal above and below the transition. In this way it is possible to identify which of the symmetry group generators is missing in the low temperature phase. In the following discussion magnetic effects are not taken in account.

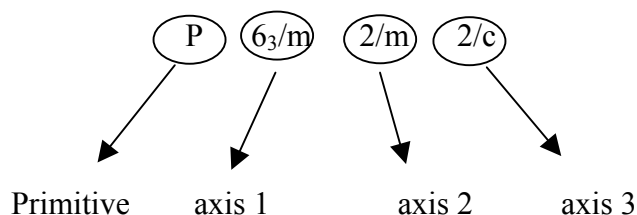


**Figure 3.5:** Meaning of the space group notation for  $\text{BaVS}_3$  at ambient pressure and temperature.

$\text{BaVS}_3$  crystallizes in a hexagonal structure. The space group of the structure is  $P6_3/m2/m2/c$  ( $a = 6.719 \text{ \AA}$  and  $c = 5.619 \text{ \AA}$ ) at room temperature, which is characterized by  $\text{VS}_3$  chains running along the  $c$  axis. The name of the space group is composed of four parts (Fig. 3.5). The  $P$  indicates that the unit cell is primitive. The  $6_3/m$  notation is related to the symmetries of the highest symmetry axis and, in the case of  $\text{BaVS}_3$ , it is the  $c$  axis. The number 6 stands for the  $60^\circ$  rotations, but after every rotation a translation for a half the length of the unit cell along the  $c$  direction should be performed to transform the crystal into itself. Repeating these screw rotations 6 times shifts the unit cell by three  $c$  lattice vectors, and that is the meaning of the index 3. The  $m$  indicates a mirror plane perpendicular to the  $c$  axis. The other two axes have a 2 fold rotational axis. One mirror plane (labeled by  $m$ ) is perpendicular to the  $a$ -axis and one glide plane (labeled by  $c$ ) is perpendicular to the  $b$ -axis.

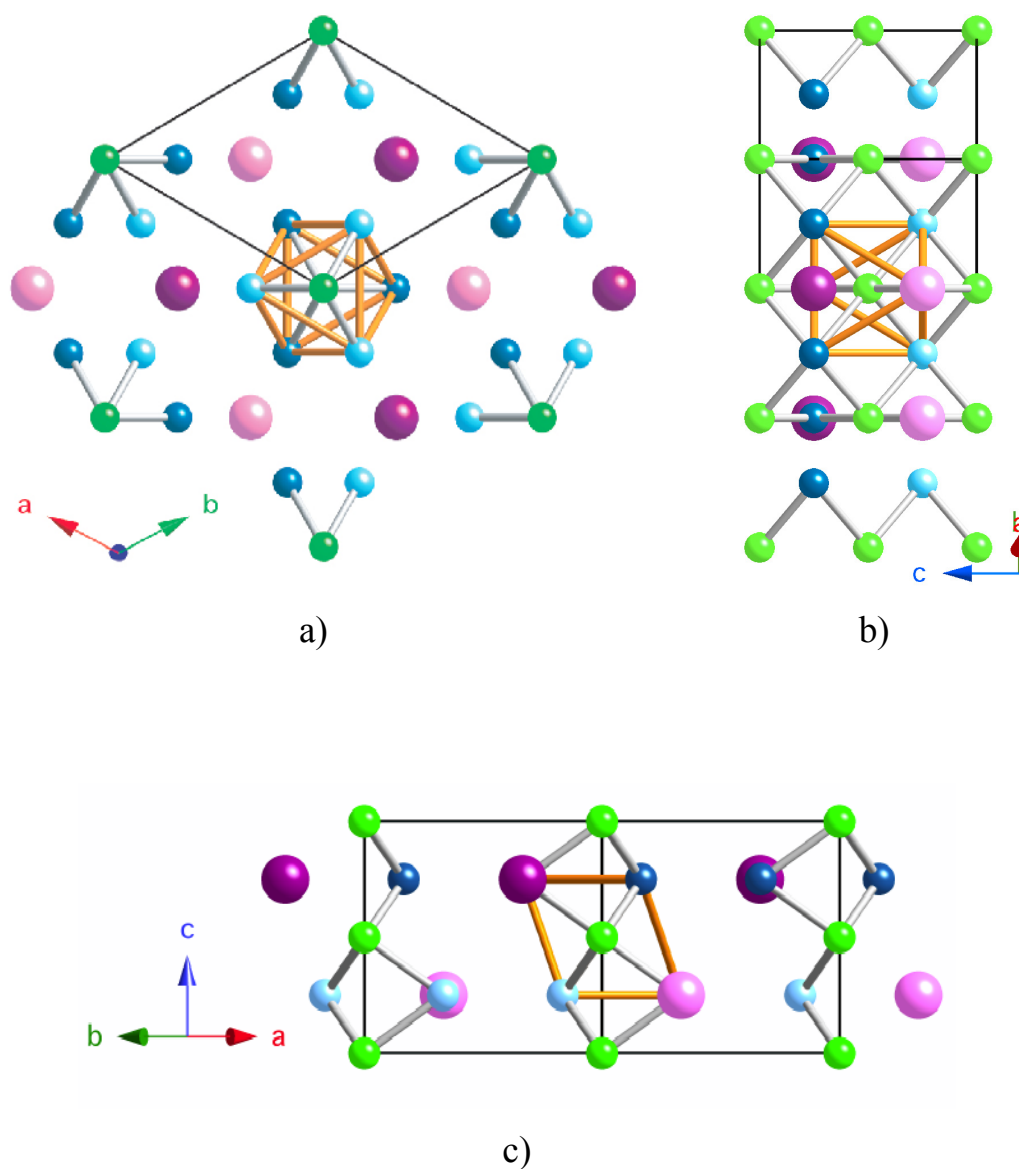


**Figure 3.6:** Ball and stick representation of BaVS<sub>3</sub> crystal oriented in three suitable directions (a), b) and c)) for studying symmetries of the lattice. Vanadiums are green, Bariums are violet (light at  $\frac{1}{4}c$  dark at  $\frac{3}{4}c$ ) and Sulfurs are blue (light at  $\frac{1}{4}c$  dark at  $\frac{3}{4}c$ ). Picture made by use of the [www.crystallmaker.com](http://www.crystallmaker.com).

The 24 symmetry operations for this space group are listed in International tables for crystallography (Hahn, 2002). In the subsequent discussion, we utilize the same notation as that outlined therein.

It should be noted that symmetry operations containing a translation by  $\frac{1}{2}$  of the Bravais vector along the  $c$  direction, i.e. the so called screw axes and glide plane

symmetry operations, imply the equivalence of vanadium sites and/or of bonds (repeating such operations twice has the effect of shifting one unit cell into the adjacent one).

The 24 symmetry operations fall in 12 conjugated classes which are generated by combining eight generators, (four of them are trivial, identity and translations  $t$  for a lattice vector) and the remaining four are:

- (2) – three fold axis,  $120^\circ$  rotations around the vanadium chain (Fig. 3.6a).
- (4) – conjugated class for itself,  $180^\circ$  rotation around the vanadium chain + a translation by  $\frac{1}{2}$  in  $c$  direction (Fig. 3.6a).
- (7) – fold axis,  $180^\circ$  rotation around the  $a$  axis (Fig. 3.6c).
- (13) – inversion around vanadium (only possible if the vanadium atoms form straight chains, see Fig. 3.6b).

At the second order phase transition ( $T_S$ ), the symmetry is decreased and one of these generators is excluded. Consequently, the group of symmetry operations is reduced to the one of the subgroups. There are several possible reductions, listed in Hahn (2002), and one which is appropriate for the phase of  $\text{BaVS}_3$  below  $T_S$  should be chosen.

The new crystal lattice has  $C2/m2/c2_1/m$  group symmetry, where  $C$  stands for a face centered unit cell. There is no longer a  $120^\circ$  rotation around  $c$  axis and therefore (2) has ceased to be a symmetry operation generator. Consequently the order parameter at the  $T_S$  removes this symmetry. At the transition, the vanadium chains remain straight while the sulfur octahedra become deformed (Fig. 3.7) in a zig-zag manner, causing the (additional) splitting of the  $e_g$  levels. It should be emphasized that (13) is still a generator of  $C2/m2/c2_1/m$  group and **importantly, the screw axis symmetry remains below  $T_S$**  (which will lead to  $\frac{1}{4}$  and not  $\frac{1}{2}$  filling of the bands below  $T_S$ ).

Below  $T_{MI}$ , based on X-ray-diffraction measurements of the  $\text{BaVS}_3$  single crystal, Inami *et al.* (2002) reported the existence of superlattice reflections which double the lattice constant  $c$ . They postulated the  $Imm2$  group, where  $I$  stands for a body centered unit cell, to be most probable space group below  $T_{MI}$ . In agreement with the NMR data they found that the low-temperature insulator phase contains two inequivalent



vanadium sites within the doubled unit cell aligned along the  $c$  axis in an alternating manner:

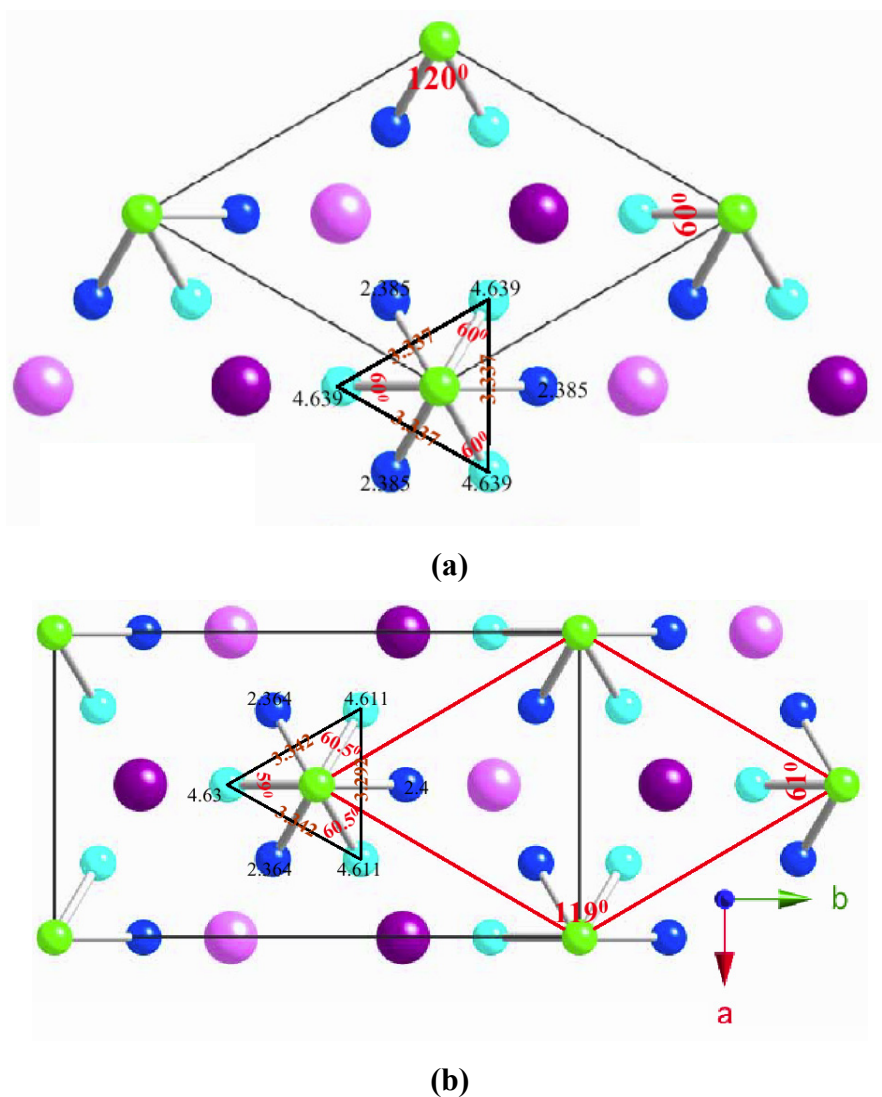


**Figure 3.7:** Projection view, along the  $c$ -direction, of the crystal structure of  $BaVS_3$  (a) in the hexagonal structure at room temperature (b) in the orthorhombic structure at 100 K. Vanadium atoms are green, barium atoms are violet (light at  $\frac{1}{4}c$  dark at  $\frac{3}{4}c$ ) and sulfurs atoms are blue (light at  $\frac{1}{4}c$  dark at  $\frac{3}{4}c$ ). The vanadium-sulfur distance is marked by black numbers. The in-plane distances of sulfur are denoted by brown numbers. All the distances are given in Angstroms. The red numbers refer to in-plane angles between sulfur or vanadium atoms.

It should be noted that, using the analysis of the homogenous group-subgroup relations between space groups that lead to Fig. 3.8, it is not possible to support the assumption of the  $Imm2$  symmetry in the insulating state. As seen on group-subgroup chain (Fig. 3.8), there are necessarily three steps between the high temperature

$P6_3/m2/m2/c$  phase and  $Imm2$ . This comes from the fact that the aforementioned symmetry analysis treats only the homogeneous ( $q = 0$ ) deformations (generators) and not, *e.g.*, the doubling of the unit cells ( $4V$ ). In other words, the  $Imm2$  symmetry can be achieved with one intermediate phase transition (at  $T_S$ ) only by allowing for an order parameter with a finite wavevector  $\mathbf{Q}$  (here  $Q_c = \pi/c$ ).

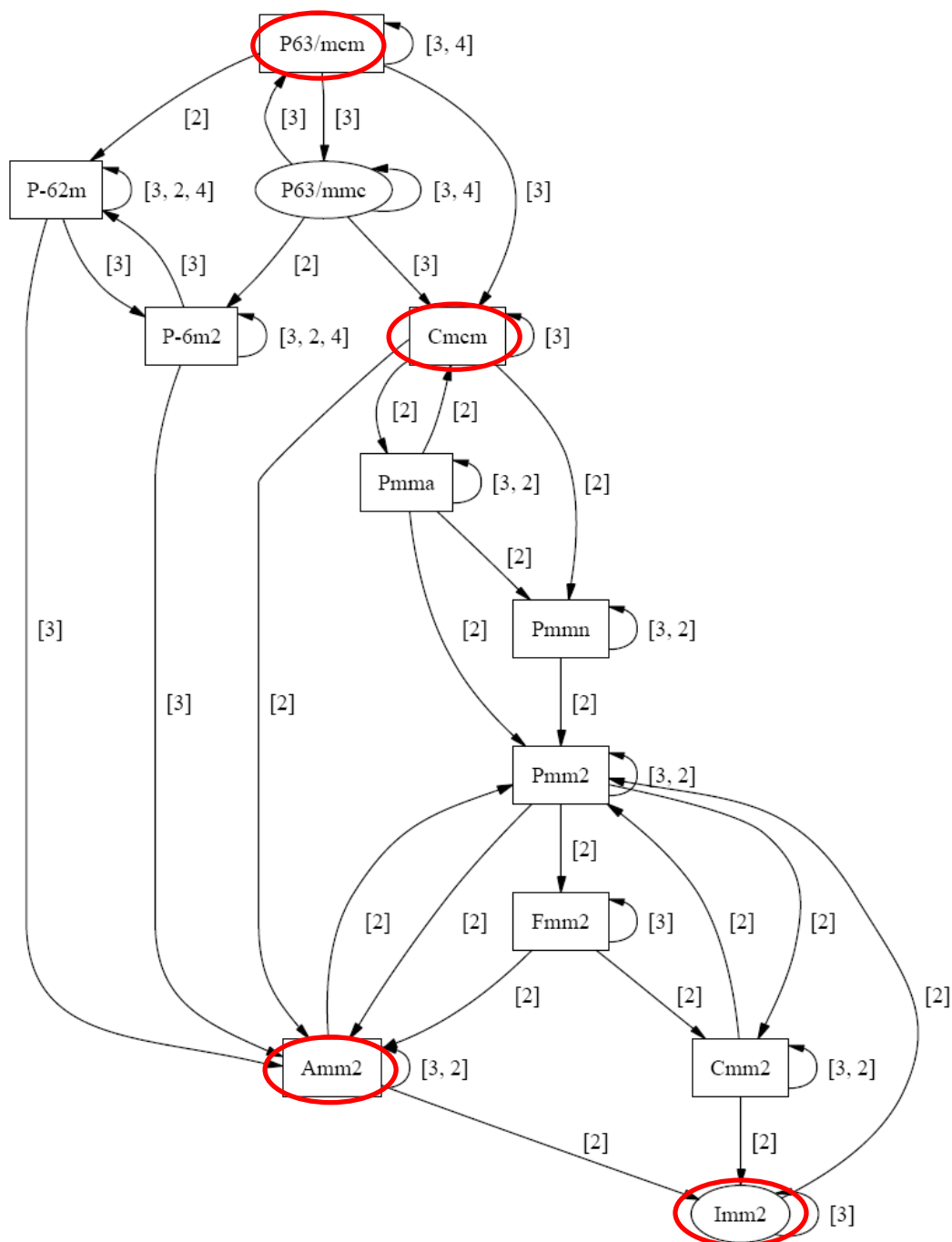


**Figure 3.8:** A graphic representation of the  $P6_3/m2/m2/c$  to  $Imm2$  group-subgroup chain obtained from the SUBGROUPGRAPH program (Ivantchev *et al.*, 2000).

### 3.3 Localized limit

Instead of the detailed symmetry analysis of the observed phase transitions (for which we would need more specific experimental data), it is also interesting to retain only the main symmetry properties of single electron along with the electron-electron interactions (above either  $T_S$  or  $T_M$ ), and consider the nature of the resulting electronic instabilities. It is this approach that underpins the following discussion, in which we attempt to define the minimal theoretical model capable of rationalizing the observed behavior.

As already discussed, the crystal field results in the splitting of the 5-fold degenerate  $d$ -level into a doubly-degenerate  $e(t_{2g})$  level and a single  $d_z^2$  level above  $T_S$  (see Fig. 3.4). At  $T_S$ , the zigzag displacement of the sulfur triangles, which could be considered as a Jahn-Teller distortion supplementary to the  $a/b$  distortion, lifts the degeneracy of the  $e_g$  levels. From the ARPES data (*vide infra*) it can be seen that these levels form narrow  $e_g$  (0.1 eV) bands in addition to the broad  $d_z^2$  band (5 eV). The width of this latter band is significant, with a correspondingly low density of states at the Fermi level. The (anti)crossing of the  $e_g$  and  $d_z^2$  is observed in the Brillouin zone and the Fermi level is pinned by the high density of  $e(t_{2g})$  states, leaving approximately half of the electrons in the low lying  $d_z^2$  band while the remainder of them are in the  $e(t_{2g})$  bands. On the other hand, the Hubbard  $U$  is typically of the order of 1eV for  $3d$  electrons (Fang and Terakura, 2002), i.e., it is larger than the width of the  $e(t_{2g})$  bands but smaller or close to the width of the  $d_z^2$  band. This is why, in the absence of the theoretical results for the intermediate regime, the strong (localized) and weak (extended) coupling limits will now be briefly addressed.

#### 3.3.1 Construction of the model

In the localized limit, appropriate for strong couplings, it is possible to construct four different states for the two electrons in the following way (Kiss and Fazekas, *private communication*):

$$\begin{array}{cc}
 \left| \frac{1}{2}, \frac{1}{2} \right\rangle & \boxed{\begin{array}{|c|c|} \hline d_z^2 & e_{ga} \\ \hline \end{array}} & \left| \frac{1}{2}, -\frac{1}{2} \right\rangle & \boxed{\begin{array}{|c|c|} \hline d_z^2 & e_{gb} \\ \hline \end{array}} \\
 \left| -\frac{1}{2}, \frac{1}{2} \right\rangle & \boxed{\begin{array}{|c|c|} \hline e_{ga} & d_z^2 \\ \hline \end{array}} & \left| -\frac{1}{2}, -\frac{1}{2} \right\rangle & \boxed{\begin{array}{|c|c|} \hline e_{gb} & d_z^2 \\ \hline \end{array}}
 \end{array}$$


---

where 1,2 denote the position of the electron within the unit cell, and  $a$ ,  $b$  and  $d$  indicate the respective orbitals (two  $e(t_{2g})$  and one  $d_z^2$ ). Vanadium-sulfur octahedral are sketched as squares. This treatment results in a Hilbert space, containing four elements, which is just large enough to describe the ordering at both second-order phase transitions. In this vector basis, pseudo spin operators  $\tau = 1/2$  and  $\eta = 1/2$ , acting separately on the  $d_z^2$  and  $e(t_{2g})$  orbitals, can be introduced. Using these pseudo spin operators, we can construct 15 independent local order parameters. For example, three of them are:

$$\tau^z \left| \pm \frac{1}{2}, e_g \right\rangle = \pm \frac{1}{2} \left| \pm \frac{1}{2}, e_g \right\rangle$$

- determines if the  $d_z^2$  orbital is on the left or the right of vanadium

$$\tau^x \left| \pm \frac{1}{2}, e_g \right\rangle = +\frac{1}{2} \left| \mp \frac{1}{2}, e_g \right\rangle$$

- transforms 

$e_g$	$d_z^2$
-------	---------

 into

$$\tau^y \left| \pm \frac{1}{2}, e_g \right\rangle = \pm \frac{1}{2i} \left| \pm \frac{1}{2}, e_g \right\rangle$$

$d_z^2$	$e_g$
---------	-------

 and back again,

acting only on the  $d_z^2$  orbitals. Similarly, the operator  $\eta^z$  determines if the electron is in the  $e_{ga}$  or  $e_{gb}$  orbital and the operators  $\eta^x$ ,  $\eta^y$  transfer an electron from one  $e(t_{2g})$  orbital to the other. It is possible to construct the remaining 9 parameters, from these 6, by mixing the  $\tau$  and  $\eta$  operators. For example:

$$\tau^z \eta^z \left| \pm \frac{1}{2}, \pm \frac{1}{2} \right\rangle = \frac{1}{4} \left| \pm \frac{1}{2}, \pm \frac{1}{2} \right\rangle, \quad \tau^z \eta^z \left| \pm \frac{1}{2}, \mp \frac{1}{2} \right\rangle = -\frac{1}{4} \left| \pm \frac{1}{2}, \mp \frac{1}{2} \right\rangle.$$

In order to find the basis of the irreducible representations, the way in which the states and order parameters (defined above) respect the presented symmetries of the crystal, should be determined. At the second order phase transition the symmetry is reduced and the number of the irreducible representations is lowered. All of the operators, which form the basis of the irreducible representations that drop out at the phase transition, are appropriate to realize the corresponding symmetry reduction. In the case of the transition at  $T_S$ , the order parameter can be constructed as a linear combination of  $\eta^x$  and  $\eta^z$ . That type of order parameter will cause a ferro-orbital order (one of the  $e_g$  orbitals is selected) removing the  $120^\circ$  rotations around the  $c$  axis.

At  $T_M$ , the order parameter  $\tau^z$  can simultaneously realize the tetramerization (doubling

of the unit cell) and the  $V_A - V_B - V_B - V_A$  order. This transition is analyzed here in more detail as it gives dramatic changes in the electronic properties of the  $\text{BaVS}_3$ . Considering the interactions between two unit cells through the formation of spin singlets below  $T_S$ , there are four different situations:



The direction of the spins is irrelevant for the two formations on the right, and therefore the spins are not shown. The ones on the left are energetically more favorable than those on the right due to the negative contribution arising from the spin pairing. When two  $e_g$  electrons are nearest neighbors, it corresponds to the antiferro-type ordering of the  $\tau^z$  orbital order parameter.

This type of ordering may assist the formation of the spin pairs through the direct  $S_1 S_2$  coupling. We can also consider direct interactions between the orbital parameters described with the coefficient  $K$ , and write down the Hamiltonian expressing all of the interactions outlined in this section:

$$H_{12} = \left( \frac{1}{2} - \tau_1^z \right) \left( \frac{1}{2} + \tau_2^z \right) J \vec{S}_1 \vec{S}_2 + \left( \frac{1}{2} + \tau_1^z \right) \left( \frac{1}{2} - \tau_2^z \right) J \vec{S}_1 \vec{S}_2 + K \tau_1^z \tau_2^z - HS. \quad (3.1)$$

### 3.3.2 Testing and interpretation of the model

To verify that the obtained Hamiltonian is appropriate for our system, the calculated values of physical properties should be compared with the measured data. For example, Fig. 3.9 shows the magnetic susceptibility obtained using the above Hamiltonian. In good agreement with the experimental measurements, the calculated susceptibility has a Curie-like temperature dependence at high temperature and a cusp at  $T_M$ .

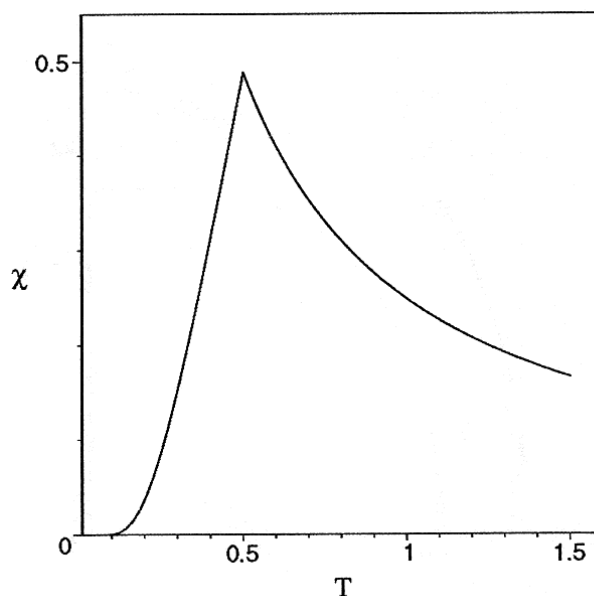


**Figure 3.9:** The calculated spin susceptibility as a function of temperature for  $J = 0.8$  and  $K = 2$ .

Based on the above discussion, the following model, schematically presented in Fig. 3.10, can be proposed: The unit cell contains two and four octahedra above and below  $T_{MI}$ , respectively. The crystal field and the Jahn-Teller distortion split the five-fold degenerate  $d$ -level, resulting in a doubly-degenerate  $e(t_{2g})$  level and a single  $d_z^2$  level (see as well Fig. 3.4). At  $T_S$ , the breaking of the  $C3$  symmetry lifts the degeneracy and allows the system to occupy only the lower energy  $e(t_{2g})$  orbital, thus resulting in ferro-orbital order. Below  $T_S$ , the unit cells start to interfere by forming local spin singlets. The interactions will produce a unit cell containing four vanadium atoms, with two different vanadium sites (one with an electron in the  $e_g$  level and the other with an electron in the  $d_z^2$  orbital), ordered in an alternating fashion along the  $c$  direction:  $d_z^2-e_g-e_g-d_z^2$ . Finally, at  $T_{MI}$ , inter-chain correlations synchronize the 4 V unit cells and produce a 3D order, and the system undergoes the MI transition. These conclusions are in agreement with the experimentally observed four-vanadium unit cell below  $T_{MI}$ .

As a final point, let us recall that, at  $T_x = 30$  K, the system undergoes a third second-order phase transition, which is a magnetic one. The neutron diffraction experiments by Nakamura *et al.* (1999) revealed magnetic reflections below  $T_x$ . The propagation vector is determined to be incommensurate (0.226, 0.266, 0) in the hexagonal index, which means a ferromagnetic (FM) order along the chain. Since the overall spin susceptibility signal is antiferromagnetic, the magnetic moment in-between the chains

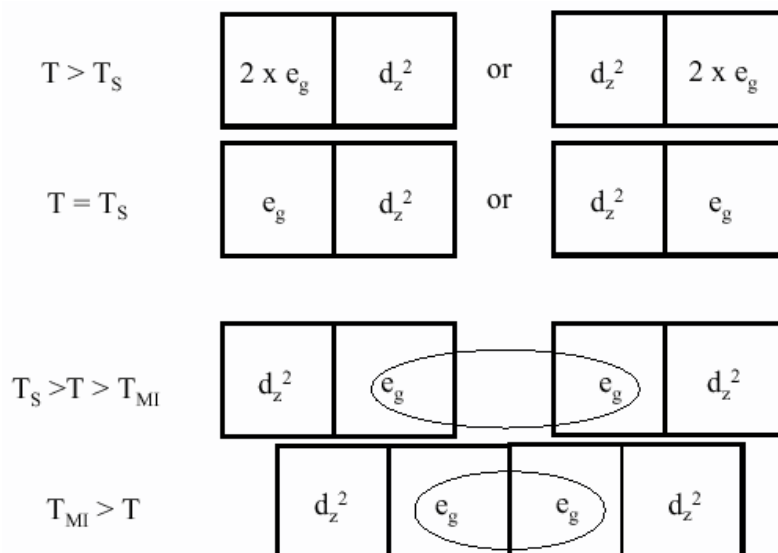


**Figure 3.10:** Microscopic model. Schematic representation of possible electron arrangements, above and below  $T_S$  or  $T_{MI}$ , considering the length of unit cell along the  $c$  axis and orbital degrees of freedom involved. The vanadium-sulfur octahedra are sketched by squares while the ovals represent the formation of spin singlets.

must be turning over in order to compensate the ferromagnetic signal. This statement is in agreement with the above wave-vector. We shall refer to this type of order in later sections as interchain-compensated FM or simply ICFM. The ordered moment is estimated to be approximately  $0.5 \mu_B/V$ . At ambient pressure this transition is deep in the insulating phase making it impossible to follow by measuring transport properties. This is in stark contrast with the high-pressure behavior around and above  $p_{cr}$ . The measured ferromagnetic order along the  $V$ -chains suggests that  $J$  is negative in  $H_{12}$  (Eq. (3.1)), *i.e.*, that direct interactions between localized moments tend to order them ferromagnetically.

Although the model presented in this section completely neglects the electron hopping, except possibly in  $J$  of  $H_{12}$ , some of its properties are probably relevant for the low-T behavior of  $BaVS_3$ . Especially interesting in this sense is its behavior below 15K at ambient pressure when giant charge-density waves, CDW (Fagot *et al.*, 2003), possibly accompanied by the orbital ordering of the type described above, develops in the system. However, this requires further experimental confirmation, in particular by NQR measurements of the electric field gradients at the  $V$ -sites.

### 3.4 Itinerant limit

The band theory of solids starts from the analysis of the electronic levels in a periodic potential within the independent electron approximation, which neglects the interactions between electrons. That is, an electron is assumed to be acted upon only by the field of the fixed atomic cores plus an appropriately chosen field (*e.g.*, Hartree or Wigner-Seitz field) arising from the charge distribution of all the outer-shell electrons. There are several approaches to calculate the band structure in this way. One such method that is widely used is the linear augmented plane wave (LAPW) method (Singh, 1994).

#### 3.4.1 *Ab initio* calculation of the band structure

Two slightly different LAPW calculations have been carried out for the room temperature structure of BaVS<sub>3</sub> (Mattheiss (1995), Whangbo *et al.*, (2002)). In both cases the reported dispersion relations are quite similar (*vide infra* Fig. 3.12a and Fig. 3.13a). The S(3*p*)-V(3*d*) valence-conduction-band manifold spans an energy range of roughly 9 eV which extends from about -6eV to +3 eV. The approximate positions and widths of the individual subband complexes, in the AHL plane of the Brillouin zone (Fig. 3.11), are shown in Fig. 3.12a.

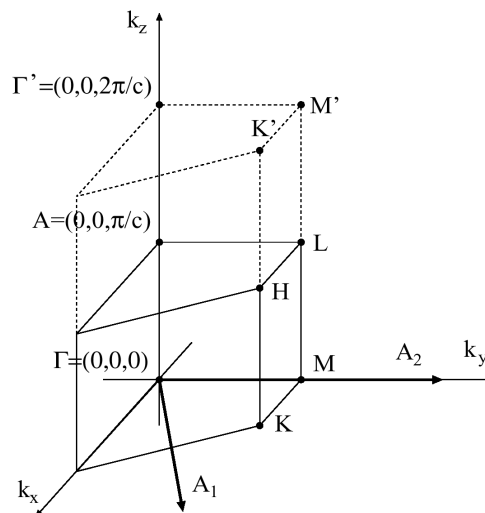


**Figure 3.11:** 1/8 of the Brillouin zone (solid lines) unfolded (dashed lines) along the *c* (*z*) directions of the hexagonal Bravais lattice. Primitive vectors in the plane of the reciprocal space are marked by **A**<sub>1</sub> and **A**<sub>2</sub>. Unfolding is introduced to stress that due to the screw axis symmetry (there are 2 equivalent V-sites along the length *c*) no Bragg reflection is associated with the point A.



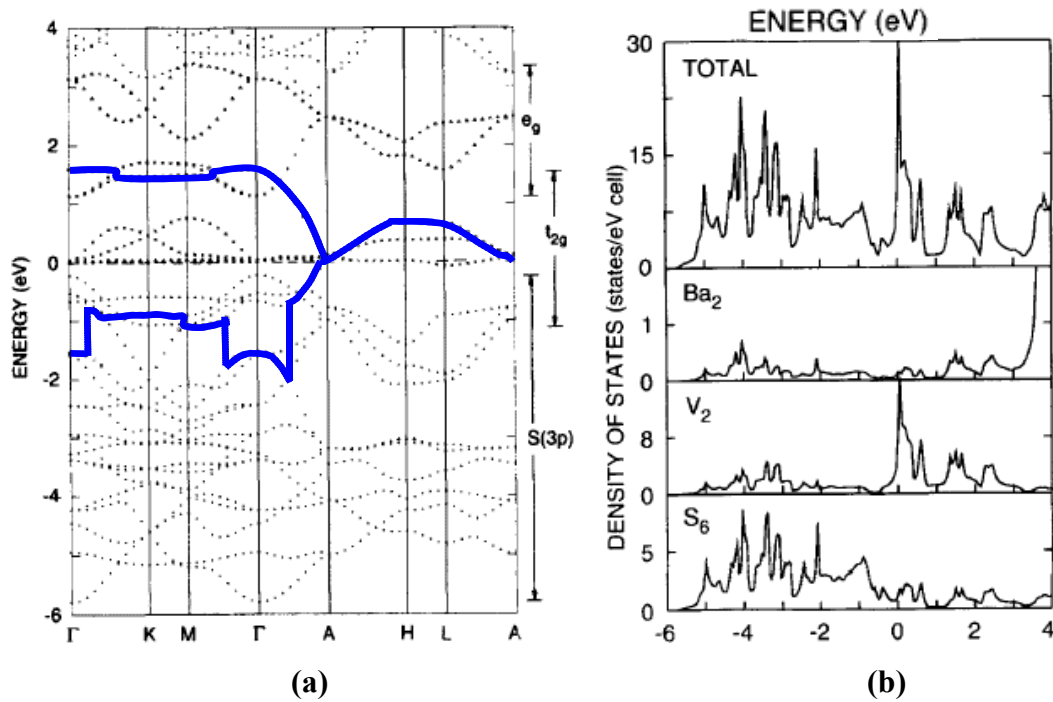


**Figure 3.12:** Band structure of BaVS<sub>3</sub> calculated for the hexagonal phase at 300 K by LAPW calculations,  $E_F = 0$ . **(a)** Band dispersion relations along symmetry lines in the Brillouin zone. The band in which the  $d_z^2$  orbital has the dominant contribution is marked by a blue line. No gap is present at A. On the right side are shown the approximate positions and widths of the individual subband complexes. **(b)** Total and muffin-tin-projected density-of-states plots. Data from Mattheiss (1995).

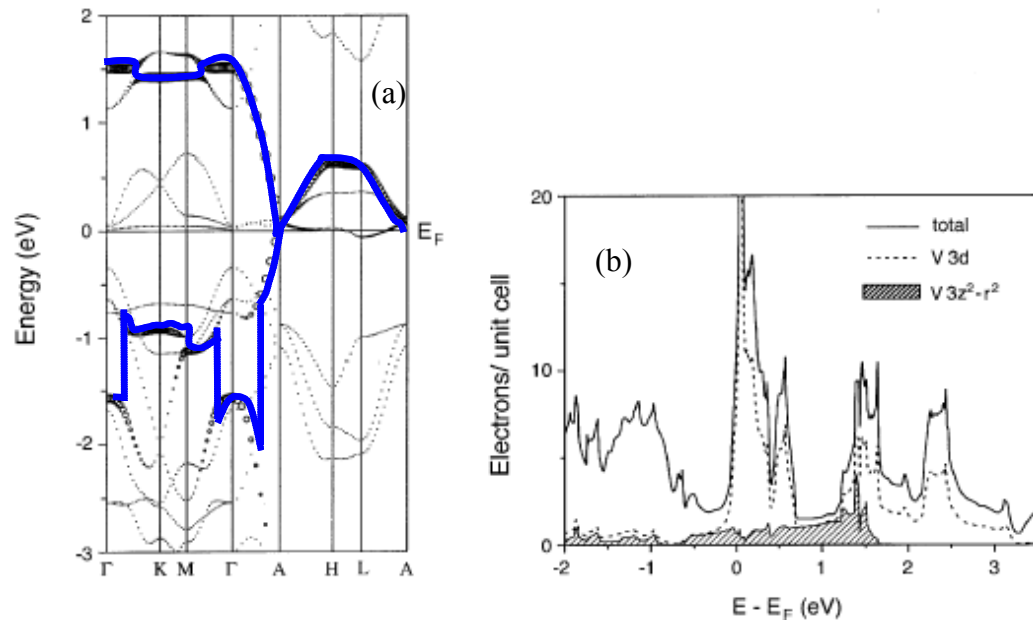


**Figure 3.13:** Band structure of BaVS<sub>3</sub> calculated for the hexagonal phase at 300 K by full-potential-LAPW calculations. **(a)** Band dispersion relations along symmetry lines in the Brillouin zone. The weight of the  $d_z^2$  orbital contribution is shown by the circle size. The blue line is the result of the LAPW calculation shown in Fig. 3.12. **(b)** Total and partial density-of-states plots. Data from Whangbo *et al.*, (2002).

The Fermi level  $E_F$  is pinned by the high density of states of the four relatively narrow ( $\sim 0.7$  eV)  $t_{2g}$  ( $d_z^2$  and  $e_g$ ) bands. The short V-V distance along the  $c$  direction yields a broad ( $\sim 3$  eV)  $d_z^2$  band which crosses the Fermi level. Using the tight binding language, the overlaps (hoppings) producing this band have two components, direct and indirect (via intermediate S( $3p$ ) orbitals). These contributions are clearly seen in Fig. 3.13 a, wherein the weight of the  $d_z^2$  orbital in the structure of the band is marked by the difference in the circle size. The band filling is such that the lowest  $t_{2g}$  ( $d_z^2$ ) band is close to full (there are 0.14 holes per cell), while the compensating electrons occupy the  $e_g$  band (0.14 electrons per cell) thus predicting the metallic behavior of the BaVS<sub>3</sub>.

The corresponding band results for the orthorhombic phase ( $T = 100$  K) are shown in Fig. 3.14a, revealing only minor changes in the electronic band structure. Probably the most important difference between the two structurally different phases is the factor-of-two increase in the number of carriers at  $E_F$ . This can be easily observed in the density-of-states (DOS) calculations in Fig. 3.12b and Fig. 3.14b. The Fermi level is pinned by the large DOS peak essentially related to the  $e_g$  levels. In the hexagonal phase, the Fermi level falls on the low-energy shoulder while in the orthorhombic phase it coincides with the peak resulting in the increase of the carrier number.

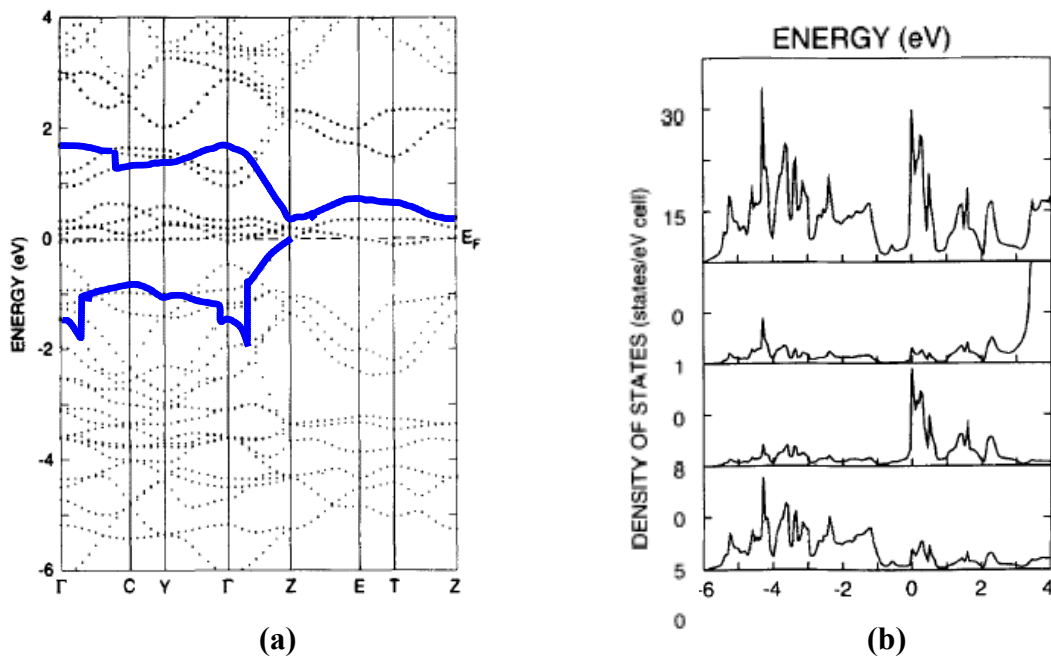


**Figure 3.14:** Band structure of BaVS<sub>3</sub> calculated for the orthorhombic phase at  $T = 100$  K by LAPW calculations. **(a)** Band dispersion relations plotted along symmetry lines in the Brillouin zone. The band in which the  $d_z^2$  orbital has the dominant contribution is marked by blue line. **(b)** Total and muffin-tin-projected density-of-states plots. Picture adopted from Mattheiss (1995).

## 3.4.2 The tight binding approximation

In order to get a better physical insight into the nature of the bands of BaVS<sub>3</sub> in the region of the Fermi level, it is useful to analyze them in the tight binding approximation (Friedel, 1969; Kittel, 1953) and calculate the bands analytically (Kupčić *et al.*, in preparation). Indeed, the DOS calculations show that the majority of the vanadium atom orbital weight is found above the Fermi level, suggesting weak V(3*d*) - S(3*p*) hybridization effects at the Fermi level. The Ba component in the valence band energy range is small, showing that Ba is essentially an ionic donor. Overall, these results suggest that the ionic model (*i.e.*, Ba<sup>2+</sup>, V<sup>4+</sup>, S<sup>2-</sup>, also our starting point for the localized model) is a reasonable starting point for the tight binding band calculation for both hexagonal and orthorhombic BaVS<sub>3</sub>.

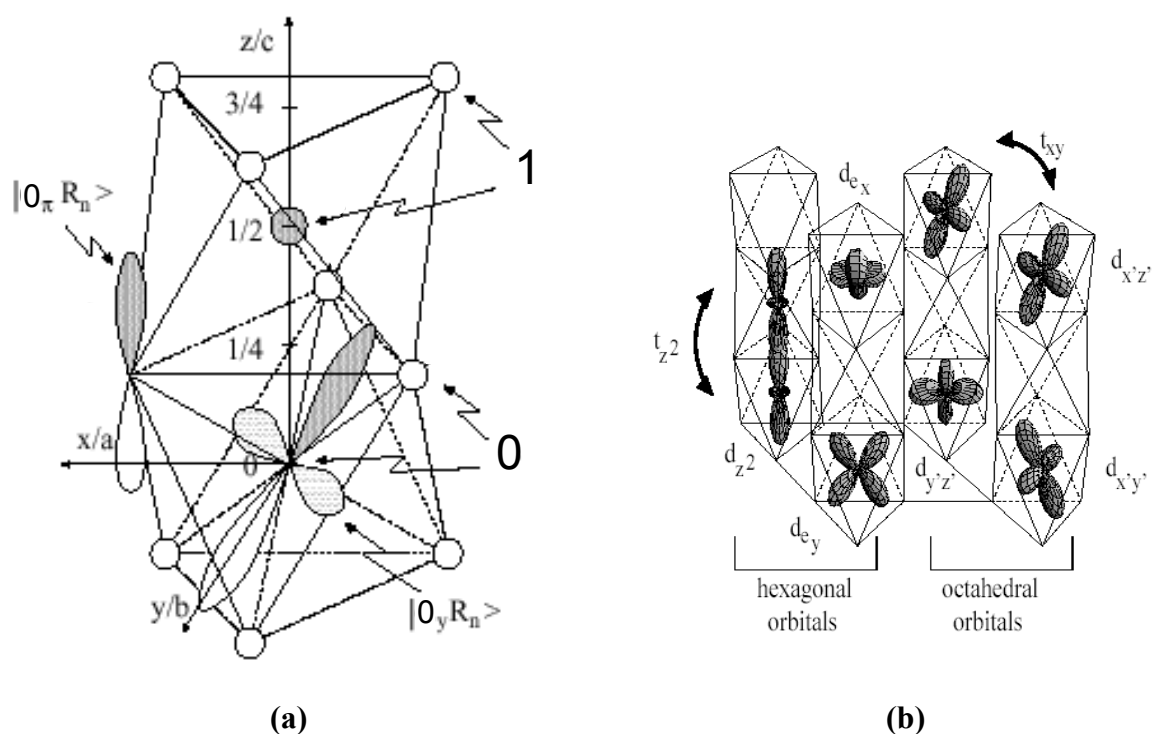


**Figure 3.15:** (a) A building block of (Ba)VS<sub>3</sub> chains presented schematically. It is formed from two V atoms centered within two face-shared S octahedral units, marked by 0 and 1. The vanadium and sulfur are represented by grey and white circles, respectively. One vanadium and one sulfur orbital are explicitly shown. (b) The octahedral *t*<sub>2g</sub> orbitals compared to the *d*<sub>z<sup>2</sup> and *e*(*t*<sub>2g</sub>) orbitals.</sub>

The tight binding approximation (TB) begins with the single atom wave functions and exploits the description of bonds by overlap integrals. The bonds split the atomic energy levels depending on **k** and form the band. The width of the band is proportional to the strength of the bonds (overlap integrals). In BaVS<sub>3</sub> the bonding orbitals of interest are the three octahedral vanadium *t*<sub>2g</sub> orbitals (or the three hexagonal orbitals, *d*<sub>z<sup>2</sup> and 2-fold degenerate *e*(*t*<sub>2g</sub>) orbitals) and one molecular orbital</sub>

constructed from three  $2p_z$  sulfur states ( $\pi_z$ ) (see Fig. 3.15). There are two formula units per unit cell and therefore a total of eight orbitals should be taken in account. The orbitals of interest are denoted in the following way:

$$\begin{aligned} |\lambda_x \bar{R}_n\rangle &= \left| d_x^2 \left( \vec{r} - \bar{R}_n - \lambda \cdot \frac{1}{2} \hat{r}_c \right) \right\rangle, \\ |\lambda_y \bar{R}_n\rangle &= \left| d_y^2 \left( \vec{r} - \bar{R}_n - \lambda \cdot \frac{1}{2} \hat{r}_c \right) \right\rangle, \\ |\lambda_z \bar{R}_n\rangle &= \left| d_z^2 \left( \vec{r} - \bar{R}_n - \lambda \cdot \frac{1}{2} \hat{r}_c \right) \right\rangle, \\ |\lambda_\pi \bar{R}_n\rangle &= \left| \pi_z^2 \left( \vec{r} - (\bar{R}_n + \vec{r}_s) - \lambda \cdot \frac{1}{2} \hat{r}_c \right) \right\rangle, \end{aligned}$$

where  $\bar{R}_n$  is the Bravais lattice vector giving the position of the lower vanadium,  $\hat{r}_c$  is a primitive vector along c direction,  $\vec{r}_s$  is position of the molecular sulfur orbital,  $\lambda = 0$  or  $1$  for the lower or upper block, respectively.

Once the relevant orbitals are chosen (omitting all others) the corresponding selection is done for overlap integrals, keeping only the largest contributions. The primary effect of the crystal field  $H_{cf}$  on the site energies in the hexagonal phase comes from the  $S_6$  octahedra surrounding the V site in question. These contributions are diagonal in the representation chosen above:

$$E_l^\lambda = \langle \lambda_x \bar{R}_n | H_{cf} | \lambda_x \bar{R}_n \rangle, \quad l = x, y, z,$$

and determine the energy of the  $t_{2g}$  triplet relative to the energy of the  $e_g$  doublet as illustrated in Fig. 3.4. In the same way, the site energy of the  $\pi_z$  sulfur orbital is equal to  $E_\pi^\lambda = \langle \lambda_\pi \bar{R}_n | H_{cf} | \lambda_\pi \bar{R}_n \rangle$ . The rest of the lattice contributions appear in the off-diagonal site energies:

$$\Delta_{ll'}^\lambda = \langle \lambda_x \bar{R}_n | H_{cf} | \lambda_{l'} \bar{R}_n \rangle, \quad l \neq l',$$

resulting in the splitting of the triply degenerate  $t_{2g}$  into a doubly-degenerate  $e(t_{2g})$  and a single  $d_z^2$  as shown in (Fig. 3.4.)

Let us first consider the corresponding inter-chain bondings. Since the distance

between the neighboring vanadium ions in the plane perpendicular to the  $c$  axis is much larger than along the chain, it is natural for the intra-plane bond energies to retain only the  $\sigma$  overlaps between two in-plane neighboring vanadium ions (as shown in Fig. 3.16):

$$t_{xy} = \langle \lambda_l \vec{R}_n | H_{cf} | \lambda_l \vec{R}_n \pm n \hat{a}_1 \pm m \hat{a}_2 \rangle, \quad l = x, y, z.$$

Here  $n$  or  $m$  (either -1 or 1), together with the primitive vectors ( $\hat{a}_1$ ,  $\hat{a}_2$ , perpendicular to the  $c$  axis), serve to describe the positions of all six neighboring vanadium ions.

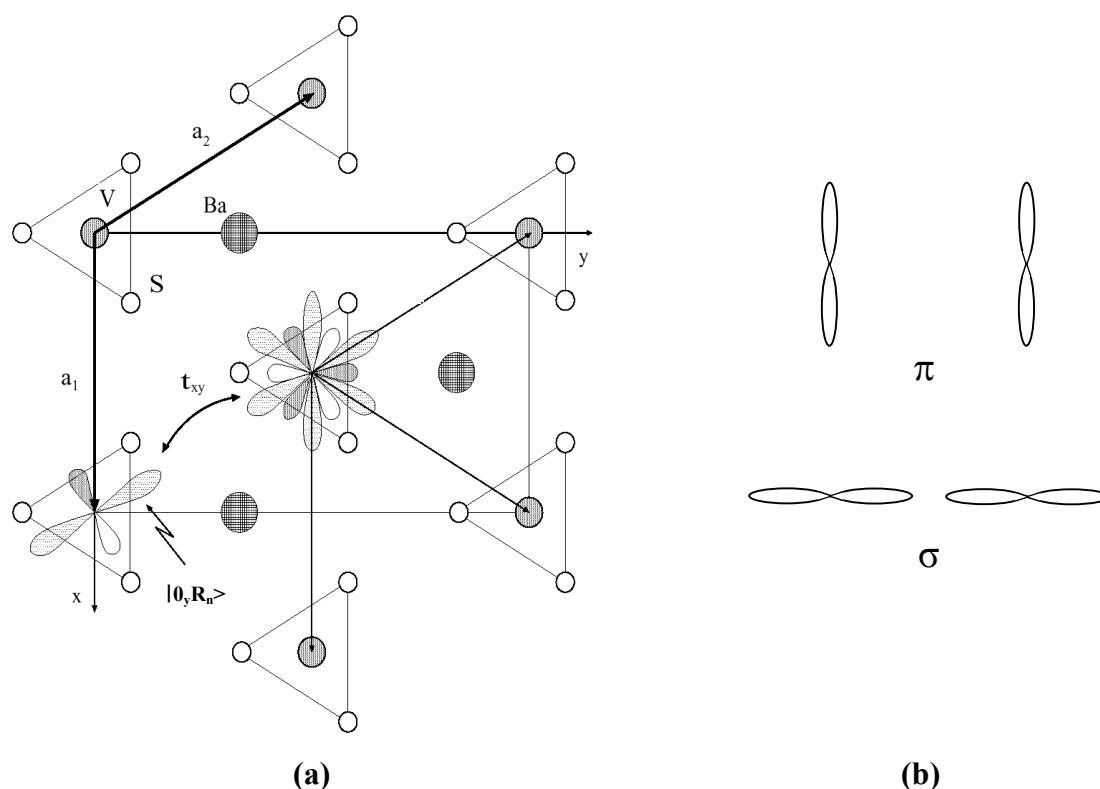


**Figure 3.16:** (a) The  $xy$  plane projection of the 0-V and 0-BaS<sub>3</sub> layers in the hexagonal lattice. According to Fig. 3.15 the intra-plane and the upper and lower out-of-plane lobes of the  $e(t_{2g})$  orbitals are labeled by light grey, dark grey and white, respectively. (b) The difference between the  $\sigma$  and  $\pi$  type overlap illustrated on the example of  $p$  type orbitals.

The electron propagation along the chains is more complex as the hopping may occur either directly between adjacent vanadium ions (V-V hopping) or via sulfur as an intermediate state (V-S-V hopping). If the site energies  $E_V^\lambda$  and  $E_S^\lambda$  are similar, these two processes tend to be equally important. However, in the simplest case  $E_V^\lambda - E_S^\lambda$  is the largest energy parameter in the model. The  $\pi_z$  sulfur band is completely occupied and can be safely disregarded, reducing the problem from four artificially dimerized

bands (the  $c$  axis is the screw symmetry axis in the hexagonal phase) to three (six) vanadium bands intersecting the Fermi level. This could be a poor approximation for BaVS<sub>3</sub> but it is a good starting point for our discussion.

The solution of the simplified three band model is already non-trivial as it involves a high number of overlap integrals in order to describe the electron propagation. In the hexagonal phase, the electron propagation is described by following overlap integrals:

$$\begin{aligned}
 t_{a_3}^{ll} &= \langle 0_l \vec{R}_n | H_{cf} | 1_l \vec{R}_n \rangle & l = x, y, z & \quad \text{-diagonal intra-chain hopping, staying in} \\
 & & & \quad \text{the same type of orbital.} \\
 t_{a_3}^{ll'} &= \langle 0_l \vec{R}_n | H_{cf} | 1_{l'} \vec{R}_n \rangle & l \neq l' & \quad \text{-off-diagonal intra-chain hopping,} \\
 & & & \quad \text{changing the type of orbital.} \\
 t_{a_3nm}^{ll} &= \langle 0_l \vec{R}_n | H_{cf} | 1_{l'} \vec{R}_n \pm n\hat{a}_1 \pm m\hat{a}_2 \rangle & l = x, y, z & \quad \text{-diagonal out-of-plane inter-chain} \\
 & & & \quad \text{hopping, staying in the same type of} \\
 & & & \quad \text{orbital.}
 \end{aligned}$$

For the orthorhombic phase, due to the distortion of the S<sub>6</sub> octahedra, additional contributions should be regarded, such as:

$$\begin{aligned}
 t_{a_3nm}^{ll'} &= \langle 0_l \vec{R}_n | H_{cf} | 1_{l'} \vec{R}_n \pm n\hat{a}_1 \pm m\hat{a}_2 \rangle & \text{-off-diagonal out-of-plane inter-chain} \\
 & & l \neq l' & \quad \text{hopping, changing the type of orbital,}
 \end{aligned}$$

which introduce the mixing between three (six) bands of the hexagonal phase. The  $t_{a_3}^{ll}$  and  $t_{a_3}^{ll'}$  hoppings enter through two combinations  $t_{a_3}^{zz} = t_{a_3}^{ll} + 2t_{a_3}^{ll'}$  and  $t_{a_3}^{ee} = t_{a_3}^{ll} - t_{a_3}^{ll'}$  representing the  $\sigma$  overlaps between the  $d_z^2$  and  $e(t_{2g})$  orbitals, respectively.

### 3.4.2.1 Analysis of the three-band model

Once the model is defined, by determining all the interesting terms of the Hamiltonian, the appropriate values for the overlap integrals should be chosen. This can be accomplished, *e.g.*, in such a way as to obtain the best agreement with the LAPW calculations presented earlier. The result of this type of elaboration of the three band model presented above is shown in Fig. 3.17. All three bands are artificially dimerized in the  $z$  direction: there is no gap in the A point, as required by the screw-axis symmetry of the lattice. The most noticeable feature is the quasi one dimensionality of the antibonding bands, dispersive primarily in the  $k_z$  direction

(along  $A\Gamma$  line). The bonding sub-bands have a significant dispersion in the  $k_x k_y$  plane and the Fermi level is pinned by the high density of  $e(t_{2g})$  levels ( $E_F \neq 0$  in all TB graphs).

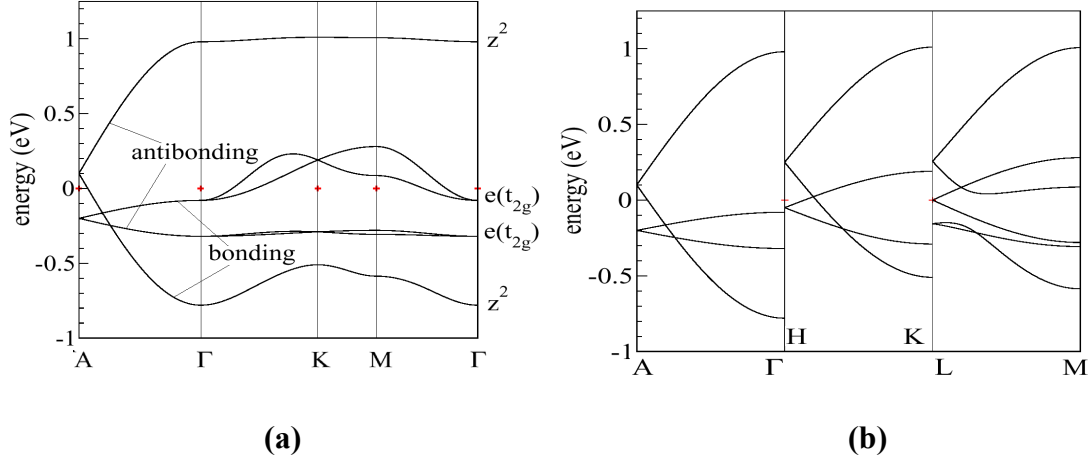


**Figure 3.17:** Electronic band structures for the three (six) band model, **(a)** along the symmetry lines in the Brillouin zone of Fig. 3.11, **(b)** in the  $k_z$  direction along the  $A\Gamma$ ,  $HK$  and  $LM$  lines. No gap is present at  $A$ . The calculation is carried out with the following set of parameters:  $d_z^2 - d_z^2$  overlap  $t_{\hat{a}_3}^{\parallel} (l=z) = -0.4$  eV,  $e(t_{2g}) - e(t_{2g})$  overlap  $t_{\hat{a}_3}^{\parallel} (l=x,y) = 0.1$  eV, in-plane overlaps which mix  $d_z^2$  and  $e(t_{2g})$   $t_{xy} = -0.05$  eV, diagonal-out-of-plane overlaps  $t_{\hat{a}_3 nm}^{\parallel} = -0.02$  eV, and the  $d_z^2 - e(t_{2g})$  splitting  $3\Delta = 0.3$  eV. It should be noted that the zero of energy is taken arbitrarily ( $E_F$  is pinned by the high density of the  $e(t_{2g})$  bands).

With such a model in hand, it is possible to tune the strength of a particular overlap integral or the magnitude of a splitting between energy levels and investigate the resulting influence on the electronic band structure. Implicit is the idea that tuning of this kind includes the single particle effects of the correlations not included in LAPW or LDA schemes. For example, if the splitting between the  $d_z^2$  and  $e(t_{2g})$ ,  $3\Delta$ , is not too large in comparison with  $|t_{\hat{a}_3}^{zz}|$ , the bonding  $d_z^2$  band in Fig. 3.17 is almost completely occupied. Consequently, the contributions to various response functions associated with the  $e(t_{2g})$  states are very small in this limit. On the contrary, if the  $3\Delta$  is larger than  $|t_{\hat{a}_3}^{zz}|$ , the antibonding  $e(t_{2g})$ -like bands are half-filled, as shown in Fig. 3.18. This opens the tempting possibility to explain the anomalous physics in this material in terms of the intra and inter-band scattering processes in these two narrow  $e(t_{2g})$  bands. However, this alternative is not in agreement with the LAPW calculations.

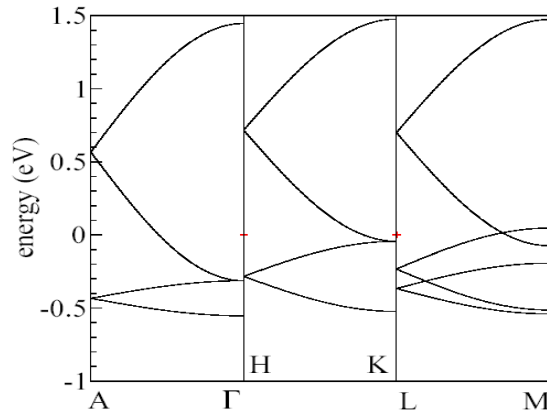


**Figure 3.18:** Electronic dispersion, for the three (six) band model, in the  $k_z$  direction for the same set of parameters as used to generate Fig. 3.17, except that the parameter describing the  $d_z^2 - e(t_{2g})$  splitting is now set to be  $3\Delta = 1$  eV. The zero of energy is taken arbitrarily.

Actually, to understand the electronic properties of the system it is necessary to know the shape of the Fermi surface for the energy scales of interest which are typically of the order  $k_B T$  (0.025 eV for  $T = 300$  K). The band calculations described above are meant to be good approximations for  $\text{BaVS}_3$  giving an insight into **the high temperature** band structure in this narrow energy window. However, properties such as the SDW/CDW fluctuations, the ARPES spectra and the conductivity, together with its anisotropy ratio are associated with different response functions. Therefore, in order to shed some light on these properties, it is necessary to have some degree of flexibility present in the calculations. The LAPW approach is unsuitable in this respect as the only degree of freedom available is the choice of the muffin tin potential. In contrast, the potential versatility of the tight binding calculations has already been demonstrated in the context of the  $d_z^2 - e(t_{2g})$  splitting. As will be shown below, the further exploitation of the flexibility inherent in the TB approach is a very informative exercise.

Before putting this analysis into practice, it is worthwhile to mention the hopping  $t_{xy}$ . In the hexagonal phase, this overlap results in the anticrossing of bands along the LM line (Fig. 3.17 and Fig. 3.18). In the orthorhombic phase, this phenomenon is additionally apparent along the  $A\Gamma$  line. In the latter case, the two  $e(t_{2g})$  bands are split and the lower one anticrosses the  $d_z^2$  band. With such an anticrossing close to the Fermi level, this matrix element may be of qualitative importance in lowering the anisotropy of the transport properties to the observed values, as will be discussed elsewhere (Kupčić *et al.*, in preparation).



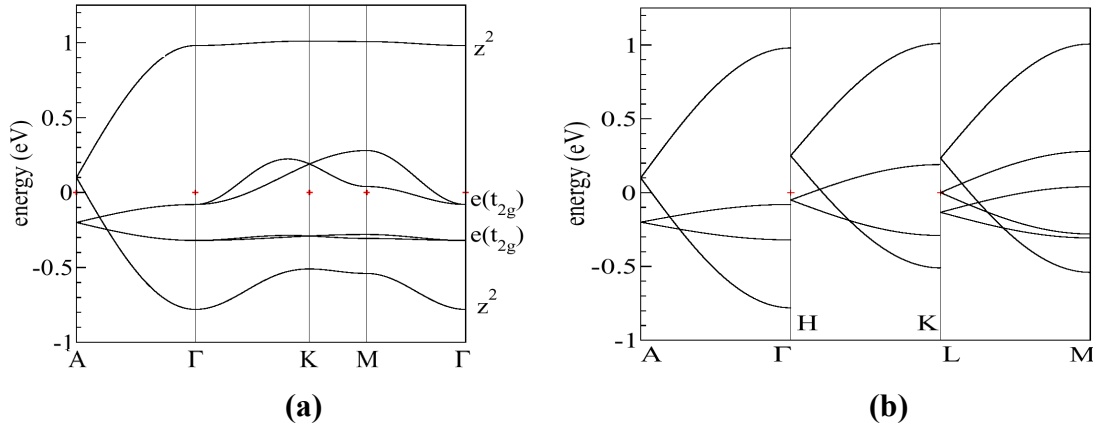


**Figure 3.19:** Electronic dispersions for the three (six) band model (a) along the symmetry lines in the Brillouin zone and (b) in the  $k_z$  direction. The calculations are carried out with the same set of parameters as used to generate Fig. 3.17 except that the hopping between the  $d_z^2$ -like band and the  $e(t_{2g})$  block is neglected. The zero of energy is taken arbitrarily.

In contrast to the anisotropy of the transport properties, the anisotropy of the SDW and/or CDW fluctuations, seen in the X-ray spectroscopy through diffuse lines with the wave vector  $Q_c = \frac{1}{2} c^*$  (Fagot *et al.*, 2003), is large. Therefore, it is appealing to investigate the effect of the mixing between the  $d_z^2$ -like band and the  $e(t_{2g})$ -block on the *nesting properties* of the  $\frac{1}{4}$  filled  $d_z^2$  band, important for CDW/SDW fluctuations. The simplest way to accomplish this is by switching off the overlap  $t_{xy}$  between the orbitals  $d_z^2$  and  $e(t_{2g})$ . As seen by comparing Fig. 3.18 and Fig. 3.19, this does not cause a significant change in the intraband nesting properties of the  $d_z^2$  band. In particular, the small mixing effect which occurs on the  $A\Gamma$  line in the orthorhombic phase can be safely neglected in this context.

In addition, or as an alternative, to the nesting of the intraband type, it is also possible to have nesting in between the bands (interband nesting). The system will adopt the type of nesting which, in the presence of interactions, minimizes the overall (free) energy. As it is difficult to rigorously determine, on theoretical grounds, which nesting will be preferred, one can only speculate on the basis of indirect arguments. Indeed, there are models which attribute the MI transition in  $\text{BaVS}_3$  to nesting in between the  $d_z^2$  and  $e_g$  bands (Mitrovic *et al.*, submitted). It is, however, unlikely that such nesting can produce the small energy scales (below 100K) necessary to explain the SDW/CDW excitations observed in  $\text{BaVS}_3$ . On the other hand, the intraband nesting in the  $d_z^2$  band is nearly one-dimensional and will therefore be discussed in more detail below. When one is interested primarily in such nesting effects, the hopping between the two  $e(t_{2g})$  orbitals can be set equal to zero. The result of this simplification is shown in Fig. 3.20.

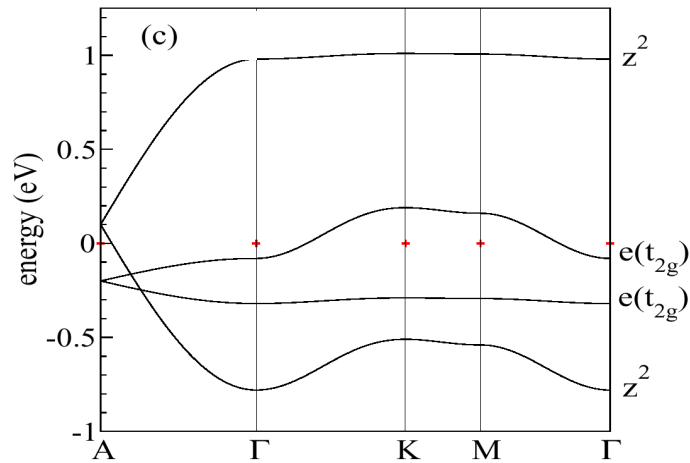


**Figure 3.20:** Electronic dispersions of the three band model, along the symmetry lines, with all off-diagonal elements set to zero. Other parameters are same as those used to generate Fig. 3.17. The zero of energy is taken arbitrarily.

Inspection of Fig. 3.20, in the context of the above discussion, shows that the mixing between the  $d_z^2$  orbital and the  $e(t_{2g})$  block can be roughly ignored in the discussion of the (intraband) nesting properties of the  $\frac{1}{4}$  filled  $d_z^2$  band. This is in stark contrast to d.c. conductivity where this mixing is quite probably crucial. In the case that the mixing is neglected, the three-band Hamiltonian can be decoupled into two separated subspaces, with the  $e(t_{2g})$  states serving mostly as the reservoir of electrons. However, before turning to this discussion let us briefly mention the role of sulfur.

#### 3.4.2.2 The influence of sulfur and the four band model

The inclusion of the sulfur  $\pi$  orbital leads to the four band model. The results from such a treatment, which best illustrate the possible importance of the  $\pi_z$  contribution, are shown in Fig. 3.21. The curves displayed therein show that, for the chosen set of parameters, the dispersion of the  $e(t_{2g})$  bands depends only weakly on the details describing the sulfur  $\pi_z$  band. On the other hand, the width and the position of the  $d_z^2$  band exhibit dramatic changes, reflecting the fact that both the  $\pi_z$  and  $d_z^2$  bands are characterized by (strong)  $\sigma$  overlaps in the  $z$  direction. The corresponding bond energies are thus competing.

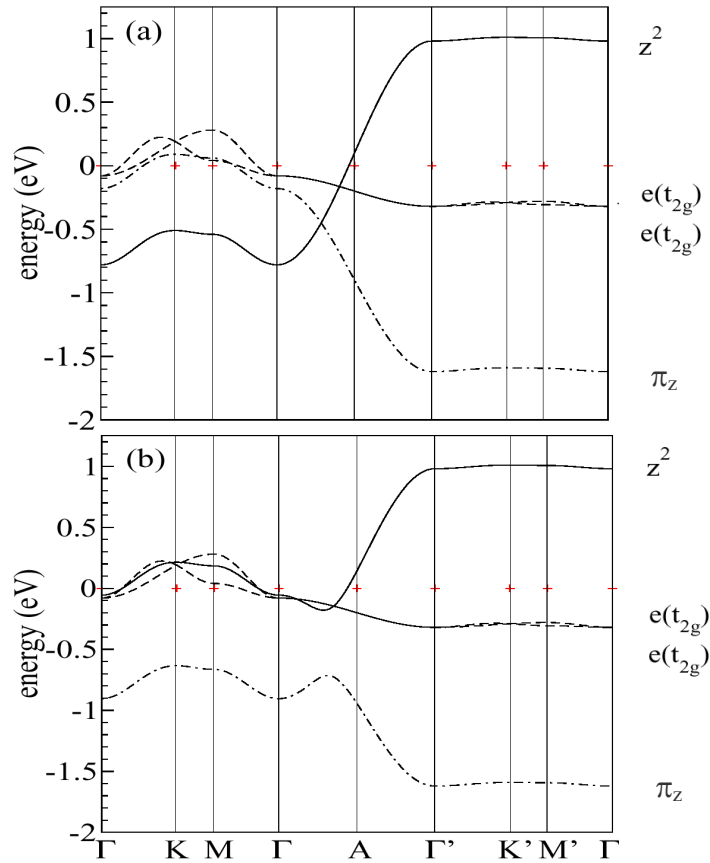


**Figure 3.21:** Electronic band structures of the four-band model in the unfolded zone of Fig. 3.11, demonstrating the importance of the sulfur in BaVS<sub>3</sub>. Overlaps determined for the three band model shown in Fig. 3.17 remain unchanged. New parameters, describing the function of the  $\pi_z$  orbital, are:  $\pi_z$  -  $\pi_z$  overlap  $t_{a_3}^{z\pi} = 0.4$  eV, site energies  $E_z = 0.2$  eV and  $E_\pi = -0.8$  eV, and overlap  $\pi_z - d_z^2$  equals either (a)  $t_{a_3}^{z\pi} = 0$  eV or (b)  $t_{a_3}^{z\pi} = 0.15$  eV. The zero of energy is taken arbitrarily.

In the case of a small overlap between the  $d_z^2$  and the  $\pi_z$ ,  $t_{a_3}^{z\pi} \rightarrow 0$ , the  $\pi_z$  band is completely filled, leading to the closed outer subshell of the sulfur ions (resulting in  $S^{2-}$ ). The vanadium bonding  $d_z^2$  band is almost completely filled. The increase of the bond energy  $t_{a_3}^{z\pi}$  introduces mixing between the two bands. For large enough bond energy, the upper band moves above the  $e(t_{2g})$  bands, and there is a complete transfer of electrons between the bonding  $d_z^2$  and  $e(t_{2g})$  antibonding bands. The latter ones are again half-filled, as was the case for large  $3\Delta$  (in the 3-band model shown in Fig. 3.18). However, irrespective of the mechanism responsible for the half-filling, there is no experimental evidence to support such a situation. Nevertheless it should be stressed that the variation of the overlap between the  $\pi_z - d_z^2$  can change dramatically the band dispersion in BaVS<sub>3</sub>. This result reveals the possible importance of sulfur in this compound, in analogy with the role of oxygen in high- $T_c$  cuprates. As a consequence, it can be expected that the system would be very sensitive to the sulfur stoichiometry. Further analysis of the electronic band structure as a function of the

$\pi_z - d_z^2$  overlap is performed by Whangbo *et al.* (2002) and the reader is referred to that work for more detail. In the ensuing discussion, however, the explicit contribution of sulfur will be omitted and its effect will be implicitly manifested in the simple 3-band (quasi-1D) model by way of the sulfur-enhanced inverse effective mass (of the  $d_z^2$  band) along the chain direction. It is this model that will be used in the discussion of the formation of SDW/CDW correlations through the nesting properties of the  $d_z^2$  band of Fig. 3.20, and of their effect on the measured ARPES spectra.

### 3.4.3 ARPES and tight binding: A synergistic cooperation

It is pertinent to recall, once again, that the 1D lattice fluctuations of the vanadium chains were observed in the high temperature range between  $T_S$  and  $T_{MI}$ . The most prominent candidates for the tetramerization,  $Q_c = \pi/c$ , of the vanadium unit cell are the vanadium electrons of the  $1/4$  filled  $d_z^2$  band ( $2k_F = \pi/c = 0.5c^*$ ). The effect is related to the high temperature band structure discussed above. As is well known for weak electron-electron couplings, the enhancement of the charge and/or spin fluctuations occurs when the bands, such as  $d_z^2$  in  $\text{BaVS}_3$ , have 1D nesting properties. It is at that point that the screw axis symmetry conservation, that we insisted so much upon, enters explicitly: it makes the  $d_z^2$  band  $1/4$  filled (no gap in the A point of Fig. 3.20). The direct Umklapp, proportional to the gap in the A point (which would make the band  $1/2$  filled at constant number of electrons), is thus absent from the weak coupling theory. In the absence of Umklapp scattering, the CDW and SDW fluctuations are equally enhanced (Riera and Poilblanc, 2000). This enhancement is accompanied in turn by the Luttinger liquid behavior of the electron spectral density, as measured by ARPES. When SDW/CDW  $2k_F$  fluctuations are coupled to the (heavy) lattice, or when 3-dimensionality arises, as is the case in  $\text{BaVS}_3$ , the Luttinger liquid behavior tends to be replaced by a pseudogap in the electron spectral density at the Fermi level.

As an example of an experimental measurement that can be qualitatively explained in terms of the simple band structure from Fig. 3.20, the ARPES observed at 40 K is presented in Fig. 3.22. The spectrum shown therein was obtained using an experimental setup with a total energy and momentum resolution of  $\Delta E = 15$  meV and  $\Delta k = 0.04 \text{ \AA}^{-1}$ . The intensity map taken in the  $\Gamma$ -Z direction, parallel to the chains, reveals two bands: a dispersive band with bandwidth of few eV, identified as a one-dimensional  $d_z^2$  band; and a rather non-dispersive structure located at  $\sim -0.4$  eV, associated with the  $e(t_{2g})$  states. Due to the strong electron-electron interactions the measured spectral weight is renormalized, as it is often the case, masking the quasi

particle peak. From the saturation of the leading edge shift the charge gap was estimated to  $\Delta_{ch} = 60\text{-}70$  meV, which is in good agreement with the value obtained from transport measurements below  $T_{MI}$  (presented in Chapter 4).

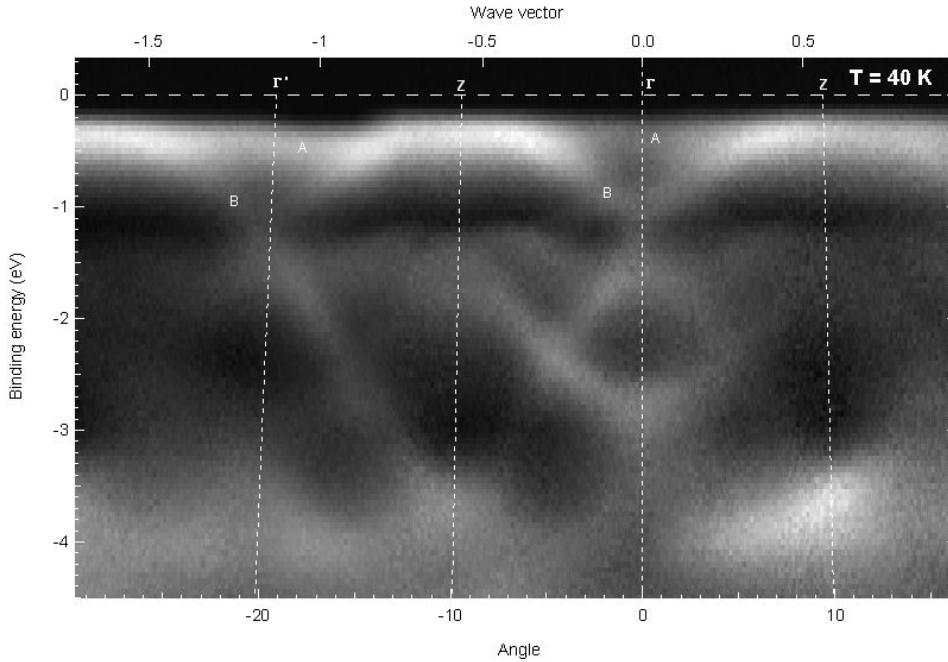


**Figure 3.22:** ARPES intensity map taken in the direction parallel to chains at 40 K. The zone boundaries are plotted from the calculated value. The Z point of the orthorhombic zone corresponds to the A point of the hexagonal zone. The spectrum is normalized and a background subtracted to enhance the features.

From the curvature at the bottom of the wide band around -1eV, in the point  $\Gamma$  of Fig. 3.22, it appears that this band would cross the Fermi level at  $k_F \approx \pi/2c$ , if there were no gap of some 80 meV. This determination of  $k_F$  agrees with the idea that the gap is produced by the evolution of 1D  $2k_F = \pi/c$  fluctuations, independently observed by x-ray scattering (Fagot *et al.*, 2003), into the 3D long-range order characterized by the 3D wavevector  $[1, 0, 0.5]$ . The 3D order itself is consistent with the full 3D nesting properties of the high temperature  $d_z^2$  band of Fig. 3.20. If, following the arguments of the above discussion, the  $d_z^2$  vanadium site energies of Fig. 3.20 are taken to be modulated by a deformation potential (with an amplitude of 80 meV) along the aforementioned wavevector, the gap opens at the Fermi level (Fig 3.23).

The X-ray experiments also show that a  $4k_F$  (additional to the  $2k_F$ ) deformation of the orthorhombic lattice appears below  $T_{MI}$ , although the corresponding precursor is not seen. It develops not as a harmonic of the  $2k_F$  deformation but independently of it. The screw axis symmetry is thus removed, which completes the lattice transformation in the *Imm2* phase. The corresponding effect in the band structure is the appearance of the gap at the A point. This gap is far above the Fermi level and thus it is not included

in Fig. 3.23. By analogy with organic conductors, it can only act on the physics at the

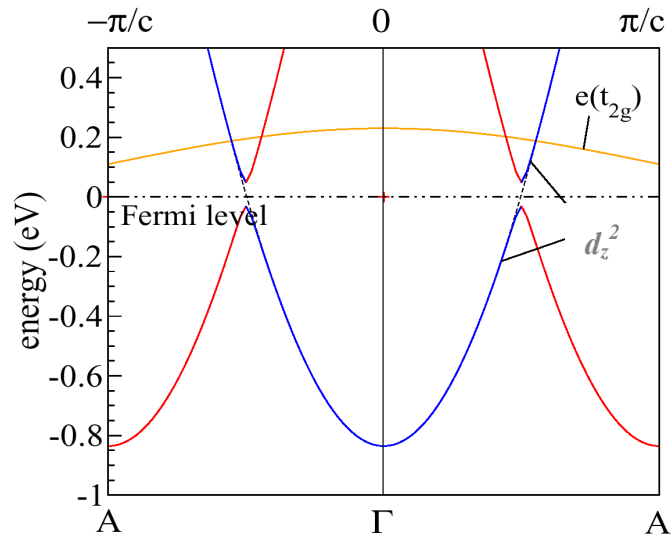


**Figure 3.23:** Electronic dispersions of the three band model, along the symmetry lines, modulated by the deformation potential with the wavevector  $[1, 0, 0.5]$  and the amplitude of 80 meV. The  $e(t_{2g})$ ,  $d_z^2$  band and its  $2k_F$  shadow are indicated by yellow, blue and red lines respectively. Parameters of the model are:  $d_z^2 - d_z^2$  overlap  $t_{a_3}^{||} (l=z) = -1.4$  eV,  $e(t_{2g}) - e(t_{2g})$  overlap  $t_{a_3}^{||} (l=x,y) = 0.1$  eV, in-plane overlaps which mix  $d_z^2$  and  $e(t_{2g})$   $t_{xy} = -0.05$  eV, diagonal-out-of plane overlaps  $t_{a_3nm}^{||} = 0.02$  eV, the  $d_z^2 - e(t_{2g})$  splitting  $3\Delta = 1.935$  eV, and the  $2\Delta(2k_F) = 80$  meV (Kupčić *et al.*, in preparation.)

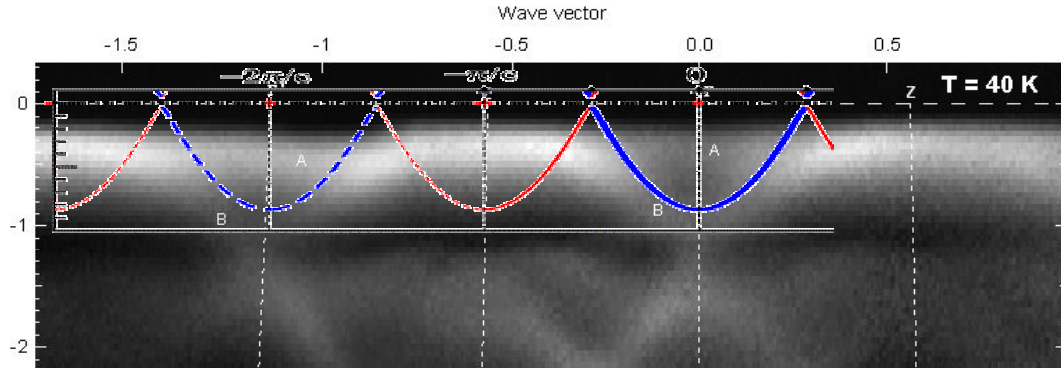


**Figure 3.24:** The ARPES intensity map, shown in Fig. 3.22, taken at 40 K. is compared with theoretical results from Fig. 3.23 (blue and red lines). The intensity of the shadow bands is proportional to the square ratio of the  $2k_F$  deformation potential so that the band width is hardly visible.

Fermi level indirectly, by activating the appropriate Umklapp interactions. The latter are presumably included through the empirical value (80 meV) of the  $2k_F$  deformation potential. The  $e(t_{2g})$  band is kept undistorted in Fig. 3.23 in order to emphasize its small overall width; too small to produce under distortion the effects which can be resolved by the present state-of-the-art ARPES measurements. This also holds for the  $2k_F$  shadow bands (red in Fig. 3.20) whose spectral weight is proportional to the small amplitude of the deformation potential, *i.e.*, to the magnitude of the gap. With this in

mind, the comparison of the theoretical modeling (of Fig. 3.23) with the relevant experimental results (shown in Fig. 3.24), reveals a remarkable agreement.

### ***3.5 Concluding remarks***

In conclusion to this chapter, we have seen the important role played by symmetry operations in understanding the consequence of the structural phase transitions on the electronic structure of our compound. In addition, these notions constitute important inputs for the various theoretical models presented herein. In the localized limit, a reasonably general qualitative description of electronic instabilities can be obtained by consideration of a single vanadium electron in the crystal field. Such an approach obviously masks the complexity of the situation somewhat. *Ab initio* calculations, using the LAPW formalism, provide a more quantitative description of the electronic structure of the various phases of the material. At the same time they validate, to some extent, the assumptions made in the localized model and provide a framework from which to obtain values for the overlap integrals for use in the tight binding calculations. However, in contrast to the TB approach, the LAPW methodology lacks the flexibility required for understanding those properties of the material which are associated with different kinds of response functions.

Significant synergistic effects can be realized by combining the LAPW and TB calculations with the ARPES and X-ray diffuse scattering measurements. In particular, we were able to use this combination to derive the minimal band model, which, after including the interactions in the wide band, can produce quasi-degenerate CDW/SDW fluctuations of the commensurability 4. The predicted long-range orders at  $T_S$  and  $T_M$  are also in good agreement with observations. The remaining question that has only been alluded to in this chapter is that of the (magnetic) coupling between the wide and the narrow band electrons. This question will be taken up in more detail in Chapter 5, where further discussion of the non-Fermi liquid aspects of the problem will be presented.

Despite the elucidation of the minimal model capable of describing the electronic instabilities present at the phase transitions, the details of the behavior of the material in the narrow energy range around the Fermi level remain obscure. In order to shed light upon those aspects and to enable further cooperation between experiment and theory, one needs to employ techniques that directly probe this energy range. From the experimental side, this involves the careful measurement of properties such as the electrical resistivity, magnetotransport and thermoelectric power. The remainder of this thesis is dedicated to exactly this goal.

---

---



### **3.6 References**

Abragam A. and B. Bleaney. 1970. *Electron Paramagnetic Resonance of Transition Ions*. Oxford, Carendon Press. UK.

Ballhausen C. J. 1962. *Introduction to Ligand Field Theory*. New York, McGraw-Hill. U.S.A.

Fagot S., P. Foury-Leylekian, S. Ravy, J. P. Pouget and H. Berger. 2003. One-dimensional instability in BaVS<sub>3</sub>. *Phys. Rev. Lett.*, **90**(19), 196401.

Fang Z. and K. Terakura. 2002. Structural distortion and magnetism in transition metal oxides: crucial roles of orbital degrees of freedom. *J. Phys.-Condes. Matter*, **14**(11), 3001-14.

Friedel J. 1969. *Physics of Metals I. Electrons* J. M. Ziman, editor. Cambridge Univ. Press. UK. p.341.

Hahn T. editor. 2002. *International Tables for Crystallography: Space-Group Symmetry*. Amsterdam, Kluwer Academic Publishers. The Netherlands.

Inami T., K. Ohwada, H. Kimura, M. Watanabe, Y. Noda, H. Nakamura, T. Yamasaki, M. Shiga, N. Ikeda and Y. Murakami. 2002. Symmetry breaking in the metal-insulator transition of BaVS<sub>3</sub>. *Phys. Rev. B*, **66**(7), 073108.

Ivantchev S., E. Kroumova, G. Madariaga, J. M. Pérez-Mato and M. I. Aroyo. 2000. SUBGROUPGRAPH: a computer program for analysis of group-subgroup relations between space groups. *J. Appl. Cryst.*, **33** 1190.

Kiss A. and P. Fazekas, *private communication*.

Kittel C. 1953. *Introduction to solid state physics*. The University of California at Berkeley, Wiley.

Kupcic I. *et al.*, Tight binding calculations in BaVS<sub>3</sub>, *in preparation*.

Landau L. D. and E. M. Lifshitz. 1980. *Statistical Physics 3<sup>rd</sup> Edition Part 1*.

---

---

Pergamon Press. Oxford, UK.

Mattheiss L. F. 1995. Electronic-Structure Of Quasi-One-Dimensional Bavs3. *Solid State Commun.*, **93**(10), 791.

Mihaly G., I. Kezsmarki, F. Zamborszky, M. Miljak, K. Penc, P. Fazekas, H. Berger and L. Forro. 2000. Orbitally driven spin pairing in the three-dimensional nonmagnetic Mott insulator BaVS3: Evidence from single-crystal studies. *Phys. Rev. B*, **61**(12), R7831.

Mitrovic S., P. Fazekas, C. Sondergaard, D. Ariosa, N. Barisic, H. Berger, D. Cloetta, L. Forró, H. Höchst, I. Kupcic, D. Pavuna and G. Margaritondo. Experimental Electronic Structure and Interband Nesting in BaVS3. *Submitted for publication*.

Nakamura H., H. Tanahashi, H. Imai, M. Shiga, K. Kojima, K. Kakurai and M. Nishi. 1999. Neutron scattering study of BaVS3: orbital-ordered spin-singlet system. *J. Phys. Chem. Solids*, **60**(8-9), 1137.

Riera J. and D. Poilblanc. 2000. Coexistence of charge-density waves, bond-order waves, and spin-density waves in quasi-one-dimensional charge-transfer salts. *Phys. Rev. B*, **62**(24), R16243-R46

Singh. D. 1994. Plane waves, pseudopotentials and the LAPW method. Amsterdam, Kluwer Academic. The Netherlands.

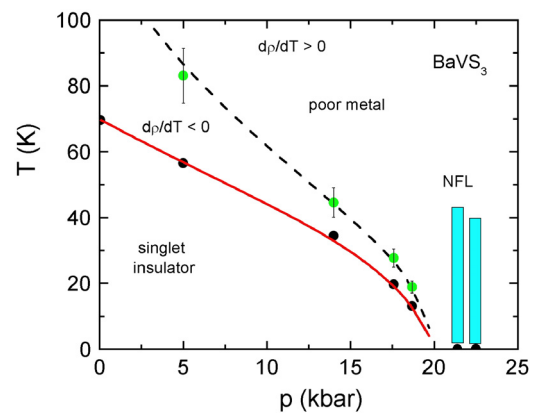
Takano M., H. Kosugi, N. Nakanishi, M. Shimada, T. Wada and M. Koizumi. 1977. Electrical, Magnetic And Structural Transitions Of BaVS<sub>3</sub>. *J. Phys. Soc. Jpn.*, **43**(3), 1101.

Whangbo M. H., H. J. Koo, D. Dai and A. Villesuzanne. 2002. Analysis of the electron localization, the anisotropy of electrical conductivity, the orbital ordering, and spin- exchange interactions in BaVS3 on the basis of first principles and semi-empirical electronic structure calculations. *J. Solid State Chem.*, **165**(2), 345.



## Chapter 4

# FOLLOWING THE METAL-INSULATOR PHASE BOUNDARY BY RESISTIVITY



<b>4.1</b>	<b>AMBIENT PRESSURE</b>	<b>64</b>
4.1.1	SAMPLE CHARACTERIZATION	66
<b>4.2</b>	<b>INTERMEDIATE PRESSURES (1BAR &lt; <math>p</math> &lt; 1.7GPa)</b>	<b>68</b>
<b>4.3</b>	<b>MAGNETORESISTIVITY (1BAR &lt; <math>p</math> &lt; 1.7GPa)</b>	<b>70</b>
<b>4.4</b>	<b>CONCLUDING REMARKS</b>	<b>75</b>
<b>4.5</b>	<b>REFERENCES</b>	<b>76</b>

In this chapter, I present the low pressure part of the  $p$ - $T$  phase diagram. Although this is a well-studied part of the phase diagram, several refinements of known results, such as the importance of the stoichiometry and the pressure dependence of  $T_S$ , *etc.*, are obtained. This chapter also serves as an introduction to the exciting behavior of the studied material at pressures above 1.7 GPa, which will be presented in subsequent chapters.

## 4.1 Ambient pressure

The band structure calculations of BaVS<sub>3</sub> discussed in the Chapter 3 were shown to give reasonable predictions for the shape of the bands on the eV scale. However, in the narrow energy window of the order of 0.01 eV ( $\sim 100$  K) around the Fermi level, they do not account for the detailed behavior. One property that is particularly useful in gaining an overview of this low energy physics is the electrical resistivity. Therefore, in the following material, we present the results of the electrical resistivity measurements along the *c*-axis, in broad temperature and pressure ranges. Before continuing, let us stress the fact that the conductivity ratio of BaVS<sub>3</sub> above  $T_{MI}$  at ambient pressure is surprisingly low ( $\sigma_c/\sigma_a \approx 3$ ). In addition, for these low pressures, this ratio is almost independent of the temperature, as discussed in Chapter 2.

In an attempt to clarify the transport properties above  $T_S = 240$  K, where the structural phase transition occurs, the electrical resistivity was measured in an extended temperature range at ambient pressure (Fig. 4.1). The measurement was performed in a homemade sample holder (Appendix 1) which allows transport measurements up to 1000 K. BaVS<sub>3</sub> is very sensitive to heat treatments (Gardner *et al.*, 1969) since it starts to lose sulfur at high temperatures. Therefore, the measurements were carried out only up to 600 K.

In this regime, the electrical resistivity exhibits a linear, metallic-like, temperature dependence. The resistivity has a high absolute value, e.g.,  $\rho \sim 0.7$  m $\Omega$ cm at 300 K with a corresponding mean free path of  $l \sim 5$ -8 Å (Forró *et al.*, 2000). This fact classifies BaVS<sub>3</sub> in a relatively new class of materials known as *bad metals* or novel conductors (Emery and Kivelson, 1995). In these materials, with a short mean free path (often even shorter than the lattice spacing), the Ioffe-Regel criterion (IRC) is violated. This criterion determines the maximum resistivity below which one can speak about metals. Beyond this value, the system is an insulator. However, materials which exhibit resistivities with a metallic temperature dependence beyond the IRC, such as BaVS<sub>3</sub>, have recently been discovered (Emery and Kivelson, (1995), Takenaka *et al.*, (2002)). The IRC is based on the concept of a propagating quasiparticle that is valid provided the mean free path is longer than the corresponding de Broglie wavelength:  $\lambda > \lambda_F = 2\pi/k_F$ . In a solid, this condition may not be violated until  $l$  is roughly equal to the lattice spacing  $a$ .

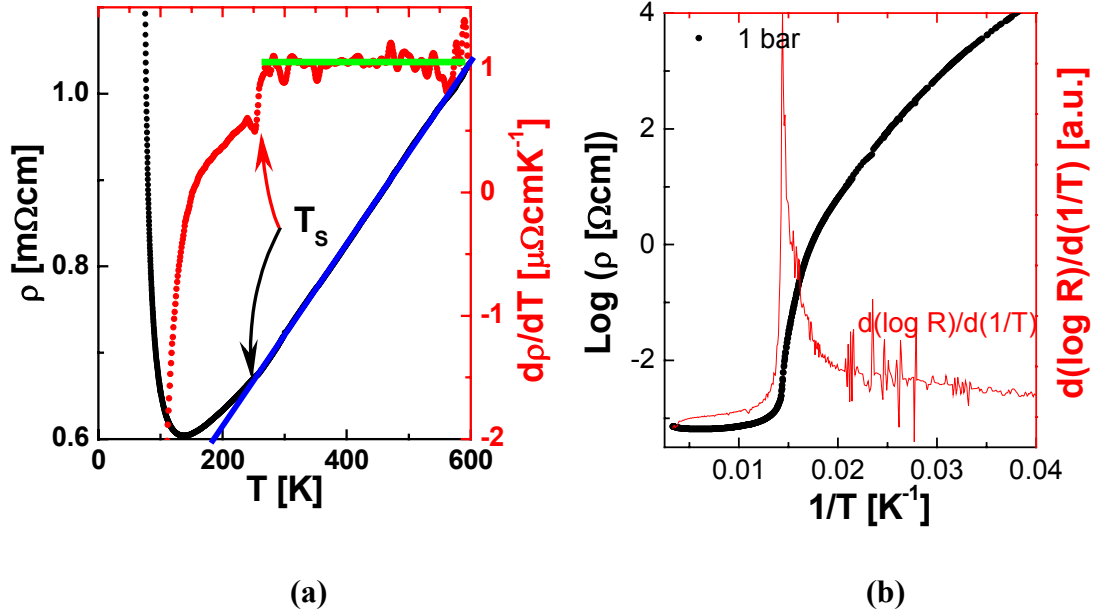


**Figure 4.1:** Black lines describe the temperature dependence of electrical resistivity of BaVS<sub>3</sub> shown on: **(a)** the linear scale in the in the 0-600 K range revealing the linear temperature dependence above  $T_S$ , **(b)** the Arrhenius plot giving insight into the electrical properties of the insulating phase. Red scales are related to **(a)** temperature derivative and **(b)** logarithmic derivative of the electrical resistivity disclosing the weak change of slope of resistivity at  $T_S$ , and the temperature of the MI transition, respectively. The green and the blue lines are guides to the eye.

The weak change of the slope at 240 K indicates the onset of the structural transition. The zigzagging and the deformation of the chain of sulfur octahedra lift the degeneracy of the  $e(t_{2g})$  orbitals (Chapter 3) at  $T_S$  (maintaining the screw axis symmetry). Below this temperature, the derivative of the electrical resistivity gradually changes its slope, and at even lower temperatures its sign. This latter change, however, occurs well above  $T_{MI} = 69$  K (shown in Fig.1a). The derivative of resistivity clearly demonstrates that  $T_S$  does influence the electronic structure, a fact which was overlooked in previous studies. Therefore, instead of attributing the upper boundary of the MI precursor region to  $T_S$ , the previous studies attributed it to the temperature defined by the minimum of the resistivity ( $d\rho/dT = 0$ ). At  $T_{MI}$  (derived from the peak in the logarithmic derivative of electrical resistivity (Forró *et al.*, 2000), shown in Fig. 4.1b), the system undergoes the MI phase transition. The Arrhenius plot in Fig. 4.1b gives insight into the nature of the insulating state. After an abrupt jump, of about 3 orders of magnitude, the resistivity becomes activated and approximately follows the relation:

$$\rho(T) = \rho_0 \exp\left(\frac{\Delta_{ch}}{k_B T}\right) ,$$

where  $\Delta_{ch}$  is the charge gap, estimated as 700 K. If one assumes that the charge gap is related to  $T_{MI}$  by the BCS (Bardeen, Cooper and Schrieffer) relationship,  $\Delta_{ch}/k_B T_{MI}$ , an unusually large ratio of  $\approx 10$  is obtained. This value is particularly striking when compared to the predicted BCS mean field ratio of 3.76.

#### 4.1.1 *Sample characterization*

In the context of the first work on BaVS<sub>3</sub> by (Gardner *et al.*, 1969) it was already noted that the electrical properties depend strongly on the purity of the crystals. More extensive work on the sample purity was presented in the paper of (Massenet *et al.*, 1979) The resistivity and the magnetic susceptibility on stoichiometric and sulfur deficient single crystals were reported. The stoichiometric samples, obtained by heating and cooling the grown crystals in a saturated sulfur atmosphere (hereafter this procedure is called the “sulfur treatment”), had antiferromagnetic behavior with a maximum of magnetic susceptibility close to  $T_{MI}=70$  K. The sulfur deficient crystals were ferromagnetic with an ordering temperature of 16 K. The reported resistivity for both types of crystals was, as previously observed for the pressed powders, metallic like from room temperature down to 150 K. For the antiferromagnetic crystal, there was a steep increase of resistivity below 70 K. On the contrary, the resistivity of ferromagnetic crystals increases regularly below 150 K.

Because of the above variability, we used the measured transport properties of BaVS<sub>3</sub> crystals as a means of identifying the high quality ones. More than hundred crystals were characterized until the proper method for sample synthesis and sulfur treatment was found. The aim was to obtain single crystals which satisfy the following criteria, which we believe to be indicative of high quality BaVS<sub>3</sub> samples:

- metallic behavior at high temperatures,
- a well defined change of the slope at  $T_S$ ,
- a sharp MI transition,
- no sign of saturation of resistivity in the insulating phase (attributed to an impurity band).

Several examples of typical characterization curves are shown in Fig. 4.2. For easier comparison, all the recorded data are normalized by their room temperature resistance. From the presented set of samples, the one marked as N<sup>o</sup>: 00 (shown in red) best satisfies the aforementioned criteria and was therefore selected for further investigations. Its quality was also verified by anisotropy measurement of magnetic

---

susceptibility in 4 to 80 K temperature range, shown in the inset in Fig. 4.2. In contrast with earlier measured samples (see, for example, Mihály *et al.*, (2000)), the low temperature anisotropy does not show any sign of saturation or upturn, attributed to impurities. In addition, the changes in the anisotropy attributed to the phase boundaries,  $T_{MI}$  and  $T_x$  are sharper and better defined.

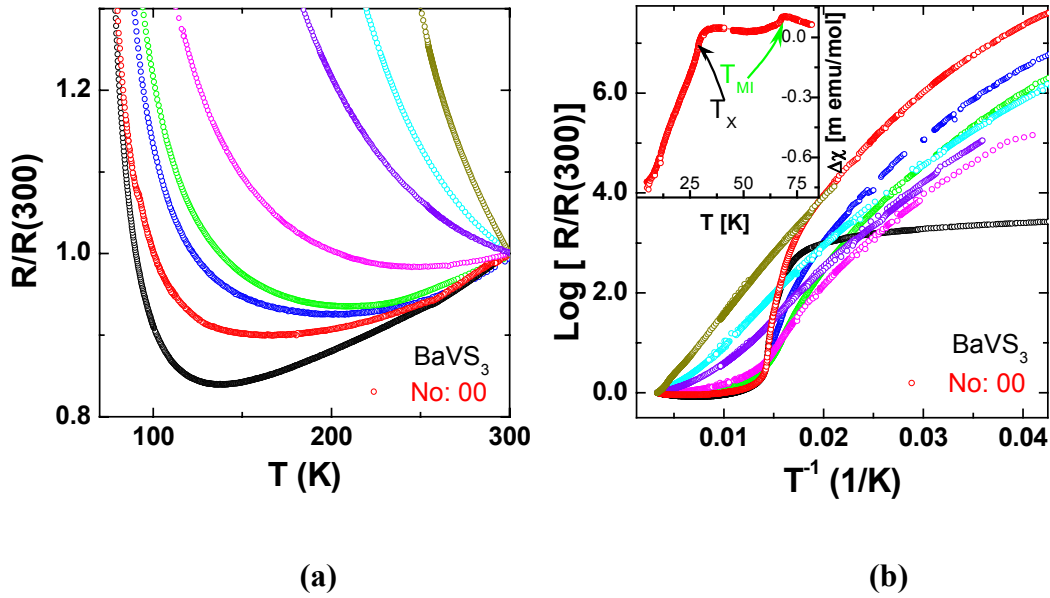


**Figure 4.2:** Temperature dependence of the electrical resistivity of different samples of  $BaVS_3$ . **(a)** Linear plot of normalized resistivity focusing on the metallic phase. **(b)** Recorded and normalized data shown in the Arrhenius plot making apparent the sharpness of the MI transition and the details of the insulating phase. Inset shows the anisotropy of the magnetic susceptibility for the best quality (hereafter called No: 00) sample. Each color corresponds to one sample and the sample N<sup>o</sup>: 00 is marked in red.

Our recent resistivity measurements on impure or sulfur deficient single crystals of  $BaVS_3$  under pressure, Chapter 5, have sparked a new interest for this kind of sample since, in contrast to the pure samples, they do not show hysteresis in the proximity of the quantum critical point (QCP). They become even more intriguing if magnetic susceptibility and resistivity measurements of 15 % Sr substituted  $Ba_{1-x}Sr_xVS_3$  single crystals, Chapter 6, are taken into account. The interesting aspect of this particular material is that the MI transition is observable in the electronic properties of the system while the magnetic susceptibility remains Curie-like down to low temperatures ( $\sim 15$  K), where the system undergoes the FM transition. Therefore, it is of interest to determine if a similar behavior can be observed in sulfur deficient samples. To this end, a more detailed study of the off-stoichiometric  $BaVS_3$  samples, shown in Fig. 4.2, is currently in progress.



## 4.2 Intermediate pressures ( $1\text{bar} < p < 1.7\text{GPa}$ )

The band structure calculations mentioned in Chapter 1 (Solovlyev *et al.* (1994), *etc.*) predicted that  $\text{BaVS}_3$  would be sensitive to the change of pressure. Indeed, this is consistent with the measurements of Graf *et al.* (1995) and Forró *et al.* (2000) that reveal a strong suppression of the MI transition by pressure. Fig. 4.3a shows temperature dependence of the resistivity for various pressures for our cleanest sample,  $N^\circ: 00$ .

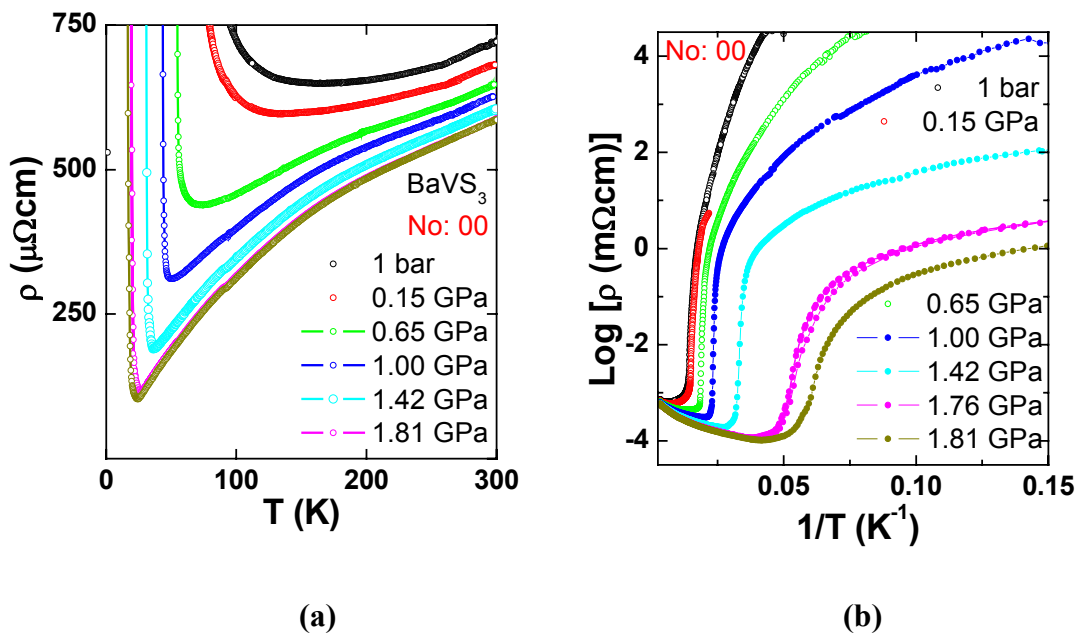


**Figure 4.3:** (a) Temperature dependence of resistivity for various pressures revealing the electronic properties of the metallic phase. (b) Arrhenius plot uncover the low temperature insulating behavior.

As expected, the  $T_{MI}$  is shifted to lower temperatures by the increase of pressure, thus extending the temperature range in which the metallic state is observed. The low temperature part of resistivity retains the activated temperature dependence (Fig. 4.3b). By increasing pressure, the charge gap decreases in such a way as to maintain a roughly constant value of the relation  $\Delta_{ch}/k_B T_{MI} \approx 10$ . The pressure dependence of the MI transition temperature was determined from the spikes of the logarithmic derivative,  $d(\log \rho)/d(1/T)$ , as shown in Fig. 4.4a. The narrowness of the spikes indicates that the transition remains sharp under pressure. As seen in Fig. 4.4b, the value of  $T_{MI}$  decreases linearly with pressure. The negative shift of the metal-insulator transition temperature, in the pressure range of 1bar to 1.75 GPa, varies as  $T_{MI} = 70 - 29.15 \cdot p$ . Extrapolation of this relation to zero indicates the  $T_{MI}$  transition

would disappear at  $\sim 2.4$  GPa.

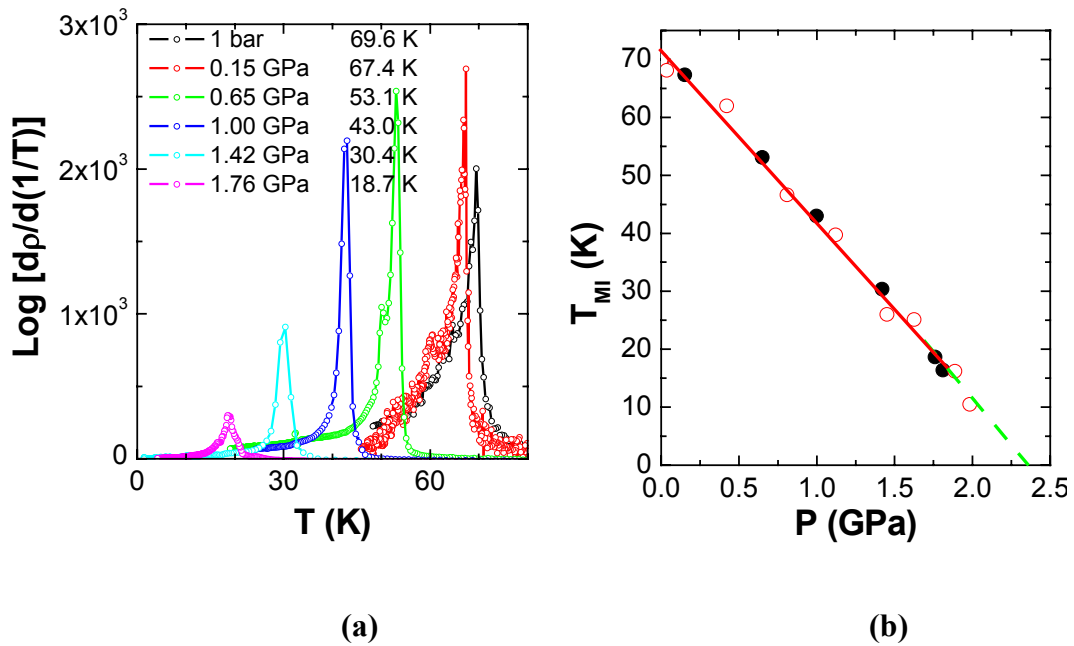


**Figure 4.4:** (a) Logarithmic derivative,  $d(\log \rho) / d(1/T)$ , for several pressures. The position of the spike defines the MI transition temperature. (b) The MI phase boundary as a function of pressure. The red line is a guide for eye. The linear high pressure extrapolation of  $T_{MI}$  with pressure is marked by a green dashed line. The results obtained on sample N<sup>o</sup>: 00 are marked by open red circles. The black circles indicate the results of the measurements on a second sample.

Finally, let us mention that resistivity measurements under pressure on high purity samples (N<sup>o</sup>: 00) revealed that increasing the pressure shifts the structural phase transition ( $T_S$ ) to higher temperatures and, by 0.65 GPa, is already out of our experimentally accessible temperature range (300 K). These observations mean that the phase on the high temperature side of  $T_{MI}$  is associated with the orthorhombic structure, stabilized to higher temperatures by hydrostatic pressure.

### 4.3 Magnetoresistivity ( $1\text{bar} < p < 1.7\text{GPa}$ )

At the MI transition, the sharp change in behavior of the magnetic susceptibility is observed in clean single crystals of  $\text{BaVS}_3$ . It is therefore of interest to determine how the magnetic field affects the properties of the system. The first measurements of the high field magnetoresistance in the single crystals were reported by Booth *et al.*, (1999). These authors also reported the measurements of the low-field Hall effect and the high field magnetization of polycrystalline samples of  $\text{BaVS}_3$ . The magnetoresistance varies quadratically with the increasing magnetic field, as  $\alpha(T) H^2$ , and within the experimental error (10-20%), it is independent of the field direction. An analogous observation was reported by Kézsmárki *et al.* (2001) but under hydrostatic pressures up to 1.5 GPa. In both works, similar analyses of the recorded data were used. As a result, the pressure dependence of the spin gap was determined (up to 1.5 GPa). In the following section, the main results of magnetoresistivity measurements are presented, and the principal steps of the associated analysis are discussed.

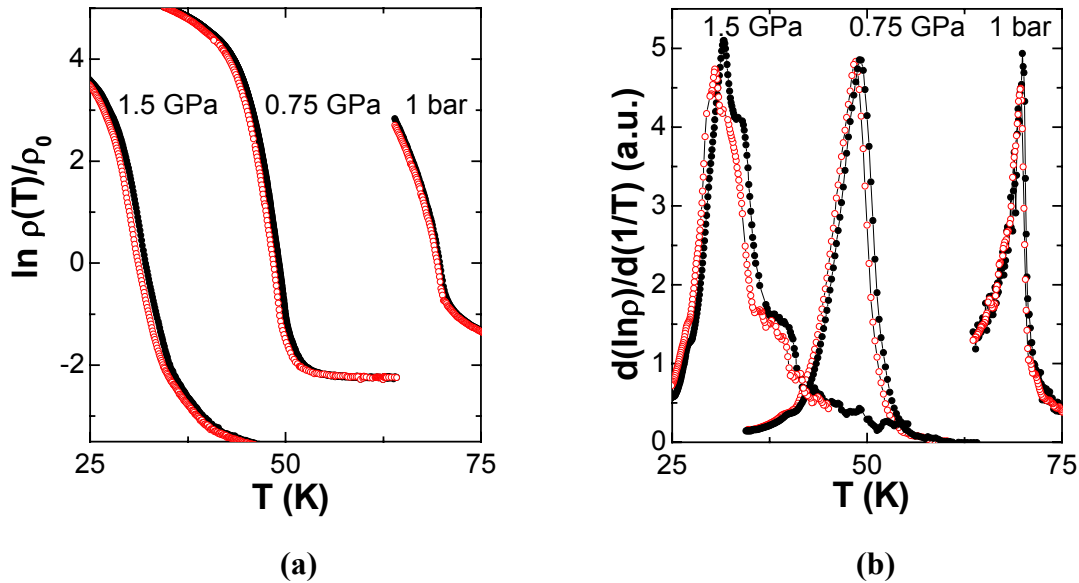


**Figure 4.5:** (a) The normalized logarithmic plot of the resistivity. The red curves, measured in 12 T, are shifted due to the magnetic field with  $\Delta T_{MI} = 0.35; 0.7; 0.9$  K relative to the zero field ones (black curves) for  $p = 1\text{bar}; 0.75\text{ GPa}; 1.5\text{ GPa}$ , respectively. (b) The logarithmic derivative of the same resistivity curves with a sharp peak at the phase transition. (Kézsmárki, 2003).

Figure 4.5a. summarizes the results of the resistivity measurements, at various pressures, in the presence of magnetic field strengths of  $H = 0$  and  $H = 12$  T (Kézsmárki *et al.* 2001). It turns out that the influence of the applied magnetic field is

not to change the shape of the resistivity curves but to shift them to lower temperatures with a concomitant shift of the phase transition (clearly seen in Fig. 4.5b). In other words, the magnetic field merely acts to shift the temperature range of the curves by  $\Delta T_{MI}$ . The value of  $T_{MI}$  itself can be determined, with high accuracy, from the logarithmic derivative of the resistivity (Fig. 4.5b). Since the temperature dependence of the resistivity, for fixed pressure, is shifted in temperature ( $T \rightarrow T - \Delta T_{MI}$ ) by switching on the magnetic field ( $0 \rightarrow H$ ), the resistivity can be expressed as:

$$\rho(T, H = 0, p) = \rho(T - \Delta T_{MI}(H, p), p).$$

Given that  $\Delta T_{MI}$  is relatively small (0.35; 0.7; 0.9 K at 1bar; 0.75 GPa; 1.5 GPa, respectively), and taking into account the above equation, the relative change of the magnetoresistance,  $\Delta\rho = \rho(T, H, p) - \rho(T, 0, p)$ , can be expanded as a power series:

$$\begin{aligned} \Delta\rho(T - \Delta T_{MI}(H, p = p_0), p = p_0) = & - \left( \frac{\partial \rho(T, p_0)}{\partial T} \right)_{H=0} \Delta T_{MI} \\ & + \frac{1}{2} \left( \frac{\partial^2 \rho(T, p_0)}{\partial T^2} \right)_{H=0} (\Delta T_{MI})^2 - \dots \end{aligned} \quad (4.1)$$

where:

$$\left( \frac{\partial^n \rho(T, p_0)}{\partial T^n} \right)_{H=0},$$

is calculated directly from the temperature dependence of resistivity in zero field. The results of the first and second order expansion in  $\Delta T_{MI}$  are compared with the recorded, subtracted resistivity data from 0 and 12 T, shown in Fig. 4.6. Already, the first order expansion gives a good approximation, except in the narrow region in the vicinity of the  $T_{MI}$ , where the second order correction is needed to achieve acceptable accuracy. As the approximation with only the linear term in  $T_{MI}$  agrees relatively well with the measured results over the broad temperature range, we will, in the interests of simplicity, neglect the higher powers terms in the following calculation.

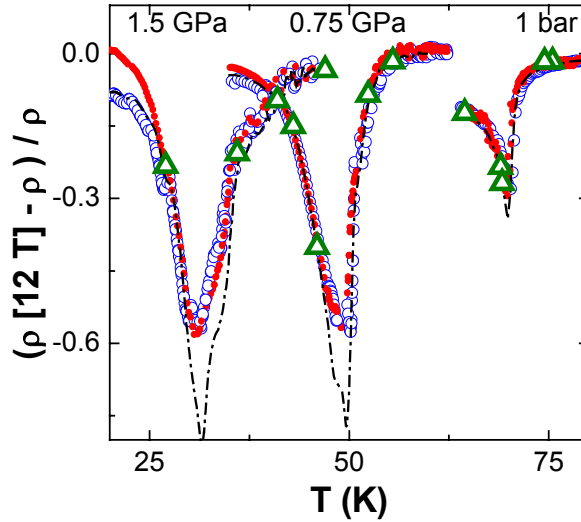


**Figure 4.6:** Analysis of the temperature dependence of the relative magnetoresistance at three pressures. The red circles indicate the measured relative resistivity. The dashed line and the blue open circles indicate the results of the first and second order approximation, respectively. By the open green triangles, the results of the magnetic-field sweeps, at selected temperatures, are indicated (Kézsmárki, 2003).

Experiments, in which the value of the magnetic field was swept from 0 to 12 T for each pressure, (shown in Fig. 4.7) at constant temperature, revealed that the magnetoresistance is very weak (at the limit of detection) at high temperatures (of the order of  $2T_{MI}$ ). As the temperature is decreased, magnetoresistance becomes larger and larger as well as adhering to quadratic field dependence:

$$\frac{\Delta\rho(T = \text{konst}, H, p = p_0)}{\rho(T = \text{konst}, 0, p = p_0)} = -\alpha(T)H^2 \quad (4.2)$$

Equations (4.1) and (4.2) are in fact equal (only dependent on the field,  $H$ ) and after dividing them by  $T_{MI}$  we get:

$$\begin{aligned} \frac{\alpha(T)H^2}{T_{MI}} &= \frac{\partial \ln[\rho(T, p_0)]}{\partial T} \frac{\Delta T_{MI}(H, p_0)}{T_{MI}} \\ \Rightarrow \frac{\Delta T_{MI}(H, p_0)}{T_{MI}} &= \frac{\alpha(T)}{T_{MI} \frac{\partial \ln[\rho(T, p_0)]}{\partial T}} H^2 = -\beta H^2 \end{aligned} \quad (4.3)$$

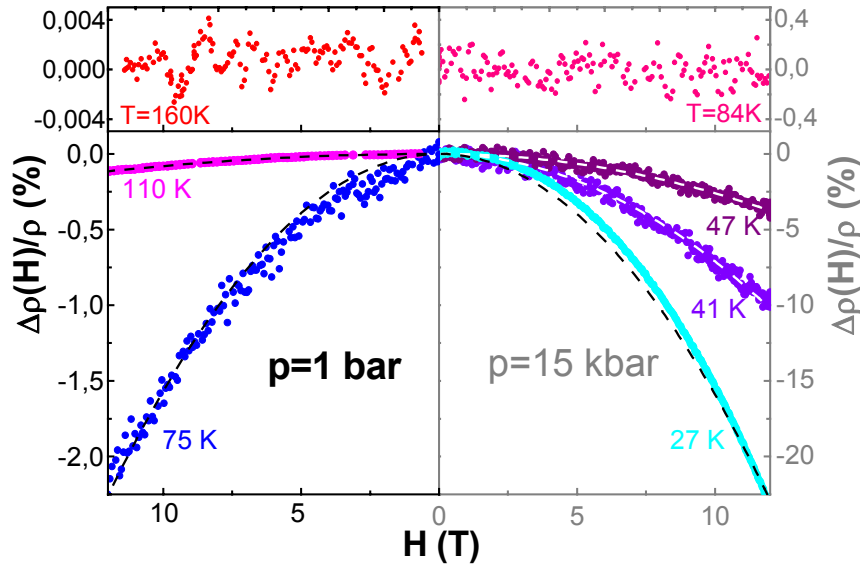


**Figure 4.7:** Magnetic-field dependence of the resistivity at various temperatures at  $p = 1 \text{ bar}$ , and 1.5 GPa. The dashed curves indicate the quadratic fit to the data. Note the different scales in the upper panel. (Kézsmárki, 2003).

implying that the relative shift of the MI transition  $\Delta T_{MI} / T_{MI}$  has a quadratic magnetic field dependence. Assuming that the observed phase boundary behavior, in the low magnetic field range of 12 T, is also valid at higher fields, a critical field ( $H_c = H(\Delta T_{MI} = T_{MI}) = 1/\beta^{1/2}$ ), which completely suppresses the MI transition, can be deduced. At the ambient pressure, the critical field has a rather high value,  $H_c \approx 170T$ , which is to be expected as the shift of  $T_{MI}$  is small. By increasing the pressure, the value of this critical field decreases and has the same scaled pressure dependence as  $T_{MI}$ .

Equation (4.3) may be rewritten in its dimensionless form as:

$$\frac{\Delta T_{MI}(H, p_0)}{T_{MI}(p_0)} = -\gamma \left( \frac{gS\mu_B H}{k_B \cdot T_{MI}(p_0)} \right)^2.$$

which, with  $S = 1/2$  and  $g = 2$ , is equivalent to the relationship which describes the suppression of the spin-Peierls transition by the magnetic field. The sensitivity of the transition to the applied field is described by the constant  $\gamma$ . The experimentally established value is universal both for organic (Northby *et al.*, 1982) and inorganic (Hase *et al.*, 1993) compounds and agrees well with the predicted value of 0.44 (Bulaevskii *et al.*, 1978) and 0.38 (Cross, 1979). In  $\text{BaVS}_3$ , the magnetoresistance

data yield a value of  $\gamma = 0.45$ , independent of the value of the applied pressure.

Another dimensionless form of equation (3) is obtained by introducing the pressure dependent spin gap  $\Delta_S(p) = 2gS\mu_B H_c(p)$ :

$$\frac{\Delta T_{MI}(H, p_0)}{T_{MI}(p_0)} = -\left(\frac{2gS\mu_B H}{\Delta_S(p_0)}\right)^2,$$

assuming that it is related to a critical magnetic field  $H_c$  via the corresponding Zeeman energy. The ambient pressure value of the spin gap based on this assumption is  $\Delta_S(1\text{ bar}) \approx 250\text{ K}$  is identical with that obtained from NMR measurements by (Nakamura *et al.*, 1997). The spin gap of the insulating phase scales with the transition temperature according to the BCS relation  $\Delta_S(p) \approx 3.6 k_B T_{MI}$ .

In addition, Kézsmárki *et al.* (2001) discussed the properties of the thermodynamic potential and predicted that, at 1 bar, the MI transition is of second order. This prediction was independently confirmed several years later by Inami *et al.*, (2002) and Fagot *et al.*, (2003). They carried out X-ray diffraction measurements of BaVS<sub>3</sub> single crystals and observed superlattice reflections, which double the lattice constant  $c$ , appearing at the MI transition temperature. The increase in intensity of the new Bragg peaks, in a mean field manner, associated with a further decrease of temperature provides evidence of the second order character of the MI transition. As the character of the shift of the MI transition with magnetic field remains the same with increase of pressure, it is plausible that the character of the MI transition remains unchanged in the 1 bar to 1.5 GPa region.

#### ***4.4 Concluding remarks***

In summary, the measurements of the resistivity under conditions of varying pressure and magnetic field, over the specified ranges, reveal several important features in the behavior of BaVS<sub>3</sub>. In the absence of a magnetic field, the temperature at which the MI transition takes place ( $T_{MI}$ ) is inversely related, in a linear fashion, to the applied hydrostatic pressure. The magnetoresistance is observed to obey a quadratic field dependence while the relative shift of  $T_{MI}$ , in response to the applied field, is found to be analogous to that of the spin-Peierls transition. The fact that the magnetic dependence of the resistivity at  $T_{MI}$  does not change in response to an increase of pressure, combined with the conclusions of previous studies, suggests that the second-order nature of the MI transition remains unaltered over the pressure range discussed herein.

When taken at face value, the above results could be understood to mean that the MI phase boundary in the  $T$ - $p$ - $H$  phase diagram of BaVS<sub>3</sub> is relatively simple. However, it is safe to say that this is not the case. As the hydrostatic pressure is increased beyond 1.7 GPa, the relatively simple behavior outlined in this chapter breaks down and the description of the phase diagram becomes much more complicated. The details of how this takes place are the subject of the following chapter.



## 4.5 References

- Booth C. H., E. Figueroa, J. M. Lawrence, M. F. Hundley, and J. D. Thompson. 1999. Effect of magnetic fields on the metal-insulator transition in BaVS<sub>3</sub>. *Phys. Rev. B* **60**(21), 14852.
- Bulaevskii L. N., A. I. Buzdin and D. I. Khomskii. 1978. spin-Peierls transition in magnetic-field. *Solid State Commun.*, **27**(1), 5.
- Cross M. C. 1979. Effect of magnetic-fields on a spin-Peierls transition. *Phys. Rev. B*, **20**(11), 4606.
- Emery V. J., and S. A. Kivelson. 1995. Superconductivity in bad metals. *Phys. Rev. Lett.*, **74**(16), 3253 (1995).
- Fagot S., P. Foury-Leylekian, S. Ravy, J. P. Pouget and H. Berger. 2003. One-dimensional instability in BaVS<sub>3</sub>. *Phys. Rev. Lett.*, **90**(19), 196401.
- Forró L., R. Gaál, H. Berger, P. Fazekas, K. Penc, I. Kézsmárki, G. Mihály. 2000. Pressure induced quantum critical point and non-Fermi-liquid behavior in BaVS<sub>3</sub>. *Phys. Rev Lett.*, **85**(9), 1938.
- Gardner R. A., M. Vlasse, and A. 1969. Preparation, properties and crystal structure of barium vanadium sulfide. *Acta Crys. B*, **25**, 781.
- Graf T., D. Mandrus, J. M. Lawrence, J. D. Thompson, P. C. Canfield, S. W. Cheong, and L. W. Rupp, Jr.. 1995. Suppression of the metal-to-insulator transition in BaVS<sub>3</sub> with pressure. *Phys. Rev B*, **51**(4), 2037.
- Hase M., I. Terasaki and K. Uchinokura. 1993. Observation of the spin-Peierls transition in linear Cu<sup>2+</sup> (Spin-1/2) chains in an inorganic compound CuGeO<sub>3</sub>. *Phys. Rev. Lett.*, **70**(23), 3651.
- Inami T., K. Ohwada, H. Kimura, M. Watanabe, Y. Noda, H. Nakamura, T. Yamasaki, M. Shiga, N. Ikeda, and Y. Murakami. Symmetry breaking in the metal-insulator transition of BaVS<sub>3</sub>. 2002. *Phys. Rev. B*, **66**(7), 073108.
- 
-

Kézsmarki, S. Csonka, H. Berger, L. Forro, P. Fazekas and G. Mihaly. 2001. Pressure dependence of the spin gap in BaVS<sub>3</sub>. *Phys. Rev. B*, **63**(8), 081106.

Kézsmarki I. 2003. Phase diagram of a Correlated d-electron system: Experimental study of BaVS<sub>3</sub>. *PhD thesis*. Ecole Polytechnique Fédérale de Lausanne. Lausanne. Swiss.

Massenet O., J. J. Since, J. Mercier, M. Avignon, R. Buder, V. D. Nguyen, and J. Kelber. 1979. Magnetic and electrical properties of BaVS<sub>3</sub> and BaV<sub>x</sub>Ti<sub>1-x</sub>S<sub>3</sub>. *J. Phys. Chem. Solids*, **40**(8), 573.

Mihaly G., I. Kezsmarki, F. Zamborszky, M. Miljak, K. Penc, P. Fazekas, H. Berger and L. Forro. 2000. Orbitaly driven spin pairing in the three-dimensional nonmagnetic Mott insulator BaVS<sub>3</sub>: Evidence from single-crystal studies. *Phys. Rev. B*, **61**(12), R7831.

Nakamura H., H. Imai and M. Shiga. 1997. Possible orbital ordering in a spin-singlet ground state: V-51 NMR and NQR study of BaVS<sub>3</sub>. *Phys. Rev. Lett.*, **79**(19), 3779.

Northby J. A., H. A. Groenendijk, L. J. Dejongh, J. C. Bonner, I. S. Jacobs and L. V. Interrante. 1982. Field-dependent differential susceptibility studies on Tetrathiafulvalene-AuS<sub>4</sub>C<sub>4</sub>(CF<sub>3</sub>) - Universal aspects of the spin- Peierls phase diagram. *Phys. Rev. B*, **25**(5), 3215.

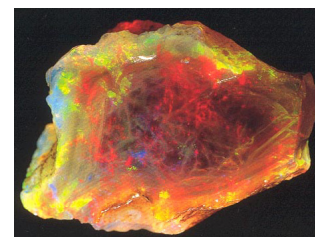
Solovyev I. V., V. I. Anisimov, and E. Z. Kurmaev. 1994. LMTO-ASA Band structure calculations of BaVS<sub>3</sub>, BaTiS<sub>3</sub> and their solid solutions. *Physica Scripta*, **50**(1), 90.

Takenaka K., R. Shiozaki, S. Okuyama, J. Nohara, A. Osuka, Y. Takayanagi and S. Sugai. 2002. Coherent-to-incoherent crossover in the optical conductivity of La<sub>2-x</sub>Sr<sub>x</sub>CuO<sub>4</sub>: Charge dynamics of a bad metal. *Phys. Rev. B*, **65**(9), art. no.-092405



## Chapter 5

# CROSSOVER FROM THE NON-FERMI LIQUID TO THE FERMI LIQUID STATE

Opal<sup>1</sup>

<b>5.1</b>	<b>COLLAPSE OF THE INSULATING PHASE</b>	<b>81</b>
<b>5.2</b>	<b>QUANTUM CRITICAL POINT (QCP)</b>	<b>83</b>
<b>5.3</b>	<b>FERMI LIQUID VERSUS NON-FERMI LIQUID BEHAVIOR</b>	<b>91</b>
5.3.1	DISORDER AND THE QCP	94
5.3.2	MAGNETIC FIELD AND THE QCP	97
5.3.3	CLEAN BaVS <sub>3</sub> AND THE QCP	101
<b>5.4</b>	<b>NEW FEATURES IN THE VICINITY OF <math>p_{cr}</math></b>	<b>106</b>
5.4.1	HYSTERESIS, RELAXATION TIMES AND NON-LINEAR TRANSPORT	108
5.4.1.1	Characteristic energies in the system	108
5.4.1.2	Hysteresis in the magnetic field and a characteristic time scale	109
5.4.1.3	Current instability	111
5.4.1.4	Memory effects	114
5.4.1.5	Magnetoresistance as a function of pressure and temperature	116
5.4.1.6	Power law parameters and the magnetic field	119
<b>5.5</b>	<b>FERROMAGNETIC VERSUS INTERCHAIN-COMPENSATED-FERRO-MAGNETIC INSTABILITIES AT LOW <math>T</math>/HIGH <math>P</math></b>	<b>120</b>
<b>5.6</b>	<b>SUMMARY OF THE PHYSICS OF BaVS<sub>3</sub></b>	<b>123</b>
<b>5.7</b>	<b>REFERENCES</b>	<b>129</b>

<sup>1</sup>In OPAL, as a consequence of a phase transition, a strong reflection of light is observed due to the fluctuations in its index of refraction on length scales comparable to the wavelengths of a visible light.

In this chapter, we see how the behavior of the system at high pressures is governed by the proximity of a quantum critical point. The implications of this observation to the understanding of the physics of BaVS<sub>3</sub> are discussed in some detail.

## 5.1 Collapse of the insulating phase

In the previous chapter we have seen that the metal-insulator (MI) transition is sensitive to pressure. Based on the phase boundary analysis, it was found that the transition is of the second order in the pressure range of 1 bar to 1.5 GPa (hereafter referred to as the “low pressure range”). The negative shift of the  $T_{MI}$  was established to be linear with pressure.

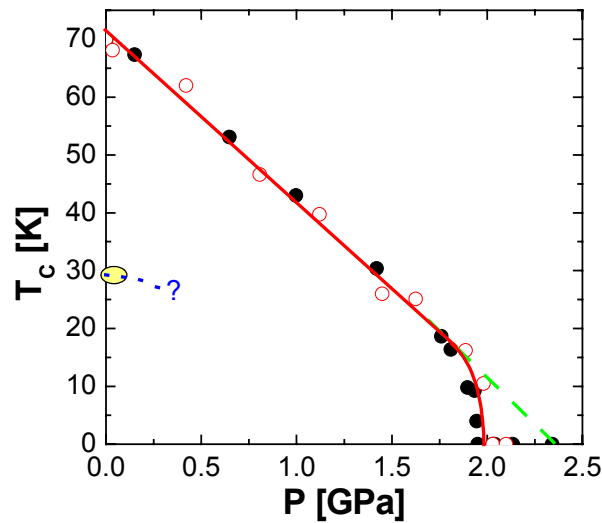


**Figure 5.1:** MI phase boundary as a function of pressure. The red line is a guide for the eye. The linear extrapolation of  $T_{MI}$  to high pressure is marked by a green dashed line. The results for two samples, marked by black and open red circles, are presented. The ICFM transition at 30 K is indicated by the yellow spot.

The metal-insulator transition temperature ( $T_{MI}$ ), shown in Fig. 5.1, varies as  $T_{MI} = 70 - 29.15 \cdot p[\text{GPa}]$  and extrapolates to zero at  $\sim 2.4$  GPa. This linear suppression of  $T_{MI}$  with pressure is followed up to  $\sim 1.75$  GPa ( $T_{MI}(p = 1.75 \text{ GPa}) \sim 18.5$  K). However, as the pressure is increased beyond this value, the  $T_{MI}$  phase boundary does not reach its extrapolated zero value at  $\sim 2.4$  GPa. Instead, within the space of 0.2 GPa, the  $T_{MI}$  falls rapidly from  $\sim 15$  K to zero and **the phase boundary collapses**.

The Interchain-Compensated-Ferro-Magnetic (ICFM) transition at 30 K corresponds to the appearance of the FM order along the V-chains, which is compensated over large distances transverse to the chains (Nakamura *et al.*, 1999). Noteworthy in this respect is the 2D lattice of the chain magnetic moments, in which the interchain AF

interactions are frustrated up to small orthorhombic deformations of the crystal lattice. The behavior of this transition with pressure is unknown, as indicated by the question mark in Fig 5.1. In addition, large charge redistribution is observed at ambient pressure below some 15 K which, importantly, is not related to any additional change of the lattice symmetry (Fagot *et al.*, 2004).

In this chapter, the high pressure part of the phase diagram, up to 2.7 GPa, will be discussed. It will be shown that, in the pressure range slightly above  $p \sim 1.75$  GPa in the critical region around  $p_{cr}$ , the physical properties of the BaVS<sub>3</sub> are governed by the proximity of the quantum critical point. In this region of pressures, the physical properties are very sensitive to the external magnetic field, doping (or impurities), and an applied current. All of these aspects are reflected in the electrical resistivity which exhibits non-Fermi liquid behavior described by  $\Delta\rho \propto T^n$  with  $n < 2$ .

## 5.2 Quantum Critical Point (QCP)

Above the critical pressure,  $p_{cr}=1.97\text{GPa}$ , the insulating state is completely suppressed and a metallic behavior is observed in the whole temperature range (Fig. 5.2). The resistivity decreases monotonically with temperature from the room temperature value of  $\rho(300\text{ K}, 2.03\text{ GPa}) = 580\ \mu\Omega\text{cm}$  to the value of  $63\ \mu\Omega\text{cm}$  at 20 K. This result suggests that, within this range of conditions, there is no phase transition which affects the conduction electrons.

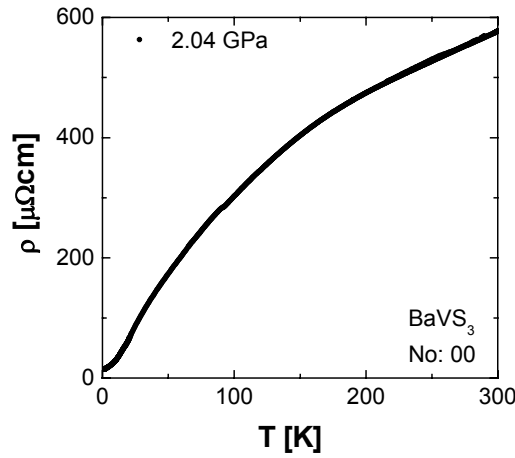


**Figure 5.2:** The resistivity at the pressure of 2.04 GPa shows a metallic behavior in the whole measured temperature range. The MI transition is completely suppressed.

Closer examination of the low temperature resistivity (Fig. 5.3), however, reveals a weak shoulder around 15-20 K and a power-law temperature dependence in the temperature range from 2 to 15 K (lower temperatures are beyond the reach of our experimental technique):

$$\rho = \rho_0 + AT^n. \quad (5.1)$$

The strength of the shoulder (see Appendix 2) and the values of the exponent  $n$ , as well as the coefficients  $A$  and  $\rho_0$ , at  $p_{cr}$ , are found to vary between samples (e.g., the power law coefficient varies from 1.1 to 1.5). For a sample with high purity and good stoichiometry (as is the case for the sample shown in Fig. 5.3),  $n = 1.5$ . This power law dependence of the resistivity in the vicinity of the second order phase transition is probably related to the proximity of a quantum critical point (QCP) (Sachdev, 1999).



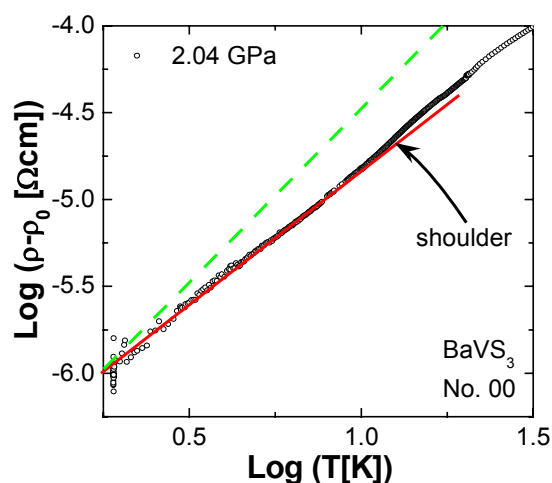


**Figure 5.3:** The low temperature (up to 40 K) part of the resistivity at 2.04 GPa is presented in a log-log plot, which reveals the existence of a shoulder around 15 K and the power-law temperature dependence of the resistivity below 15 K. The power-law fit for this sample (red curve) gave a coefficient of  $n=1.5$  (although for a range of samples it is found to vary between 1 and 1.5). The green dashed line indicates the Fermi liquid behavior for  $n = 2$ .

The Landau-Fermi liquid theory for the metallic state asserts that, at low energies, the electrons in a metal behave essentially as a collection of weakly interacting particles and that the resistivity thus exhibits a power-law temperature dependence with  $n = 2$  (Kittel, 1953). At high pressures (see, *e.g.*, Fig. 5.3) BaVS<sub>3</sub> violates this condition. This, non-Fermi-liquid (NFL) physics is related to the presence of a phase transition at the temperature of absolute zero, which is achieved by changing (by means of increased pressure) the parameters in the Hamiltonian of the system. The crossing of the phase boundary at  $T=0$  means that the quantum ground state of the system changes in some fundamental way. The parameters of the system can also be tuned by applying external perturbations such as magnetic field or doping. (However, doping or even imperfect annealing is associated with disorder which influences the system and therefore should be handled with care). Such control parameters can cause the system to pass from an ordered ground state, at  $T=0$  into a non-ordered one, thereby crossing a critical point in which quantum effects, if ever, are important. Although this definition of a QCP is strictly valid only for  $T=0$ , for regions of the phase diagram that are sufficiently close to the critical point, the temperature and pressure dependences of the system are still determined by the nature of the QCP.

In order to better understand this behavior in the context of BaVS<sub>3</sub>, it is worthwhile to discuss some general aspects of phase transitions. Second order phase transitions are characterized by a correlation length and a correlation time ( $\tau$ ) which diverge as the

critical temperature  $T_C$  is approached. The order parameter (e.g., the magnetization in a ferromagnet) fluctuates more coherently and slowly over increasing distances, implying the existence of a frequency scale ( $\omega \sim 1/\tau$ ) associated with the critical fluctuations that vanishes at the transition. A quantum system behaves classically if the temperature exceeds the frequency of interest. If the transition happens at the finite temperatures,  $\hbar\omega \ll k_B T$  close to the transition and the critical fluctuations therefore behave classically. However, quantum phase transitions (QPTs), where  $T_C = 0$ , are qualitatively different and in the case  $\hbar\omega > k_B T$ , their critical fluctuations must be treated quantum mechanically. It should be noted in this respect that the function  $\hbar\omega(T)$  can tend to zero slower than linearly with  $T$ . In this case, the transition will be "classical" even if  $T_C \approx 0$ . By a similar reasoning we can conclude that, in the system with finite  $T_C$ , we can expect to find a quantum regime above  $T_C$  if, in this regime,  $\hbar\omega(T)$  is a faster than linear function of  $T_r = T - T_C$ .

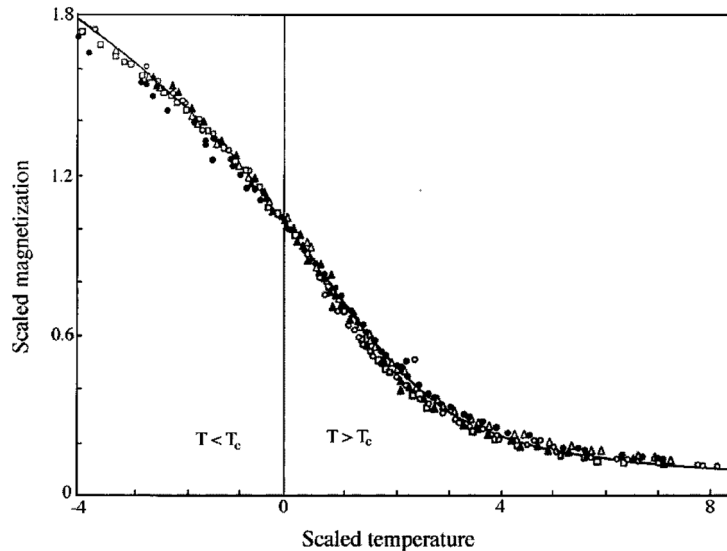


**Figure 5.4:** An example of a scaling analysis in the case of a classical phase transition. Experimental magnetization  $M(H, T)$  data for five completely different materials (CrBr<sub>3</sub>, EuO, Ni, YIG, and Pd<sub>3</sub>Fe) plotted in their scaled forms. Despite their differences, the data for all materials fall onto a single scaling function, which is that calculated for the  $d = 3$  Heisenberg model (Milošević and Stanley, 1976).

Quantum critical phenomena were initially investigated using a scaling analysis, based on an extension of the Landau theory of phase transitions (Landau and Lifshitz, 1980) which, in the classical version, describes the classical critical behavior near a second order phase transition at  $T_C$ . All scaling theories (see the reviews by Fisher (1967) and Kadanoff *et al.* (1967)) for the continuous phase transitions give the so-called scaling laws, which serve to relate the various critical exponents. For example, the magnetization ( $M$ ), the constant-field specific heat ( $C_H$ ), and the isothermal

susceptibility ( $\chi_T$ ) have the following power law temperature dependences:  $M \sim T_r^\beta$ ,  $C_H \sim T_r^{-\alpha}$ ,  $\chi_T \sim T_r^{-\gamma}$ , where  $T_r = (T - T_C) / T_C$  is the reduced temperature (in quantum phase transitions,  $T_r$  is replaced by  $T$  since  $T_C = 0$ ). The classical critical exponents were shown to be related by simple scaling laws such as  $\alpha + 2\beta + \gamma = 2$  (Stanley, 1999).

The scaling analysis can be used to make universal plots of the data. For example, in the case of magnetization  $M(H, T_r)$ , where  $H$  is the magnetic field,  $M$  can be represented graphically (as  $M$  vs  $T_r$ ) for a sequence of different values of  $H$ . If all the curves of this family are properly rescaled, the scaling hypothesis predicts that they fall onto a single curve (Fig. 5.4 shows an example of the classical phase transition). The fact that the rescaled dependence is the same (apart from two material-dependent scale factors) for all five different materials shown is truly remarkable. It allows the classification of the critical systems into “universality classes”. Two systems with the same values of critical-point exponents and hence the same scaled functions are said to belong to the same universality class. Furthermore, using the procedure called renormalization; the critical point can (in general) be associated with the fixed point of a suitable chosen transformation upon the system’s Hamiltonian. This latter association can be used as a tool for obtaining the values of the various critical-point exponents. In the case of a quantum phase transition, the situation becomes complicated above the critical dimension and the classical scaling relations (in general) break down. There are, however, scaling relationships at QCPs that have no classical analogue. These identities follow from the scaling equivalence of energy, inverse time, and temperature.

The application of ideas such as those presented above, to the problem of BaVS<sub>3</sub>, will paraphrase the recent review (Coleman, 1999) of the behavior of the heavy fermion systems in the proximity of a quantum criticality. This review develops some of early (Doniach, 1977) ideas (Fig. 5.5) in describing dense Kondo systems (Schlottmann, 1989). In some respects, BaVS<sub>3</sub> can be considered in a similar manner. Taking two (equivalent) V per unit cell, two electrons are available for the vanadium  $d$ -states. As already mentioned in Chapter 3, it appears that these two electrons are shared equally between the  $d_z^2$  and  $e_g$  orbitals. If, as a consequence of the Jahn-Teller lifting of the level degeneracy at  $T_S$ , only one  $e_g$  orbital per V-site is present at the Fermi level, it is  $\frac{1}{4}$  filled. At the other extreme, when both  $e_g$  orbitals are equally occupied, they are each  $\frac{1}{8}$  filled. While the case of a  $\frac{1}{2}$  filled local state, usually considered in the Kondo context, has been previously addressed by various methods, with the result that local Coulomb interactions tend to favor such occupation (Grilli *et al.*, 1990; Mrkonjić and

Barišić, 2003; Koga *et al.*, 2004), the case of higher commensurabilities, such as  $\frac{1}{4}$  or  $\frac{1}{8}$ , is more intricate. The question of the commensurability  $\frac{1}{4}$  was discussed in the weak-coupling limit for the 1D band, such as  $d_z^2$ , and it was shown (Barišić, 1985; Giamarchi and Millis, 1992) that the build-up of the  $2k_F$  correlations in this band favors the  $\frac{1}{4}$  commensurability (see also Chapter 3). Alternatively, it was argued using dynamic mean field theory (DMFT) (Georges *et al.*, 1996) which takes care of local Coulomb induced correlations, moreover specifically for BaVS<sub>3</sub> (Lechermann *et al.*, 2004), that large local interaction on the V-site tends to share the electron equally between the  $d_z^2$  and the  $e_g$  states. The required value for the local interaction was estimated to be of the order of 5-7 eV, which is quite large for the V-ion (Friedel, 1969).

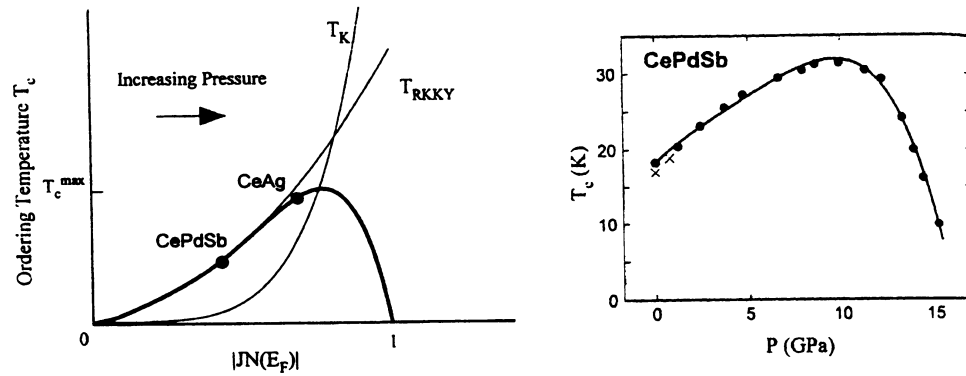


**Figure 5.5:** Doniach's (Fazekas, 1999) phase diagram for the Kondo lattice problem. Left: the magnetic-non magnetic phase boundary (bold line) obtained from the interaction dependence of the characteristic temperatures (thin lines) for the Kondo singlet and RKKY phase. Right: the pressure dependence of the Curie temperature of CePdSb (cicles) showing a good agreement with theoretical predictions (bold line) (Cornelius *et al.*, 1997).

Regardless of which correlations are dominant, the experimental situation is one in which an equal number of local and conducting electrons are present in the system. Assuming that the local  $e_g$  moment interacts via an some coupling ( $J_K$ ) with the spin of any conduction  $d_z^2$  band electron, the situation is roughly analogous to the standard Kondo lattice theory (Stewart, 2001). In this context, we can therefore extend the minimal model (used to investigate the effect of SDW fluctuations on the spectrum of the  $d_z^2$  band, presented in Chapter 3), in which the  $d_z^2$  and  $e_g$  electron systems were kept practically independent, in order to discuss the consequences of the coupling  $J_K$  in between them. Of course, the structure and in particular the sign of  $J_K$ , remain to be determined in terms of the band and interaction parameters of the  $d_z^2/e_g$  model.

Actually, there are two important magnetic scales to be taken into account (Coleman, 1999). In addition, there are also scales related to charge correlations, but the latter are

not expected to be critical for the behavior in the vicinity of the magnetic phase transition. On the other hand, these scales may be related to the main correlation effects deep in the conducting phase, as exemplified by the behavior of the behavior of the  $tJ$  models (Anderson, 1997). Coming back to magnetic effects with this in mind, the Kondo temperature ( $T_K$ ) sets the scale below which an isolated local moment is screened (taking, e.g.,  $J_K > 0$ ) by the spin of the conducting electrons. Above  $T_K$ , on the other hand, the Ruderman - Kittel - Kasuya - Yosida (RKKY) interaction (Ruderman and Kittel, 1954; Yosida, 1957; Kasuya, 1956; Stearns and Wilson, 1964) characterizes the coupling induced between two local moments promoted by the spin correlations of the conduction electrons (which tend to have an ordering effect on the former). When the ratio of the single-ion Kondo temperature  $T_K$  to the RKKY interaction scale  $T_{RKKY}$  exceeds a critical value, intercell magnetism vanishes since the magnetic moment of the localized electron is screened within the unit cell. The ratio  $T_K/T_{RKKY}$  is tuned, for example, by the interactions within the conducting band (the Hubbard  $U$  etc.). These interactions single out the periodicity of the RKKY interaction between local moments through the choice of the wavevector  $Q$  of the dominant intraband magnetic correlations. The RKKY effect on local moments is the largest when the interactions in the conduction band are strong enough to produce the long-range order, e.g. intraband SDW with the wavevector  $Q$ . Through the interaction  $J_K$ , this SDW orders the local moments, also with the wave vector  $Q$ .

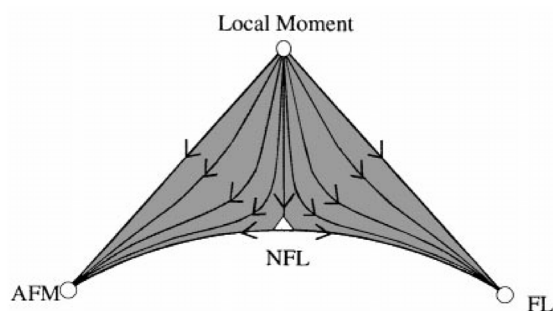


**Figure 5.6:** Schematic scaling diagram for the Kondo lattice competition of the two low temperature phases on the example of AFM - FL. QCP is marked by the white point at the end of the separatrix between two different types of trajectories. (Coleman, 1999)

If, following Coleman (1999), we think of the above order among magnetic moments as one extreme and the Fermi liquid of Kondo-like particles (relevant when the SDW correlations in the conduction band are weak), as the other, we can identify the two as competing attractive fixed points in the renormalization scheme. Such a theory tells us that, in this situation, these two fixed points are linked by a branching fixed point (Fig. 5.6). As the temperature is lowered, the effective Hamiltonian evolves away from the high-temperature behavior, in which the local moments and the Fermi gas of conduction electrons are decoupled, to one of **two** alternate attractive **fixed points**. By

tuning the conduction band interactions to the critical value of  $T_K / T_{RKKY}$ , the system is forced to evolve along a separatrix to the QCP. More importantly, a wide range of renormalization lines, close to this critical separatrix, will pass close to this new fixed point and, over a large temperature range. Their properties, excitations and interactions will therefore be dominated by the physics of this QCP.

The peculiarity of  $\text{BaVS}_3$  is that, unlike in the 3D case, it is not necessary to go to the limit of strong interactions in the conduction band to trigger the magnetic (SDW) instability. The conduction band in  $\text{BaVS}_3$  in the above sense is the quasi-1D (Q1D)  $d_z^2$  band and, even if the intraband interactions are small to intermediate (as might be more appropriate for the vanadium-based physics), it still produces the  $Q_c = 2k_F$  magnetic instability by its nesting properties. In this limit, it is important that the broad band is considered as  $1/4$  rather than  $1/2$  filled, i.e., that the screw axis is (approximately) conserved in the crystal structure below the MI transition. The direct Umklapp scattering is then unimportant (Barišić and Brazovskii, 1981; Emery *et al.*, 1982) and the  $2k_F$  SDW is degenerate with the  $2k_F$  CDW (Bychkov *et al.*, 1966; Solyom, 1979; Emery, 1979). As will become apparent later, this effect turns out to be relevant for the discussion of nonmagnetic MI transitions observed in some compounds of the wider  $\text{BaVS}_3$  family.

It is important to note that it is the change in the degree of the Q1D in the first place that controls the magnetic SDW instability in  $\text{BaVS}_3$ . This is in contrast to the change in the ratio of the interactions and the overall bandwidth that are usually assumed in the 3D case. As the hydrostatic (or chemical) pressure in the system is increased, we are carried from our starting point of a Q1D  $d_z^2$  band to a more isotropic, Q3D  $d_z^2$  band, where the  $2k_F$  correlations are wiped out and (close to  $T=0$ ) one ends up in the more or less correlated Fermi-liquid limit of Fig. 5.6, with more or less pronounced local charge and spin correlations.

In summary, the scaling diagram of Fig. 5.6 puts forward two different viewpoints of the same problem of a critical magnetic fluid. The first approach starts on the magnetic side where the system is considered as a structure of localized moments which (for  $J_K > 0$ ) get screened out when the single-ion Kondo temperature is large enough to develop a dense Kondo effect (for  $J_K < 0$  a singlet is replaced by a triplet). In this scheme, the quasiparticles are composite states formed between local moments and conduction electrons. These states form a renormalized Fermi liquid. At the QCP the locally correlated states, which characterize the Kondo lattice, disintegrate to reveal the underlying lattice of magnetic moments interacting through the RKKY

---

interaction. The second approach, the so-called spin fluctuation limit, starts from the Fermi gas (FG) side and regards the QCP as a magnetic transition of the local moments mediated by the conducting electrons, which in turn affects the Fermi surface. From the point of view of the FG side, the non-Fermi liquid behavior develops because of infinitely long-range and retarded interactions between quasiparticles at the QCP.

### 5.3 Fermi Liquid versus Non-Fermi Liquid behavior

“Proximity to magnetism” in the phase diagram is not an unusual condition for many  $d$ - and  $f$ - electron systems which display non-Fermi liquid physics. Therefore it should not be surprising if this also turns out to be the case for  $\text{BaVS}_3$ . This is especially true if we keep in mind the existence of the ICFM (or FM) phase below  $T_X = 30$  K at 1 bar and its possible extension to high pressures. Unfortunately, for low pressures, this phase lies deep in the insulating phase which makes impossible to follow its evolution under pressure by electrical transport measurements. Consequently, we can only speculate about the evolution of ICFM (or FM), in the insulating phase, in the vicinity of the QCP. However, if the pressure is increased beyond  $p_{cr}$  we can obtain some insight into the competing state on the high pressure side of the QCP. Based on the temperature and magnetic dependences of resistivity in the proximity of  $p_{cr}$ , we can then decide upon the nature of the ground state in the insulating phase.

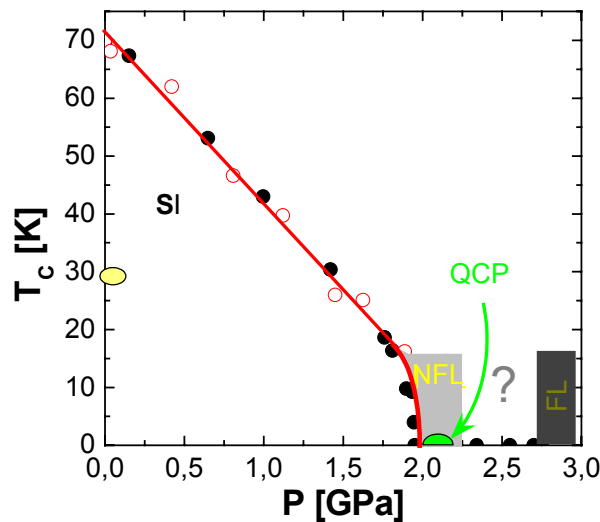


**Figure 5.7:** Possible scheme for the  $p$ - $T$  phase diagram of  $\text{BaVS}_3$  in case that the insulating phase and the magnetic order are related.

Taking into account that, in the “low pressure” region, the MI transition does not change its character (see Chapter 4), it is reasonable to presume that the insulating behavior and the related SDW magnetic order go simultaneously to zero at  $p_{cr}$ . On the other hand, it seems that the ICFM/FM order is not a consequence of RKKY



interactions between  $e_g$  moments and  $d_z^2$  electrons but rather of the direct interactions between the  $e_g$  moments. This can be rationalized on the basis that the FM order along the chains is established at  $T_X$  in spite of the imposed 4 V periodicity in the unit cell. Thus, as a working hypothesis, it can be assumed that  $T_{MI}$  and  $T_X$  are unrelated; consequently  $T_X$  should not have a crucial role in the behavior of resistivity at  $p_{cr}$ . This assumption leads to the phase diagram shown in Fig. 5.7, where the  $T_X$  phase boundary is disregarded. Actually it will be argued later, in section 5.5, that  $T_{MI}$  and  $T_X$  probably cross each other at some value of the applied pressure.

Proceeding along the lines indicated in Fig. 5.7, it should be noted that by increasing the pressure to 2.7 GPa, the exponent of the power law coefficient reaches  $n = 2$ , (Fig. 5.8) revealing the *Fermi liquid* side of the phase diagram (FL in Fig. 5.7). Based on this observation, the spin fluctuation theory is applied to discuss the experimental results.

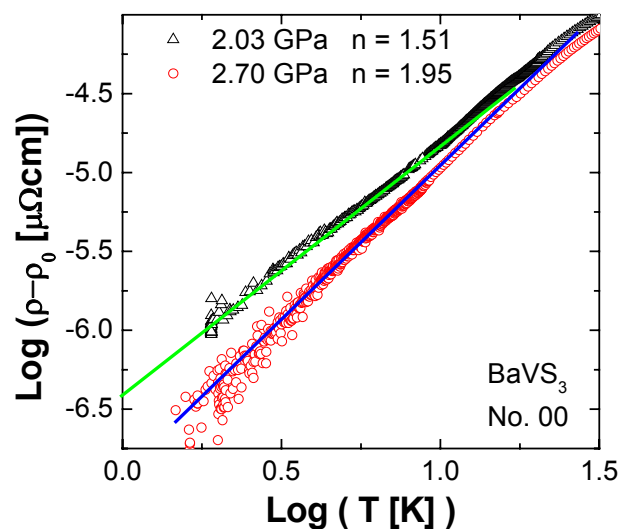


**Figure 5.8:** Logarithmic plot of the resistivity in  $\text{BaVS}_3$  for a pressure close to the QCP (black points), and in the FL phase (red points).

QCPs have been studied by many authors in the framework of the spin fluctuation model. In the pioneering paper, Hertz (1976) showed that in quantum systems at  $T = 0$ , static and dynamical properties are inextricably mixed. Therefore, that in contrast to the classical  $T > \omega$  phase transitions, the value of the dynamic exponent  $z$  affects the static critical behavior. Technically this implies that one cannot solve the thermodynamic properties of the phase transition without also solving the dynamics.

At the QCP, the correlation time  $\tau$  diverges more rapidly than the correlation length  $\xi$  according to the relation:

$$\tau \propto \xi^z .$$

Hertz identified  $z$  as an anomalous scaling dimension of time  $[\tau] = [\xi]^z$ , raising the effective dimensionality of the QCP from  $D + 1$  to  $D_{\text{eff}} = D + z$ , where  $D$  is the dimensionality of the system.

$\rho - \rho_0 (T)$	Hertz/Millis	Moriya et al.	Lonzarich
AFM, $z = 2$ D = 2	$T$	$T$	
FM, $z = 3$ D = 2		$T^{4/3}$	$T^{4/3}$
AFM, $z = 2$ D = 3	$T^{3/2}$	$T^{3/2}$	$T^{3/2}$
FM, $z = 3$ D = 3	$T$	$T^{5/3}$	$T^{5/3}$

**Table 5.1:** Temperature dependence of the resistivity in the spin fluctuation theories of Hertz (1976), Millis (1993), Moriya and Takimoto (1995), and Lonzarich (2004) for the NFL behavior as a function of  $z$ , the dynamical scaling dimension and  $D$ , the dimensionality of the system.

There are number of ways to see the coupling between the static and dynamical properties at QCPs. From a general scaling point of view one may argue that, as the temperature is increased from zero, the system is taken away from the QCP in much the same way as increasing the frequency from zero takes the system away from either a quantum or a classical phase transition. The frequency and temperature have the same dimensions (at  $k_B = \hbar = 1$ ) which implies that if the system is at a QCP, going to a finite frequency will affect the system in the same way as increasing the temperature. The two processes will be thus characterized by the same critical exponent  $z$ . Since the thermodynamic observables depend on the temperature, this further implies that the scaling relations (or homogeneity laws) for these quantities will also depend on  $z$ . The corresponding low- $T$  dependences of the resistivity, for the spin-fluctuation models, are given in Table 5.1.

Since spin-fluctuation theory predicts that  $z$  adopts the values of 2 and 3 at

antiferromagnetic and ferromagnetic QCPs, respectively, it should be possible to use  $z$  as self-consistent descriptor to distinguish between the AFM or FM nature of QCPs in three dimensions ( $D = 3$ ). In addition, the results of various models are known to depend upon the dimension  $D$ , the dynamic exponent  $z$ , the reduced temperature ( $t = T/T^*$ , where  $T^*$  is a characteristic temperature), and a control parameter  $s$ , which is related to a Hamiltonian parameter such as pressure, doping or magnetic field. However, any kind of microscopic disorder, such as that present in all doped systems, is not included in these theories. In this sense, the interplay between the spin fluctuations and the disorder present within such systems tends to average some of the fine effects. For this very reason, we will begin our investigation of the QCP in  $\text{BaVS}_3$  with a discussion of the low quality samples (measured as  $\rho(300\text{K})/\rho(T \rightarrow 0)$  at  $p_{\text{cr}}$ ). Subsequently, we will present the detailed of measurements of high quality samples. Throughout the course of both of these discussions we will discover some new, unexpected and non-standard physics in  $\text{BaVS}_3$ .

### 5.3.1 *Disorder and the QCP*

In the last 10 years, a considerable theoretical effort has been applied to achieve a better understanding of the role of disorder. Independently of the precise nature of the QCP, it is known that the critical behavior at the quantum phase transition must be substantially modified if one adds quenched, nonmagnetic or magnetic disorder to the system. Some examples of this phenomenon are presented below.

Works by Bhatt and Fisher (1992), Dobrosavljević *et al.* (1992) and Miranda *et al.* (1995) proposed that, near the metal-insulator transition, the disordered correlated metals contain localized moments. The change in the interactions between the impurity sites and the host spins can be considered as a modification of the characteristic energy scale, the Kondo temperature  $T_K$ . The random distribution of the magnetic impurity Kondo temperatures may be connected with either the randomness of the itinerant-electron exchange couplings with local moments (Dobrosavljević *et al.*, 1992), or with the randomness in the densities of conduction electron states (Bhatt and Fisher (1992). Indeed, both types of randomness affect the single universal parameter – the Kondo temperature – which characterizes the state of the single magnetic impurity.

The interplay of nonmagnetic disorder and spin fluctuations near the QCP, where magnetism has been suppressed to  $T \rightarrow 0$  has been studied by Rosch (1999, 2000). He claimed that the strongly anisotropic scattering from critical spin fluctuations is

---

appreciably influenced by weak but isotropic scattering from small amounts of disorder. The anisotropic scattering from spin waves affects only small areas of the Fermi surface and therefore the transport properties strongly depend on how other scattering mechanisms redistribute quasiparticles and scatter them into those small regions. As a result of his calculations, it was determined that, in high purity-systems near the AFM QCP, the power-law coefficient ( $n$ ) changes from 1.5 to 1 upon going from dirty to clean systems.

In the model of Belitz and Kirkpatrick (2002) the QCP in itinerant ferromagnets was investigated. They showed that the correlation effects in the underlying itinerant-electron system lead to an effective long range interaction between the spin fluctuations. It was pointed out that, in sufficiently clean systems and at sufficiently low temperatures the, transition should always be of the first order. The role of quenched non-magnetic disorder was also discussed and it was concluded that, in the sufficiently disordered systems, the first-order phase transition is suppressed and is replaced by a continuous transition.

The purpose of this short overview of models was to point out that all of them, regardless of the details of the particular model, predict considerable changes in physical properties of the system in the proximity of QCP due to the disorder. Therefore, it should not be a surprise if this is also the case of BaVS<sub>3</sub>.

One way to quantify the disorder in the system is by measuring the residual resistivity ratio (RRR) defined as  $R(300 \text{ K}) / R(T \approx 0)$  when  $T_{MI}$  is suppressed by pressure. Roughly, it is inversely proportional to the relative strength of impurity scattering.

The first group of BaVS<sub>3</sub> samples were associated with values of the RRR around 10 at high pressures (above  $p_{cr}$ ). These samples are considered to be of low quality due to impurities and/or sulfur off-stoichiometry. They all display a power-law temperature dependence for  $p > p_{cr}$  (in the metallic part of the phase diagram) at temperatures below 15 K. However, the power-law exponent  $n$  is found to be sample dependent and *varies* from **1.1 to 1.25**. The data concerning this set of samples can be found in Appendix 2.

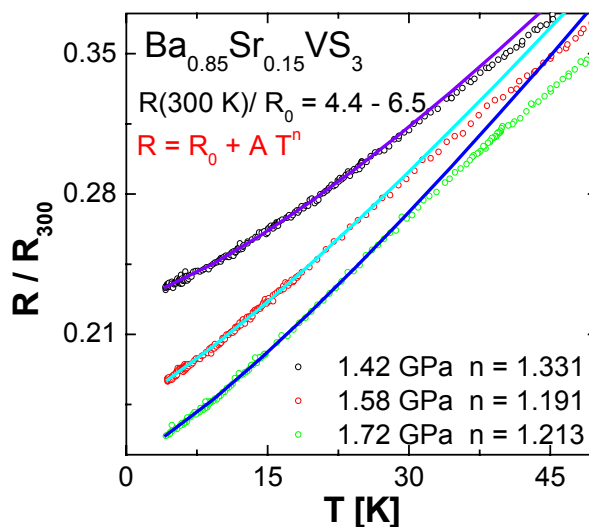


**Figure 5.9:** Temperature dependence of the normalized resistivity of  $\text{Ba}_{1-x}\text{Sr}_x\text{VS}_3$ ,  $x = 0.15$ , at three different pressures above  $p_{cr} = 1.15$  GPa.

The second group of samples, in which the barium is partially substituted by the isoelectronic strontium, is interesting from another point of view. We have found, as will be discussed in detail in Chapter 6, that this substitution reduces the MI transitions significantly, in much the same way as the pressure does. As a result, the critical pressure for these compounds is lowered. However, as the substitution is isoelectronic, the electronic properties of the strontium-substituted compounds are expected to be comparable with those of impure  $\text{BaVS}_3$  (with RRRs of around 10). Three different concentrations of Sr ( $x = 0.06, 0.10$  and  $0.15$  with RRRs ranging between 5 and 15), were examined and indeed, above  $p_{cr}$ , showed the expected, low temperature power-law behavior. The coefficient ( $n$ ) for these samples was found to vary from 1.13 to 1.33. The results for the highest concentration of Sr ( $x = 0.15$ , RRR = 4.4 at 1.42 GPa and 6.6 at 1.72 GPa) are shown in Fig. 5.9. Interestingly  $n$  is weakly pressure dependent and there is no palpable shoulder in the resistivity around 15 K; instead the resistivity follows the power-law behavior in temperature up to 35 K.

As an example of a high purity sample of  $\text{BaVS}_3$ , the one shown in Fig. 5.3 has, at a pressure just above  $p_{cr}$ , an RRR of higher than 50 and a power-law exponent ( $n$ ) equal to 1.5. Since both of the aforementioned groups of samples with low RRRs showed similar tendencies (in the high  $p$  / low  $T$  range), it can be concluded that the increase of disorder changes the power-law exponent from 1.5 towards lower values ( $\sim 1.1$ ). A wider study which attempts (i) to distinguish the consequences of sulfur off-stoichiometry and the disorder due to the isoelectronic substitution on the power-law

exponent, and (ii) to find the functional dependence of the power-law exponent and the RRR, is currently in progress.

### 5.3.2 Magnetic field and the QCP

The magnetic field is another parameter which is expected to have an important influence on the behavior of the system. Therefore the resistivity has been measured as a function of both the field strength and the temperature. The sample chosen for the presentation of the results in this section belongs to the first group of samples, mentioned above, associated with RRRs ( $p > p_{cr}$ ) of around 10. The reason for this choice, which was alluded to earlier, is that the disorder present in the impure samples tends to average some of the fine features of the measured data and hence simplifies their initial interpretation.

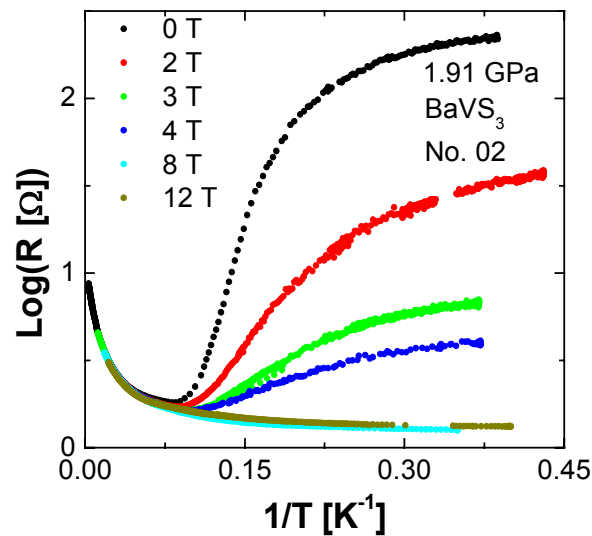


**Figure 5.10:** The Arrhenius plot of the resistivity at 1.91 GPa for several magnetic fields shows the suppression of the insulating phase by increase of the field.

The most spectacular consequence, *independent of the sample quality*, is observed at the pressures just below  $p_{cr}$ , when the system is still in the insulating phase. By applying a magnetic field under these conditions, the insulating behavior is “switched off”. The results for one of the measured samples, at the pressure of 1.91 GPa, are shown in Fig. 5.10. *The resistivity changes by two orders of magnitude upon increasing the magnetic field from 0 to 8 T.* The suppression of the insulating phase is not accompanied by the suppression of the MI transition temperature to 0 K. As

shown on Fig. 5.11a, at these pressures in the presence of a magnetic field, *the MI transition becomes ill defined*. That is, the peak in the logarithmic derivative of the resistivity (whose position defines  $T_{MI}$ ), becomes weaker and weaker with the increase of the magnetic field. However, the value of  $T_{MI}$ , as well as the width of the peak, is almost *independent of the applied magnetic field*.

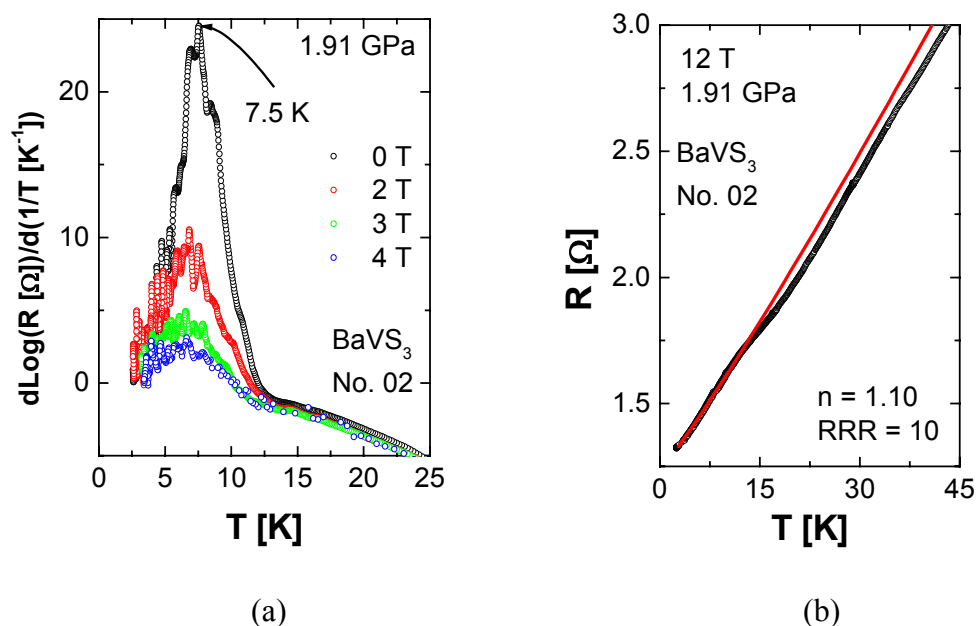


**Figure 5.11:** (a) The logarithmic derivative of the resistivity at 1.91 GPa for four magnetic fields. By applying the magnetic field, the peak is diminished without changing its position or its width (in temperature). (b) Low temperature part of the 12 T and 1.91 GPa resistivity curve reveals the power-law temperature dependence below the shoulder which persists at 15 K.

The interpretation of the behavior of the insulating phase in the magnetic field would require a detailed microscopic description of the phase transition, which is still lacking. Nevertheless, based on analogy with organic conductors that exhibit a spin-Peierls transition that also disappears in high magnetic fields, Kezsmarki (2003) has suggested the same mechanism for  $\text{BaVS}_3$ . This analogy is also consistent with the leading role given here to the SDW correlations in the quasi-1D  $d_z^2$  band.

At 8 T (and 1.91 GPa) the system is metallic in the whole temperature range. The low temperature part of the resistivity in a magnetic field of 12 T, at this same pressure, is shown in Fig. 5.11b. The power-law temperature dependence of the resistivity is

observed in the range of 2 to 15 K with the coefficient  $n \sim 1.1$ , which corresponds to values measured with zero field above  $p_{cr}$ . Closer examination of the low temperature behavior of the resistivity clearly reveals the shoulder around 15 K.

The suppression of the insulating phase can be also followed by measuring magnetoresistance at low temperatures (Fig. 5.12). At the lowest measured temperatures (2.6 and 4.4 K), the system is still in the insulating phase while the applied field is absent. Increasing the magnetic field to  $\sim 8 - 9$  T causes the resistivity drop for 99 % and 96 % respectively, transforming the system into a metal. Above 8 - 9 T the magnetoresistance shows a well pronounced upturn at temperatures above  $T_{MI}$  ( $\sim 7.5$  K at 1.91 GPa). A similar behavior, although much less pronounced, is observed at 10 and 15 K with the minimum occurring at fields of 8.5 and 10 T, respectively. At **temperatures higher than 15 K** (the highest measured temperature was 45 K) **the resistance is decreasing with  $B$**  in the whole of the measured field range. It should be noted that all measured samples have a comparable suppression of the insulating phase by magnetic field but some of them do not show a positive upturn in the magnetoresistance at higher fields (around 9 T), see Appendix 2.

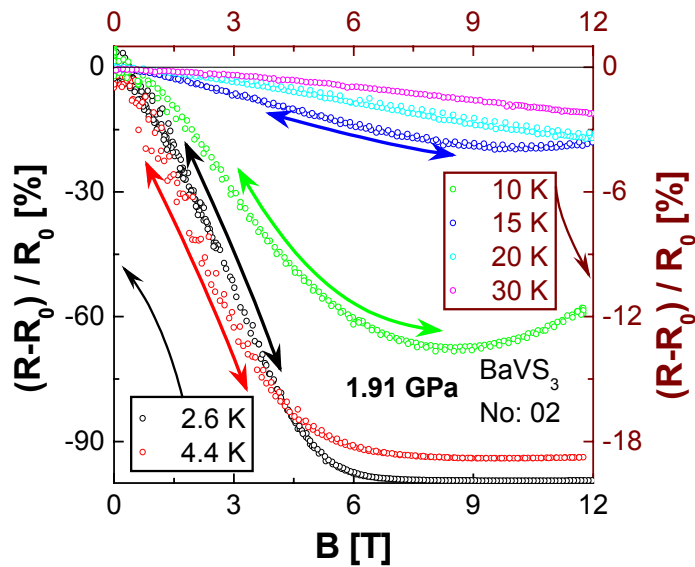


**Figure 5.12:** Magnetoresistance for several temperatures at a pressure of 1.91 GPa. The left scale (black) corresponds to the two lowest temperatures (2.6 and 4.4 K marked by the black legend) while the right (brown) scale is related to temperatures (denoted by brown legend) above  $T_{MI}$  ( $\sim 7.5$  at this pressure). The magnetic field was swept in both directions as indicated by the arrows.

As described above, the dominant effect of the magnetic field at pressures just below



$p_{cr}$  is the modification and the suppression of the long range order characterizing the insulating phase. If however, the pressure is increased above  $p_{cr}$  the magnetoresistance reveals the scattering processes in the NFL regime. In general, a simple way to distinguish spin from orbital effects is by the sign of the magnetoresistance. The suppression of the spin scattering of the conduction  $d_z^2$  electrons (and in particular of their  $2k_F$  backward scattering), by ordering the spins with the homogeneous external magnetic field, reduces the amount of scattering and the resistivity decreases. On the contrary, the positive contribution to the resistivity is usually due to orbital effects. Here we shall adopt this point of view noting that the interplay of the spin and orbital effects can also lead to more complicated effects, which will be ignored in the discussions that follow.

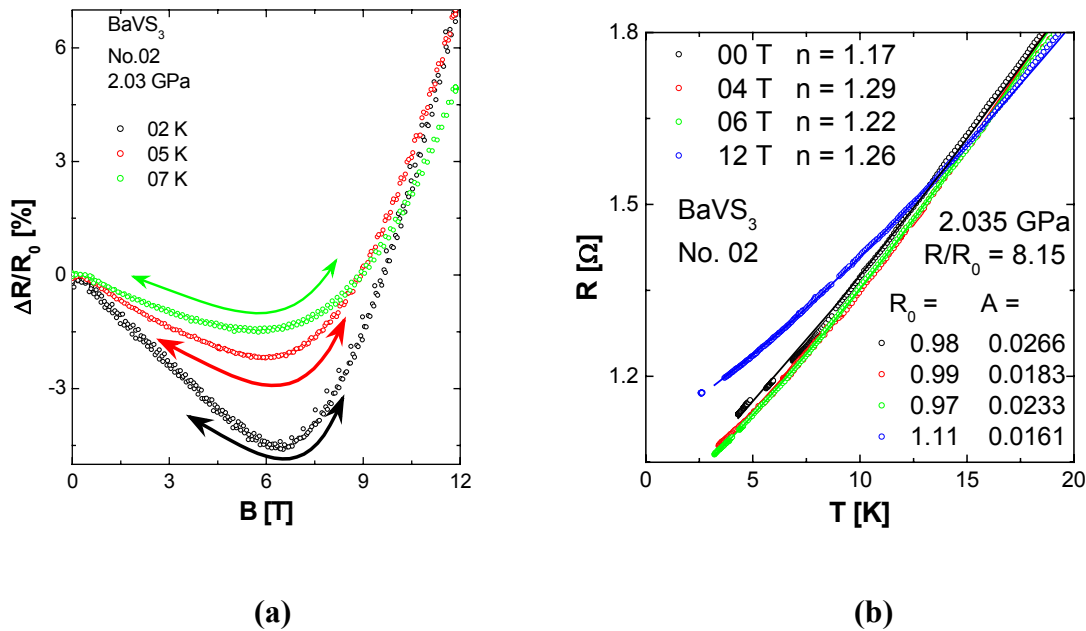


**Figure 5.13:** (a) The relative change of resistivity at 2.03 GPa as a function of the magnetic field for three different temperatures. Arrows indicate the direction of the change of the magnetic field. (b) Resistivity as a function of temperature at 2.035 GPa for several magnetic fields. The low temperature part of the resistivity obeys the power-law temperature dependence  $R = R_0 + AT^n$ .

In Fig. 5.13a, the low temperature (2, 5 and 7 K) magnetoresistance measured at 2.03 GPa (just above  $p_{cr}$ ) is shown. The behavior observed therein discloses what we believe to be the competition between the spin and orbital contributions. At low fields the main contribution comes from impeding the scattering on spins. At fields around 6.5 T the curves pass through minima due to the appearance of the positive orbital term. The magnetic field was varied in both directions as marked by arrows. At 12 K a weak minimum is still present in the magnetoresistance (data not shown in Fig.5.13) but further increase of the temperature weakens the positive orbital contribution to the

magnetoresistance and the effect of the magnetic field on the resistivity is always negative in the measured field range. The temperature at which the minimum disappears can be estimated from the temperature dependence of the resistivity for several fields shown in Fig. 5.13b. ***The 12 T curve crosses all the other curves at the temperature of 15 K***, which means that below this temperature there is a minimum but above it the magnetoresistance is always negative. It should be pointed out that in the temperature range 1.5 - 15 K the coefficient  $n$  is around 1.23, varying by less than 5% as a function of magnetic field. This variation is within the error bar of the measurement.

All of the results presented thus far can be tentatively interpreted in the framework of the phase diagram shown in Fig. 5.7. In the region of pressures close to  $p_{cr}$ , the QCP governs the behavior of the system. This can be described by the  $d_z^2-e_g$  models mentioned above, in which the behavior close to the QCP is tuned by pressure, magnetic field, and impurities. The impurities constitute discrete, random perturbations which confirm their importance in the physical properties of the system in close proximity to the QCP. Their presence tends to average some of the fine features so that measurements on impure samples can be quite informative. However, the treatment of the microscopic effects of the disorder, within the aforementioned theoretical methods, is difficult. In contrast, the magnetic field, like pressure, is a parameter of the system which changes in a continuous way (without inducing disorder in the system). In the context of experiments in which the strength of the field is varied, the only possible origin of a discontinuity/singularity in the physical properties of a pure sample is the system itself. As this situation is comparatively easy to handle theoretically, it becomes important to study (very) clean systems.

### 5.3.3 *Clean BaVS<sub>3</sub> and the QCP*

Two samples, which fulfilled the criteria for the high quality samples based upon spin susceptibility and resistivity measurements, (discussed in Chapter 4), were chosen for the purpose of obtaining a deeper understanding of the nature of the QCP. Their high RRRs  $\sim 50$  just above  $p_{cr}$  confirm the high quality of the samples. Both samples exhibit the shoulder around 15 K in the resistivity measurements performed at 2.04 GPa (Figs. 5.2 and 5.3). In order to avoid possible confusion, all of the subsequent results presented in this chapter are for the sample denoted as Nr. 00. The reader may rest assured, however, that all facets of the measurements are reproducible.

According to the results for models presented in Table 5.1, the system is **3**

---

**dimensional and AFM in the insulating phase.** Notice that the fourfold SDW can be regarded, to some extent, as the AFM doubling of the high temperature unit cell with 2 V sites. The 3 dimensionality of the resistivity in the metallic phase close to the QCP can be confirmed indirectly, at least above 15 K, by comparing the measured high temperature parts of the resistivity curves at 1 bar and 2.7 GPa (Chapter 7, Figs. 7.1 and 7.2). This comparison shows that the high temperature behavior remains virtually unchanged in response to a strong increase in the pressure. The small difference in the resistivity slopes can be attributed to the change of the bandwidth as a function of pressure. The 2.7 GPa the resistivity curve is smooth in the whole temperature range (this is consistent with the TEP data under pressure as shown in Chapter 7) and there is no reason to suppose that this feature would change as the system is cooled. From the anisotropy measurement of the electrical resistivity at 1 bar we know that at this pressure the electrical properties are fairly isotropic ( $\rho_{ab}/\rho_c \sim 3.8$ ) and by the above reasoning we may conclude that this anisotropy ratio remains essentially unchanged in response to increasing pressure (the experimental confirmation is in progress). On the other hand, given the absence of the MI transition at high pressures, it is presumably the case that the 3D nesting of the  $d_z^2$  band becomes imperfect under these conditions.

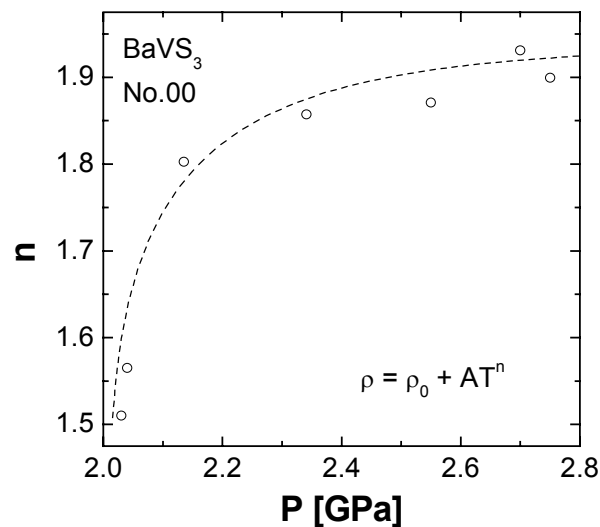


**Figure 5.14:** Pressure dependence of the resistivity exponent  $n$ . The dashed line is to guide the eye.

Let us examine the pressure dependence of the low temperature resistivity coefficients  $n$ ,  $A$ ,  $\rho_0$  in more detail. The qualitative theoretical phase diagrams (Millis, 1993; Rosch, 2000; Continento, 1989; 1993; Continento *et al.*, 1996; Ioffe, 1995) predict three different regions on the FL side of the phase diagram. In the first (low

temperature) region, the FL behavior appears. The boundary line with the second region varies as  $T_{1-2} = a_{1-2} (p-p_{cr})^{z/2}$ , which implies a linear behavior as a function of pressure in the case of AFM. The second region is a quantum–classical crossover regime, where the energy of the fluctuations becomes comparable with  $k_B T$ . In the third region, at temperatures above  $T_{2-3} = a_{2-3} (p-p_{cr})^{z/D+z-2}$  (also linear with pressure in case of a 3D AFM), the system is a NFL. The low temperature measurements and the resulting values of  $n(p)$  in BaVS<sub>3</sub>, shown in Fig. 5.14, suggest a rather different behavior. That is, it seems that the first (low temperature) region does not exist and the NFL is continuously transformed to the FL. At the pressure closest to the  $p_{cr}$  of 2.03 GPa,  $n$  is equal to  $1.51 \pm 0.01$  and is monotonically increased, with increasing pressure, to the value of  $2.00 \pm 0.05$  at 2.7 GPa. This behavior is not unique for BaVS<sub>3</sub>, it is also observed in other systems such as: U<sub>2</sub>Pt<sub>2</sub>In and U<sub>3</sub>Ni<sub>3</sub>Sn<sub>4</sub> (Estrela *et al.*, 2001a; 2001b), UGa<sub>3</sub> (Nakashima *et al.*, 2001), CeIn<sub>3</sub> (Knebel *et al.*, 2002), SmB<sub>6</sub> (Gabani *et al.*, 2003). One possible reason for not seeing the FL at low temperatures is that it lies out of our experimental range; due to technical reasons the lowest measured temperature was limited to 1.7 K.

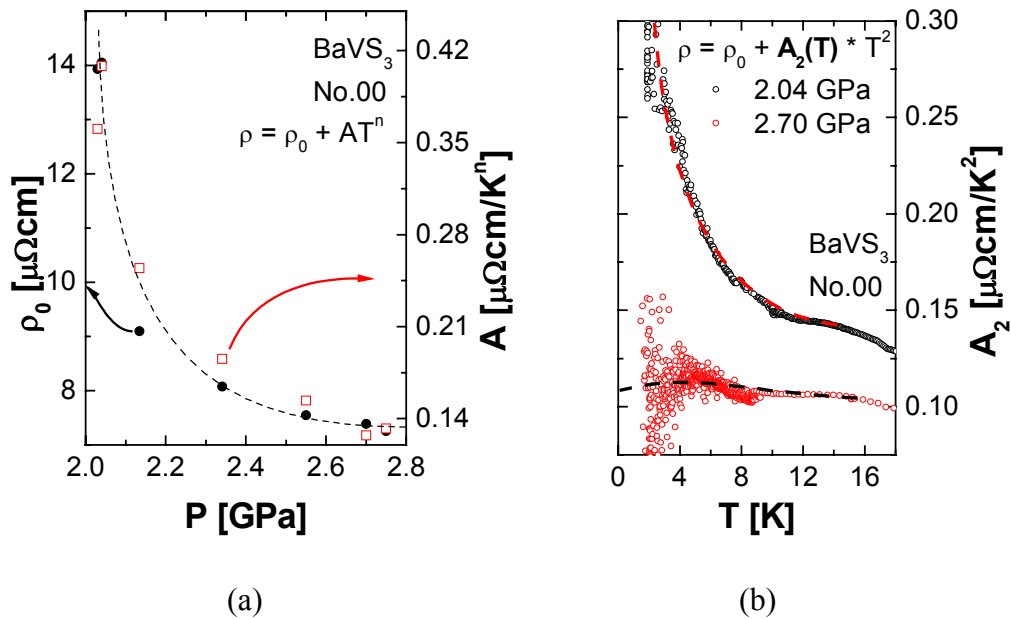


**Figure 5.15:** (a) Pressure dependence of the prefactor  $A$  (red squares) and the “residual” resistivity  $\rho_0$  (black circles) as the results of the fits  $\rho = \rho_0 + AT^n$  in the temperature range  $1.7 < T < 15$  K. (b) Quasiparticle- quasiparticle scattering cross section  $A_2 = (\rho(T) - \rho_0) / T^2$  vs. temperature for two pressures; the first at 2.04 GPa close to the critical pressure and the second at 2.7 GPa in the FL regime. The dashed lines are guides to eye.

The crossover from the NFL to the FL regimes is also clear when seen through the

coefficient  $A(p)$ , as shown in Fig. 5.15a. When the material is driven away from the QCP, the coefficient  $A$  decreases. The value of  $A$  at critical pressure is  $0.42 \mu\Omega\text{cm}/\text{K}^n$  and as pressure is increased it saturates to the FL value of  $0.14 \mu\Omega\text{cm}/\text{K}^2$ . This latter value is comparable to the numbers found in other systems (e.g.,  $\text{CeRu}_2\text{Ge}_2$  at  $p = 9.1$  GPa  $A = 0.23 \mu\Omega\text{cm}/\text{K}^n$  or  $\text{MnSi}$  at  $p = 1.5$  GPa,  $A = 0.18 \mu\Omega\text{cm}/\text{K}^n$ ). Similar, strong pressure dependence of the prefactor  $A$  in the critical region is also found in the  $\text{CeIn}_3$  (Knebel *et al.*, 2000).

The second way of analyzing the pressure data ( $p > p_{cr}$ ) is by fixing the value of the power law coefficient to  $n = 2$  (FL) and fitting  $A_2$  as a function of pressure and temperature. In the FL ( $\rho = \rho_0 + A_2(T) T^2$ ), the coefficient  $A_2$  is a measure of the strength of electron-electron interactions. Just above the critical pressure towards the lower temperatures,  $A_2(T, 2.03 \text{ GPa})$  exhibits a divergence (Fig. 5.15b), as predicted, for example, in spin-fluctuation theory, providing a clear indication of the NFL regime. Similar behavior is often found for the  $f$ -electron systems (Knebel *et al.*, 2002), but it is quite rare with  $3d$ -electrons. In contrast to the 2.03 GPa data, the  $A_2(T, 2.7 \text{ GPa})$  at 2.7 GPa remains more or less constant in the low temperature region, as is expected in the FL regime. The value of  $A_2$  gives an estimate of the pressure variation of the effective mass  $m^*$  assuming that  $m^* \propto A_2^{1/2}$  ( $\propto$  specific heat coefficient  $\gamma$ ), which is valid far from the critical pressure,  $p_{cr}$ . The effective mass is increased by a factor of 2 as a consequence of the anomalous scattering observed in the NFL regime.

Finally, the commonly ignored residual resistivity  $\rho_0(p)$  certainly warrants our attention. In all models, to the best of our knowledge, its discussion is omitted. Importantly, however, it is a quantity which by its definition describes the behavior of the system at the temperature of absolute zero. In the Fermi gas, FL or some other model which describes a metallic state,  $\rho_0$  simply arises from the (local) changes of the periodic crystal potential caused by imperfections. It is certain that by some external parameter (e.g., pressure or magnetic field) it is impossible to change the number and/or configuration of the extrinsic defects in the material. However the results presented in Fig. 5.15a clearly reveal a strong pressure dependence of  $\rho_0$  and indicate that its origin is different than the scattering on static impurities. That is, there is an intrinsic, static or dynamical disorder in the system at low  $T$ .

In the FL phase  $\rho_0(2.7 \text{ GPa}) = 7.25 \mu\Omega\text{cm}$ , and its value is related exclusively to the number of defects. Therefore, it is useful to check the RRR which is about 80 at this pressure confirming the high quality of the sample. As the QCP is approached from above, the system enters into the critical regime in which quantum fluctuations are

present at absolute zero. They provide extra scattering processes (at  $T = 0$ ) and therefore increase  $\rho_0$ . It should be noted, in this respect, that the zero-point motion of harmonic modes does not contribute to  $\rho_0$ . Thus for its large value in the vicinity of the QCP, anharmonic fluctuations should be taken into account. The scaling of  $\rho_0$  and  $A$  with pressure shows that the same physics is reflected in both parameters, supporting the idea of linking the intrinsic fluctuations with behavior of  $\rho_0$ . It should be noted that the decrease of the  $\rho_0$  with pressure is also common for both the dirty BaVS<sub>3</sub> samples and for Sr substituted samples (such as those shown in Fig. 5.9). Comparable behaviors of the  $\rho_0$  with pressure can be also found in other systems like CeIn<sub>3</sub>, U<sub>3</sub>Ni<sub>3</sub>Sn<sub>4</sub>, U<sub>2</sub>Pt<sub>2</sub>In, SmB<sub>6</sub>. Therefore, ***to understand the properties of the QCP it is of crucial importance to understand the origin of  $\rho_0$ .*** The increase of  $\rho_0$  in the NFL regime can be used to determine the nature of the QCP.

---

---

### 5.4 New features in the vicinity of $p_{cr}$

Taking into account the results presented thus far, we could conclude that the phase diagram suggested in Fig. 5.7 provides a suitable general description of the basic properties of BaVS<sub>3</sub>. Naturally, based upon the latter part of the previous discussion we may wish to replace the question mark by a continuous crossover from the NFL to the FL, with  $n$  varying from 1.5 to 2, which would be in agreement with the scaling diagram of Fig. 5.6. In this scenario, the insulating phase and the magnetic order are related and, as a consequence, the collapse of the insulating phase means the magnetic QCP is positioned at  $p_{cr}$ . The spin-Peierls coupling to the lattice is not explicitly invoked in this scenario. The indication that something more complicated than the simple scaling may take place is already visible in the transport properties of the system at 1.76 GPa (Fig. 5.16), the same pressure at which the MI boundary starts to collapse.

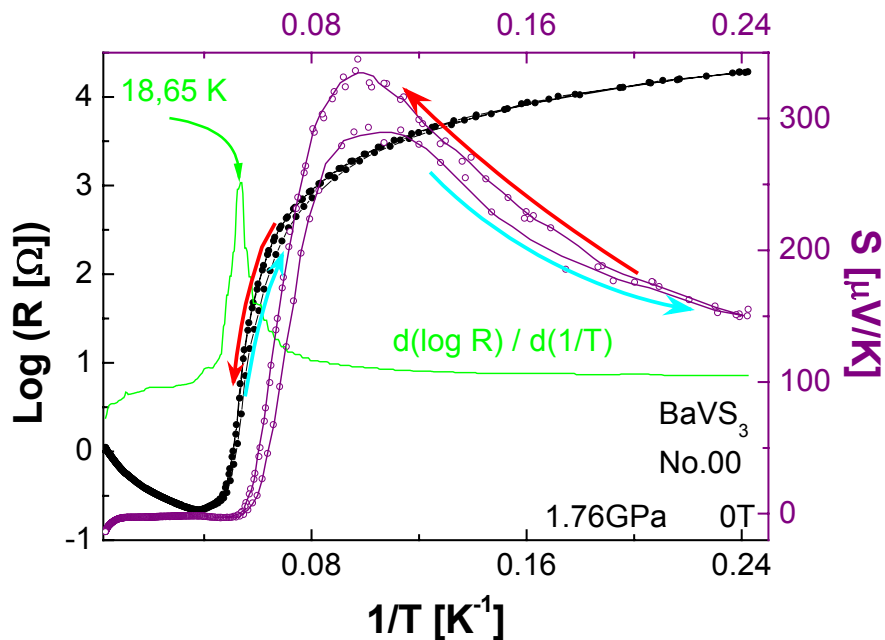


**Figure 5.16:** The logarithm of the resistance (left scale, black) and the thermoelectric power (right scale, pink) as a function of  $1/T$  under a hydrostatic pressure of 1.76 GPa. The black scale corresponds to the logarithm of the resistance marked by black dots and lines while the pink scale is related to the thermoelectric power marked by the pink dots (the pink line is a guide to the eye). The logarithmic derivative of the resistance, marked by the solid green line, is used to determine  $T_M$ . The heating and cooling phases are denoted by red and blue arrows, respectively.

As the MI transition is traversed in temperature at  $p=1.76$  GPa, *hysteresis appears* in

both resistance and thermoelectric power (Fig. 5.16). Until the observation of this behavior, we had considered the transition to be of the second order, and associated with the magnetic QCP at  $p_{cr}$ . However, the existence of hysteresis suggests that it becomes first order in the pure samples. The transition temperature at  $p=1.76$  GPa, determined simultaneously from the logarithmic derivative of resistance and the upturn in the thermoelectric power, is  $T_{MI} \sim 18.5$  K. With further increase of pressure, the MI phase *boundary collapses*, within 0.2 GPa, as in the case of the impure samples, but remains first order. Indeed, in temperature dependent measurements, the hysteresis becomes more and more pronounced as  $p_{cr}$  is approached and  $T_{MI}$  is suppressed to lower temperatures. This is clearly seen by comparing the resistance curve at  $p=1.76$  GPa (Fig. 5.16) with the corresponding resistivity curve at  $p=1.9$  GPa (Fig. 5.17), when both are plotted over the same temperature range.

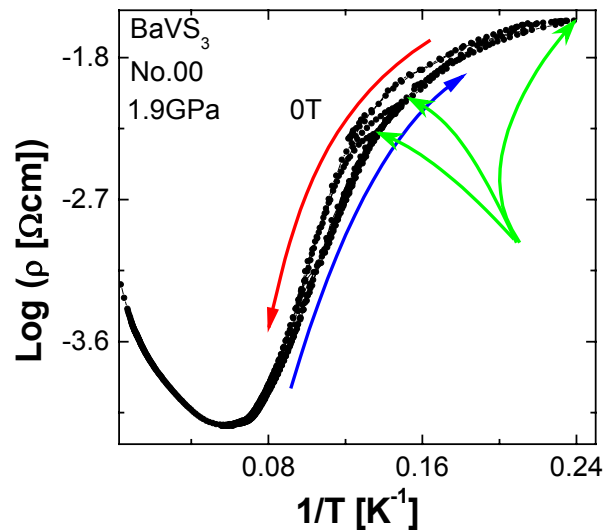


**Figure 5.17:** The Arrhenius plot of the resistivity at pressure of 1.9 GPa. From the logarithmic derivative (not shown),  $T_{MI}$  is estimated to be 10 K. The red and blue arrows denote the envelope warming curve and envelope cooling curve, respectively. Green arrows indicate the temperatures at which the cooling was stopped and the heating was begun.

The cooling - heating cycles were repeated several times from 17 K down to 4 K and each time the curves closed a loop (Fig. 5.17). If cooling is stopped before reaching 4 K and heating is started (indicated by green arrows) the resistivity stays more or less unchanged until it joins the heating curve initiating a minor hysteresis loop in the absence of external magnetic field. This behavior (Chaddah *et al.*, 1992) is characteristic for phase coexistence in the vicinity of a first order phase transition.



It is tempting to reconcile the two behaviors by the coupling of the magnetic SDW order to the lattice. On one hand, the hysteresis is a clear sign of the first order phase transition. On the other hand, the QCP at  $p_{cr}$ , marked by the NFL behavior (both in pure and impure samples), is usually associated with a second order phase transition. It should be pointed out that in the disordered samples no trace of hysteresis was found and the phase boundary looks as if it were second order. However, before entering into considerations about the possible origin of the hysteresis, and their impact on the understanding of the physical properties of BaVS<sub>3</sub>, let us focus on some additional experimental facts revealing further relevant properties of the system.

#### 5.4.1 *Hysteresis, relaxation times and non-linear transport*

##### 5.4.1.1 *Characteristic energies in the system*

In this section, we will present the results from the magnetotransport measurements on the high quality samples. The first feature discussed comes from the proximity of the QCP and the others follow from the relevant energies in the system. It is useful to rewrite Eq. (5.1) in a different form,

$$\rho = \rho_0 \cdot \left( 1 + \left( \frac{T}{T_0} \right)^n \right),$$

which allows the definition of a characteristic energy of the system  $k_B T_0 = k_B (\rho_0 / A)^{1/n}$ .  $T_0$  gives an idea of the electron energy scale involved in the NFL or the FL. The calculated value for  $T_0$  at the critical pressure is  $\sim 11$  K, and it remains unchanged by increasing pressure (Fig. 5.18). The same order of the characteristic temperature  $\sim 15$  K could be extracted from Fig. 5.15b (approximately corresponding to the beginning of the eye guide lines). At these temperatures, the strength of the electron-electron interactions, associated with  $A_2$  (see Fig. 5.15), shows an upturn or a saturation (NFL or FL), depending on the pressure. This temperature is of the same order as  $T_{MI}$  ( $\sim 18$  K) at the 1.76 GPa where the phase boundary collapses with increasing pressure. It is also interesting that these temperatures are comparable with the temperatures (**10 to 15 K**) unto which the *power law fits extend* in the NFL phase, corresponding to the *position of the shoulder* in resistivity (Fig. 5.11b) or to the temperature at which the *magnetoconductivity changes slope from negative to positive* (Fig. 5.13). All these facts suggest us that at, low temperature, the behavior of the system in the magnetic field is characterized by energies of the order of 10 K, not

---

included in the straightforward spin-Peierls model.

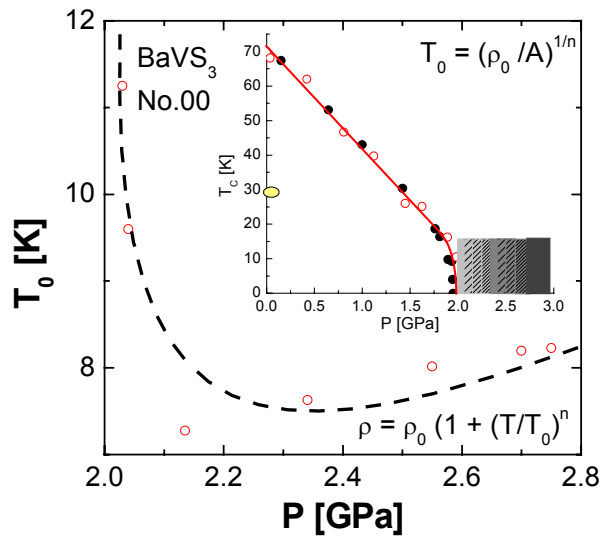


**Figure 5.18:** Pressure dependence of the characteristic energy of the system  $T_0$  (red circles on the main figure). The dashed line is a guide to eye. The inset is the remainder of the phase diagram.  $T_x$  is marked by the yellow point, the MI phase boundary by the red line, and NFL-FL crossover by the squares changing the color from light to dark grey symbolizing the evolution of the power-law exponent  $n$  from 1.5 to 2.

#### 5.4.1.2 Hysteresis in the magnetic field and a characteristic time scale

Since the characteristic spin ( $\mu_B H$ ) energy of a magnetic field of a few Tesla is of the same order (10T is approximately 8K) it should be expected that such fields perturb the system. Pursuing this idea further, it should be recalled that, in impure samples, the moderate magnetic field of 8 T at 1.91 GPa suppresses the MI transition. This is accompanied by a reduction of the resistivity by two orders of magnitude (Fig. 5.12) and, a sample-dependent positive upturn at higher fields (around 9T). Similar effects are also observed on high quality samples but, in those cases, the negative magnetoresistance is accompanied by a large hysteresis (Fig. 5.19).

Several other interesting effects were also observed. In a manner reminiscent of the observed hysteresis as a function of temperature (*e.g.*, Fig 5.17), minor hysteresis loops are also present in isothermal plots of resistivity vs magnetic field (an example is shown later in Fig 5.23) proving coexistence of the phases at fields below 9T. ***Above this field the magnetoresistance is positive and hysteresis is absent, indicating that the spins are ordered and only one phase is present.***

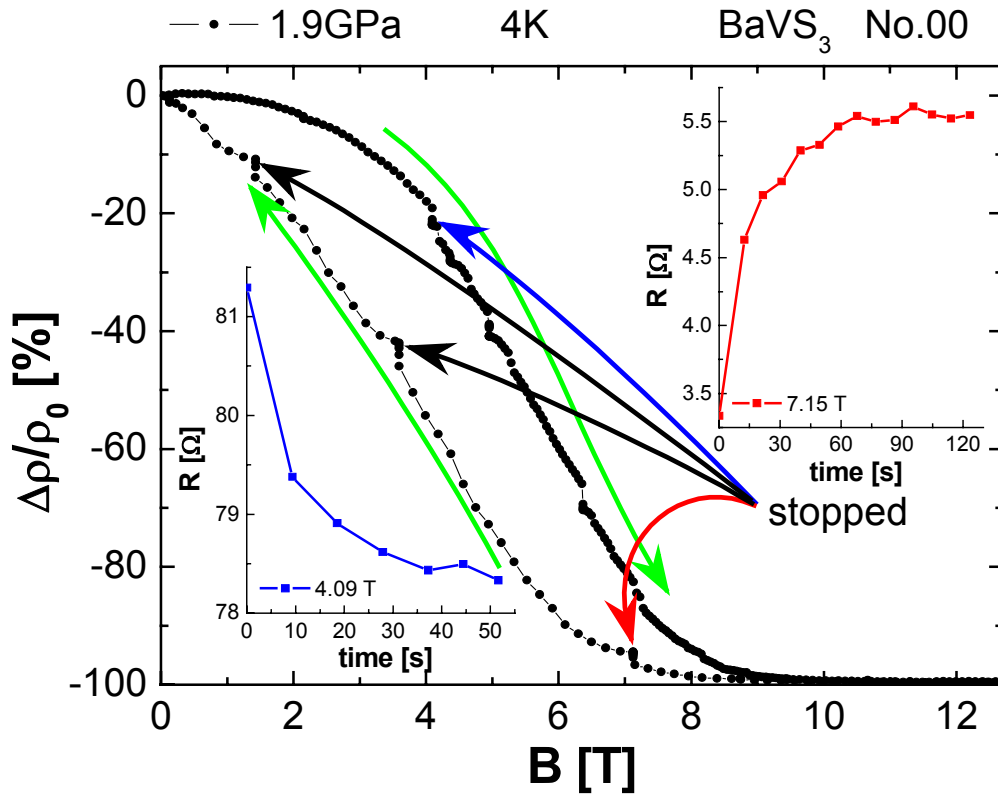


**Figure 5.19:** Relative change of the resistivity at 1.9 GPa and at 4 K as a function of the magnetic field strength. The direction of the evolution of the magnetic field is indicated by green arrows. The field sweep was stopped several times as indicated by black, red and blue arrows and the relaxation with time of the system was observed. At places indicated by the red and blue arrows the time dependence of resistivity is presented in the two insets (red and blue curves, respectively).

If the sweep of the magnetic field is stopped the system *relaxes* on *time scales of ~50 seconds*. This is shown in the insets of Fig. 5.19, for two different magnetic fields, at 7.15 T coming from the lower field and at 4.09 T after decrease of the field. These measurements uncover the kinetic aspects of the phase transition that are related to the movement of domains. This new time scale imposes the definition of the measuring protocol. All the measuring instruments need a fixed responding time and therefore it is important to know how a certain point was recorded. To keep the interpretation of the data consistent (and as simple as possible) the same protocol for resistivity measurement was consistently respected: after setting the desired value for the d.c current, a period of 2 seconds was allowed to elapse before the voltage was read. The polarity of the current was then changed and, after a further 2 seconds, the voltage was read again. From these two points in the  $I$ - $V$  graph the resistivity was determined (more details are given in Appendix 1).

### 5.4.1.3 Current instability

In addition to the system's sensitivity to pressure, Sr substitution as well as impurities and magnetic fields, Fig. 5.20 depicts one more peculiarity. The results shown were obtained by driving the sample close to  $p_{cr}$  by setting the pressure at 1.9 GPa and then fine-tuning it with the magnetic field, towards the metallic state. As expected (from Fig. 5.19) the MI transition is still present, with a decreased value of resistivity, at a magnetic field of 6 T. At 12 T the system is supposed to be metallic in the whole accessible temperature range, but this turns out to be only partially true.

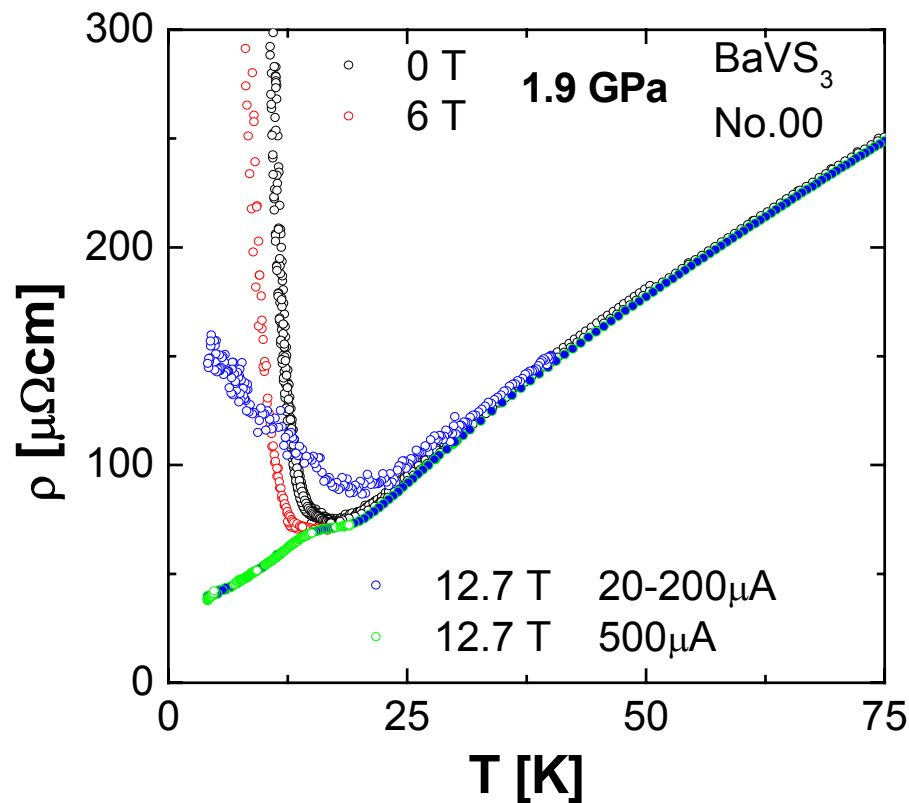


**Figure 5.20:** Resistivity as a function of temperature and current for three magnetic fields, at a pressure of 1.9 GPa. For the two lowest fields, no current dependence was observed. At 12.7 T electrical properties differ if the resistivity was measured keeping the DC current as low as possible (20 - 200  $\mu\text{A}$ ) or at higher current of 500  $\mu\text{A}$ .

If the resistivity is measured by a d.c current higher than 500  $\mu\text{A}$ , the recorded curve (Fig. 5.20) shows a shoulder around 15 K with the expected low temperature power-law dependence. On the other hand, if the current is lowered as much as possible (held between 20 and 200  $\mu\text{A}$ , fixed by a good signal to noise of the measurement),

the resistivity reveals a new feature. ***Around 25 K the recorded curve deviates from the metallic behavior with a broad upturn but never shows the singularity of the MI transition.*** It is unexpected that the 12 T low-current curve deviates from metallic behavior at higher temperatures shown by the curves taken at lower fields (Fig. 5.20). It is hard to connect this feature with any of the curves recorded earlier in BaVS<sub>3</sub>. It appears as if the system swings between the insulating and metallic state and is driven, by a high enough current, into the metallic state.

The observed sensitivity to the strength of the direct current motivated the measurement of the  $dV/dI$  characteristic as a function of the applied current  $I$  for several values of the magnetic field  $B$ . In contrast to the d.c. measurements described in connection with Fig. 5.19, the a.c. method is used here. The frequency of the main a.c. current is taken to be in the range 2 Hz -10 Hz and superimposed to it is a much smaller current of 17.5 Hz. Both corresponding times are small with respect to the overall relaxation time of some 50 s, determined in Fig. 5.19 (as are the times involved in the d.c. measurements). However the time scales used in the two types of measurements cannot be brought in full correspondence and therefore the two sets of data should not be compared too closely.

The results of the a.c. measurement are shown in Fig. 5.21. On the abscissa is the value  $I$  of the main current as it changes in time, while the small 17.5 Hz signal is used to determine  $dV/dI$  for the chosen mesh of  $I$  values. The corresponding mesh of  $dV/dI$  values is connected by fine black (red) lines. Surprisingly, already at 0 T the recorded curve does ***not show a constant Ohmic*** trace, but rather a  $V$ -shaped behavior. The second significant feature in Fig. 5.21 is the appearance of ***abrupt and random jumps*** in  $dV/dI$  for the fields between 0 T and 9 T. It is interesting that the jumps persist after a number of cycles in  $I$  and after a sufficient time the up and down jumps drive the system back, close to any value observed previously, "closing" the loop. Since the jumps are apparently stochastic the same loop is not expected to repeat twice. By increasing  $B$ , the deviation from the Ohmic behavior is observed to change character at around 9 T, the same field at which the hysteresis closes and the magnetoresistance shows an upturn (Fig. 5.19 and Fig. 5.23). The  $V$  shape in Fig.5.21 is replaced by a peak centered at  $I = 0$  A, and the jumps do not occur any more. As the appearance of jumps is apparently associated with the movement of the domains this indicates the ***absence of domains above 9 T***. The strength and the frequency of the current thus appear to be powerful tools in the investigation of the structure and the dynamics associated with the first order transition in BaVS<sub>3</sub>.

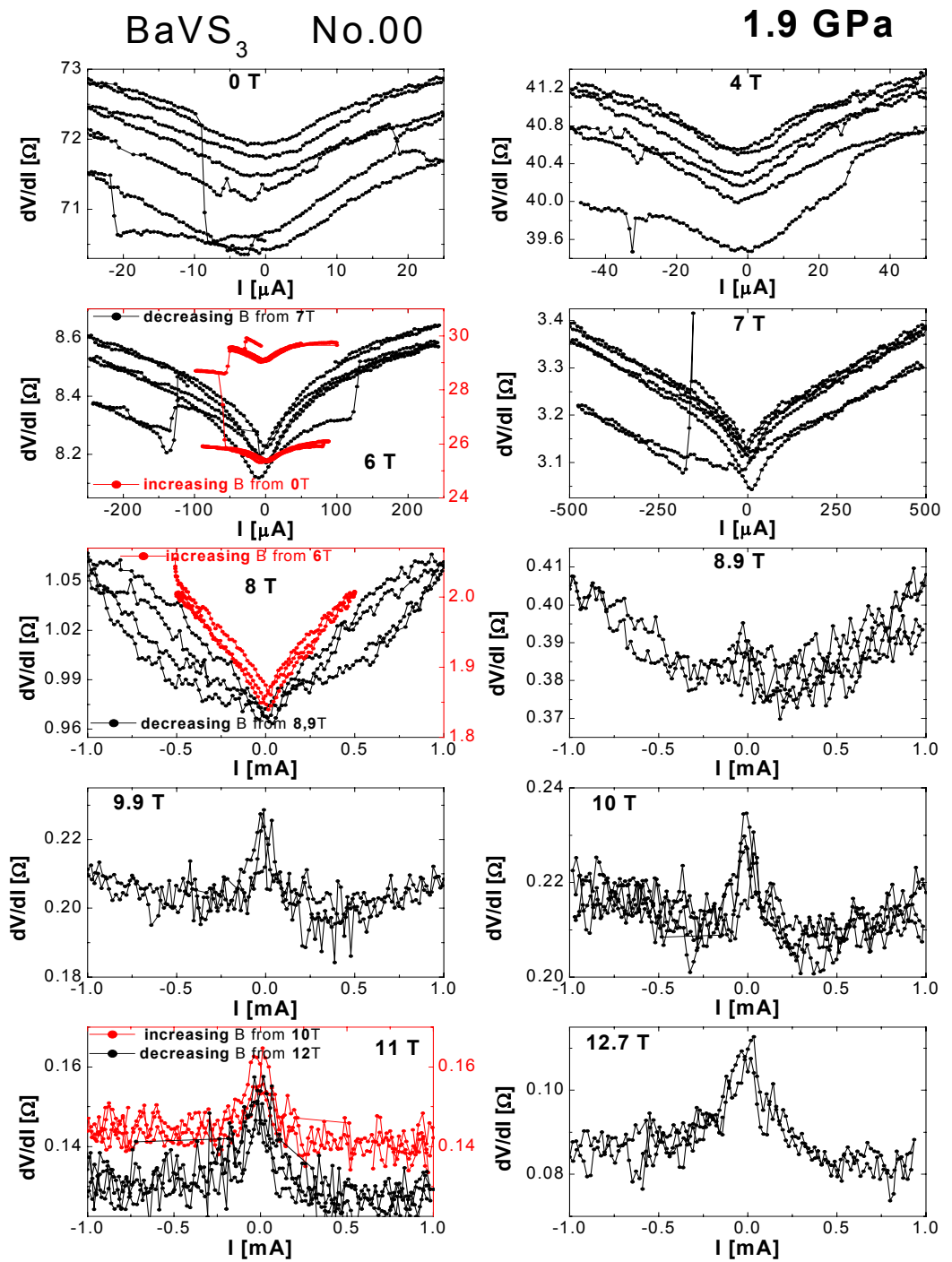


**Figure 5.21:** The  $dV/dI$  characteristics, at  $T = 4 \text{ K}$ , as a function of current for several magnetic fields, showing the instability of the system to the current. The black and red colors are related to the direction of the change of the field before recording the characteristic.

#### 5.4.1.4 *Memory effects*

The hystereses in temperature below 15 K, and in magnetic field below 8 T, correspond to behaviors of the system which are history dependent. Therefore, it is important to know at which temperature and in which direction (increasing or decreasing) the field has been changed before a curve is recorded. An example of this history dependence is shown for the resistivity at the pressure of 1.945 GPa, in Fig 5.22. Firstly, the system was cooled from high temperatures in the field of 12 T showing a metallic behavior in the whole measured temperature range, due to the suppression of the MI transition by the magnetic field. A shoulder in resistivity is observed at 15 K. Below this temperature, the resistivity at 12 T is higher than the resistivity at 9.88 T, which is in agreement with the upturn in magnetoresistance which occurs independently of the pressure at 4 K and 8T (Fig. 5.23 in shown Section 5.4.1.5).

The next three curves, marked by numbers 2, 3 and 4 in the upper panel of Fig. 5.22, were recorded after changing the field at a temperature above 15 K and measured only while the system was cooled. The only exception was the 9.88 T curves for which the full temperature cycles were repeated several times.

All of the other curves in the lower panel of Fig. 5.22, denoted by numbers from 5 to 16, were recorded after firstly, changing the magnetic field at low temperatures ( $\sim 1.5$  K), heating to above 15 K and then cooling back to 1.5 K. The curves numbered from 5 to 10 were taken after a decrease of the magnetic field, while the curves numbered from 11 to 16 were taken after an increase of the magnetic field. To clarify this somewhat complex protocol with an example we can follow the course of one particular cycle. After cooling the system to 1.5 K at 4 T (green curve marked by number 6) the magnetic field was decreased to 2 T (the jump in resistivity is indicated by the vertical green arrow). The temperature was then increased to 20 K (red curve number 7), reduced back to 1.5 K (red curve number 8) and, finally, the field was changed once more (indicated by the red vertical arrow).

At low magnetic fields (up to 4 T) small jumps in the resistivity curves are noticeable. This is probably a consequence of domain kinetics and thus may be connected with the similar jumps observed in magnetoresistance measurements (Fig. 5.19) or current dependent measurements (Fig. 5.21). It should be pointed out that the temperature of the **15 K**, temperature at which the hysteresis closes and the shoulder appears, *resets the system anew for the history dependence*.

---

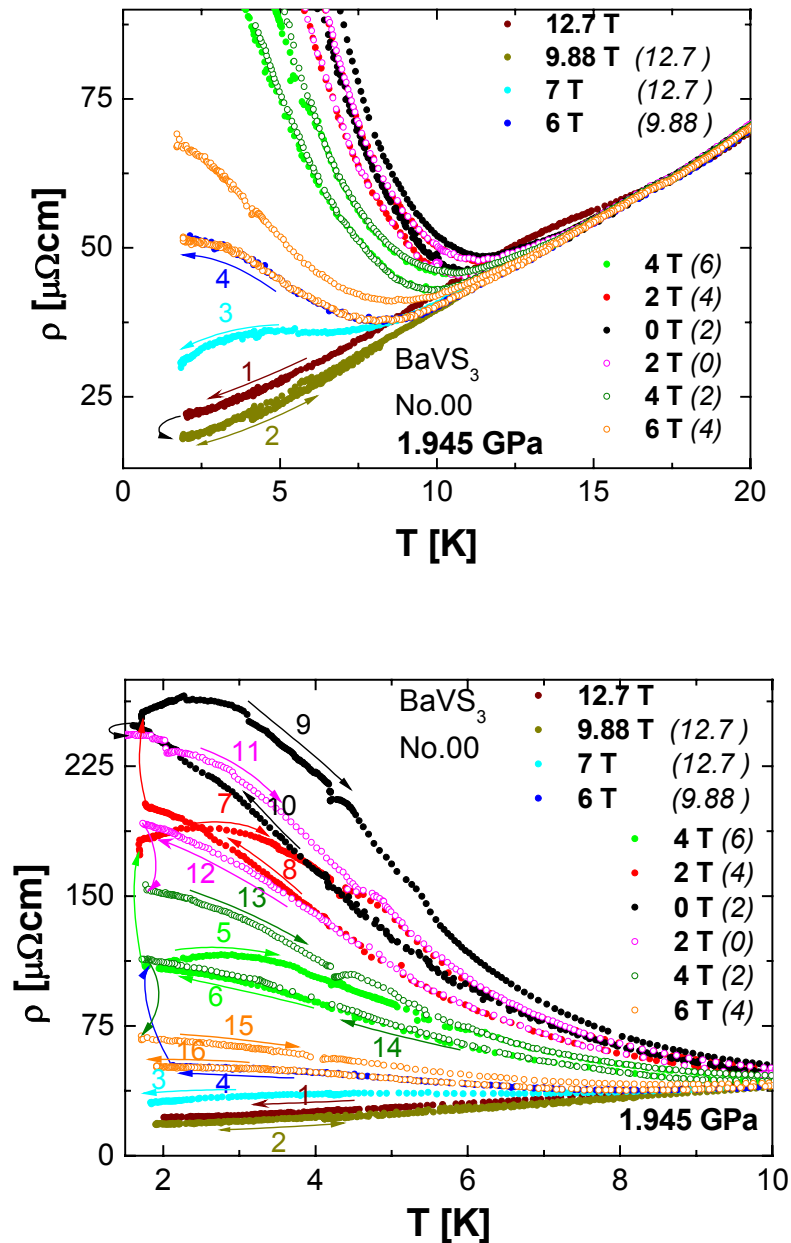
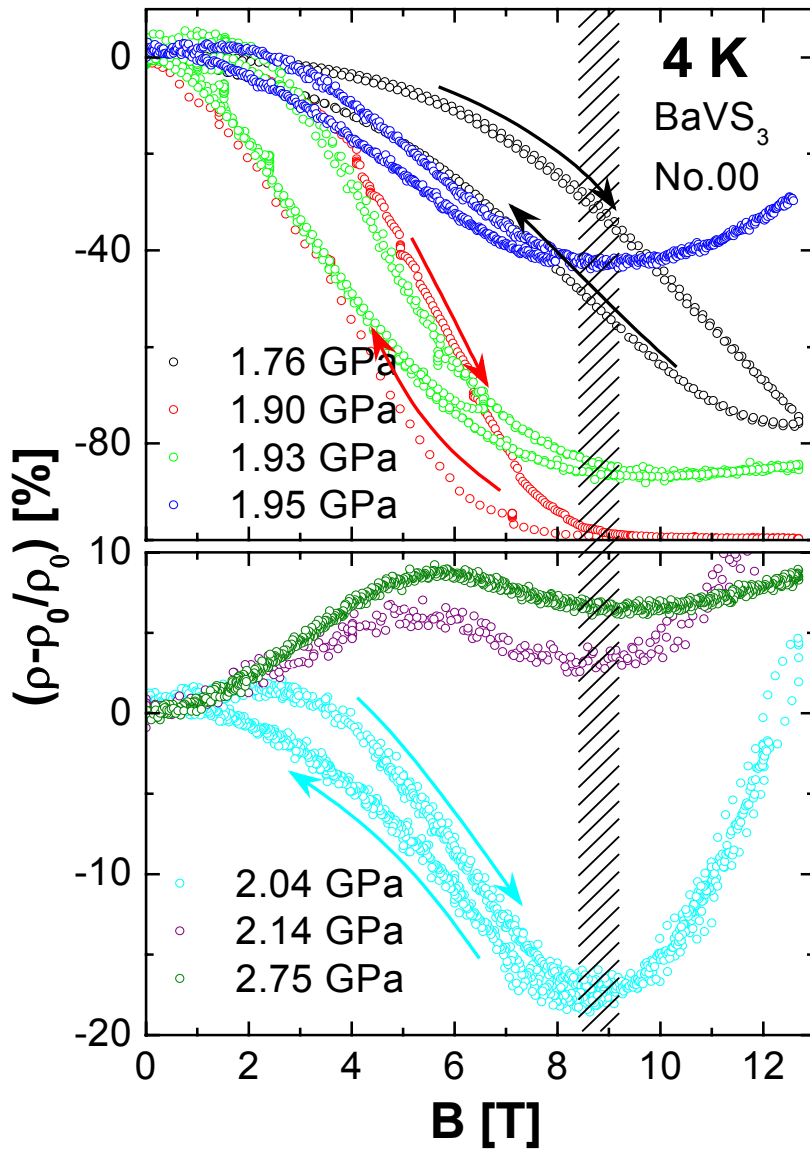


Figure 5.22: The upper and lower panels show, on different scales, the same temperature dependence of resistivity for several magnetic fields at 1.945 GPa. The numbers on the curves, together with the matching colored arrows indicate the respective order and direction of the temperature change under which the correspondingly colored curve was recorded. The vertical arrows are guides for the eye, also indicating the temperature at which the magnetic field has been changed (the color of the arrow matches the color of the cooling curve and the arrow points to the beginning of the next heating curve). For easier orientation, the legend contains two numbers, the **first bold** one, indicates the strength of the magnetic field at which the temperature cycle was recorded and the *second italic* number (*in parentheses*) gives the strength of the preceding field.



5.4.1.5 Magnetoresistance as a function of pressure and temperature

In Fig. 5.23, the magnetoresistance at 4 K (the temperature of liquid Helium which is easy to realize and stably maintain) is shown for several pressures. The pressure range of interest starts at 1.76 GPa, where the MI phase boundary begins to collapse and the



**Figure 5.23:** The relative magnetoresistance at 4 K for the pressures below (upper panel) and above (lower panel)  $p_{cr}$ . The minor hysteresis loop is shown at the pressure of 1.93 GPa (similar loops were also observed at other pressures). The magnetic field was changed in the direction indicated by arrows. For  $p > 1.9$  GPa, the dashed area indicates the characteristic field (energy) of the system (independent of pressure) at which the hysteresis closes and the magnetoresistance has an upturn.

hysteresis begins to emerge (either by increasing the pressure or by switching on the

magnetic field) and extends to 2.7 GPa, where the resistivity, below 15 K, has a power law temperature dependence with the (FL) exponent  $n = 2$ .

All the curves (except the 1.76 GPa curve for which the MI transition is not completely suppressed either at 8 T or 12.7 T) share a common behavior: an upturn between 8 and 9 T. (marked by the dashed area in Fig. 5.23). This is the very same value of the field at which the hystereses close, a fact that is independent of whether the magnetoresistance is related to the suppression of the insulating phase or is measured above  $p_{cr}$  in the metallic phase. This indicates that the energy corresponding to  $\sim 8$  T is the characteristic energy of the system both above and below  $p_{cr}$ .

Interestingly the hystereses also close at zero magnetic field which was checked by changing the polarity of the field and thereby measuring the magnetoresistance in the range of -12.7 to 12.7 T. The recorded curves (not shown) have a similar to shape the hysteresis reported in the magnetotransport study of the AFM-FM transition by Singh *et al.* (2002). The direction of the field variation in the hysteresis loop is indicated by arrows.

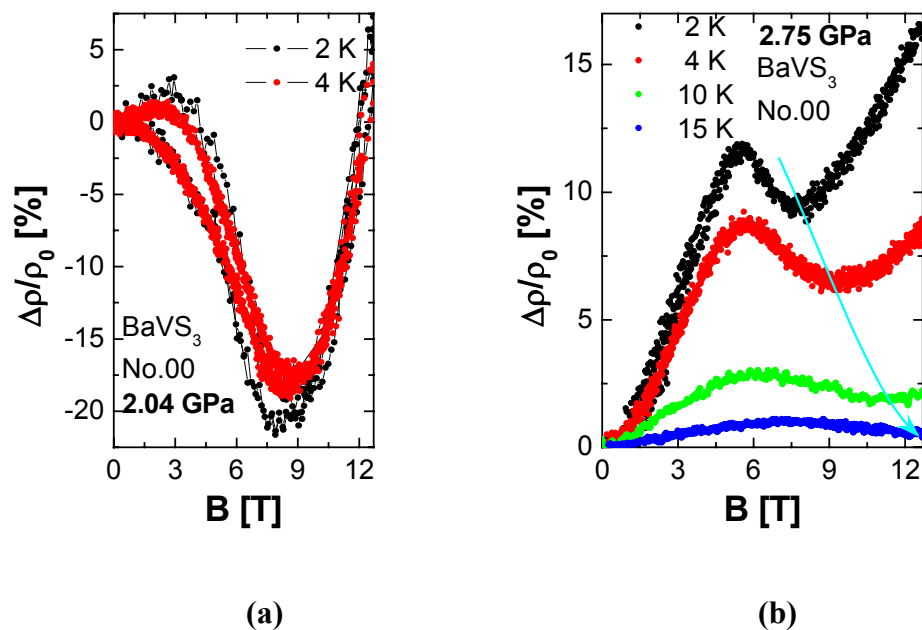


**Figure 5.24:** Isothermal magnetoresistance curve recorded at different temperatures and pressures. (a) The 2 and 4 K curves at 2.04 GPa. (b) Curves taken at 2.75 GPa for several temperatures. The cyan arrow indicates the position of the dip for various temperatures.

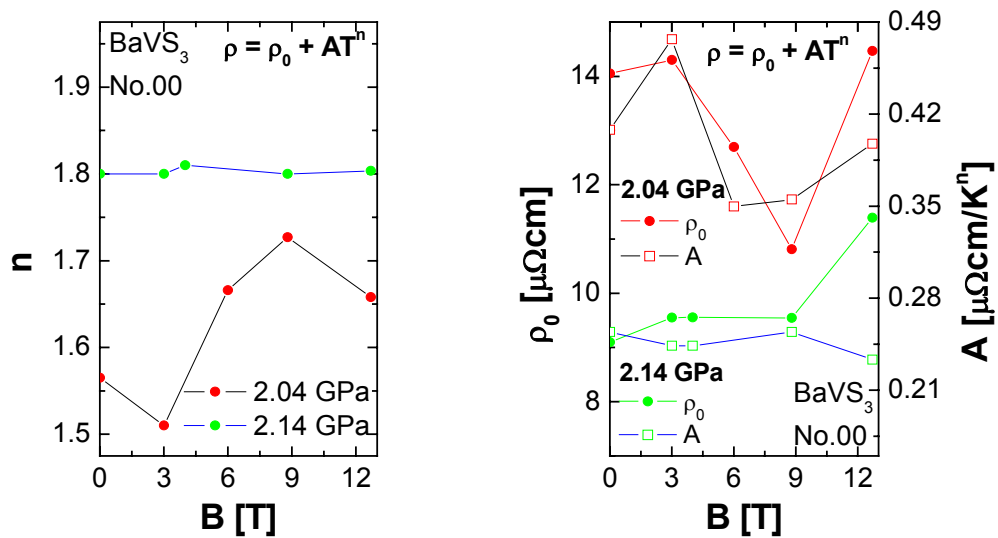
The existence of the minor hysteresis loops within magnetic sweeps was checked at several different pressures. Since the recorded curves resemble each other, only one example in-between the envelopes of the 1.93 GPa (green) curve is shown in

Fig. 5.23. It is interesting to notice that, already at the pressure of 0.1 GPa above  $p_{cr}$ , the magnetoresistance is positive and it does not show any sign of hysteresis. This behavior remains unchanged to the highest measured pressure of 2.75 GPa.

The magnetoresistance was also recorded as a function of temperature at fixed pressure. Generally, the effects of the magnetic field are diminished as the temperature is increased (shown in Fig. 5.24b). Above 15 K the relative magnetoresistance is small and negative for all pressures. The examples of the low temperature behavior ( $< 15$  K) of the pressure just above  $p_{cr}$  (2.04 GPa) and in the FL phase (2.75 GPa) are shown in Fig. 5.24. The 2.75 GPa curves reveal the broadening of the dip around 8 T and its shift to higher fields with increasing temperature (as indicated by the cyan-colored arrow).

### 5.4.1.6 Power law parameters and the magnetic field

In Fig 5.25, the magnetic field dependences of all power-law parameters are presented for two pressures (2.04 and 2.14 GPa) in the proximity of  $p_{cr}$ , in similar way to that done previously for the pressure dependences shown in Fig. 5.14 and Fig. 5.15. At 2.14 GPa the parameters are weakly dependent on the magnetic field. On the contrary, just above  $p_{cr}$ , the coefficient  $\rho_0$  (at 2.04 GPa) assumes a  $B$  dependence identical to that of  $\rho$  measured at a higher temperature (e.g. at 4 K, Fig. 5.24), nicely followed by the coefficient  $A$  (as was also the case for pressure). Already from the pressure dependence of the parameters it could be observed that the increase of the exponent  $n$  is accompanied by the decrease of the coefficients  $A$  and  $\rho_0$ , in a similar fashion to that observed in their magnetic field dependencies. The presented curves were recorded only during the cooling of the system and therefore the existence of hystereses can not yet be commented upon.



**Figure 5.25:** Magnetic field dependencies of the resistivity power-law exponent  $n$  (left panel), prefactor  $A$  (squares, right panel) and the “residual” resistivity  $\rho_0$  (circles, right panel) resulting from the fits  $\rho = \rho_0 + AT^n$  for two pressures ( $p=2.04$  and  $2.14$  GPa).

## 5.5 Ferromagnetic versus Interchain-Compensated-Ferromagnetic instabilities at low $T$ /high $P$

Taking into account the high-pressure results, presented above, the phase diagram proposed in Fig. 5.7 should obviously be reconsidered. Importantly, the presence of *hysteresis* in the vicinity of  $p_{cr}$  has important consequences on the possible scenarios for the transition. Interestingly, hysteretic behaviors in temperature and magnetic field, similar to those found at  $p_{cr}$  in BaVS<sub>3</sub>, have also been observed in Ce(Fe<sub>0.96</sub>Al<sub>0.04</sub>)<sub>2</sub> (Singh *et al.* 2002), a system with a first-order transition from ferromagnetism to antiferromagnetism. This gives a hint that something similar could also possibly take place in our system of interest. For example, the minor hysteretic loops as well as history dependent effects are similar between the two systems. In this respect, it should be remembered that the chain spins are nearly frustrated on the orthorhombic lattice in BaVS<sub>3</sub> and that the transition therein thus probably concerns the ordering of the chain spins between chains (Mihaly *et al.* 2000).

The possibility of the ICFM – FM first order transition at  $p_{cr}$  is supported by the magnetic susceptibility measurements (Appendix 2, Yamasaki *et al.*, 2000) at ambient pressure from which we know that the 30 K transition can be either FM or ICFM, depending on the sample quality. Even more, those results give the impression that any type of disorder or sulfur deficiency prefers the full FM arrangement. From all these arguments it seems reasonable to assume that these phases are energetically close to one another and that any kind of perturbation, such as magnetic or electric field, can switch the system from *ICFM to FM* through a first order phase transition. The lack of the hysteresis in the impure samples can be attributed to disorder, which already at ambient pressure can cause FM below 30K. For this reason, the ICFM - FM phase transition does not occur at  $p_{cr}$  in the impure samples.

An alternative explanation for the appearance of hysteresis at  $p_{cr}$  could be the transition from the ICFM to the paramagnetic state. However, because of the *shoulder in resistivity* that is observed at pressures above  $p_{cr}$  and at temperature around 15 K, this scenario is unlikely. That is, knowing that the high temperature phase is paramagnetic, the simplest explanation for this shoulder (for  $p \sim p_{cr}$ ) is some kind of *FM order* below 15 K. Furthermore, as previously discussed, this is exactly the same temperature at which the MI phase boundary deviates from its linear pressure dependence and collapses. The logical conclusion is that the collapse of the insulating phase and the shoulder in resistivity for  $p > p_{cr}$ , are connected. As long as there is a larger characteristic energy in the system, like the insulating charge gap, the FM order

---

is rearranged (only) between chains, driving the system to ICFM. This leads us to the conclusion that the ICFM order in pure samples is a consequence of the metal-insulator transition. In its absence, the system prefers the full FM order.

An additional argument for the FM order above  $p_{cr}$  and below 15 K comes from the investigations of the sister compounds  $Ba_{1-x}Sr_xVS_3$  and  $BaVSe_3$ . The presence of Sr suppresses the  $T_{MI}$  transition in a similar manner to the pressure (Chapter 6) and, for  $x=0.15$ , the transition temperature is 50 K at ambient pressure. Interestingly, this transition does not have a strong impact on the susceptibility, which remains Curie-like close below the transition, and the system shows the FM order at 20 K. It was already shown that in these compounds are associated with quite high levels of disorder ( $RRR \approx 10$  like in the impure samples of  $BaVS_3$ ). Thus, as was the case for the impure  $BaVS_3$  samples, it is expected that the system finishes in the FM phase at low temperatures. In this sense, the chemical pressure does not affect the low temperature (15 K) FM order in the insulating phase. The other isoelectric substitution, where S is replaced by Se, seems to have a similar effect. Comparing resistivity and thermoelectric power measurements of  $BaVS_3$  at 2.7 GPa and  $BaVSe_3$  at ambient pressure reveals a strikingly similar behavior for both systems. Furthermore, the measured susceptibility (Kelber *et al.*, 1979) of  $BaVSe_3$  has a paramagnetic character at high temperatures similar to impure  $BaVS_3$  and undergoes the metal-to - FM metal transition at  $\approx 40$  K. Unfortunately, despite considerable effort over recent years, single crystals of the  $BaVSe_3$  are not yet available. Therefore the RRR ratio cannot be determined and the contribution of impurities cannot be analyzed.

On the other hand, the pure and impure samples have a *similar NFL* behavior of the resistivity around  $p_{cr}$ , showing comparable tendencies as functions of pressure, temperature and magnetic field. The main difference between them concerns the appearance of hysteresis. It is worthwhile mentioning that the NFL behavior is independent of whether the conducting system fluctuates towards the FM insulator (through the second order phase transition) or towards the ICFM insulator (through the first order phase transition). The *common feature* for both fluctuation regimes is therefore considered in what follows.

The above discussion suggests that, in impure samples, the FM transition survives the collapse of the nonmagnetic MI phase with the 4V unit cell at  $p_{cr}$ . This would imply that the FM boundary crosses the MI phase boundary and remains stable by further increase of pressure. This is supported by the high-pressure (up to 2 GPa)

---

measurements of the transport properties of  $\text{BaVSe}_3$  showing only a weak pressure dependence of the FM transition temperature. The crossing of the FM boundary and the MI boundary implies that the MI transition is no longer associated with the largest energy in the system, therefore the MI boundary collapses. Thus, the ***FM order below 15 K, independent of pressure, is not intimately related to the MI transition.***

In the clean samples, the scenario is slightly different in the respect that the low temperature phase is ICFM and not FM. By the collapse of the magnetically active insulating phase in which the 4V unit cell is replaced by 2V, the system is perturbed, and it chooses the FM order through a first order phase transition. The FM gives the dominant energy scale in the system around  $p_{cr}$  and the MI boundary collapses similarly for both pure and impure samples alike. As a consequence, the non-Fermi liquid behavior appears as the result of fluctuations between the FM metal and FM insulator (unit cell 2V and 4V). That is, the FM is unessential for the NFL, except in the clean samples where the first order phase transition between the FM and ICFM insulator affects the conduction-electron properties at the Fermi level. It seems that, in turn, the ***ICFM order below 30 K and below  $p_{cr}$  is imposed by the magnetic nature of the MI transition*** in the clean samples.

With this we have presented the major experimental facts obtained on the  $\text{BaVS}_3$  family of materials, in a broad temperature, pressure and magnetic field ranges, on both pure and disordered/chemically-substituted samples. In the next section we will give our final point of view concerning the physical scenario for the description of this unique material.

## 5.6 Summary of the physics of $\text{BaVS}_3$

Recently Fagot *et al.* (2003) reported *X-ray scattering measurements with strong diffusive lines* at the critical wave vector  $q_c=0.5 c^*$  above the MI transition at ambient pressure. This corresponds to a pretransitional structural fluctuation in which the chains fluctuate independently from one other with a periodicity along the chain of  $4V$ . This periodicity cannot come from the dynamical  $q=0$  Jahn-Teller or any other similar fluctuations but it must be imposed by electron correlations at finite  $q$ : The fluctuations of the 3D lattice are 1D, which means that their origin must be searched for in the phonon coupling with 1D electrons. Indeed, our recent ARPES results clearly demonstrate the existence of the *quasi-1D  $d_z^2$  band*. Associating  $q_c$  with  $2k_F$ , this band is quarter-filled. At the MI transition the diffusive 1D lines condense into Bragg spots, which is a sign of a long-range 3D order. The diffusive lines at high temperatures suggest 1D instability, and consequently the  $T_{MI}$  is ascribed to the Peierls (*CDW*) or spin-Peierls (*SDW*) transition.

The ARPES measurements also showed the presence of the narrow  $e_g$  band which pins the Fermi level. From the fact that the new  $2k_F$  periodicity is commensurate along  $c$  (having four V per unit cell), it is concluded that the *electrons are shared 1 to 1 between the  $d_z^2$  and  $e_g$  bands*. Koga *et al.* (2004) showed, in the case of a two band model with two electrons per site that, if the Coulomb interactions are larger than the width of one of the bands as well as the splitting between them, the occupation of the narrow band tends to be 1 electron, making the band half filled. A similar result is known in the physics of high- $T_c$  materials (Mrkonjić and Barišić, 2003). In the case of the  $\text{BaVS}_3$ , the *screw axes symmetry is weakly broken below the MI transition, the Umklapp scattering is small*, (Barišić and Brazovskii, 1981), *and therefore even the bands may be roughly considered as quarter filled*. The exact 1:1 sharing of electrons between such bands is probably due to the closeness of the bands in the absence of interactions and their fine tuning to the quarter filling by the fourfold commensurability effect of Coulomb interactions analogous to that in the case discussed for half filling. The quarter filling of the  $d_z^2$  band has an important consequence: a quarter filled quasi-1D band develops simultaneously strong  $2k_F$  SDW or CDW correlations (Emery, 1979; Solyom, 1979). On the other hand, the strong breaking of the screw axis symmetry along the  $c$ -axis would result in the pronounced dimerization of the cell, making bonds and/or sites quite different. As a consequence, the bands should be regarded as half filled, with appreciable Umklapp. In the case of the half filled band (Emery, 1979; Emery *et al.*, 1982; Solyom, 1979, Fabrizio and Tosatti, 2004), the  $2k_F$ -SDW can be preferred then to the  $2k_F$ -CDW,

---



which is being inhibited by the Umklapp process ( $4k_F$  then coincides with the reciprocal vector  $G$ ). However, there is no evidence that this process is important for the dominance of the SDW (i.e., spin Peierls) instability in the clean samples of  $\text{BaVS}_3$ . That is, the screw axis is preserved above  $T_{MI}$  but the quasi-1D  $2k_F$  fourfold commensurability of the precursor lattice fluctuations is present although there is no trace of a  $4k_F$  quasi-1D precursor effects. The static  $4k_F$  component, which appears only below  $T_{MI}$ , breaking the screw-axis symmetry, is small and behaves as the secondary order parameter (Fagot *et al.*, 2004). The d.c. anisotropy measurements of the resistivity agree with the results of the band calculations in that the  $e_g$  electrons play a part in the conductance. Therefore, it is necessary to ***open simultaneously an energy gap*** for both types of electrons when the system undergoes the MI transition.

Actually, the  $2k_F$  CDW or SDW instability occurs in the broad 1D  $d_z^2$  band at the temperature of 70 K (gap of 0.05 eV, Mihaly *et al.* (2000), Graf *et al.* (1995)) and it corresponds to the dominant energy in the system which can be sufficient to rearrange the  $e_g$  electrons. It seems that the bands (anti)cross close to the Fermi level, and at this point the opening of a gap in one of the bands introduces a new periodicity which automatically opens a gap for all electrons.

For 1D systems, the CDW and the SDW transitions are energetically close (Riera, and Poilblanc, 2000). SDW may have a small advantage but even a small disorder in the system seems to be sufficient to switch the instability to the CDW. Accordingly, in the ***clean BaVS<sub>3</sub>*** samples the transition appears to be ***SDW with a periodicity of 4V***, accompanied by a decrease in susceptibility. The scenario of SDW transition is also supported by the phase boundary analysis of  $\text{BaVS}_3$  performed as a function of magnetic field by Kézsmárki (2003, p. 60). He determined the value of the dimensionless constant ( $\gamma$ ) in the following relationship, which describes the suppression of the MI transition with the magnetic field, to be  $\gamma = 0.45 \pm 0.04$ :

$$\frac{\Delta T_{MI}(H)}{T_{MI}} = -\gamma \left( \frac{g\mu_B SH}{k_B T_{MI}} \right)^2$$

This value is in good agreement with the value found in organic (Northby *et al.*, 1982) and inorganic compounds (Hase *et al.*, 1993), and with the theoretical predictions by Bulaevskii *et al.* (1978) and Cross (1979). The  $2k_F$  SDW dimerization of the 2 V "dimerized" unit cells along the chains and the associated magnetic order impose constraints on the narrow  $e_g$  electrons. It is most likely that due to the ***SDW of the  $d_z^2$  band***, and its local magnetic field ***to which the  $e_g$  electrons couple induces the SDW***

**order** on them as well. Consequently, the susceptibility is reduced. On the other hand, in the **impure samples**, the transition seems to be of the **CDW** nature, which imposes the periodicity of  $4V$  with no constraints on the spins and therefore does not have a large impact on susceptibility. Thus, the magnetic susceptibility continues to be Curie-like across the MI phase boundary.

The latest NQR, NMR (Nakamura, *et al.*, 1997) and Muon Spin Relaxation ( $\mu$ SR) (Higemoto *et al.*, 2002) measurements on the clean samples **have not found two types of local charges or magnetic sites** close below the MI transition and this is in agreement with the above-described picture. It seems that at  $\sim 30$  K, the system starts to order magnetically which is seen as a peak in the temperature derivative of the a-axis susceptibility  $d\chi_a / dT$ , and as a sudden break in the anisotropy  $\chi_c - \chi_a$  at  $T_x = 30$  K (Mihaly *et al.*, 2000). By neutron diffraction experiments, a magnetic order with  $\sim 0.5 \mu_B/V$  moment was detected with the incommensurate wave-vector  $(0.226, 0.226, 0)$  (Nakamura *et al.*, 1999). The NQR measurements revealed a huge and markedly asymmetric electrical-field gradient (EFG) appearing at  $T_x$  which suggests the presence of **orbital ordering in the spin-ordered state**. This is supported by the observation of a slow muon spin relaxation time, suggesting the presence of two types of magnetic sites. The volume fraction of the magnetic sites gradually increases with decreasing temperature down to about **15 K** where it saturates. This suggests that this is the temperature at which the **system is magnetically ordered**.

Recent x-ray measurements of Fagot *et al.*, (2004) have detected a strong increase of the  $2k_F$  satellite spots at 5 K with respect to that at 40 K. This suggests an important charge rearrangement between these two temperatures. This large CDW is probably accompanied by orbital reordering but accurate measurements especially those of NQR are lacking so far. It was already shown that the temperature scale of 15 K has an important role in the physics of  $\text{BaVS}_3$  at  $p_{cr}$  but now we see that this may also be the case at ambient pressure. It should be noted, in this respect, that the V chains form a **triangular lattice**, frustrated when the magnetic order along the chains is ferromagnetic. Recently, Mihály *et al.*, (2000) carried out variational calculations on clusters, taking into account orbital-dependent hopping matrix elements and proposed the formation of a spin-pair liquid, which shows no static order between  $T_{MI}$  and  $T_x$ . They suggested that the ordering below  $T_x$  is not accompanied by a considerable entropy change because of the pre-existing short-range order, which can explain why there is no appreciable anomaly in specific heat at  $T_x$ . We believe that this might be the correct scenario for  $\text{BaVS}_3$ , but in a different temperature range (15 - 30 K and not between  $T_x$  and  $T_{MI}$ ) and with different ( $d_z^2$  and one  $e_g$ ) types of orbitals and therefore

---

different orbital-dependent hopping.

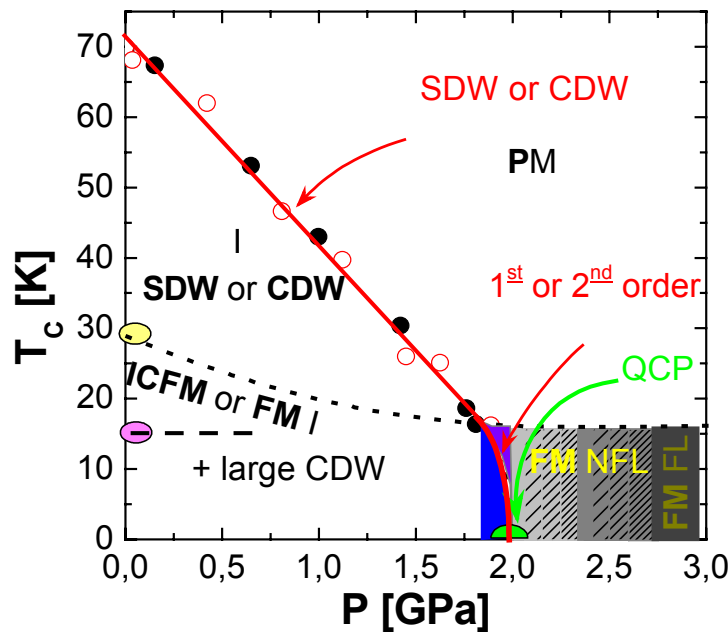


**Figure 5.26:** The proposed temperature-pressure phase diagram of  $\text{BaVS}_3$ . Below  $p_{cr}$  all the phases or phase boundaries have double names related to the pure or impure samples, respectively. The MI phase boundary is marked by the red line. The temperature at which the (new) magnetic order starts to appear ( $T_x \sim 30$  K) is marked by the yellow spot while the temperature by which the magnetic order is completed ( $\sim 15$  K) is marked by a magenta spot. The probable extensions of these two points to high pressures are denoted by the dotted and dashed lines, respectively. The green spot symbolizes the QCP (at  $p_{cr}$ ), and the blue, the violet and the gray fields stand for the related fluctuation regions. The gray regions are related to crossover from NFL to FL marked by the power law temperature dependence of the resistivity. The increase of the value of  $n$  is represented by darker and darker gray color, the lightest gray symbolizing  $n = 1.5$  and the darkest  $n = 2$ .

It was already mentioned earlier that in the impure samples, the MI transition is expected to be CDW and therefore the  $e_g$  electrons remain paramagnetic. It seems that this determines the low-temperature behavior developing the ferromagnetic-like order below 25 K which is independent of the MI transition. There are only a few experiments concerning impure samples and therefore the discussion of the low temperature phase is limited. However, in the works of Masnett *et al.* (1978), and Yamasaki *et al.*, (2000) it was found that the ferromagnetic order in sulfur-deficient samples takes place at  $T_{Curie} = 15\text{K}$  and that  $^{51}\text{V}$  NMR experiments revealed the coexistence of the ferromagnetic and nonmagnetic phases. It seems to us that, in impure samples, the *spin order* is determined *by intra and inter-chain FM* interaction between the  $e_g$  spins. In contrast to that, in pure samples, the SDW-induced RKKY interactions interfere with the direct FM interactions of the  $e_g$  electrons and the overall

spin order is thus a result of the balance of the two. As the result of this discussion we propose a new phase diagram, which is presented in Fig. 5.26.

It should be finally emphasized that the SDW/CDW line in Fig. 5.26 means that the  $2k_F$  SDW/CDW is coupled to the (heavy) lattice displacements, and through this coupling produces the corresponding lattice transition. In the case of SDW coupling to the lattice it is a spin Peierls transition (Caron *et al.*, 1987; Riera and Poilblanc, 2000). The SDW/CDW correlations occur in the broad  $d_z^2$  band with a low density of states at  $E_F$ , which raises the question of whether the nesting is sufficient to account for  $T_{MI} \sim 70$  K. This question has two aspects. The first concerns the Coulomb interactions, and it is precisely for that reason that the corresponding coupling constants, *e.g.*  $n_F U$ , were considered as small, leading to the near degeneracy of SDW and CDW correlations (Emery, 1979; Solyom, 1979). On the other hand the lattice coupling constant  $\lambda$  scales as  $1/n_F$  rather than  $n_F$ , when the coupling to the lattice is associated with the deformation-induced variation of the large overlap integrals, otherwise responsible for the large width of the band. Together with nesting, this is presumably sufficient to produce the lattice instability. This can be best illustrated on the example of the mean-field critical temperature associated with the free-fermion tight-binding gas coupled to the lattice. The free fermion gas is subject only to Pauli correlations in the CDW channel and the corresponding Peierls critical temperature is proportional to (Peierls, 1955; Pytte, 1974):

$$T_p \sim E_F e^{-\frac{1}{\lambda}},$$

where  $E_F = 2t [1 - \cos(c k_F)]$ , overlap  $t \geq 0$ , and the coupling constant  $\lambda$  is equal to:

$$\lambda = n_F \frac{I^2(2k_F)}{M\omega^2(2k_F)}.$$

This coupling constant defines the value of  $T_p$ . It depends of the density of states at the Fermi level  $n_F$ , and of the electron-phonon coupling constant  $I(2k_F)$ . But as  $I(2k_F)$  is proportional to  $v_F$  (Barišić *et al.*, 1970)  $\lambda$  scales with  $n_F^{-1}$ . The large band means a low density of states ( $n_F^{-1} = 2t \sin(c k_F) = v_F/c$ ). Therefore, it can be concluded that the low density of states gives a high mean-field critical temperature, further enhanced by Coulomb interactions, which is the case for BaVS<sub>3</sub>.

From the expression for  $T_p$ , an increase of the Peierls phase transition temperatures upon applying hydrostatic pressure is expected, due to the increase of the overlap  $t$

which reduces the density of states at  $E_F$ . Instead, as the **pressure is increased** from 1 bar towards the  $p_{cr}$  the **MI transition is linearly suppressed** to lower temperatures. The main reason for the decrease of  $T_{MI}$  with  $p$  is not attributed to the described intra-chain effect but to the simultaneous increase of the 3 dimensionality of the system (Forro *et al.*, 1990), leading to imperfect nesting (Horovitz, 1972; Gor'kov 1995). Finally, it is worthwhile noting that the coupling of the electronic instabilities to the (heavy) lattice makes the quantum effects less pronounced.

Within the framework outlined above, the principal results of transport measurements on BaVS<sub>3</sub>, under pressure and in the presence of a magnetic field, are now briefly summarized below.

1) ***The presented phase diagram provides an explanation for the origin of the NFL behavior and the source of the hysteresis in the clean samples.*** As the FM order seems to survive the collapse of the MI transition at  $p_{cr}$ , the origin of the instability of the system and its NFL behavior, is associated with the quantum fluctuations between the unit cell of 2V and 4V, with the latter being favored by the nesting in the  $d_z^2$  band. In the pure samples, the nesting favors the SDW whereas in the disordered samples the CDW is preferred. In clean systems, prior to the establishment of the 4 V order along the chains, there is a coexistence of both phases, probably combined with ICFM/FM mixing, seen in hysteresis loops.

2) ***The quadratic magnetic field dependence of  $T_{MI}$  at intermediate pressures is in agreement with the similar behaviors reported for other systems.*** An example is TTF-MBDT (M = Au and Cu), MEM (TCNQ)<sub>2</sub> or (PER)<sub>2</sub>M(mnt) (M = Pt and Au) as suggested by Bonfait *et al.* (1991). In the BaVS<sub>3</sub> family, ***the dependence is related to the SDW and/or CDW phase transition in the  $d_z^2$  band*** (0-1.7 GPa). The effects of the magnetic field on the MI transition in this pressure range are consistent with theoretical predictions for Peirels transitions by Tiedje *et al.* (1975), or Bray (1978).

3) ***The high pressure (around  $p_{cr}$ ) suppression of the MI transition with field*** and the enormous associated magnetoresistance is attributed to the ***collapse of the SDW or CDW 4V unit cell***. The low - temperature order (< 15 K, seemingly independent of pressure) is associated with the  $e_g$  electrons.

4) ***The negative magnetoresistance up to 8 T below 15K is related to the additional spin ordering of the  $e_g$  electrons by the increase of the magnetic field.*** This order is also seen as a shoulder in resistivity in temperature-dependent measurements.

## **5.7 References**

Anderson, P.W., 1997, *The Theory of Superconductivity in the High-T<sub>c</sub> Cuprates*, Princeton University Press, Princeton

Barišić S. and S. Brazovskii. 1981. Recent developments in condensed matter Physics, Plenum, ed. J.T. Devreese.

Barišić S., J. Labbe and J. Friedel. 1970. Tight binding and transition-metal superconductivity. *Phys. Rev. Lett.*, **25**(14), 919

Belitz D., and T. R. Kirkpatrick. 2002. Fluctuation – Driven quantum phase transitions in the clean itinerant ferromagnets. *Phys. Rev. Lett.* **89**, 247202.

Bhatt R. N. and D. S. Fisher. 1992. Absence of spin diffusion in most random lattices. *Phys. Rev. Lett.*, **68**(20), 3072-75

Bonfait G., E. B. Lopes, M. J. Matos, R. T. Henriques, and M. Almeida. 1991. Magnetic field dependence of the metal – insulator transition in (PER)<sub>2</sub>Pt(MNT) and (PER)<sub>2</sub>Au(MNT). *Solid State Comm.* **80**, 391.

Bray J. W. 1978. Magnetic field dependence of the spin – Peierls transition. *Solid State Comm.* **26**, 771.

Bulaevskii L. N., A. I. Buzdin and D. I. Khomskii. 1978. Spin-Peierls transition in magnetic-field. *Solid State Commun.*, **27**(1), 5-10

Bychkov Y. A., L. P. Gorkov and Dzyaloshinskii. 1966. Possibility of superconductivity type phenomena in a 1- dimensional system. *Soviet Physics JETP-USSR*, **23**(3), 489

Caron L. G., C. Bourbonnais, F. Creuzet and D. Jerome. 1987. Evolution of the spin peierls transition in the (TMTTF) 2AsF<sub>6</sub>,PF<sub>6</sub>,Br salts under pressure. *Synth. Met.*, **19**(1-3), 69-74

Chaddah P., S. B. Roy, S. Kumar and K. V. Bhagwat. 1992. Minor hysteresis loops and harmonic-generation calculations in a generalized critical-state model. *Phys. Rev.*

*B*, **46**(18), 11737-44

Coleman P. 1999. Theories of non-Fermi liquid behavior in heavy fermions. *Physica B*, **261**,353-58

Continentino M. A. 1993. Universal behavior in heavy fermions. *Phys. Rev. B*, **47**(17), 11587-90

Continentino M. A. 1996. On the zero temperature critical point in heavy fermions. *Z. Phys. B-Condens. Mat.*, **101**(2), 197-203

Continentino M. A., G. M. Japiassu and A. Troper. 1989. Critical approach to the coherence transition in kondo lattices. *Phys. Rev. B*, **39**(13), 9734-37

Cornelius A. L., A. K. Gangopadhyay, J. S. Schilling and W. Assmus. 1997. Hydrostatic high-pressure studies on the ferromagnetic kondo- lattice compounds CePdSb and CeAg to 16 GPa. *Phys. Rev. B*, **55**(21), 14109-12

Cross M. C. 1979. Effect of magnetic-fields on a spin-peierls transition. *Phys. Rev. B*, **20**(11), 4606-11

Cross M. C. and D. S. Fisher. 1979. New theory of the spin-Peierls transition with special relevance to the experiments on TTFCuDBT. *Phys. Rev. B*, **19**(1), 402-19

De Visser A., P. Estrela and T. Naka. 2002. High pressure transport study of non-Fermi liquid behaviour in  $U_2Pt_2In$  and  $U_3Ni_3Sn_4$ . *Int. J. Mod. Phys. B*, **16**(20-22), 2998-3003

Dobrosavljevic V., T. R. Kirkpatrick and G. Kotliar. 1992. Kondo effect in disordered-systems. *Phys. Rev. Lett.*, **69**(7), 1113-16

Doniach S. 1977. Kondo lattice and weak antiferromagnetism. *Physica B & C*, **91**(JUL), 231-34

Emery V. J. 1979. in *Highly conducting 1D solids*, Plenum, ed. J.T. Devreese et al.

Emery V. J., R. Bruinsma and S. Barisic. 1982. Electron-Electron umklapp scattering

---

---

in organic superconductors. *Phys. Rev. Lett.*, **48**(15), 1039-43

Estrela P., A. de Visser, F. R. de Boer, T. Naka and L. Shlyk. 2001. Recovery of the Fermi-liquid state in  $U_3Ni_3Sn_4$  by pressure. *Phys. Rev. B*, **63**21(21), 212409

Estrela P., A. de Visser, T. Naka, F. R. de Boer and L. C. J. Pereira. 2001. High-pressure study of the non-Fermi liquid material  $U_2Pt_2In$ . *Eur. Phys. J. B*, **23**(4), 449-54

Fabrizio, M., E. Tosatti, 2004, One-Dimensional Multi-Band Correlated Conductors and Anderson Impurity Physics, *cond-mat/0410728*

Fagot S., P. Foury-Leylekian, S. Ravy, J. P. Pouget, M. Anne, G. Popov, M. V. Lobanov and M. Greenblatt. 2004. Structural aspects of the metal-insulator transition in  $BaVS_3$ . *cond-mat*, 0410110

Fagot S., P. Foury-Leylekian, S. Ravy, J. P. Pouget and H. Berger. 2003. One-dimensional instability in  $BaVS_3$ . *Phys. Rev. Lett.*, **90**(19), 196401

Fazekas P. 1999. Lecture notes on electron correlation and magnetism. Singapore, World Scientific Publishing Co. Pte. Ltd.

Fisher M. E. 1967. Theory of equilibrium critical phenomena. *Rep. Prog. Phys.*, **30**(615)

Forró L. 1990. Pressure effect on the ohmic and non-linear transport of  $K_{0.3}MnO_3$ . *Solid State Comm.* **73**, 265.

Friedel J. 1969. Physics of Metals I. Electrons. J. M. Ziman, editor. Cambridge Univ. Press. UK. p.341.

Gabani S., E. Bauer, S. Berger, K. Flachbart, Y. Paderno, C. Paul, V. Pavlik and N. Shitsevalova. 2003. Pressure-induced Fermi-liquid behavior in the Kondo insulator  $SbB_6$ : Possible transition through a quantum critical point. *Phys. Rev. B*, **67**(17), 172406

Georges, A., G. Kotliar, W. Krauth, M.J. Rozenberg, 1996, Dynamical mean-field

---

---



theory of strongly correlated fermion systems and the limit of infinite dimensions, *Rev. Mod. Phys.* **68**,13

Giamarchi T. and A. J. Millis. 1992. Conductivity of A luttinger liquid. *Phys. Rev. B*, **46**(15), 9325-31

Gorkov L. P. and A. G. Lebed. 1995. Metal-Phase stability Of (TMTSF)<sub>2</sub>ClO<sub>4</sub> in high magnetic- fields, where TMTSF Is Tetramethyltetraselenafulvalene. *Phys. Rev. B*, **51**(5), 3285-88

Graf T., D. Mandrus, J. M. Lawrence, J. D. Thompson, P. C. Canfield, S. W. Cheong and L. W. Rupp. 1995. Suppression of the metal-to-insulator transition In BaVS<sub>3</sub> with pressure. *Phys. Rev. B*, **51**(4), 2037-44

Grilli M., B. G. Kotliar and A. J. Millis. 1990. Mean-Field Theories Of cuprate superconductors - A Systematic Analysis. *Phys. Rev. B*, **42**(1), 329-41

Hase M., I. Terasaki and K. Uchinokura. 1993. Observation of the Spin-Peierls transition in linear Cu<sup>2+</sup> (spin-1/2) chains in an inorganic compound CuGeO<sub>3</sub>. *Phys. Rev. Lett.*, **70**(23), 3651-54

Hertz J. A. 1976. Quantum critical phenomena. *Phys. Rev. B*, **14**(3), 1165-84

Higemoto W., A. Koda, G. Maruta, K. Nishiyama, H. Nakamura, S. Giri and M. Shiga. 2002. Muon spin relaxation study of magnetism of a triangular lattice BaVS<sub>3</sub>. *J. Phys. Soc. Jpn.*, **71**(10), 2361-64

Horovitz B. 1977. Peierls instability and superconductivity in quasi-one-dimensional conductors. *Phys. Rev. B*, **16**(9), 3943-54

Ioffe L. B. and A. J. Millis. 1995. Critical-Behavior of the uniform susceptibility of a Fermi- liquid near an antiferromagnetic transition with dynamic exponent  $z=2$ . *Phys. Rev. B*, **51**(22), 16151-58

Kadanoff L. P., W. Gotze, D. Hamblen, R. Hecht, E. A. S. Lewis, Palciaus.Vv, M. Rayl, J. Swift, D. Aspnes and J. Kane. 1967. Static phenomena near critical points - theory and experiment. *Rev. Mod. Phys.*, **39**(2), 395-&

Kasuya T. 1956. A Theory of metallic ferromagnetism and antiferromagnetism on Zener's model. *Prog. Theor. Phys.*, **16**(1), 45-57

Kelber J., A. H. Reis, A. T. Aldred, M. H. Mueller, O. Massenet, G. Depasquali and G. Stucky. 1979. Structural and magnetic-properties of one-dimensional barium vanadium triselenide. *J. Solid State Chem.*, **30**(3), 357-64

Kézsmárki I. 2003. Phase diagram of a correlated *d*-electron system: experimental study of BaVS<sub>3</sub>. Budapest, Hungary, BUTE.

Kittel C. 1953. Introduction to solid state physics. The University of California at Berkeley, Wiley.

Knebel G., D. Braithwaite, P. C. Canfield, G. Lapertot and J. Flouquet. 2002. Electronic properties of CeIn<sub>3</sub> under high pressure near the quantum critical point. *Phys. Rev. B*, **6502**(2), 024425

Koga A., N. Kawakami, T. M. Rice and M. Sigrist. 2004. Orbital-selective Mott transitions in the degenerate Hubbard model. *Phys. Rev. Lett.*, **92**(21), 216402

Landau L. D. and E. M. Lifshitz. 1980. Statistical Physics. Oxford, Reed.

Lechermann F., S. Biermann and A. Georges. 2004. Importance of inter-orbital charge transfers for the metal-to-insulator transition of BaVS<sub>3</sub>. *cond-mat*, 0409463

Lonzarich G. G. 1997. The electron. Cambridge/New York, Cambridge University Press.

Massenet O., R. Buder, J. J. Since, C. Schlenker, J. Mercier, J. Kelber and D. G. Stucky. 1978. BaVS<sub>3</sub>, A Quasi one dimensional ferromagnet or anti-ferromagnet depending on stoichiometry. *Mater. Res. Bull.*, **13**(3), 187-95

Mihaly G., I. Kezsmarki, F. Zamborszky, M. Miljak, K. Penc, P. Fazekas, H. Berger and L. Forro. 2000. Orbitally driven spin pairing in the three-dimensional nonmagnetic Mott insulator BaVS<sub>3</sub>: Evidence from single-crystal studies. *Phys. Rev. B*, **61**(12), R7831-R34

Millis A. J. 1993. Effect of a nonzero temperature on quantum critical-Points in itinerant fermion systems. *Phys. Rev. B*, **48**(10), 7183-96

Milosevic S. and H. E. Stanley. 1976. Local properties at phase transitions. North-Holland, Amsterdam.

Miranda E., V. Dobrosavljevic and G. Kotliar. 1997. Disorder-driven non-Fermi-liquid behavior in Kondo alloys. *Phys. Rev. Lett.*, **78**(2), 290-93

Moriya T. and T. Takimoto. 1995. Anomalous properties around magnetic instability in heavy- electron systems. *J. Phys. Soc. Jpn.*, **64**(3), 960-69

Mrkonjic I. and S. Barisic. 2003. Singular behavior of the emery model with O-O hopping for high- Tc superconductors. *Eur. Phys. J. B*, **34**(1), 69-84

Nakamura H., H. Imai and M. Shiga. 1997. Possible orbital ordering in a spin-singlet ground state: V-51 NMR and NQR study of BaVS<sub>3</sub>. *Phys. Rev. Lett.*, **79**(19), 3779-82

Nakamura H., H. Tanahashi, H. Imai, M. Shiga, K. Kojima, K. Kakurai and M. Nishi. 1999. Neutron scattering study of BaVS<sub>3</sub>: orbital-ordered spin-singlet system. *J. Phys. Chem. Solids*, **60**(8-9), 1137-40

Nakashima M., Y. Haga, F. Honda, T. Eto, G. Oomi, T. Kagayama, N. Takeshita, T. Nakanishi, N. Mori, D. Aoki, R. Settai and Y. Onuki. 2001. Non-Fermi-liquid behaviour around the magnetic quantum critical point in UGa<sub>3</sub>. *J. Phys.-Condes. Matter*, **13**(24), L569-L76

Northby J. A., H. A. Groenendijk, L. J. Dejongh, J. C. Bonner, I. S. Jacobs and L. V. Interrante. 1982. Field-Dependent differential susceptibility studies on Tetrathiafulvalene-AuS<sub>4</sub>C<sub>4</sub>(CF<sub>3</sub>) - universal aspects of the spin- Peierls phase-diagram. *Phys. Rev. B*, **25**(5), 3215-25

Peierls R. E. 1955. Quantum theory of solids. Oxford, Oxford Univ. Press.

Pytte E. 1974. Peierls instability in Heisenberg chains. *Phys. Rev. B*, **10**(11), 4637-42

Riera J. and D. Poilblanc. 2000. Coexistence of charge-density waves, bond-order

---

---

waves, and spin-density waves in quasi-one-dimensional charge-transfer salts. *Phys. Rev. B*, **62**(24), R16243-R46

Rosch A. 1999. Interplay of disorder and spin fluctuations in the resistivity near a quantum critical point. *Phys. Rev. Lett.*, **82**(21), 4280-83

Rosch A. 2000. Magnetotransport in nearly antiferromagnetic metals. *Phys. Rev. B*, **62**(8), 4945-62

Ruderman M. A. and C. Kittel. 1954. Indirect exchange coupling of nuclear magnetic moments by conduction electrons. *Physical Review*, **96**(1), 99-102

Sachdev S. 1999. Quantum phase transitions. Cambridge, England, Cambridge University Press.

Schlottmann P. 1989. Some exact results for dilute mixed-valent and heavy-fermion systems. *Phys. Rep.-Rev. Sec. Phys. Lett.*, **181**(1-2), 1-119

Singh K. J., S. Chaudhary, M. K. Chattopadhyay, M. A. Manekar, S. B. Roy and P. Chaddah. 2002. First-order transition from ferromagnetism to antiferromagnetism in Ce(Fe<sub>0.96</sub>Al<sub>0.04</sub>)<sub>2</sub>: A magnetotransport study. *Phys. Rev. B*, **65**(9), 094419

Solyom J. 1979. Fermi gas-model of one-dimensional conductors. *Adv. Phys.*, **28**(2), 201-303

Stanley H. E. 1999. Scaling, universality, and renormalization: Three pillars of modern critical phenomena. *Rev. Mod. Phys.*, **71**(2), S358-S66

Stearns M. B. and S. S. Wilson. 1964. Measurements of conduction-electron spin-density oscillations in ferromagnetic alloys. *Phys. Rev. Lett.*, **13**(9), 313

Stewart G. R. 2001. Non-Fermi-Liquid behavior in *d*- and *f*-electron metals *Rev. Mod. Phys.* **74**(4), 797

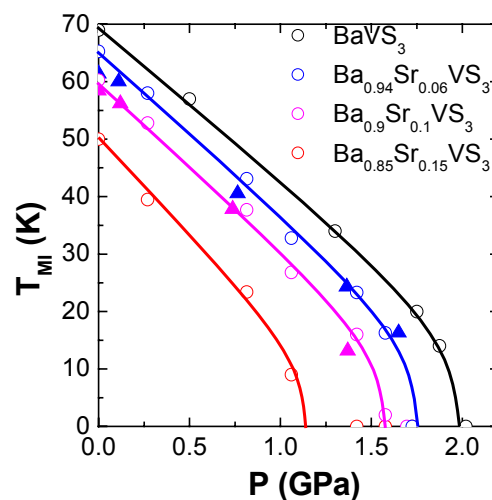
Tiedje T., J. F. Carolan, A. J. Berlinsky, and L. Weiler. 1975. Magnetoresistance of TTF-TCNQ. *Can. J. Phys.*, **53**, 1593.

Yamasaki T., H. Nakamura and M. Shiga. 2000. Ferromagnetism of sulfur deficient BaVS<sub>3</sub>-delta. *J. Phys. Soc. Jpn.*, **69**(9), 3068-71

Yosida K. 1957. Magnetic properties of Cu-Mn alloys. *Physical Review*, **106**(5), 893-98

## Chapter 6

# CHEMICAL PRESSURE



<b>6.1</b>	<b>CHEMICAL PRESSURE: THE CONCEPT</b>	<b>138</b>
<b>6.2</b>	<b>Ba-Sr ISOVALENT SUBSTITUTION</b>	<b>140</b>
6.2.1	RESISTIVITY UNDER PRESSURE	141
6.2.2	MAGNETIC PROPERTIES	144
6.2.3	IMPLICATIONS	146
<b>6.3</b>	<b>S-Se ISOVALENT SUBSTITUTION</b>	<b>148</b>
6.3.1	PREVIOUS STUDIES	148
6.3.2	TRANSPORT PROPERTIES OF BaVSe <sub>3</sub>	149
<b>6.4</b>	<b>CONCLUDING REMARKS</b>	<b>151</b>
<b>6.5</b>	<b>REFERENCES</b>	<b>152</b>

In this chapter we see how various types of isovalent chemical substitution manifest themselves as a chemical-pressure effect. This phenomenon thus provides a tool with which we can manipulate the accessible range of the  $p$ - $T$  phase diagram.

## 6.1 *Chemical pressure: The concept*

We have seen in the previous chapter that by changing the hydrostatic pressure, we are able to vary the relative atomic coordinates and hence modify parameters of the material such as the inter-ionic distances (through compression) or bond angles (through torsion). Such changes impact the properties of the material, in the first instance, by affecting the overlap integrals. In  $\text{BaVS}_3$ , we were able to attribute the manifestation of this effect to the increase in the effective dimensionality of the system under pressure resulting in imperfect nesting of the Fermi surface. Consequently, at high enough pressures (above  $p_{cr}$ ) the metal-insulator transition is completely suppressed and the physical properties of the system are changed dramatically.

An alternative means by which the inter-site distances can be modified is isovalent substitution, which results in the so-called “chemical pressure” effect. This is the subject of the present chapter. The effect is already well known in, for instance, materials such as organic conductors (Yoshino *et al.*, 2003), superconductors (Licci *et al.*, 1998), and manganites (Subramanian *et al.*, 1999). This approach is convenient since it often allows the measurement of the relevant physical properties at ambient pressure. However, changing the chemical composition of the material inevitably introduces a random element into the analysis. This is in contrast with variations in the hydrostatic pressure, which impact only the lattice structure, and hence constitute a “clean”, more controlled perturbation.

Despite the “unclean” nature of chemical substitution, we have already seen how the investigation of impure, sulfur-deficient, samples of  $\text{BaVS}_3$  can give precious information about the physical properties of this system. For instance, we have exploited the results of measurements on the impure samples to better understand the SDW and/or the CDW origin of the MI transition. In these discussions we were not able to unambiguously distinguish between those effects arising from the sulfur deficiency and other types of disorder. Therefore, we can use the chemical substitution to our advantage in two distinct ways. Firstly, we can manipulate the *chemical pressure* so as to ***bring the system to the desired place of the pressure phase*** diagram and thus measure the properties of the system with ambient pressure experimental setups. Secondly, we can confidently ***investigate the impact of other defects*** by separating them from the sulfur deficiency effects.

The low energy physics of  $\text{BaVS}_3$  is related to the one vanadium electron shared

---

between the vanadium  $t_{2g}$  bands. The shape of these bands (particularly important around Fermi level) is determined by the crystal field and the overlaps between the ions (as shown in Chapter 3). Therefore, it is of interest to substitute either the barium or sulfur atoms and thereby change the surrounding of the vanadium atoms. These substitutions modify the overlap integrals and hence the effective dimensionality of the system. In this section we present the results of two different types of substitutions. The first concerns the effect of partial substitution of Ba by Sr in a series of compounds with structural formulae of the type  $\text{Ba}_{1-x}\text{Sr}_x\text{VS}_3$ . In the second type of substitution, S is entirely replaced by Se and the measurements are performed upon  $\text{BaVSe}_3$ .

---

---



## 6.2 Ba-Sr isovalent substitution

$\text{Ba}_{1-x}\text{Sr}_x\text{VS}_3$  single crystals with nominal compositions  $x_n = 0.15, 0.30, 0.50,$  and  $0.70$  were grown with a standard solid state synthesis method (Gauzzi *et al.*, 2003). Stoichiometric powders of metallic V, BaS, and S were ground, intimately mixed for various times, and pressed into pellets. The pellets were then placed in sealed quartz tubes at  $950^\circ\text{C}$  for 72 hours. This procedure yielded needle shaped single crystals of 0.1 - 0.3 mm in length, aligned along the  $c$  axis, as shown by optical microscopy. Hereafter such samples will be referred to as grown samples. The room temperature crystal structure, the Sr/Ba cation composition, and the sulfur content were refined by means of X - ray diffraction using a Philips PW 1100 single crystal diffractometer equipped with graphite monochromatized Mo  $K_\alpha$  radiation. This analysis confirmed that, at high  $T$ , all Sr - substituted crystals investigated herein were in possession of a hexagonal structure of the  $\text{CsCoCl}_3$  type with the same  $P6_3/m2/m2/c$  space group as the clean  $\text{BaVS}_3$  phase. Attempts to grow unsubstituted or fully substituted crystals using the above method were unsuccessful.

**Table 6.1:** Selected structural parameters and magnetic transition temperatures of the studied crystals. The data regarding the unsubstituted  $\text{BaVS}_3$  samples are averages of values taken from literature (Gardner *et al.* (1969), Massenet *et. al* (1978)). Below  $T_x$ , the order in the V-chains is FM in all samples but the inter-chain order changes from the Inter-chain Compensated FM (ICFM) to FM as  $x$  is increased.

Sr content $x$	0.0	0.06	0.10	0.13	0.18
nominal Sr content $x$	0.0	0.15	0.30	0.50	0.70
cell volume [ $\text{\AA}^3$ ]	219.972	219.932	218.538	217.329	216.862
$a$ [ $\text{\AA}$ ]	6.721	6.718	6.717	6.699	6.693
$c$ [ $\text{\AA}$ ]	5.623	5.633	5.593	5.592	5.590
S coordinate $x/a$	0.1656	0.16544	0.16525	0.1657	0.16616
V - S distance [ $\text{\AA}$ ]	2.385	2.385	2.377	2.380	2.380
$T_x$	30	6	12.5	20.0	21.5
Order below $T_x$	ICFM	ICFM	FM	FM	FM

In Table 6.1, we report a summary of selected structural data on the single crystals studied here. It is apparent that the actual Sr concentration in the samples is much smaller than the nominal one. The maximum Sr content obtained is  $x = 0.18$  for  $x_n = 0.70$ . As for the variations of the lattice parameters, one notes that the smaller Sr cation induces a sizeable shrinking of the unit cell, as expected. The shrinking effect is anisotropic in that it first takes place along the  $c$  - axis and then subsequently in the  $ab$  - plane.

The study of the obtained crystals by means of resistivity under pressure, d.c. magnetization measurements, and anisotropy measurements of the magnetic susceptibility, are still in progress but the salient features of the principal results are already in sight and are therefore presented below.

### 6.2.1 *Resistivity under pressure*

The resistivity under variable pressures of up to 2 GPa was measured on the samples with Sr content  $x = 0.06, 0.1, 0.15$  and  $0.18$ . The needle – shaped crystals grow along the  $c$  – axis and therefore the resistivity was measured along this longest (0.1 - 0.3 mm) axis. The samples with a Sr concentration of 0.18 are not included in the discussion since they exhibit a very broad MI transition and their residual resistivity ratio (RRR), defined as  $R(300\text{K})/R(T \rightarrow 0\text{K})$ , at 2 GPa is less than 2, indicating the high disorder in the samples. On the other hand, the other samples have a well defined MI transition with the RRR around 10 which is comparable to the impure  $\text{BaVS}_3$  samples. A typical result of the resistivity measurement under pressure of the Sr-substituted samples is shown in Fig. 6.1. The results shown therein correspond to the sample with the highest concentration of Sr ( $x = 0.15$ ) and the lowest RRR, among those discussed. Despite the high Sr content, this sample still exhibits a well defined  $T_{\text{MI}}$ , as determined from the peak in the  $d(\ln R)/d(1/T)$  vs.  $1/T$  plot.

In a manner reminiscent of the unsubstituted samples ( $x = 0$ , Chapter 4 and Chapter 5), we observe a metallic behavior in this material at high temperatures (Fig. 6.1a). There is no sign of the saturation of resistivity at low temperatures and low pressures (Fig. 6.1b). The MI transition is progressively suppressed (to lower temperatures) by increasing pressure and, finally, the resistivity follows a power law temperature dependence for low temperatures and sufficiently high pressures (above  $p_{cr}$ ). To ensure that the observed effects are not related to the off-stoichiometry of sulfur in

---

---

the grown samples, one sample, of the two that were measured from each batch, was additionally enriched by sulfur (sealed in the quartz tube and reheated in the presence of S).

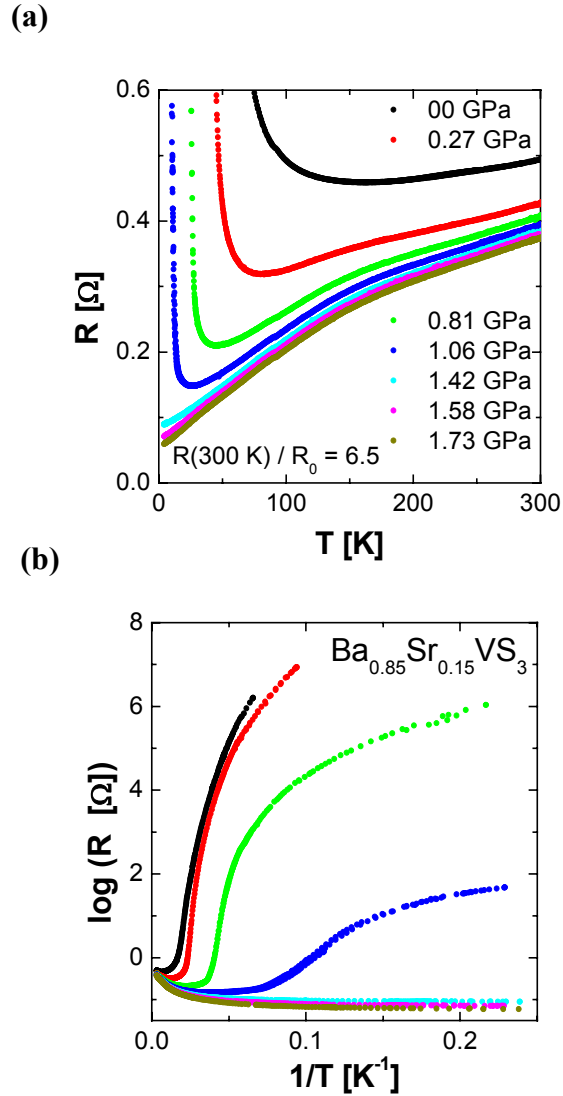


**Figure 6.1:** The results of the resistance measurements on  $\text{Ba}_{0.85}\text{Sr}_{0.15}\text{VS}_3$  under pressure presented. **(a)** Resistance as a function temperature of reveals (i) the metallic behaviour at high temperatures, and (ii) the low temperature power law dependence for pressures above 1.42 GPa. **(b)** Logarithm of the resistance as a function of the inverse temperature demonstrates that there is no sign of the saturation of resistance at 1 bar and low temperatures, and that the MI transition is sharp.

The results of the suppression of the MI transition, for different Sr concentrations and sulfur treatments, are summarized in the pressure – temperature ( $p$ – $T$ ) phase diagram in Fig. 6.2. **Both samples** of the same batch **exhibit an identical pressure dependence**. This result can be interpreted to mean that either the grown samples

possess a good sulfur stoichiometry or that *the  $T_{MI}$  is insensitive to the small sulfur deficiency*. In this context, it should be noted that all BaVS<sub>3</sub> samples, with an RRR > 5 at 2 GPa, show a  $T_{MI} \sim 70$  K with identical pressure dependencies. This suggests that the MI transition temperature is relatively unaffected by defects or small sulfur deficiency. Therefore, it can be safely concluded that the *Sr substitution* is responsible for the observed manifestation of the *chemical pressure in the crystal*.

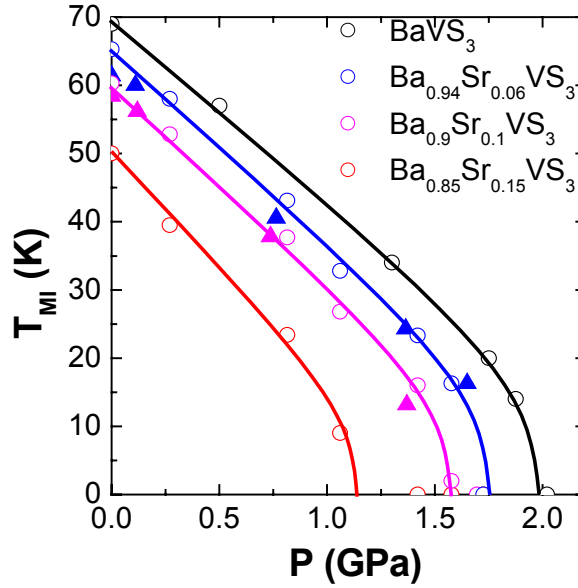


**Figure 6.2:** MI phase boundary as a function of pressure for four different concentrations of Sr. The lines are a guides for the eye. Samples from the same batch are marked by the identically colored open circles and full triangles. The former was additionally sulfur treated.

The effect of the suppression of  $T_{MI}$  with increasing  $x$  is monotonic at all measured pressures, as shown in Fig. 6.3. This suggests that, at least in terms of this property, the chemical pressure may simply be regarded as an addition to the hydrostatic pressure. By comparing the chemically induced suppression of  $T_{MI}$  at ambient pressure to the suppression of the MI transition by hydrostatic pressure (in BaVS<sub>3</sub> samples) the content of Sr can be approximately expressed as an equivalent pressure:

$$p_{chemical} [GPa] = \frac{0.45 [GPa]}{0.1 [\%]} \cdot x [\%] . \quad (6.1)$$

This relation predicts a complete suppression of the MI transition around 1.3 GPa in the sample with  $x = 0.15$  which is comparable with the value of 1.15 GPa determined from the resistance measurement under pressure.

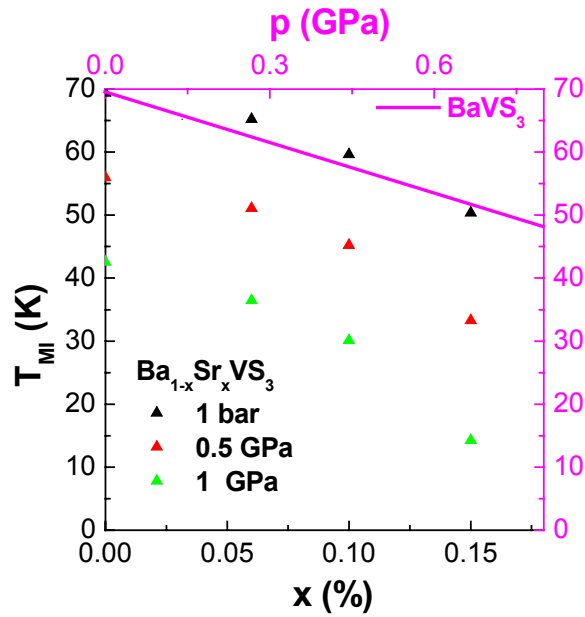


**Figure 6.3:** The MI transition temperature as a function of Sr content  $x$  (bottom scale) at several pressures (1bar, 0.5 and 1 GPa, marked by black, red, and green triangles respectively). At the ambient pressure, the suppression of the MI transition by chemical pressure (black triangles) is compared with the effect of the hydrostatic pressure (pink scale), indicated by the pink line.

The shift of the MI transition to lower temperatures with increase of the Sr content in  $\text{Ba}_{1-x}\text{Sr}_x\text{VS}_3$  can be interpreted by taking into account the structural parameters from Table 6.1. One notes that the lattice parameter  $a$ , directly related to the inter-chain distance, scales with  $T_{MI}$ . Its decrease, with **increasing  $x$** , presumably **augments the effective dimensionality of the system** towards the more isotropic case. Therefore the MI transition temperature is shifted to lower values in response to an increase in Sr content in a similar fashion as that observed case of hydrostatic pressure. These observations provide support for the SDW-CDW scenario proposed in Chapter 5.

### 6.2.2 Magnetic properties

The study of the magnetic properties of the Sr-substituted samples, by means of magnetization and susceptibility measurements, are in progress. Already the first results show interesting features and are therefore presented below. Before presenting these results, we should recollect that the deficiency of sulfur in the  $\text{BaVS}_3$  samples changes the nature of the magnetic inter-chain correlations resulting in a full ferromagnetic order below  $T_x$  (as discussed in Chapter 1 and Chapter 3). For this reason, it is very important to distinguish the grown samples from those additionally enriched with sulfur.

The magnetization measurements were performed on the grown samples, in the 5-300 K range, using a commercial RF SQUID apparatus. Each sample has been studied in the usual zero - field cooling (ZFC) and field - cooling (FC) modes by applying an external field of 10 Gauss. In Fig. 6.4, as an example, we show the magnetization curves of the heavily substituted ( $x = 0.18$ ) sample indicating a clear ferromagnetic transition at 21.5 K. Measurements were repeated at all other available concentrations of Sr and the results are listed in Table 6.1. As the substitution level  $x$  progressively increases, the Interchain Compensated FM (ICFM) ordering temperature ( $T_x$ ) is progressively decreased and the ICFM order is replaced by FM, at which point the ordering temperature begins to increase with increasing  $x$ .

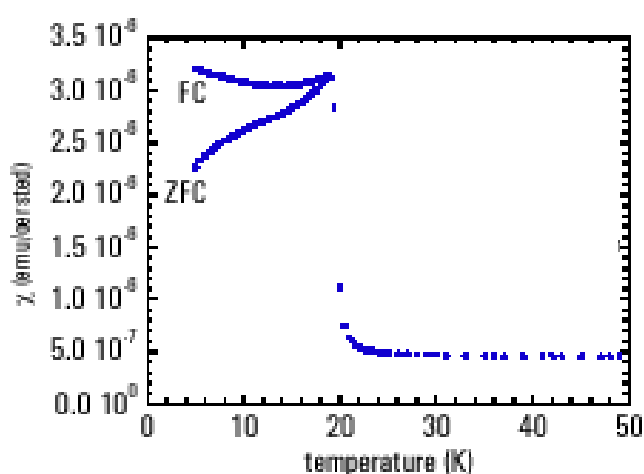


**Figure 6.4:** Zero – field cooled and the field cooled magnetization measurement performed with a field of 10 Gauss along the  $c$  - axis on the as grown  $x = 0.18$  sample. The sample shows a ferromagnetic transition at 21.5 K.

The fact that the FM order develops at the low temperature and high concentration of Sr is also evident from the anisotropy magnetic susceptibility measurement, carried out on a sensitive torque magnetometer (Miljak, private communication), shown in Fig. 6.5. At temperatures around 23 K, a strong change of anisotropy is observed which indicates that the system starts to develop the ferromagnetic order. The measured sample was the very same sulfur-treated single crystal of  $\text{Ba}_{0.85}\text{Sr}_{0.15}\text{VS}_3$  studied by the pressure-dependent resistance measurements shown in Fig. 6.1. It is apparent from these measurements that the resistivity shoulder, that could be expected to coincide with the FM transition, is not observed. The most plausible explanation for its absence is that it is smeared out by disorder.

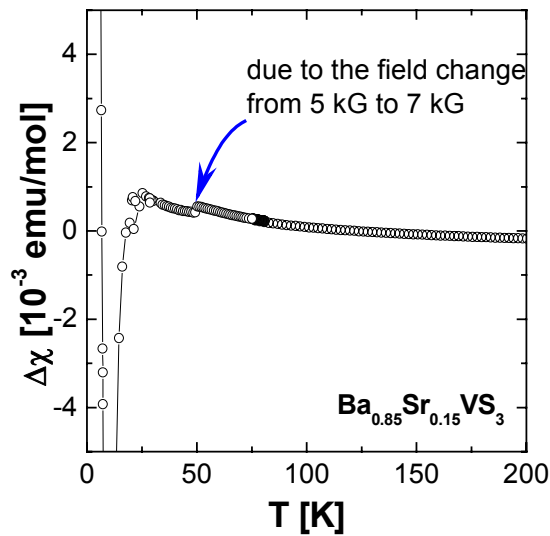


**Figure 6.5:** Temperature dependence of the spin susceptibility anisotropy for the  $\text{Ba}_{0.85}\text{Sr}_{0.15}\text{VS}_3$ . The kink around 50 K, marked by the blue arrow, is an artefact due to the change of the magnetic field from 5 to 7 kG.

### 6.2.3 Implications

As mentioned above, the resistivities of the  $\text{Ba}_{1-x}\text{Sr}_x\text{VS}_3$  samples under pressure have all the typical features of the  $\text{BaVS}_3$  samples (provided the RRRs (2GPa) of the former are larger than 5). The slight difference observed upon Sr substitution is that the chemical pressure shifts the MI phase boundary along the  $p$  axis of the  $p$ - $T$  phase diagram, according to Eq. (6.1). On the contrary, the result for the **susceptibility anisotropy** for the Sr-substituted samples **is qualitatively different** from that reported by Mihály *et al.* (2000) for the pure  $\text{BaVS}_3$  single crystal. At the MI transition, there is no sign of a sudden break in the susceptibility anisotropy. Instead the behavior **remains Curie like down to 23 K**, where the FM order sets in.

It is interesting to consider the above susceptibility results in the context of the SDW/CDW scenario, for the MI transition in  $\text{BaVS}_3$ , proposed in the previous chapter, In the pure sample, the transition was associated with the SDW in the  $d_z^2$  band (to which the  $e_g$  electrons couple magnetically, causing the steep decrease in the overall susceptibility below  $T_{MI}$ ) while in the impure samples, it is expected to be the CDW transition (with no significant consequences on susceptibility, as it is indeed observed in the case of the  $\text{Ba}_{0.85}\text{Sr}_{0.15}\text{VS}_3$  sample). In addition, it should be noted that, in this respect, the disappearance of SDW does not have an important impact on

the MI transition temperature.

Despite the above presented efforts to clarify experimentally the origin of the magnetic order at  $T_x$  it is still hard to be entirely conclusive. Additional measurements of magnetic properties on sulfur treated and untreated  $\text{Ba}_{1-x}\text{Sr}_x\text{VS}_3$  compounds as well as sulfur deficient  $\text{BaVS}_{3-\delta}$  samples, combined with the other (*e.g.* resistivity) measurements, should be performed. This would help to understand whether the two magnetic orders below  $T_x$  are related to the SDW or the CDW nature of the MI transition or not. If these two transitions do turn out to be unrelated, it would assist in the separation of effects such as sulfur deficiency, other defects, chemical and hydrostatic pressure on the magnetic properties of the system.

---

---



### 6.3 *S-Se isovalent substitution*

Another system which can help us to understand the properties of BaVS<sub>3</sub> is the triply substituted BaVSe<sub>3</sub>. In contrast, to the Ba<sub>1-x</sub>Sr<sub>x</sub>VS<sub>3</sub> samples, where a fraction of the inter-chain Ba ion are exchanged with the smaller Sr, causing the chemical pressure, this system involves the complete replacement of the ligand sulfur ions by the larger, isovalent, ions of selenium.

#### 6.3.1 *Previous studies*

Kelber and his co-workers first reported the synthesis of single crystals BaVSe<sub>3</sub> (Kelber *et al.*, 1979). They solved its crystal structure at 283 K in the hexagonal space group *P6<sub>3</sub>/mmc* (identical to the one of BaVS<sub>3</sub>), with  $a = 6.9990 \text{ \AA}$  and  $c = 5.8621 \text{ \AA}$ . From the scans ( $2\Theta$ ) of a polycrystalline sample it was concluded that the BaVSe<sub>3</sub> undergoes a structural transition to an orthorhombic unit cell ( $b' \approx 3^{1/2} a$ ,  $a' \approx a$ ,  $c' = c$ ) at 303 K (in BaVS<sub>3</sub> at ambient pressure the structural phase transition occurs at 240 K, and with increasing the pressure it shifts to higher temperatures). Reported magnetic susceptibility measurements, between 4 and 300 K, indicate that BaVSe<sub>3</sub> is ***paramagnetic down to 41 K, where ferromagnetic ordering takes place***, with a magnetic moment in the ordered phase of  $0.2 \mu_B$  per vanadium atom.

**Table 6.2:** Selected structural parameters and magnetic transition temperatures of the reported polycrystals (Kelber *et al.*, 1979).

Se content	BaVS <sub>3</sub>	BaVS <sub>2</sub> Se	BaVS <sub>1</sub> Se <sub>2</sub>	BaVSe <sub>3</sub>
cell volume [ $\text{\AA}^3$ ]	218.905	227.962	237.043	248.084
$a$ [ $\text{\AA}$ ]	6.7065	6.8015	6.8906	6.9924
$c$ [ $\text{\AA}$ ]	5.6200	5.6901	5.7647	5.8588
S/Se coordinate $x/a$	0.1641	0.1686	0.1669	0.1678
$T_x$	23	40	45	47

An extensive study on the impact of Se substitution in polycrystalline BaVS<sub>3-x</sub>Se<sub>x</sub> was carried out by Poulsen (1998). Several different concentrations corresponding to  $x = 0, 1, 2, 3$  were synthesized and a detailed structural analysis was reported. Selected

structural parameters are shown in Table 6.2. The lattice parameters vary almost linearly with the increase of  $x$ . No change of lattice symmetry at room temperature was observed; therefore the enlargement of the unit cell is attributed to the larger size of Se, as compared to S. All samples are paramagnetic at high temperatures and ferromagnetic at low temperatures. The FM transition temperature  $T_x$  increases with the increase of the quantity of Se in the compound. Neither the role nor the quantity of disorder in the samples was commented upon by the authors of this work but the ferromagnetic order observed in the  $x = 0$  sample (BaVS<sub>3</sub>) indicates that the quality of the measured samples was rather poor.

### 6.3.2 *Transport properties of BaVSe<sub>3</sub>*

Here we report the results of resistivity and thermoelectric power measurements on polycrystalline BaVSe<sub>3</sub> under pressures of up to 2 GPa.. The results of these measurements are summarized in Fig 6. The resistivity has a metallic behavior in the whole measured temperature range (4 to 300 K). At the temperature of 40 K at which the magnetic susceptibility indicates a ferromagnetic order, a kink is visible in resistivity. The intercept due to the grain boundaries is decreased as the pressure is augmented. Similar features are also observed in the thermoelectric power except that latter transport coefficient is insensitive to the grain boundaries. The observed linear temperature dependence of thermoelectric power is a characteristic of metals. The low temperature hump is attributed to phonon drag, as discussed in Chapter 7. A small kink is also observed in the thermoelectric power at the temperature at which ferromagnetic order sets in. It should be noted that the thermoelectric power of BaVSe<sub>3</sub> is almost pressure independent and exhibits a negative sign which is a characteristic of a metal with dominantly electron-like charge carriers. However, the absolute value of the thermoelectric power at  $T=300$  K ( $S \approx 35 \mu\text{V/K}$ ) is one order of magnitude higher than that usually found in ordinary metals (around  $2 \mu\text{V/K}$ ).

The main reason for our interest in the measurements on BaVSe<sub>3</sub> is derived from their striking resemblance to the curves recorded at 2.7 GPa, in the Fermi liquid phase of BaVS<sub>3</sub>, discussed in more detail in Chapter 7. This resemblance suggests that the isovalent substitution of S by Se can also be regarded as a chemical pressure. The bigger Se ion decreases the direct overlap of V ions along the  $c$  axis by increasing their mutual distance. At the same time, however, the ligand-mediated overlap

---

---

between chains is increased. Therefore the system becomes more 3D and consequently never undergoes the MI transition, having at 1 bar properties similar to those of  $\text{BaVS}_3$  at 2.7 GPa.

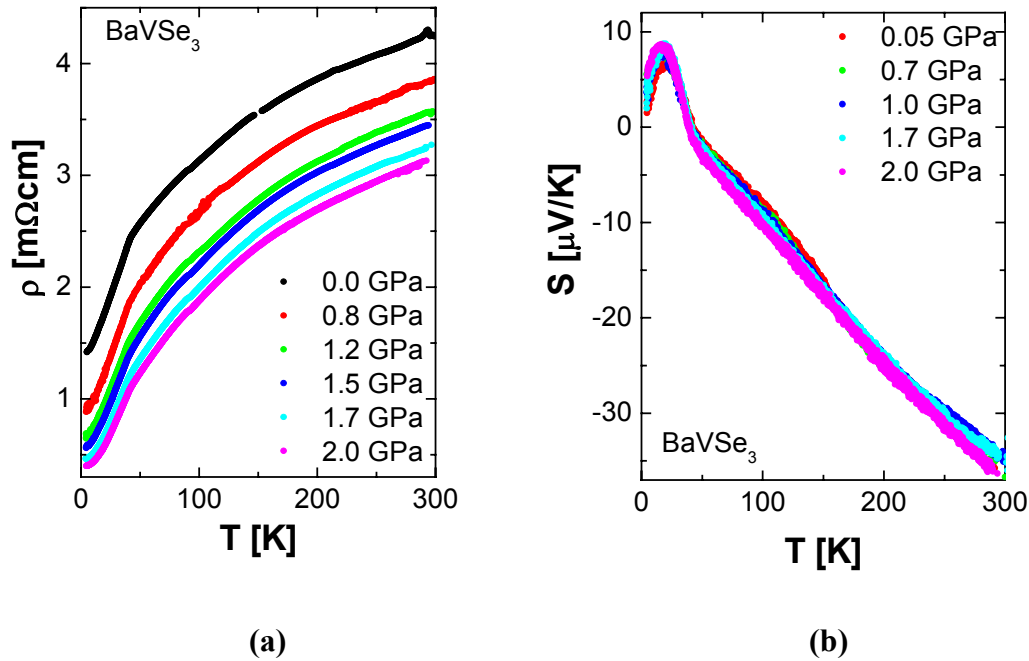


**Figure 6.6:** (a) Resistivity and (b) thermoelectric power of  $\text{BaVSe}_3$  in the temperature range 4 – 300 K, under pressures up to 2 GPa.

It should be noted that the pure  $\text{BaVSe}_3$  does not have substitutional disorder, which renders additional confidence to the reported results. The 1 bar measurements of magnetic susceptibility performed on  $\text{BaVSe}_3$  by the standard method, revealed the ferromagnetic order below 40 K. This implies that the FM order found along the V-chains at ambient pressure below 30 K in  $\text{BaVS}_3$  is a good candidate for explaining the shoulder in resistivity observed above  $p_{cr}$  at 15 K.

## **6.4 Concluding Remarks**

In summary, the results presented in this chapter strongly support the fact that substitution by both Sr and Se results in a chemical pressure effect. We have used these results to infer several important facts about the unsubstituted material that is the major focus of the present study, BaVS<sub>3</sub>. Firstly, different measurements on the Sr-substituted samples combine to show that the MI transition is not necessarily accompanied by a change in the magnetic properties of the system. Such a conclusion is supportive of the basic SDW-CDW scenario proposed in Chapter 5. Secondly, the magnetization measurements on the Se-substituted samples identify the FM along the V-chains (with an unspecified inter-chain ordering) as the best candidate for the possible magnetic behavior of BaVS<sub>3</sub> at high pressures, in the absence of direct experimental evidence.

Another interesting aspect of the measurements on BaVSe<sub>3</sub> is the behavior of the thermoelectric power (TEP) at ambient pressure. As will become apparent during the course of the subsequent chapter, the behavior of TEP under different conditions can be used to uncover many interesting properties of BaVS<sub>3</sub>. For example, it will be shown that the temperature dependence of the latter compound's TEP is profoundly different above and below  $p_{cr}$ . Importantly, as alluded to above, the behavior of the TEP in BaVSe<sub>3</sub> at ambient pressure closely resembles that of BaVS<sub>3</sub> above  $p_{cr}$ . This can be taken as proof of the ability of chemical substitution to advantageously influence the position of the system on the pressure phase diagram.

---

---

## 6.5 References

Gardner R. A., M. Vlasse, and A. Wold. 1969. Preparation, properties and crystal structure of barium vanadium sulfide. *Acta Cryst. B*, **25**, 781.

Gauzzi A., F. Licci, N. Barisic, G. L. Calestani, F. Bolzoni, E. Gilioli, M. Marezio, A. Sanna, C. Franchini and L. Forro. 2003. Chemical pressure-induced ferromagnetism and stabilization of the metallic state in  $\text{Ba}_{1-x}\text{Sr}_x\text{VS}_3$ . *Int. J. Mod. Phys. B*, **17**(18-20), 3503-08

Kelber J., A. H. Reis, A. T. Aldred, M. H. Mueller, O. Massenet, G. Depasquali and G. Stucky. 1979. Structural and magnetic-properties of one-dimensional barium vanadium triselenide. *J. Solid State Chem.*, **30**(3), 357-64

Licci F., A. Gauzzi, M. Marezio, G. P. Radaelli, R. Masini and C. Chailout-Bougerol. 1998. Structural and electronic effects of Sr substitution for Ba in  $\text{Y}(\text{Ba}_{1-x}\text{Sr}_x)(2)\text{Cu}_3\text{O}_w$  at varying w. *Phys. Rev. B*, **58**(22), 15208-17

Massenet O., R. Buder, J. J. Since, C. Schlenker, J. Mercier, J. Kelber, and D. G. Stucky. 1978.  $\text{BaVS}_3$ , a quasi one dimensional ferromagnet of antiferromagnet depending on stoichiometry. *Mat. Res. Bull.*, **13**(3), 187.

Mihály G., I. Kézsmárki and F. Zámorszky, M. Miljak, K. Penc, P. Fazekas, H. Berger, and L. Forró. 2000. Orbitaly driven spin pairing in the three-dimensional nonmagnetic Mott insulator  $\text{BaVS}_3$ : Evidence from single-crystal studies. *Phys. Rev. B* **61**, R7831.

Miljak M., *private communication*.

Poulsen N. J. 1998. Crystal structure, magnetic susceptibility, and electric resistivity of polycrystalline  $\text{Ba}_{1-x}\text{K}_x\text{VS}_{3-\delta}$ ,  $\text{Ba}_{1-x}\text{K}_x\text{VSe}_{3-\delta}$ , and  $\text{BaV}(\text{S},\text{Se})_3$  synthesized under high pressure. *Solid State Ionics*, **108**(1-4), 209-20

Poulsen N. J. 1998. Rietveld refinement and magnetic properties of polycrystalline  $(\text{Ba},\text{K})\text{VSe}_3$  and  $\text{BaV}(\text{S},\text{Se})(3)$ . *Mat. Res. Bul.*, **33**(2), 313-22

---

---

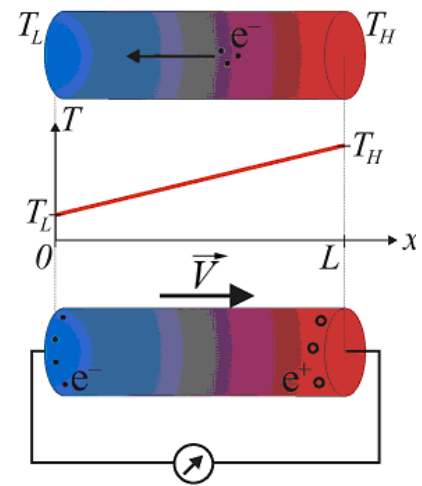
Subramanian M. A., A. P. Ramirez and W. J. Marshall. 1999. Structural tuning of ferromagnetism in a 3D cuprate perovskite. *Phys. Rev. Lett.*, **82**(7), 1558-61

Yoshino H., K. Murata, K. Saito, H. Nishikawa, K. Kikuchi and I. Ikemoto. 2003. Chemical pressure effect on bandwidth and dimensionality of quasi-one-dimensional organic conductors: (DMET)(2)X [X = Au(CN)(2), AuI<sub>2</sub>, AuCl<sub>2</sub>, IBr<sub>2</sub>, I<sub>3</sub>, AuBr<sub>2</sub>, and SCN]. *Phys. Rev. B*, **67**(3), art. no.-035111



## Chapter 7

# THERMOELECTRIC POWER OF $\text{BaVS}_3$ UNDER PRESSURE



<b>7.1</b>	<b>THERMOELECTRIC POWER</b>	<b>156</b>
<b>7.2</b>	<b>THE CASE OF <math>\text{BaVS}_3</math></b>	<b>158</b>
7.2.1	MAIN FEATURES OF TEP BELOW $p_{cr}$ AND ABOVE $T_{MI}$	159
7.2.2	FINE FEATURES OF TEP - MAGNETO-TEP	161
7.2.3	MAIN FEATURES OF TEP ABOVE $p_{cr}$	165
<b>7.3</b>	<b>CONCLUDING REMARKS</b>	<b>167</b>
<b>7.4</b>	<b>REFERENCES</b>	<b>169</b>

In this chapter we see how the measurement of a different transport property (thermoelectric power) can give us an alternative window through which to view the narrow energy range around the Fermi level.



## 7.1 Thermoelectric power

The thermoelectric power (TEP), also known as the Seebeck coefficient, is another transport coefficient which, in addition to the resistivity discussed in Chapters 4-6, provides information about the behavior of the conduction electrons in the narrow energy window of the order 0.01 eV ( $\sim 100$  K) around the Fermi level. The simplest means by which one can conceptually grasp TEP is to consider it as the ratio of the electronic heat current to the charge current divided by temperature. Its magnitude and temperature dependence tell us whether we are dealing with metallic or non-metallic materials. In addition, TEP can reveal correlation effects, the peculiarity of scattering events, polaron formations, and many other related properties.

For example, in the case of metals, assuming that the band electrons carry the charge as well as all of the heat current, the Boltzmann transport theory leads to Mott's well-known expression for the Seebeck coefficient (Dugdale, 1977):

$$S_{Mott} = \frac{\pi^2 k_B^2 T}{3e} \left( \frac{\partial \ln \sigma(E)}{\partial E} \right)_{E=E_F} \quad (7.1)$$

where  $\sigma(E)$  is the electrical d.c. conductivity of the fermions characterized by the chemical potential  $E=E_F$  and the partial derivative with respect to  $E$  is taken with all other (*e.g.* band) parameters in  $\sigma$  constant. On the other hand, for semiconductors with the charge gap  $\Delta_{ch}$  the expression for the Seebeck coefficient takes the following form:

$$S = \frac{k_B}{e} \frac{\Delta_{ch}}{2k_B T} \quad (7.2)$$

If the carriers belong to different bands, as seems to be the case in BaVS<sub>3</sub>, the resulting signal is the sum of the individual bands weighted by their respective conductivities (Ziman (1960), MacDonald (1967)).

$$S = \frac{\sum_i S_i \sigma_i}{\sum_i \sigma_i}.$$

Thermoelectric power measurement is a very rich tool for characterizing the charge degrees of freedom. We have performed the measurements of  $S$  for BaVS<sub>3</sub> as a function of pressure and temperature in the hope to learn more about the main

---

ingredients which determine its electronic properties. Furthermore, since the Non-Fermi liquid behaviour extends over a broad temperature range, we were especially curious as to whether  $S$  would exhibit a special temperature dependence, as did resistivity, in this phase.

## 7.2 The case of BaVS<sub>3</sub>

Thermoelectric power measurements in BaVS<sub>3</sub> were performed at 1 bar in a broad temperature range (up to 600 K), simultaneously with resistivity, and the results are shown in Fig. 7.1a. In this regime, both the thermoelectric power and the electrical resistivity exhibit linear, metallic-like temperature dependences with large intercepts, estimated by extrapolating from high temperatures to 0 K. In comparison to ordinary metals (Blatt *et al.*, 1976), the thermoelectric power and the electrical resistivity in BaVS<sub>3</sub> are large, *e.g.*,  $S \sim -40 \mu\text{V/K}$  and  $\rho \sim 1 \text{ m}\Omega\text{cm}$  at 600 K. Furthermore, magnetic susceptibility in the metallic regime is Curie-like (indicative of localized spins) (Mihály *et al.*, 2000). All three of these properties are characteristic for a bad metal. The high temperature thermoelectric power is negative, signifying that the charge carriers are electrons and, if BaVS<sub>3</sub> were an ordinary metal, one could easily use the data to determine that  $E_F = 0.32 \text{ eV}$ .

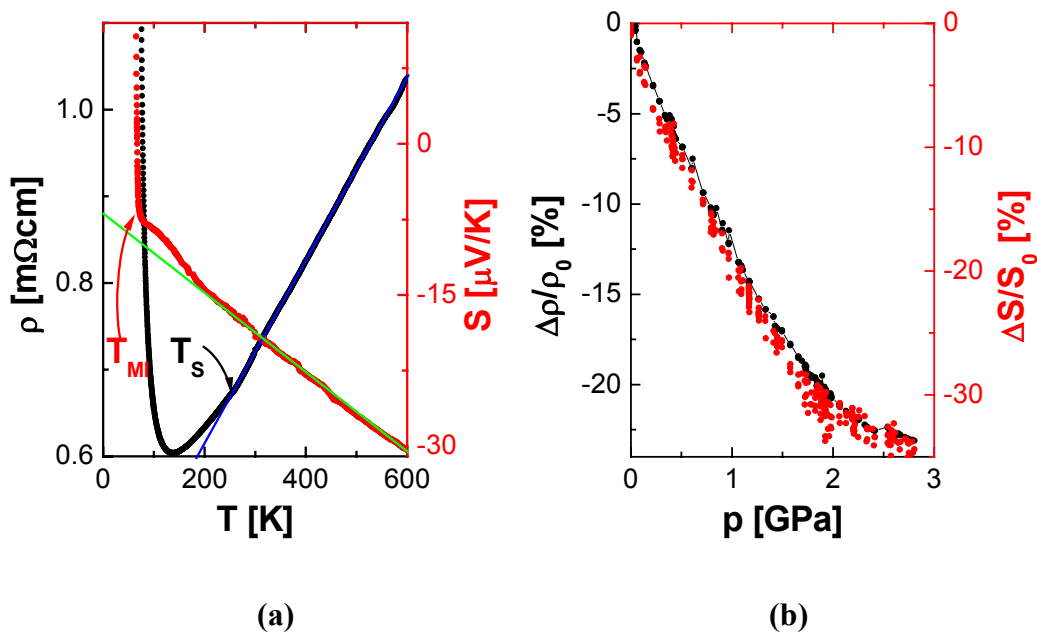


**Figure 7.1** (a) Thermoelectric power and electrical resistivity of BaVS<sub>3</sub> in the 0-600 K range. Above  $T_S = 240 \text{ K}$ , both the electrical resistivity and the thermoelectric power show linear temperature dependence indicated by blue and green eye-guide lines. (b) The pressure dependence of the relative change of the resistivity (black circles) and of the thermoelectric power (red circles) at room temperature. Note the difference between the right and left hand scales.

At  $T_S = 240 \text{ K}$  the zig-zagging and the distortion of the sulfur octahedra lift the degeneracy of the  $e_g$  orbitals (Mihály *et al.* 2000) while maintaining the screw axis symmetry. This fact is also reflected in Fig. 7.1a where, below  $T_S$ , the resistivity starts

to increase towards the MI transition, (see also Chapter 4). At the same time, however,  $S$  does not show any dramatic change. Using the single band expression give in Eq. (7.1) it should be noticed that  $\sigma(E)$  may change due to the variation of band parameters at  $T^{-1}\partial\ln\sigma(E)/\partial E$  (i.e., at a constant value of  $T^{-1}S_{Mott}$ ). Similar reasoning can be applied to the multiband models but as it is not feasible to distinguish between the various possibilities on the basis of  $S$  alone, we will defer such a discussion until a more opportune moment.

In the earlier chapters, it was already shown that  $BaVS_3$  is a system which is sensitive to pressure. It is, therefore, only mildly surprising that the Seebeck coefficient shows pressure dependence (Fig 7.1b). What is unusual for a conductor is the strong variation of  $S$  with pressure, which goes well beyond the pressure-induced changes of the band-width. As it can be seen in Fig 7.1b, both transport coefficients,  $\rho$  and  $S$ , decrease with pressure with respective (sample independent) rates of  $\sim 4.2 \mu\text{V/KGPa}$  and  $90 \mu\Omega\text{cm/GPa}$ . All of the pressure-dependent measurements presented below were performed on the pure  $BaVS_3$  sample N<sup>o</sup>: 00.

### 7.2.1 Main features of TEP below $p_{cr}$ and above $T_{MI}$

The observed linear temperature dependence of  $S$ , over a large temperature range (Fig. 7.1) already required the evocation of Mott's formula for diffusion thermoelectric power. From the large intercept of  $S$  as  $T \rightarrow 0$  (and from the high value of the electrical resistivity), it is clear that we are not dealing with an ordinary metal. A constant, temperature-independent, contribution to the thermoelectric power ( $S_0$ ) is characteristic for systems such as those exhibiting low density polaronic physics, as has been elaborated by Emin (1999) for a semiconducting case. However, the case of the analogous metal, with rather dense charge carriers strongly coupled to lattice, has never been discussed in the literature.

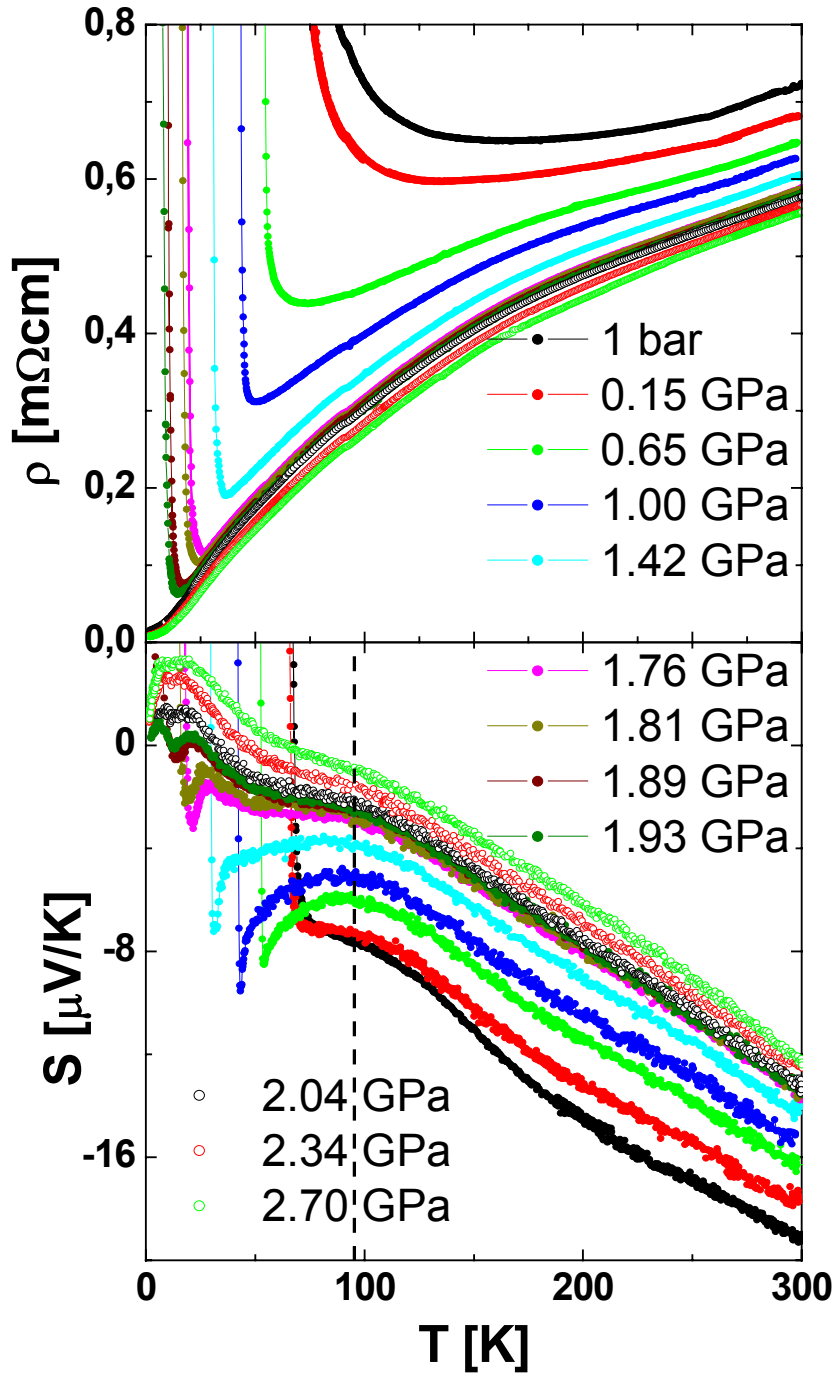


**Figure 7.2:** Temperature dependence of the resistivity and the thermoelectric power for various pressures. The black line indicates the approximate temperature below which the  $S_{fluc}$  contribution to  $S$  starts to develop (see text).

In the following discussion, we present a qualitative argument based on the polaronic picture. In this context, one should keep in mind that Kondo singlets bear some "polaronic" analogies. The adiabatic dynamics of the electron, which is coupled to the lattice degrees of freedom by the short-range interaction, results in the softening of the local lattice vibrational modes that are associated with the polaronic lattice

deformation. In particular, this affects the value of the Seebeck coefficient through the change in the local lattice vibrational entropy. As the temperature is increased, the corresponding contribution to the Seebeck coefficient rises, from its zero-temperature value, to a temperature-independent value which is realized above the Debye temperature ( $\Theta_D$ ). The expression for this latter temperature may be written as:

$$\frac{k_B}{e} \sum_i \frac{\Delta\omega_i}{\omega_i},$$

where  $\Delta\omega_i$  are the carrier-induced changes of the vibrational frequencies. In other words, the change of the lattice vibrational entropy, induced by the electrons, is carried from the hot to the cold end of the sample. This phenomenon gives rise to an additional contribution to  $S$ , denoted herein as  $S_0$ .

Since the lowest two  $e(t_{2g})$  levels are sensitive to the Jahn-Teller distortion, there is an interesting possibility that the Jahn-Teller polarons are directly present in the system, and also give rise to a contribution to the thermoelectric power. This idea is consistent with our recent optical studies, presented in Chapter 8. Furthermore, Fig. 7.2 shows that the Seebeck coefficient is strongly pressure dependent, which is also in agreement with the polaronic picture. Namely, the pressure increases the lattice spring constants and the electron overlap integrals and hence strengthens the adiabatic softening of the local lattice vibrational modes ( $\Delta\omega_i$ ). We wish to stress that, although it is possible to explain the pressure dependence of  $S$  at room temperature (Fig. 7.1b) within the context a 2 band model (Section 3.4.2), the existence of  $S_0$  necessitates the consideration of the polaronic nature of the charge carriers.

### 7.2.2 Fine features of TEP - Magneto-TEP

The above discussion of the linear temperature dependence and the offset of  $S$  was presented within the standard model of TEP. However, in Fig. 7.2., we can observe a departure from linearity at around  $T=100$  K, and a spiky contribution just above  $T_{MI}$ . These latter aspects can be considered as fine features of TEP and their interpretation is much more difficult. The material presented in this section is therefore intended to simply indicate some possibilities for the description of these fine features. It is important to stress that a single band model is used for the description of the observed changes in  $S$ . That is, the electrons are progressively dressed with new interactions as the temperature is decreased. We symbolize the new contributions as components in a sum that constitutes the total thermopower although, for a complete treatment, a more

---

detailed analysis would be required.

Increasing the pressure in the region of  $\sim 10$  K above the metal-insulator transition, introduces a new, unusually strong, spiky contribution to  $S$ :

$$S = S_{Mott} + S_0 + S_{spike} .$$

The  $S_{spike}$  is an increasingly negative contribution as the temperature decreases, which is truncated by the opening of a charge gap at  $T_{MI}$  and the concomitant sign change of  $S_{spike}$  is manifested in the spiky character of the overall  $S$ . The position of this upturn gives a very precise determination of  $T_{MI}$ , as can be verified from the logarithmic derivative of the corresponding electrical resistivity curve (Forro et al. 2000). One should notice that the  $S_{spike}$  is followed by a strong increase of the resistivity in the precursor regime to  $T_{MI}$ . Inspection of Eq. (7.1) reveals that the most likely sources of the anomalous behavior of  $S$  are the variations in the density of states as well as the spin-disorder scattering (if the phase transition has a magnetic character). Both of these parameters affect the conductivity and thereby the thermoelectric power. The heightened charge localization that occurs upon approaching the phase transition could be interpreted as a progressive band narrowing which considerably increases the thermoelectric power. As the pressure is increased towards  $p_{cr}$ , the spike in  $S$  is reduced since higher pressure acts against charge localization.

One possible contribution to the subtle changes in the electronic properties, mentioned above, may arise from the effect of electron scattering on the spins in the system. Some clue as to the importance of the contribution from spin-disorder scattering may be derived from the introduction of a new parameter. In particular, the presence of a magnetic field should affect the spin disorder and hence potentially alter the thermoelectric power.

The magneto-thermoelectric power was measured (simultaneously with the magnetoresistivity) for several pressures and the curves taken at 1.76 GPa are shown in Fig. 7.3. Although the both the shape and the maximum of the knee remain unchanged in response to the applied field, the behavior of  $S$  itself is profoundly altered by this perturbation (Fig. 7.3). A negative contribution to  $S$  is monotonically enhanced in a broad range of temperature as the field is increased from 0 to 12.7 T. We believe that this is the temperature range in which a spin fluctuation, related to the formation of short-range spin order, occurs. This measurement is the first indication of the existence of magnetic fluctuations above  $T_{MI}$ , in the precursor region.

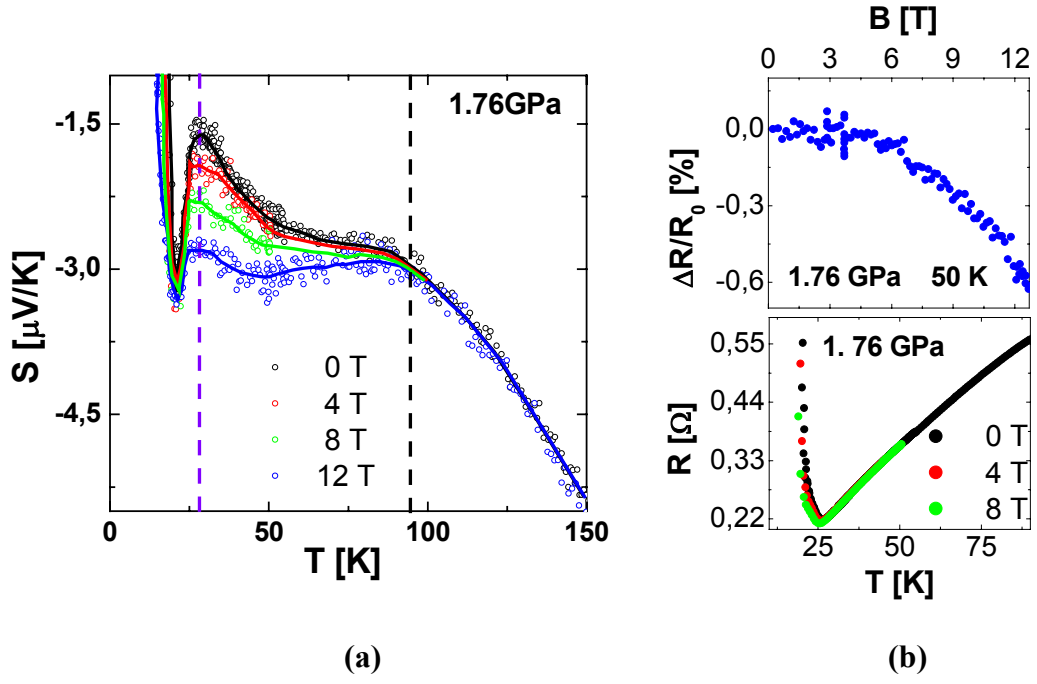


**Figure 7.3:** (a) The temperature dependence of the Seebeck coefficient under a hydrostatic pressure of 1.76 GPa in several magnetic fields, revealing the magnetic spin fluctuations. These fluctuations result in  $S_{fluct}$  which starts to develop around 100 K (vertical black line). At  $\sim 10$  K above  $T_{MI}$  (vertical violet line)  $S_{fluct}$  is replaced by  $S_{spike}$ . (b) The relative magnetoresistance at 50 K (upper panel) and the absolute magnetoresistance in the temperature range of 10 to 90 K (lower panel) at a pressure of 1.76 GPa for several magnetic field strengths.

In keeping with our stated aim for this section, we present and discuss two distinct possibilities for the interpretation of this behavior. The first one of these treats the spin fluctuations through the change in the scattering time. Taking into account that  $\sigma(E) \propto \tau(E)v(E)N(E)$ , *i.e.*, that the conductivity varies as the product of the relaxation time, the mean velocity and the density of states at the Fermi level,  $S_{Mott}$  from Eq. (7.1) can be written in a general form:

$$S_{Mott} = \frac{\pi^2 k_B^2 T}{3e} \left( \frac{d \ln \tau(E)}{dE} + \frac{d \ln v(E)}{dE} + \frac{d \ln N(E)}{dE} + const \right)_{E=E_F}. \quad (7.3)$$

It should be noticed that, in contrast to  $\sigma$ , the scattering time ( $\tau(E)$ ) affects  $S_{Mott}$  only through its energy dependence. The introduction of a magnetic field tends to align the spins in the system. In turn, this should decrease the electron spin scattering and result in a negative magnetoresistance (Fig. 7.3b upper panel). On the other hand, the presence of a magnetic field increases the absolute value of the thermoelectric power (Fig. 7.3a). Although this may seem counterintuitive at first, it can be described within the framework of Eq. (7.3), by considering the nontrivial evaluation of the  $\partial \ln \sigma(E) / \partial E$  term. While the calculation of  $\sigma$  itself is difficult; the calculation of its



energy dependence is even more so. Even if this is able to be successfully performed, for suitable applicability, one still needs to determine the derivation on the Fermi surface. This latter task is also far from trivial.

The second interpretation for the measured results is based on the following observations: (i) the magnetoresistance (Fig. 7.3b lower panel) starts to be significant only marginally above  $T_{MI}$ , suggesting a rather small change in the scattering time with B at higher temperatures (ii) the temperature dependence of TEP above  $T_{MI}$  can be separated into three ranges. The first range corresponds to temperatures larger than 100 K and is the region in which the standard model of TEP is largely applicable. The second range covers the temperatures from  $\sim 100$ K down to  $\sim 10$ K above  $T_{MI}$  (Fig. 7.2) and is associated with a negative, field-dependent, contribution ( $S_{fluct}$ ) to TEP (Fig. 7.3a). The third range, in which the contribution to  $S$  was already denoted as  $S_{spike}$ , covers the remaining 10 K down to  $T_{MI}$ . As a consequence of this behavior, TEP can be decomposed in the following manner:

$$S = \begin{cases} S_{Mott} + S_0 & 100\text{ K} < T \\ S_{Mott} + S_0 + S_{fluct.} & T_{MI} + 10\text{ K} < T < 100\text{ K} \\ S_{Mott} + S_0 + S_{spike} & T_{MI} < T < T_{MI} + 10\text{ K} \end{cases}$$

Since the change of  $S_{fluct}$  in response to the increase of the magnetic field is relatively large, especially if compared to the change in resistivity, it opens the following appealing explanation of this contribution. Assuming that magnetic fluctuations participate in the heat transport, the thermoelectric power, which is defined as the ratio between the heat and the charge current, will depend on the magnetic field. On the contrary, no radical change is expected in the charge transport under these circumstances.

From Fig. 7.3a, it appears that the increase of the magnetic field does not alter  $S_{spike}$ . On the other hand, the width of the spike, in this temperature range, is pressure independent. A simple interpretation of these features is to attribute them to the precursor region of the 3D order, which takes place at  $T_{MI}$ . This is in agreement with the finding of Fagot *et al.* (2003) that, at 10 K above the MI transition temperature, the interchain correlation length is of the same order as the interchain distance.

Finally, it should be noticed that the 1 bar curve (Fig. 7.2) does not show the spiky

contribution seen for higher pressures. The discussion of its absence would probably necessitate the introduction of further fine phenomena, which are beyond the scope of this chapter.

### 7.2.3 Main features of TEP above $p_{cr}$

The phonon-drag contribution is not specific to  $BaVS_3$ . In any crystalline solid, a thermal gradient will induce a transport of heat via lattice vibrations. As a result of phonon current and electron-phonon coupling, electrons will be "dragged" and a new contribution to  $S$  will arise (Dugdale, 1977). With increasing temperature, this contribution initially increases as the number of phonons becomes larger. At higher temperatures, where phonon-phonon scattering becomes more and more important, the phonon-drag contribution to  $S$  begins to decrease. The maximal value of  $S_{pd}$  is usually at  $\Theta_D/5$ . Using the approximate (ambient pressure) value of 180 K for  $\Theta_D$  in  $BaVS_3$ , yields a good order-of-magnitude estimate for the position of the hump maximum in  $S$ , which is at around 20K at 2.7 GPa.

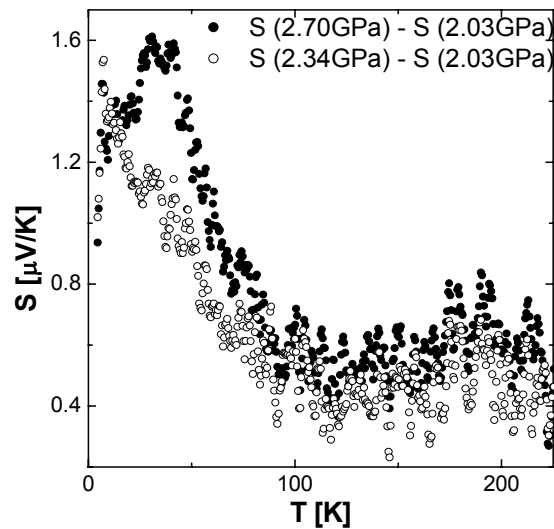


**Figure 7.4:** The relative change of the thermoelectric power for two pressures (2.3 and 2.7 GPa) approaching the Fermi liquid phase with respect to the curve taken at 2.03 GPa just above  $p_{cr}$ , in the Non-Fermi liquid regime.

Zhou and his collaborators demonstrated, for Pt as a representative example, that the phonon-drag is essentially pressure independent in a conventional  $d$ -metal (Zhou *et al.* 1960). This is not the case for  $BaVS_3$ . As illustrated in the difference plots in Fig. 7.4.,

the magnitude of  $S_{pd}$  increases with increasing pressure.

We interpret this reduced  $S_{pd}$  near  $p_{cr}$  as the manifestation of the NFL behavior in the thermopower. In Chapter 5, we saw that the  $\rho = AT^n + \rho_0$  ( $n = 1.5$ ) variation of the electrical resistivity near  $p_{cr}$  is a consequence of the fluctuations at the quantum critical point. Despite the existence of scattering with such temperature dependence,  $S_{Mott}$  is not observed to be characterized by a power law. This is due to the fact that  $\sigma(E)$  affects  $S$  only through its energy dependence on the Fermi level, which seems to be relatively weak. Nevertheless, the fluctuations do scatter the phonons and thereby reduce the drag contribution to  $S$ . By increasing the pressure to 2.7 GPa, the fluctuations are suppressed and  $n$  gradually approaches 2 (for the resistivity), while the phonon-drag of a Fermi-liquid is recovered (for the thermopower).

---

---

### 7.3 Concluding remarks

In conclusion to this chapter, we have shown that the measured results can be qualitatively understood by decomposing the total thermoelectric power into a sum of parameter-dependent quantities. As mentioned in the discussion, this decomposition is not always without problems but, in our opinion, the clarity conveyed by its evocation outweighs its deficiencies. The first, and largest, contribution to  $S$  is denoted as  $S_{Mott}$ . This is simply the standard expression Eq. (7.1) for  $S$  given by the application of the Boltzmann transport theory to metals. It is always present.

We have shown, however, that when the electron coupling to the local (*e.g.*, the Jahn-Teller) modes in BaVS<sub>3</sub> is strong, a bad metallicity in electrical transport results. This, in turn, gives rise to a constant polaronic contribution to the thermoelectric power, denoted as  $S_0$ . As higher pressures tend to act against polaron formation,  $S_0$  is strongly reduced in response to increasing  $p$ .

The observed deviation of  $S$  from linearity at around  $T=100$  K and the spiky structure just above  $T_{MI}$ , can be considered as fine features of the thermoelectric power. The spiky feature can be rationalized by the introduction of an additional contribution ( $S_{spike}$ ) which is only important at temperatures just above the magnetic-insulator transition. We can hypothesize that this contribution arises from the progressive band narrowing that occurs as a result of the heightened charge localization present on the high- $T$  side of the MI phase boundary.

At pressures below  $p_{cr}$  (*e.g.*, 1.75 GPa), three temperature ranges can be clearly discerned in the magneto-thermoelectric power measurements (Fig. 7.3). The behavior observed in the two exterior ranges is virtually independent of the magnetic field and can be rationalized by the appropriate inclusion of  $S_{Mott}$ ,  $S_0$ , and  $S_{spike}$ . The fact width of the spike arising from this later contribution is pressure independent under these conditions may be attributable to the precursor region of the 3D order. The behavior in the central region ( $T_{MI} + 10\text{K} < T < 100\text{K}$ ), however, is strongly influenced by the strength of the applied field. As the explanation of this phenomenon is complex, we have offered two alternative interpretations. The first supposes that the introduction of the magnetic field affects the scattering time ( $\tau(E)$ ) and hence  $\partial \ln \sigma(E) / \partial E$  (see Eq. (7.3)). Unfortunately, this alternative is quite difficult to quantify. The second possibility extends the decomposition approach by introducing an additional field-dependent component ( $S_{fluct}$ ), reliant on the magnetic fluctuations. Naturally, the quantification of this component is also associated with difficulty.

---

Nevertheless, its introduction can account for the observed field-dependence of the thermopower, through the modification of the heat transport while imparting relatively little effect onto the charge transport properties of the system.

When the pressure becomes high enough to suppress the insulating phase a broad peak appears in  $S$  which is derived from the phonon drag effect ( $S_{pd}$ ). The newly born metallic phase is known to exhibit the characteristics of a NFL through the power-law temperature dependence observed for the electrical resistivity. The corresponding behavior of the thermoelectric power is, however, masked by the strong phonon-drag contribution. Nevertheless, we suspect the unusual pressure dependence of  $S_{pd}$  is derived from the same quantum fluctuations which produce the NFL state.

## 7.4 References

Blatt F. J., P. A. Schroeder, C. L. Foiles, and D. Greig. 1976. Thermoelectric Power of Metals. New York, Plenum Press.

Dugdale J. S. 1977. The Electrical Properties of Metals and Alloys. London, Edward Arnold.

Fagot S., P. Foury-Leylekian, S. Ravy, J. P. Pouget and H. Berger. 2003. One-dimensional instability in  $BaVS_3$ . *Phys. Rev. Lett.* **90**(19), 196401.

Forro L., R. Gaal, H. Berger, P. Fazekas, K. Penc, I. Kezsmarki and G. Mihaly. 2000. Pressure induced quantum critical point and non-Fermi-liquid behavior in  $BaVS_3$ . *Phys. Rev. Lett.* **85**(9), 1938.

MacDonald D. K. 1967. Thermoelectricity: An introduction to the Principles. New York, Wiley.

Mihaly G., I. Kezsmarki, F. Zamborszky, M. Miljak, K. Penc, P. Fazekas, H. Berger and L. Forro. 2000. Orbital driven spin pairing in the three-dimensional nonmagnetic Mott insulator  $BaVS_3$ : Evidence from single-crystal studies. *Phys. Rev. B* **61**(12), R7831.

Emin D., (1999). Enhanced Seebeck coefficient from carrier-induced vibrational softening. *Phys. Rev. B* **59**(9), 6205.

Zhou J. S., and J. B. Goodenough. 1995. Thermoelectric-Power In Single-Layer Copper Oxides. *Phys. Rev. B* **51**(5), 3104.

Ziman J. M. 1960. Electrons and Phonons. London, Oxford University Press.

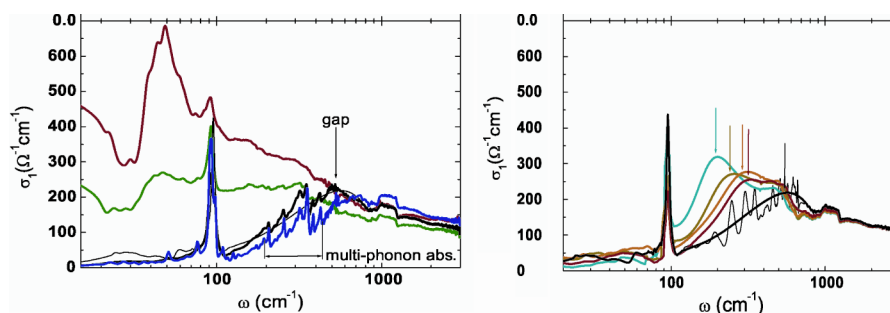
---

---



## Chapter 8

# OPTICAL CONDUCTIVITY OF $\text{BaVS}_3$ IN THE INFRARED REGION



8.1	INTRODUCTION TO OPTICAL MEASUREMENTS	172
8.2	AMBIENT PRESSURE MEASUREMENTS	173
8.3	PRESSURE DEPENDENT OPTICAL CONDUCTIVITY MEASUREMENTS	176
8.4	CONCLUDING REMARKS	178
8.5	REFERENCES	179

In this final chapter, I briefly discuss the results of optical conductivity measurements and indicate their relevance for the underlying physical picture presented in previous chapters.



## ***8.1 Introduction to optical measurements***

Optical experiments are well-known tools for obtaining information about the electrodynamic response and the electronic structure of a given material. The typical wavelengths of the light used to illuminate the samples are in the range of  $10^{-5}$ - $10^{-1}$  cm, which corresponds to an energy scale of 1 meV - 10 eV. Due to the small moment and high energy of the incident light ( $\omega = ck$ ) only “vertical processes” can be probed. This implies that information concerning the frequency dependences of the excitations can be gathered but their  $k$  dependences are concealed. Since the wavelengths are much larger than the lattice constant, the electromagnetic field is considered as being uniform on the atomic scale.

The energies of electronic excitations are in the far infrared range. Conventional light sources are inappropriate to investigate this energy range on small single crystals. Therefore, to obtain a higher brightness in this energy range, the measurements were performed at the National Synchrotron Light Source of the Brookhaven National Laboratory. We have studied the optical response in reflectance and the frequency-dependent conductivities were calculated by the Kramers-Kronig transformations.

Although the data are preliminary, mainly due to the lack of availability of the large single crystals needed for the measurements, the results obtained thus far are coherent with our understanding of the main features of BaVS<sub>3</sub>. In this chapter, therefore, the most important of our results on BaVS<sub>3</sub> are briefly summarized in an attempt to give a broader view of the underlying physics. An extensive version of the high-pressure data has already been prepared by Kezsmarki *et al.* (2003).

---

---

## 8.2 Ambient pressure measurements

The reflectivity data as a function of frequency, for selected temperatures, are presented in Fig. 8.1. The curves measured above the MI transition temperature ( $T=300\text{K}$  and  $70\text{K}$ ) tend to 1 as the frequency approaches the d.c. range. This behavior is typical for metallic systems. The Hagen-Rubens law was applied to calculate the d.c. conductivity  $\sigma_0 = \sigma(\omega \rightarrow 0)$ . The obtained values are  $710\ \Omega^{-1}\text{cm}^{-1}$  and  $370\ \Omega^{-1}\text{cm}^{-1}$  at  $300\text{K}$  and  $70\text{K}$ , respectively. The room temperature data are comparable with the d.c. transport values measured along the  $c$  direction,  $\sigma_{dc} = 1400\ \Omega^{-1}\text{cm}^{-1}$ . The lower value reported here may be due to the anisotropy ratio ( $\sigma_c/\sigma_a \sim 3.4$ ) and the fact that the measurements with unpolarized light constitute averages over all directions.

Recent measurements at  $300\text{K}$  with polarized light in the  $b$ - $c$  plane have confirmed that not only is the d.c. transport almost isotropic, but the frequency-dependent conductivity, in the  $50$  -  $800\ \text{cm}^{-1}$  range, is also devoid of anisotropy.

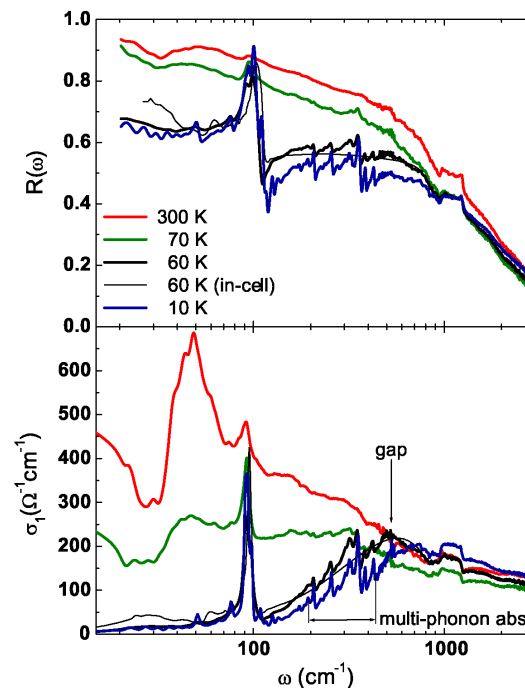


**Figure 8.1:** The reflectivity (upper panel) and conductivity (lower panel) spectra of  $BaVS_3$  at ambient pressure for selected temperatures. The position of the gap is indicated by arrow. To test the reliability of the high-pressure data (see below), the  $60\text{K}$  curve was also measured in the pressure cell at ambient pressure.

Besides the isotropic response of the conductivity in the metallic phase, the most remarkable aspect of the results is the dip in reflectance around 30 cm<sup>-1</sup>. This dip is broad and tends to fade out at lower temperatures. This behavior means that we are not dealing with a conventional infrared-active phonon. If that were the case, the dip in the signal would sharpen and increase in intensity upon decreasing temperature. Especially below  $T_M$ , when the screening by the conduction electrons vanishes, the infrared-active phonon should pop-up, as is the case with the one at 100 cm<sup>-1</sup>. This suggests that this 30 cm<sup>-1</sup> mode is intimately linked to the conduction electrons and, possibly, to their interaction with a special localized mode. We tentatively ascribe it to a Jahn-Teller (JT) phonon mode, since we know of the presence of static and dynamical JT distortions from the structural data (Chapter 3.). Generally speaking, however, the interaction of the continuum with a localized mode gives a Fano lineshape and not a dip. Nevertheless, within the resolution of our measurements, and considering the small size of the single crystal, it is conceivable that the feature at 30 cm<sup>-1</sup> is compatible with a Fano lineshape (Fano, 1961), and hence a Jahn-Teller (JT) phonon mode.

The overall features of the reflectivity can be fitted in a simple model where the conduction electrons interact with the “heavy mass” phonon mode. This is given by the formula (Damascelli, 1997):

$$\sigma(\omega) = i\sigma_0(\omega)(q - i)^2(i + x)^{-1} \quad ,$$

where  $x = (\omega^2 - \omega_T^2)/\gamma\omega$  ( $\gamma$  is the linewidth and  $\omega$  is the resonance frequency of the unperturbed vibrational state),  $q$  is the dimensionless Fano parameter reflecting the degree of asymmetry of the peak and

$$\sigma_0(\omega) = \frac{ne^2}{m^*} \tau \frac{1}{1 + \omega^2\tau^2} \quad .$$

where  $n$ ,  $m^*$  and  $\tau$  correspond to the electron number, the effective mass, and the relaxation time, respectively.

This crude (single-band model) description already gives some feeling about the mass enhancement and the relaxation time of the conduction electrons. If we take 1 electron per site,  $m^*$  is 12, which shows the tendency of the JT mode to enhance the electronic mass and thereby slow the charge propagation. This fact, together with the very short relaxation time of 10<sup>-15</sup>s, could give some clue as to the source of the bad metallicity of BaVS<sub>3</sub>.

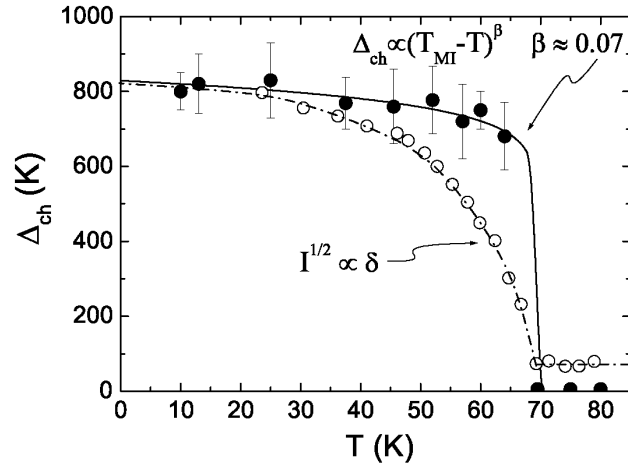


**Figure 8.2:** The charge gap,  $\Delta_{ch}$ , (solid circles), determined from optical conductivity data, shows an abrupt change (solid line is a guide for the eye) at  $T_{MI}$ . On the contrary, the order parameter of the structural deformation (Inami *et al.* (2002)) increases in a mean field manner.

As one goes below  $T_{MI}$ , the low-frequency spectral weight vanishes as the energy gap opens. The wavenumber of the separation of the optical conductivity data below and above  $T_{MI}$ , i.e. the maximum in  $\sigma_I$  below  $T_{MI}$ , determines the charge gap to be  $\Delta_{ch} = 700\text{K}$ . A detailed analysis of the temperature dependence of the optical conductivity in the insulating phase results in the temperature dependence of the charge gap (as shown in Fig. 8.2). A remarkable observation is that, below the MI transition temperature, within the precision of the experimental method; all of the recorded data (for various temperatures) fall onto a single curve. This means that the charge gap, as defined above, opens to its full value precisely at  $T_{MI}$ , and does not vary in the mean-field manner ordinarily associated with a second order phase transition (Fig. 8.2). In contrast, as shown in Fig. 8.2, the order parameter of the structural deformation (measured in X-ray diffraction experiments, by Inami *et al.* (2002)) does change in a mean-field manner. It is, however, interesting to note that for frequencies below  $500\text{ cm}^{-1}$  ( $\sim 700\text{ K}$ ) the conductivity is temperature dependent in the whole temperature range above  $T_{MI}$ .

### 8.3 Pressure dependent optical conductivity measurements

The determination of the pressure dependence of the optical conductivity in the far infrared range is very a challenging experiment. One has to collect low frequency data which necessities a large, transparent optical window. At the same time, this window has to be able to support high pressures. In our laboratory, Gaál *et al.* (*in preparation*) have succeeded in developing an optical cell with these unique properties. It was through the use of this cell that we addressed the high-pressure optical response of  $BaVS_3$ .

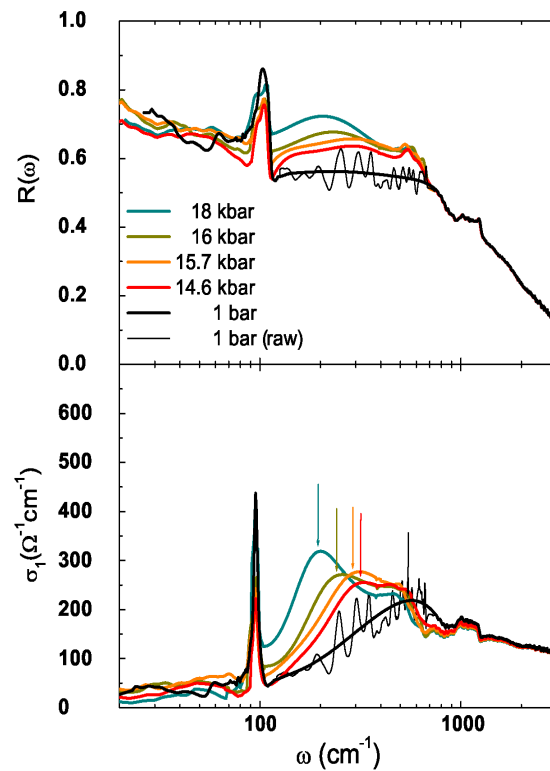


**Figure 8.3:** The reflectivity (upper panel) and conductivity (lower panel) spectra of  $BaVS_3$  at a temperature lower than  $T_{MI}$  for selected pressures. The position of the gap at each pressure is indicated by the appropriately colored arrow.

The goals were threefold: (i) study the evolution of the  $30 \text{ cm}^{-1}$  dip, attributed to JT polaron, with pressure; (ii) follow the suppression of  $T_{MI}$  as a function of  $p$ ; and (iii) to check for the presence of non-Fermi liquid features in the frequency dependent conductivity.

In this very ambitious endeavor, the first results concern the  $T_{MI}$  versus  $p$  behavior.

Again, as was the case for the temperature variation, the conductivity is pressure dependent only for frequencies below  $500\text{cm}^{-1}$  ( $\sim 700$  K). The charge gap, as measured by the maximum in the optical conductivity, shifts progressively down with increasing pressure. This is in agreement with the resistivity measurements presented in Chapter 4. Unfortunately, due to the curvature of  $\ln\rho$  in the Arrhenius plot (see Chapter 4), it was not possible to unambiguously determine the value of the gap from the d.c. resistivity data. From the data displayed in Fig. 8.3 the deduced charge gap follows nicely the  $2\Delta/k_B T_M = 12$  relation, independently of pressure (already mentioned in Chapter 4). The verification of the high value of this ratio, together with the first-order character of its temperature dependence will, however, require further theoretical and experimental investigations.

---

---

## **8.4 Concluding remarks**

In concluding this brief chapter, it is clear that a significant amount of additional work is required to be able to exploit the full potential available through the optical conductivity data. As it stands, we were already able to make several contributions to the understanding of the behavior of BaVS<sub>3</sub>. However, due to the preliminary nature of the measurements and their analysis, some caution should be exercised in extrapolating the conclusions too far.

The ambient pressure measurements of the reflectance identified an unusual feature at around 30 cm<sup>-1</sup>. The response of the signal in this region to decreased temperatures clearly shows that this feature is not a conventional infrared-active phonon. We have suggested that this feature can be ascribed to a JT phonon mode. A crude (single-band) model indicates that this could possibly be connected with the bad-metallicity in BaVS<sub>3</sub>.

Interestingly, the charge gap, as measured by the maximum in the conductivity, is found to undergo an abrupt change at the MI phase transition. This is in stark contrast to the expected mean-field manner in which the order parameter of the structural deformation responds to the presence of the second order phase transition. On the other hand it was found that the value of the frequency below which the conductivity is pressure and temperature dependent, is constant and equal to 700 cm<sup>-1</sup>; this frequency can be tentatively associated with the width of the pseudogap.

Finally, the very preliminary data presented for increased pressures indicate that the charge gap follows the  $2\Delta/k_B T_{MI} = 12$  relation. However, this and several other aspects associated with the optical conductivity, still require additional investigation.

## **8.5 References**

Dressler M. and G. Grüner. 2002. *Electrodynamics of Solids*. Cambridge University Press, Cambridge, UK.

Fano U. 1961. Effects of configuration interaction on intensities and phase shifts. *Phys. Rev.*, **124**(6), 1866.

Gaál R. *et al.*, Pressure cell for optical measurements in the Infra-Red range. *in preparation*,

Inami T., K. Ohwada, H. Kimura, M. Watanabe, Y. Noda, H. Nakamura, T. Yamasaki, M. Shiga, N. Ikeda, and Y. Murakami. 2002. Symmetry breaking in the metal-insulator transition of BaVS<sub>3</sub>. *Phys. Rev. B*, **66**(7), 073108.

Jahn H. A. and E. Teller. 1937. *Proc. R. Soc. A* **161**, 220.

Kézmárki I., G. Mihály, R. Gaál, N. Barisic, H. Berger, L. Forró, C. C. Homes and L. Mihály. 2003. Pressure induced suppression of the singlet insulator phase in BaVS<sub>3</sub>: infrared optical study. *cond-mat*, 0311335.

Mihaly G., I. Kezsmarki, F. Zamborszky, M. Miljak, K. Penc, P. Fazekas, H. Berger and L. Forro. 2000. Orbitaly driven spin pairing in the three-dimensional nonmagnetic Mott insulator BaVS<sub>3</sub>: Evidence from single-crystal studies. *Phys. Rev. B* **61**(12), R7831.

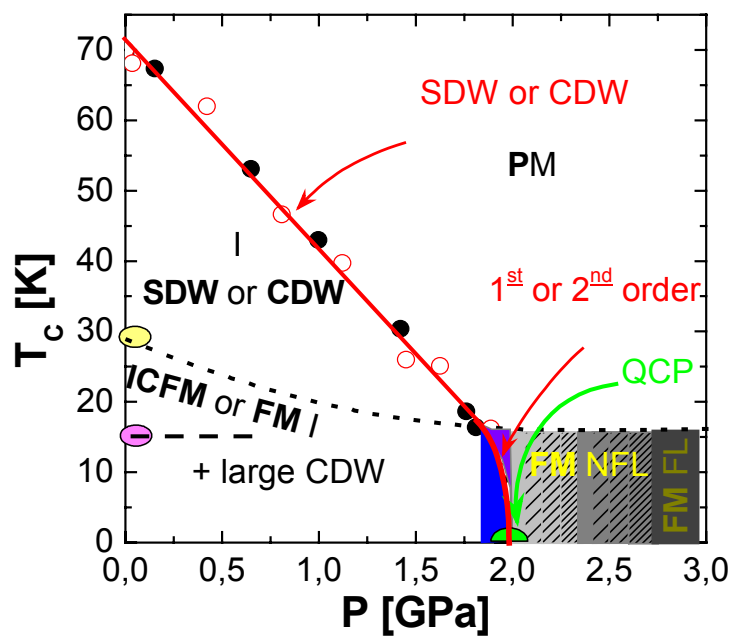
Wotten F. 1972. *Optical Properties of Solids*. New York, Academic Press, INC.





## Chapter 9

### CONCLUSIONS



#### 9.1 THE JOURNEY: FROM THE BEGINNING TO THE END

182

#### 9.2 FUTURE PERSPECTIVES

187

In concluding the thesis, I summarize the results of the measurements taken and their relationship to the way in which we have come to understand BaVS<sub>3</sub>.

## ***9.1 The journey: From the beginning to the end***

The work presented in this thesis was undertaken with the aim of both measuring and understanding the properties of the  $\text{BaVS}_3$  family of materials. This task has been achieved progressively and heuristically, by combining specific measurements and conceptual analysis to advance, step-by-step, towards the physical picture finally proposed for these materials.

The journey began with an analysis of the symmetry changes associated with the sequence of structural and/or magnetic transitions observed in those materials (section 3.2). The results were then used in the development of two minimal models, designed to provide an adequate description of the observed transport, optical, magnetic and structural properties of the material. The first model began from the point of view of low pressures and temperatures, with localized electrons (section 3.3). In contrast, the second is derived from the high temperature and/or high-pressure side, with extended electrons (section 3.4). The review of the band calculations, in this latter case, led to the tight-binding picture of the relevant bands. Importantly, this picture, with the addition of the appropriate interactions, provides a natural connection between the high and low temperature models. The bands in question are related to three vanadium states, per vanadium site, along the vanadium chain.

The main paradox in the high temperature properties of  $\text{BaVS}_3$  is the appearance of the electron-driven one-dimensional lattice fluctuations, fourfold commensurate along the vanadium chain direction, simultaneously with the only weakly anisotropic electric conductivity. These properties have served as main criteria in the choice of the minimal (three or two) band model, consisting finally of a wide quasi one-dimensional band hybridized with (one or two) narrow, rather isotropic band(s). The Peierls coupling of these bands to the lattice is already sufficient to capture the correct structural and transport behaviors in the broad sense, and is consistent with the electronic structure observed by ARPES (section 3.4.3).

The examination of the magnetic properties of the system shows, however, that Coulomb interactions play an important role in the observed behavior. The MI transition at ambient pressure is not only structural but also magnetic, resulting in the sharp decrease of the uniform magnetic susceptibility (section 1.1). Combining this information with the knowledge that the precursors of the MI transition are the one-dimensional electronically-driven lattice fluctuations, it is concluded that this transition is controlled by the Coulomb-interacting electrons of the wide quasi one-

---

dimensional band (section 3.4.3). It is here that the whole rich body of physics associated with the (quasi) one-dimensional non-Fermi liquid enters the problem. For the weak to moderate interactions appropriate for vanadium-based states, the nesting feature of the wide band enhances the intraband SDW correlations, which, when coupled to the lattice, lead to an instability of the spin-Peierls type. At the same time, through local coupling between the itinerant and localized spins, this order is imposed (via the effective RKKY interaction between localized spins) also upon the latter.

Pressure is expected, and shown by measurements of resistivity and thermoelectric power (chapters 4, 5 and 7), to have a dramatic effect on the MI phase transition. It does not only influence the overall width of the band, through the Coulomb coupling constants as in the three dimensional case, but additionally and more importantly, increased pressure affects the nesting properties of the wide band, making them imperfect. The pressure thus progressively removes the quasi one-dimensional enhancement of the SDW correlations, and so decreases the corresponding spin-Peierls transition temperature. Thus, when the MI transition temperature reaches zero at the critical pressure,  $p_{cr} \approx 2$  GPa, the system tends to be three-dimensional and metallic, although anisotropic. In our original model, which retains the interactions between the itinerant and local spins but neglects the direct (intra narrow band) interactions between the local moments, and which becomes three dimensional with pressure, the zero temperature transition corresponds in some respects to the Quantum Critical Point (QCP) of the 3D Kondo lattice (section 5.2). It is common knowledge that such a model shows a non-Fermi liquid behavior in the vicinity of the QCP.

When the system is driven away from the QCP to the high pressure side, probably by further reducing the nesting effects in the wide band, the fourfold charge and spin correlations in the wide band become unimportant with respect to the formation of the local charge and spin correlations, the latter through the remaining local interaction of itinerant and local spins. The local correlations move as particles and ultimately form the correlated Fermi liquid. This effect was studied by measuring carefully the low temperature  $T^n$  dependence of the resistivity as a function of pressure (section 5.3). In  $\text{BaVS}_3$ , above the critical pressure and for temperatures below 15 K, the power law exponent  $n$  (consistently with other quantities which parameterize the resistivity) changes from the manifestly non-Fermi liquid value  $n < 2$  close to QCP (section 5.2) tending to the conventional  $n = 2$  at high pressures, in qualitative agreement with the predictions of the model.

This picture is, however, incomplete, in particular because it neglects the direct

---

---

interactions between the local moments additional to the RKKY interactions, or, in the band language, the magnetic intraband intersite Coulomb correlations in the narrow band(s). That the latter might be important is suggested at ambient pressure by the reordering of the magnetic moments found in BaVS<sub>3</sub>, deep in the insulating phase. The order, ferromagnetic (FM) along the vanadium chains, appears below 30K. Transverse to the vanadium chains the interchain order is incommensurate, seen in susceptibility as interchain compensated FM (ICFM). It is presumably a weak order, probably because the interchain AF coupling of the chain magnetic moments, entirely frustrated in the hexagonal phase, is approximately so in the orthorhombic one. Further on, the (full) ferromagnetic order is found in the samples in which the chemical substitution, partial with Sr and entire with Se, acts equivalently to the pressure (chapter 6). In the samples containing Sr, the nonmagnetic (presumably fourfold CDW) insulating phase is removed by pressure and/or further doping. In Se samples the MI transition is already eliminated at ambient pressure. Nevertheless, the full FM order is present in the metallic phase of Sr and Se samples at low temperature. It is thus reasonable to attribute it to the direct magnetic interactions between local spins in the whole BaVS<sub>3</sub> family.

It is then also reasonable to expect that the intrachain FM order occurs in the metallic phase of BaVS<sub>3</sub>. Thus, although the ICFM order in BaVS<sub>3</sub> cannot be examined by the transport measurements in the insulating phase, these measurements, now at high pressure, are well suited to investigate the possible occurrence of some interchain kind of ordering of the intrachain FM ordered magnetic moments in the metallic phase. The corresponding measurements of the low temperature behavior of the linear and non-linear (current-dependent) electrical resistivity, of the infrared conductivity and of the thermopower in the uniform magnetic field (itself conjugated to the (full) FM ordering) represent the experimental focal point of this thesis.

First, it was found that when the critical temperature of the MI transition is (linearly) decreased by applying pressure close to 15 K (chapter 4), a small additional increase of pressure makes it collapse to zero at  $p_{cr}$  (section 5.1). Next, for pressures higher than  $p_{cr}$  a shoulder, which marks the upper bound of the low  $T$ ,  $T^*$ , regime, is observed, again around 15K (section 5.3.3). This same temperature scale has its counterpart in the magnetic scale (fields around 9T) in the measurements of the magnetoresistivity at fixed low temperature (section 5.4.1.4). Taking all of this into account it is reasonable to associate 15 K with the critical temperature of the intrachain FM ordering. The nature of the concomitant (probably weak) transverse ordering is, of course, entirely out of reach of the methods in use here.

---

---

The collapse of the MI phase, which occurs when the transition temperatures of the fourfold and uniform magnetic ordering come together under pressure, shows however that the two magnetic orderings are not decoupled. Recall, however, that this is apparently not the case at ambient pressure, when their characteristic temperatures are split. It is likely that the SDW order couples to the probably weak transverse ordering of the intrachain FM moments (section 5.5). This is why in the vicinity of  $p_{cr}$  it was interesting to measure carefully, on small energy scales, the transport properties for clean mono-crystalline samples of BaVS<sub>3</sub>. Not surprisingly, for inherently metastable situations, well developed hystereses were observed in the temperature-dependent behaviors (below 15 K) of the resistivity, the thermoelectric power, and the magnetoresistivity (chapter 5). The resistivity in the magnetic field also turns out to be strongly current dependent, showing random jumps in this dependence (section 5.4.1.3). These jumps disappear for fields larger than 9 T. The combination of these results suggests that, for the clean samples of BaVS<sub>3</sub> in the vicinity of  $p_{cr}$ , there is a domain structure for temperatures below 15 K and magnetic fields below 9 T. The nature of those domains is out of reach of the transport measurements, but apparently they have to do with the interplay between the SDW and ICFM instabilities. On the other hand, the extrinsic disorder of the impure samples wipes out (or blocks) the domain structure, probably upon replacing ICFM by the full FM. In this case, the conducting behavior in the vicinity of  $p_{cr}$  is decoupled from the (transverse) ordering of local spins, and the previous QCP analysis of the  $T^n$  laws, which ignores this ordering effect, can be applied with some confidence.

The question of fluctuations in the QCP regime was also addressed by thermoelectric power but no corresponding power law temperature dependences were observed due to masking by the strong phonon-drag contribution (chapter 7). Nevertheless, we suspect the unusual pressure dependence of the phonon-drag is related to the same quantum fluctuations, which produce the NFL state. As for the high-temperature thermoelectric power, it is marked by a contribution, which depends on the pressure but not the temperature, that can be ascribed to the Jahn-Teller polarons. We have shown, in addition that the strong electron coupling to the local modes in BaVS<sub>3</sub> results in a bad metallicity of the electrical transport. This idea is consistent with our recent optical studies, presented in chapter 8.

In the context of the present intense theoretical and experimental efforts to understand the behavior of systems with strongly correlated electrons, BaVS<sub>3</sub> is thus a very interesting material. Many aspects of the non Fermi-liquid physics are interlaced in the properties of this material. First, at ambient pressure it shows the fluctuative

---

---

behavior characteristic of the one dimensional Luttinger liquid. However, below the critical temperature for orbital ordering, the minimal model for this material may involve two bands rather than one. The second band, which enters the model in addition to the essential quasi-one dimensional one, is quasi-isotropic but narrow, and is responsible for introducing the aspects of the heavy-fermion physics into the problem. The latter becomes in some respects analogous to that of the Anderson-Kondo 3D lattice embedded into the sea of quasi-one-dimensional Luttinger electrons. The commensurate  $2k_F$  and  $4k_F$  CDWs and  $2k_F$  SDW are therefore either interfering with the local correlations or defining the nature of the RKKY interaction between the localized spins. However, in addition to the RKKY interaction, it appears that the direct (intraband) interaction between the localized (narrow-band) spins is required to describe the physics of BaVS<sub>3</sub>. The advantage of studying these phenomena in BaVS<sub>3</sub> is that, by applying large pressures, the quasi one-dimensional enhancement of the RKKY interaction can be decreased and the quasi-isotropic correlated regime studied separately. This leads to a better understanding of the intricate high-pressure behavior of the Quantum Critical Point or of the first order phase transition in clean BaVS<sub>3</sub>, which, at low temperature, separates the two regimes.

To return to the point then and close the overall circle, let us stress the primary interest that led us to BaVS<sub>3</sub> in the first place (at the end we should not forget how this journey started). As said earlier, it is of crucial importance for future development, to understand the main parameters that control the interplay between lattice, charge, orbital, and spin correlations, and to learn how to manipulate them in order to be able to engineer materials suitable for devices. Although BaVS<sub>3</sub> is probably not yet directly ready for use in new devices, it is indeed a very nice example of a material in which we can understand and manipulate the important parameters of interest. Throughout this thesis we have seen how, by applying pressure, magnetic field, and chemical substitutions, the properties of the system could be modified in a substantial way. Careful interpretation of the resulting responses of the material provided us with an insight into the underlying physical background, in particular by uncovering the fine interplay between the electrons in the  $d_z^2$  and  $e_g$  orbitals.

---

---

## 9.2 *Future perspectives*

In closing, I would like to take the liberty of including a few, more personal, words. Working with BaVS<sub>3</sub> was by no means an easy task. The samples are small, fragile, and hard to contact, not to mention the fact that high pressure measurements are not the gentlest available (the relevant forces on the crystal are measured in tons). Indeed, several times during my doctoral studies, especially during those sleepless nights spent bending over BaVS<sub>3</sub> (when I should have been home watching *Casablanca*), I thought to myself why:

of all the lab joints in all the towns in all the world, "she" walks into mine ?

But every process of learning has its price and, as the time passed by, I changed my tune. Now, at the end, I'd rather say:

BaVS<sub>3</sub>, I think this is the beginning of a beautiful friendship.

As a small token of my appreciation for all this material has done for me, I would like to record my list of wishes of things that could be done for "her":

NMR and NQR in the low temperature phase  
Magnetic susceptibility under pressure  
Neutron scattering study under pressure (on ceramic samples)  
Conduction anisotropy measurements under pressure  
Anisotropy of the frequency-dependent conductivity  
Magnetic susceptibility and resistivity of substituted or doped  
or irradiated or sulfur deficient samples under pressure

Whether it is me or someone else who will have the honor of bestowing these insights, I believe that their accomplishment will bring us all closer to unlocking the plethora of intricacies and mysteries that, by their combination, comprise "her" essence.

---

---

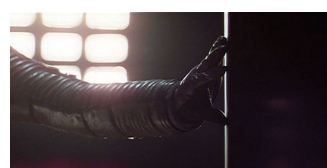
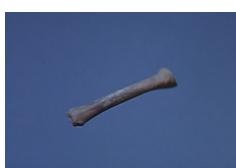
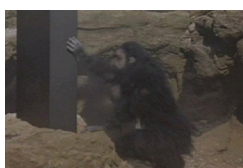




---

# Appendix A

## HOW TO MEASURE



This chapter is dedicated to those readers interested in mastering the techniques of measuring transport properties under pressure. In an effort to make the explications as simple as possible while still transmitting the important tricks and know how, the step by step procedures are given in the form of the cook book. We will start from the very beginning with the 1-bar transport measurements and describe how to contact the BaVS<sub>3</sub> sample and related compounds. Thereafter, we will show how to overcome the problems associated with the high pressure measurements.

---

---

### A.1 A.1.1 Resistivity and thermopower for beginners

Electrical **resistivity**  $\rho$  is calculated from the measured resistance  $R$  of a sample of a known length  $L$  and uniform cross section  $A$  by the following expression:

$$\rho = RA/L \quad .$$

In the case of  $\text{BaVS}_3$ , the **dimensions** of the crystals were measured by the use of an optical microscope equipped with an ocular micrometer. The resistance measurements were performed in the standard four probe configuration as shown in Fig. A.1. This method gives the real sample resistance since the current and voltage contacts are separated (this is not the case with the two point configuration where the measurements are influenced by a serial contact resistance). The procedure for measuring **resistance** is:

- a) Set the desired current (be sure that the sample is not heated by the chosen measuring current).
- b) Wait several seconds (until the voltage stabilizes), and read the voltage.
- c) Change the polarity of the current, wait several seconds, and read the voltage.
- d) The slope of the line connecting the two measured points in the  $I$ - $V$  graph gives the value of  $R$  (that way the parasitic thermal voltage,  $V_{therm}$ , does not influence the measurement,  $V = IR + V_{therm}$ ).

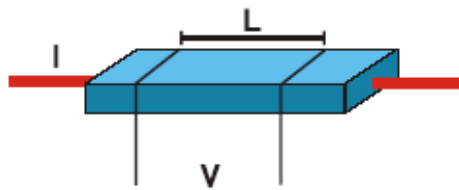


**Figure A.1:** Schematic presentation of the geometry for the resistance measurements.

To prevent the heating of the sample by the measuring current and to ensure a low noise (due to parasitic thermal voltages), it is important to have low resistance contacts. Unfortunately, this property is sometimes difficult to obtain. If the contacts are of differing quality, the usual choice is to connect the best one to the current source. This allows the highest possible measuring current, limited by the Joule heat of the current contact. One of our goals was to measure the electrical properties of

BaVS<sub>3</sub> and related compounds, in the high pressure and low-temperature region where the resistivity has a metallic character. In this region, the typical sample resistance is  $\sim 0.1 \Omega$ . Since the standard silver paint contacting techniques gave a contact resistance of  $\sim 100 \Omega$ , considerable efforts were invested in order to reduce this value. The following method resulted in *contacts* with a resistance of  $\sim 10 \Omega$ :

- a) Mask the sample with mylar, leaving the places for future contacts uncovered.
- b) Evaporate  $\sim 500 \text{ \AA}$  of chrome and then continue with evaporating  $\sim 500 \text{ \AA}$  of gold.
- c) Take the mask away, and fix wires (if measuring TEP use high purity gold wires, see TEP measurements) by conducting silver epoxy: DuPont 6838.
- d) Heat it at  $350^\circ\text{C}$  for 10 min under vacuum. (This is the lowest temperature at which the epoxy becomes conducting. On the other hand, at higher temperatures the material degrades by releasing sulfur, which reacts with silver epoxy and devastates the contacts. Vacuum prevents the oxidation of the epoxy).

Recent interest for parallel studies of susceptibility and transport properties has motivated another approach, which does not introduce magnetic impurities (like chrome, epoxy, etc.). The solution is found in spot welding which gives good preliminary results having the contact resistance of several Ohms. Their resistance to high pressures should be still tested.

Once the samples are contacted, the resistivity can be measured as explained above or, alternatively, mounted on the *sample holder for thermoelectric power measurements* (TEP).

---

---

If the sample is placed in a temperature gradient, the charge carriers will move from the hot to the cold side of samples. This will induce a voltage drop across the sample, as shown schematically in Fig. A.2. The coefficient, which connects the voltage drop and the imposed temperature gradient, is known as the Seebeck coefficient,  $S$ :

$$V = S \Delta T$$

The technical problem of this experimental method is the precise determination of the temperature gradient

between two voltage contacts. Since the intention was to use the same setup at 1 bar and in the pressure cell, a homemade sample holder of small dimensions was developed. The principal steps involved in its preparation are described below.

- a) Make flat a surface on a metal field resistor (Fig. 3) of  $\sim 500 \Omega$  by polishing it along the longest dimension (where the resistor color code is placed).
- b) Completely remove the remaining paint and metallic film from the side of the resistor leaving the top and the bottom of it (where the resistor connecting wires are) untouched. (Use the flat surface to glue (with Cyanolite) the resistor on the edge of a microscope glass slide and polish its body along the longest side. During this procedure, the connecting wire will probably detach, leaving free the metallic film below it. This is our future 50-100  $\Omega$  heater so be careful about it).
- c) Take away the two connecting wires from the top and the bottom, if they are still in place.
- d) At each side (top/bottom) connect two wires, by silver epoxy DuPont 6838, to the metallic films side (do not bake the epoxy yet).
- e) Make a differential thermocouple (e.g., chromel-constant-chromel) by welding the wires (wire diameter  $\sim 0.2$  mm). The middle wire should have the approximate length of the voltage contact distance.
- f) Fix the differential thermocouple by silver epoxy DuPont 6838 in the middle of the polished flat surface (ceramic body of the resistor).
- g) Bake the whole construction for several ( $\sim 10$ ) minutes at 400-600  $^{\circ}\text{C}$  under vacuum. (Air would oxidize the metallic films and thereby destroy

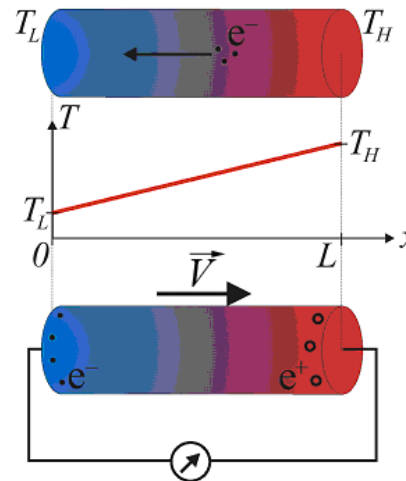
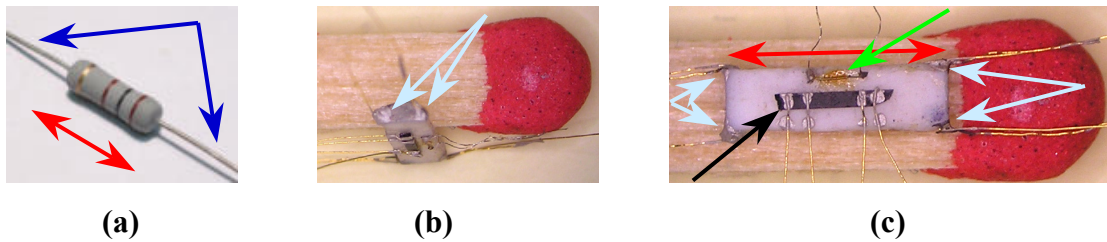


Figure A.2: Scheme of the TEP measurements

the epoxy contacts)

- h) Position the sample parallel to the thermocouple. Use the sample wires to fix the sample to the ceramic surface by gluing them with epoxy DuPont 4929 to the flat surface. To obtain a good thermal contact between the body of resistor and the sample, ensure that the part of the wire between the sample and the body of resistor is as short as possible.



**Figure A.3:** (a) Metallic film resistor. Dark blue arrows indicate the connecting wires and the red one the longest resistor dimension. (b) Top/bottom side of resistor (sample holder) in the final stage. The light blue arrows indicate the two silver epoxy contacts on the remaining metallic film, which now serves as a heater to produce a temperature gradient (all other facets are cleaned from the paint and the metallic film exposing the white ceramic body of the resistor). (c) Flat surface of the resistor with the mounted sample (black arrow) and thermocouple (green arrow). The meanings of the light blue and red arrows are the same as in a) and b). The size of the sample holder is compared to a matchstick.

The obtained sample holder, including the mounted sample, should resemble the one shown in Fig. A.3.

Once the sample holder is ready, the wires coming out of it should be connected to the measuring instruments as shown schematically in Fig. A.4. The next procedure explains *how to measure the thermoelectric power (TEP)*.

- a) Set the temperature gradient by setting the current,  $I_{Heat}$ , ( $\sim 10$  mA) through one of the heaters. Wait several seconds ( $\tau \sim 10$  sec) until the temperature gradient stabilizes.
- b) Read the voltage,  $V_{thc}$ , on the differential thermocouple (this gives the temperature difference,  $\nabla T = V_{thc}/S_{thc}$ , between the voltage contacts of the sample)
- c) Read the voltage on the sample,  $V_S$ .

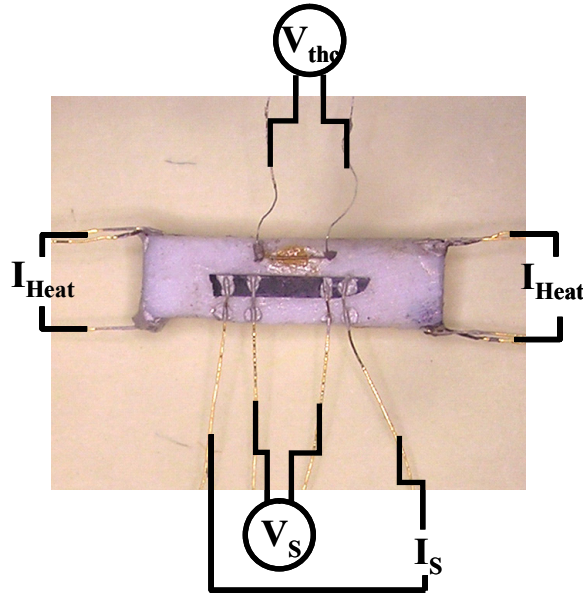


**Figure A.4:** Scheme for the TEP measurement. One of the heaters makes a temperature gradient,  $\nabla T$ , across the ceramic sample holder measured at the place of the sample voltage contacts by a differential thermocouple ( $\sim V_{thc}$ ). The same temperature gradient causes the voltage drop,  $V_S$ , on the sample. (Additionally in this arrangement resistance of the sample can be measured by setting the current  $I_S$  and the reading the voltage  $V_S$ .)

- d) Set the  $I_{Heat}$ , zero, wait  $\tau$  and read the voltages  $V_{thc}$  and  $V_S$ . (Both of them are non-zero due to the parasitic thermal voltages)
- e) The slope of the line connecting the measured points, in the  $(V_S, \nabla T)$ , graph gives the Seebeck coefficient of the sample  $S_S$ . (Actually, what is measured is the  $S_S - S_{wire}$ , were  $S_{wire}$  describes the thermoelectric power of the wires connected to the sample, usually made from high purity gold. How to deal with this aspect is described below)
- f) To obtain a more precise result, it is practical to measure several points with different  $I_{Heat}$ , between the minimal and maximal heating powers, by recording the results during a cycle of increasing and decreasing  $I_{Heat}$ . (Keep in mind that the heating power varies as  $\sim I_{Heat}^2$ . Therefore, to diminish it by a factor of 2, the current should be divided by  $\sqrt{2}$ ).

Several problems can occur while measuring the TEP in this way and may be easily spotted by monitoring measured voltages during one cycle. Problems could be related to either (i) a different heat transport between the sample holder and the sample or the thermocouple, or (ii) a too short time interval  $\tau$ , between the change of  $I_{Heat}$  and the moment of reading the voltages (the system is not in equilibrium). An example of a representative measurement and the typical signatures of both problems are shown in Fig. A.5a,b,c respectively.

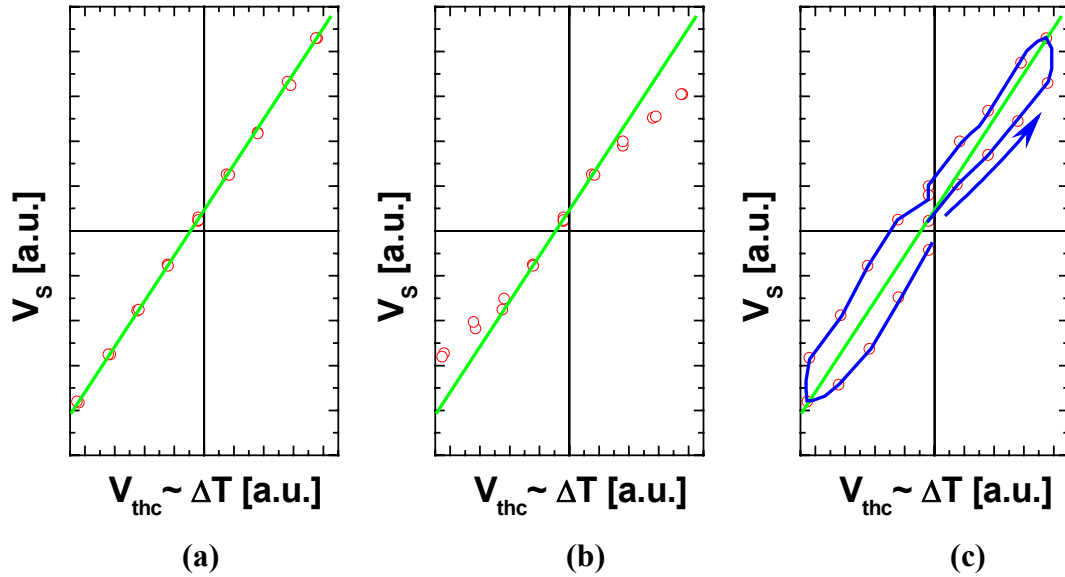


**Figure A.5:** a) Representative cycle of TEP measurement measured by two heaters. The slope of the fit (green line) gives the Seebeck coefficient of the sample. b) The effect of a weaker heat transport between the sample and the ceramic holder. c) Hysteresis due to the insufficiently long waiting time  $\tau$ . The blue line marks the order in which the data were collected. The offset of both measured voltages is attributed to the parasite thermal voltages.

There is one more problem which can appear even if the aforementioned setup is functioning well and is properly executed. If the  $I_{Heat}$  is too high it will result, not only in a temperature gradient  $\Delta T$ , but it will heat the entire sample and thereby change its Seebeck coefficient. This problem is particularly inconvenient if  $S_S$  has strong temperature dependence. In this case, the measured voltage curve will resemble to the one shown in Fig. A.5b).

As already mentioned, the previously described method actually results in values for  $S_S - S_{wire}$  as opposed to  $S_{Se}$ . This is easy to understand if we look on the sample and the connected wires as a differential thermocouple. The measured drop of voltage is equal to:

$$\begin{aligned} V &= S_{wire} (T_{room} - (T + \Delta T)) + S_S ((T + \Delta T) - T) + S_{wire} (T - T_{room}) = \\ &= \Delta T (S_S - S_{wire}) \end{aligned}$$

where  $T_{room}$  is the room temperature and  $T$  and  $T + \Delta T$  are the temperatures of the cold and the hot part of the sample.

There are three ways in which to overcome the contribution of the wires to the



measured Seebeck coefficient. The first is to simply neglect its existence, which is justified if  $S_S \gg S_{wire}$ . The second way is to use **high purity gold wires** (>99.99%) and read  $S_{wire}$  from existing tables. However, this procedure is not highly reliable since even a small quantity of magnetic impurities in the wires will result in a Kondo hump at low temperatures (below 100 K, which is quite inconvenient in the case of BaVS<sub>3</sub> given that at 2 GPa it has a metallic behaviour and an accordingly low Seebeck coefficient).

Finally, the **TEP of wires** can be directly measured and added to the measured  $S$  (be careful with the signs). The measured sample should be cautiously removed from the holder, by leaving the wires in places (cut them just at the edge of the sample). This procedure involves the replacement of the sample by BISCO and high purity Pb. BISCO is superconductive below 90 K ( $S_{BISCO} = 0$  V/K) and therefore the measured drop in voltage is related only to the  $S_{wire}$ . Pb is also convenient since  $S_{Pb}$  can be found in the tables but in contrast to gold it is very easy to obtain it in the pure state. (To simplify the determination of  $S_{wire}$ , and to avoid the problems associated with Kondo humps, it is nevertheless recommended to connect the sample with high purity gold wires).

## ***A.2 High temperature measurements***

The sample holder described above is particularly convenient as it can be (i) easily plugged in to different experimental setups without touching the sample and, (ii) allows simultaneous measurement of the resistivity and TEP. These two properties serve to facilitate the comparison of the obtained results. In the subsequent discussion, several experimental setups, used to cover following temperature and pressure ranges, are described:

high temperatures (300- 1000 K) at ambient pressure

low temperatures (1.5 to 300 K) at ambient pressure

high pressures, up to 3 GPa, in the 2-300 K temperature region.

The experimental setups for the latter two ranges were designed to fit in the superconducting magnet, to enable the possible application of high strength magnetic

---

fields (up to 12.7 T). In such a way, a large volume of the  $T$ - $p$ - $H$  phase diagram can be covered without moving the sample from the sample-holder.

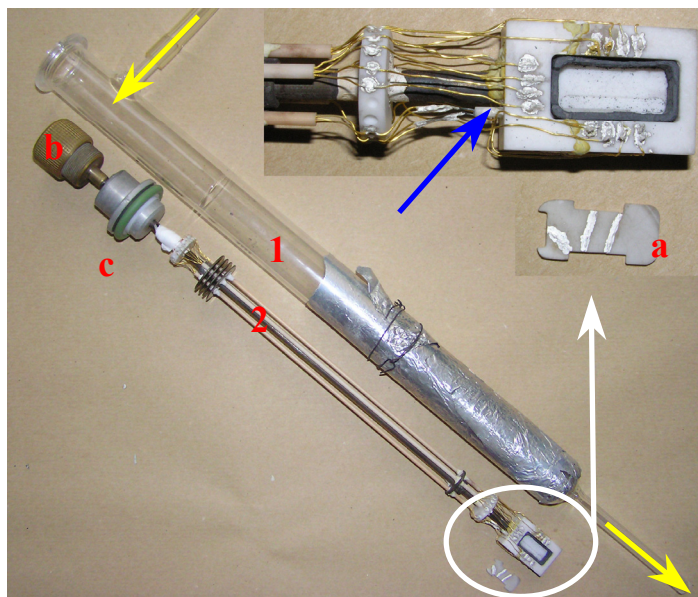


**Figure A.6:** High temperature setup (2) with its principle components. The measuring head, and its cap (a), marked by the white circle, are enlarged in the right-upper part of the figure. The position of the Pt resistance thermometer placed in the body of the measuring head is indicated by a blue arrow. A vacuum feed-through (b) is used to make a hermetic passage for the wires. Once the setup is introduced in the glass tube (1) the joint is sealed by an o-ring (c). The possible gas flow is indicated by yellow arrows.

To investigate the *high temperature* transport properties, the sample holder was plugged into the home-made experimental setup shown in Fig. A.6. The sample holder is placed in the hole of the measuring head, connected to the gold wires by silver epoxy DuPont 6838, and covered by the small ceramic plate (a), to ensure a good thermalisation. The temperature is measured by a Pt resistance thermometer placed in the body of the measuring head and connected to the gold wires. To prevent shortcuts, the gold wires are guided through ceramic tubes to a vacuum feed-through (b) from where the signal is brought by the copper wires to the measuring instruments. The whole setup (2) is placed in the glass tube with two entrances for the gases (1) to allow the possibility of exposing the system to various atmospheric conditions. (If a vacuum is desired, simply close one of the (yellow) entrances and pump on the other.) The o-ring (c) seals the joint between the elements (1) and (2). With everything assembled thus, the setup is introduced to an oven of length similar to that of the aluminum paper wrapped around the glass tube. Bigger ovens could

overheat the sensitive part of the setup (e.g., the feed-through). Aluminum paper ensures a low temperature gradient along the tube and thereby reduces the parasitic thermal voltage.

### ***A.3 High pressure measurements***

The measurement of ***low temperature*** resistivity at ambient pressure is a standard experimental method found in many laboratories and therefore won't be discussed in detail herein. In principle, the setup is similar to that used for the high temperature measurements. The presence of more than 6 wires in the measuring head brings with it the opportunity to plug in the sample holder and measure the TEP (one heater can be enough for the measurement. For the simultaneous measurement of the resistivity, at least 8 wires are needed). The remaining aspects have already been outlined above. Therefore, let us continue with more exciting (and more difficult) prospect of ***pressure measurements***.

The main idea is to use a pressure cell which has enough wires entering the cell and then plug in the sample holder and repeat the logic of the 1 bar measurement. We started with a commercially available self-clamping pressure cell (Polish, shown in Fig. A.7.) with less than 10 wires. To measure TEP, resistivity and the pressure in the cell at least 12 (6 + 2 + 4) wires are needed which are not on our disposition. Thus, the difficulty is to make a ***feed-through***, shown in Fig. A.8, which will survive extreme forces (to have 2 GPa in the cell, on the surface of the feed-through, with a diameter of 7 mm, force of several tons is applied).

---

---

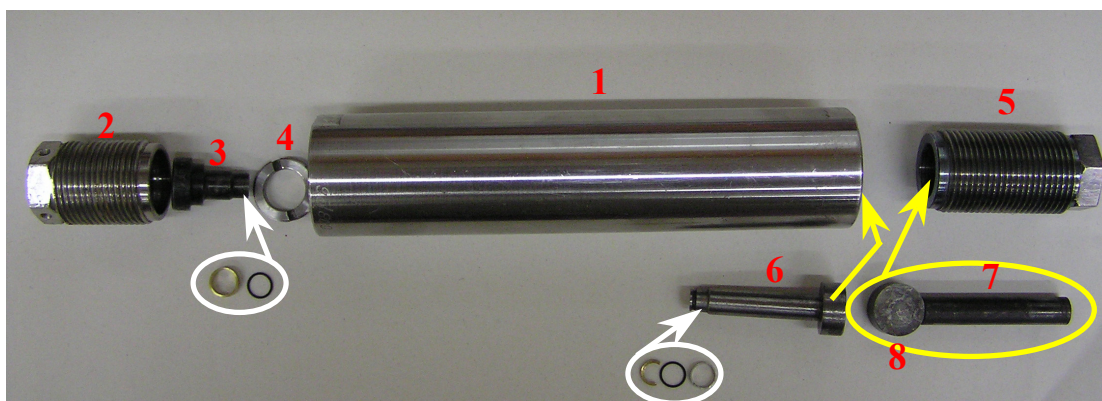


**Figure A.7:** The self-clamping pressure cell. 1- cell body, 2- fixing nut (with a passage for the wires), 3- feed-through, 4- nut to fix the feed-through, 5 -fixing nut (with a hole for the force transmitting piston (7) and disc (8)), 6- piston. Appropriate rubber and brass rings are encircled by white lines. The arrows point to the final position of a particular component.

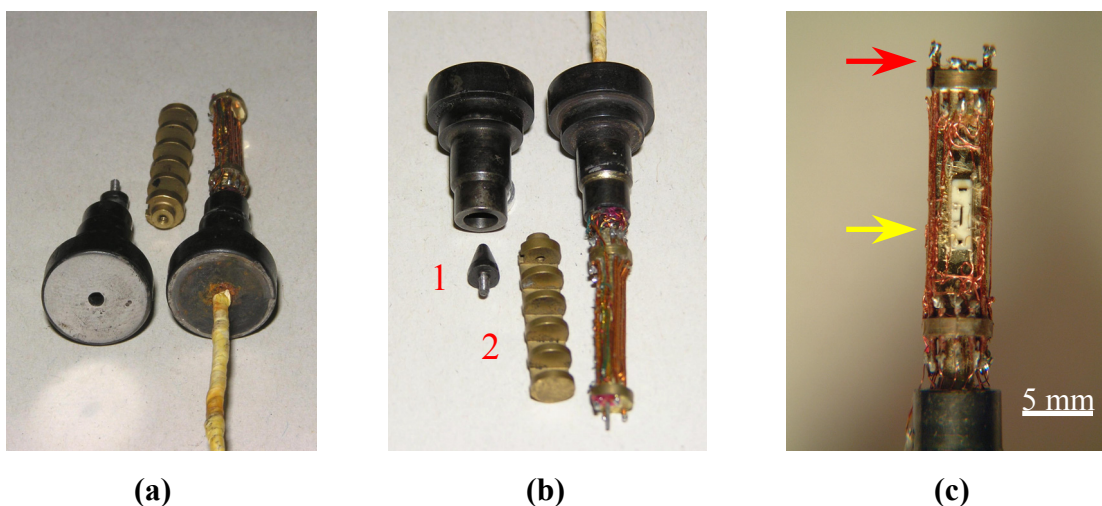


**Figure A.8:** (a) and (b) the back and the front view on the feed-through, small cone (1) and a holder (2) in the first and last phase of preparation. (c) The positions of the sample-holder and the pressure gauge are marked by yellow and red arrow, respectively.

The following steps explain how to successfully prepare the apparatus for assembly:

- a) Sonificate the wires, small cone and the feed-through in ethanol (the LakeShore phosphorous bronze wires are strongly recommended, because of their strength)
- b) Place the wires in the feed-through, and arrange them in such way that they do not cross each other, and that they closely follow the surface of the feed-through hole. (It is convenient to twist the wires at both exits of the feed-through and fix them by GM-varnish, preventing their further

- movement.)
- c) Mix the EMERSON&CUMING Stycast 2850 FT with the Catalyst 11, degas it in a desiccator, fill the feed-through hole (to ensure a good filling use a pump to suck in the Stycast) with the resulting mixture, plug in the small cone, clean the wires and the feed-through from the excess Stycast excess and apply the heat treatment as indicated in the Stycast instructions. (During the heat treatment Stycast becomes liquid and to prevent its leaking on the bottom side, a small paper ball can be used as a cork.)
  - d) Once the feed-through is ready a holder (for the sample-holder and a pressure gauge) it is screwed on the small cone and the wires are placed in the desired positions.
  - e) Finally the sample-holder and the pressure gauge are connected to the wires.

Now everything is ready and the pressure cell should be assembled as shown in Fig. A.7. The instruments should be connected according to the Fig. A.4. We chose to use kerosene as a pressure medium, although alternatives are possible. Measurements can be performed directly in the helium tank or in a glass cryostat. The cooling rate of 0.5-1 K/min still gives low noise results. (If a magnetic field is to be used, care should be exercised with the choice of materials in that they should be non-magnetic., e.g. CuBe for the pressure cell).

In closing this section, we record two more tricks. While *increasing the pressure* in the cell *above ~1 GPa the gold wires have a tendency to break*. This is due to the frizzing of the pressure medium (kerosene). There is a simple way to reduce the risk of this problem by arranging the wires in such way that they follow some bigger surface (if it is not possible glue them to a thicker wire (insulated copper wire with 1mm diameter will suffice)).

In the case that *contacts* are required for the **InSb** pressure gauge, the following procedure has enjoyed proven success. Simply mask the guage (as explained above for BaVS<sub>3</sub>), evaporate pure In, and heat it above the melting point of In (160 C°). Connect the wires (50 μm gold wires are still soft enough) with a silver epoxy. Be sure to handle InSb with care, since it is very fragile.

By arming yourself with an acceptably sized portion of luck and carefully following the above procedures, you should be able to reproduce the measurements presented in this thesis. Naturally, the contents of this section also provide the basis for variations on the theme and even the material under study. Should you choose to head down

---

---

this, or a related path, you can consider yourself warned that the successful development of the measuring protocol represents merely the beginning of a torrid odyssey. From there you are on your own. As HAL 9000 would put it: “Well I don’t think there is any question about it. It can only be attributable to human error. This sort thing has cropped up before, and it has always been due to human error.” “This conversation can serve no purpose any more. Goodbye.”



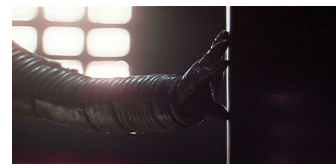
On the other hand, just because HAL “can’t do that” doesn’t rule out the possibility that you can.



---

# Appendix B

## CATALOG OF SAMPLES



As this appendix is meant to serve persons familiar with the subject, all of the relevant information is given within the figures and not commented upon in the captions; the figures are left to speak for themselves. It is hoped that this approach will leave the objectivity of the observer unspoiled, enabling him to identify either the universal phenomena or the differences in-between the samples, as he so chooses.

---

---

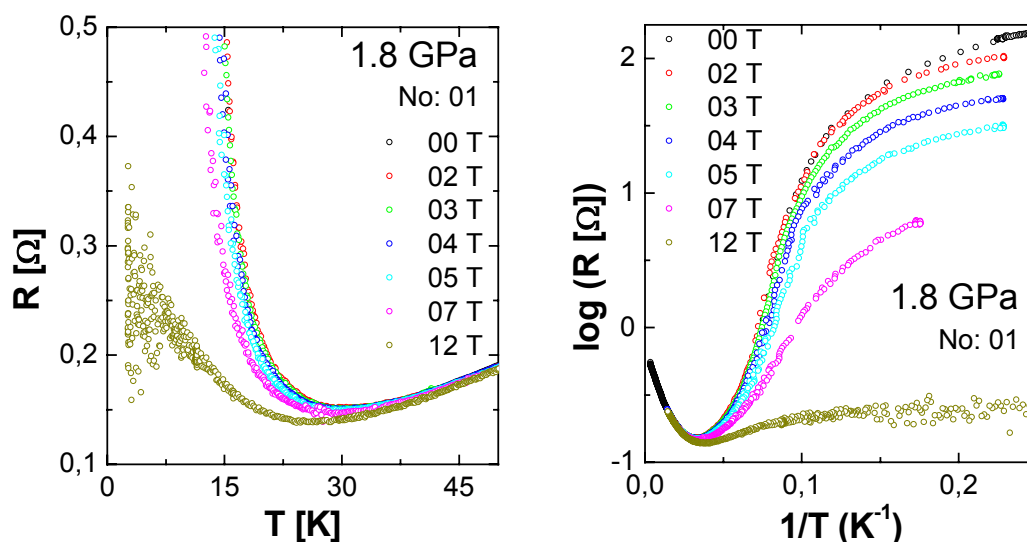


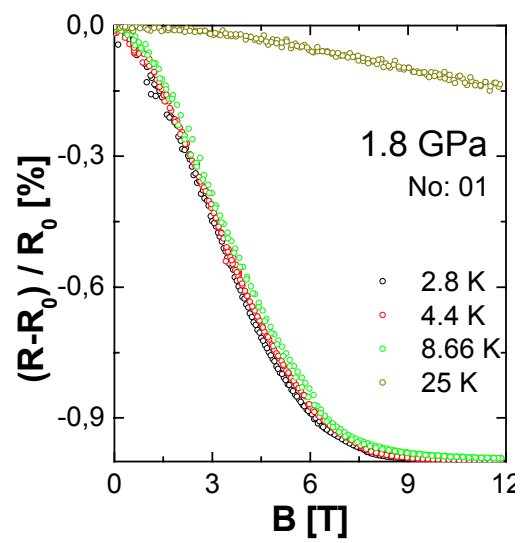
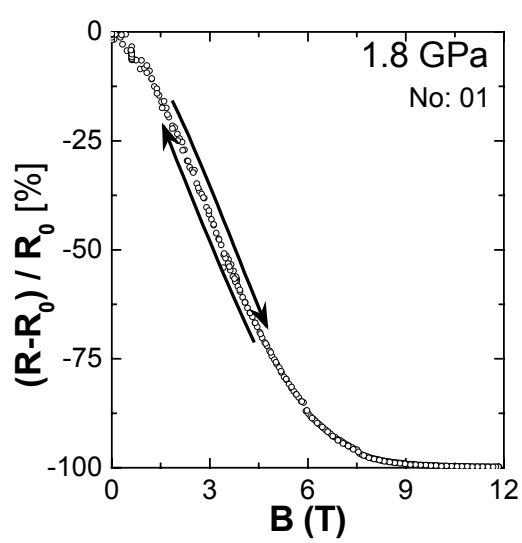
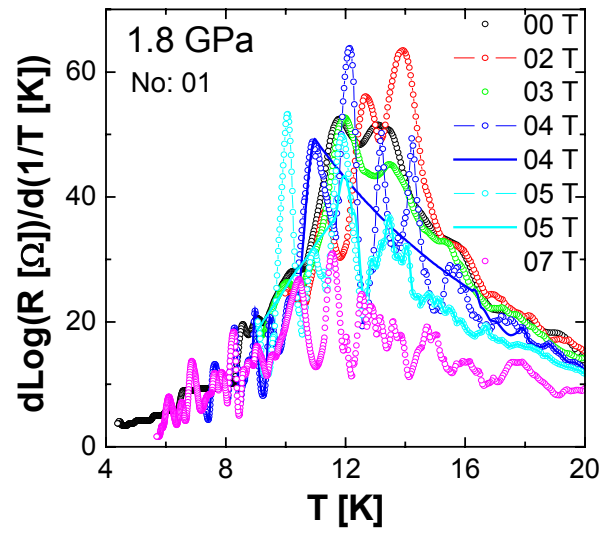
### B.1 Preamble

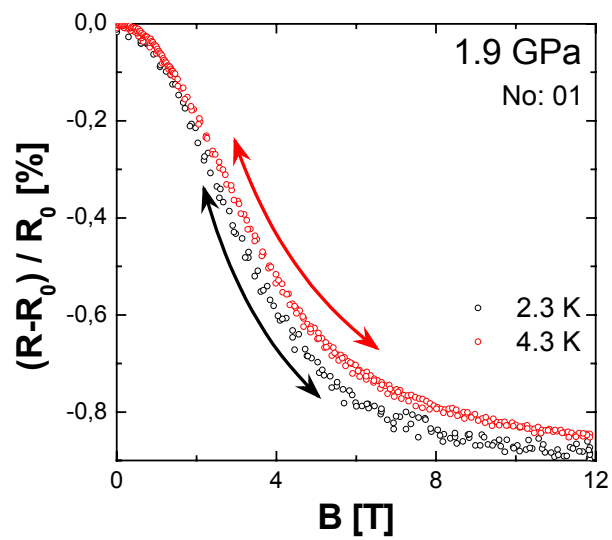
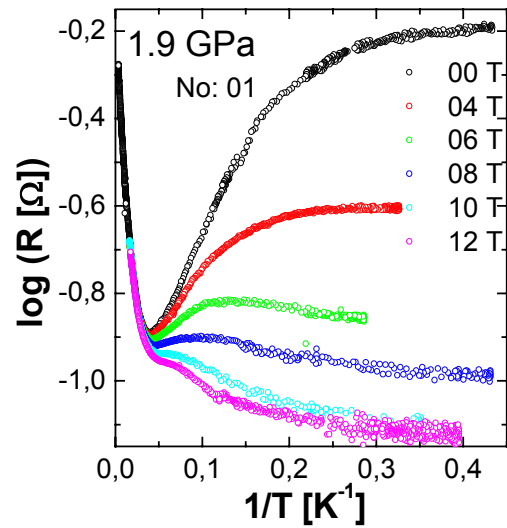
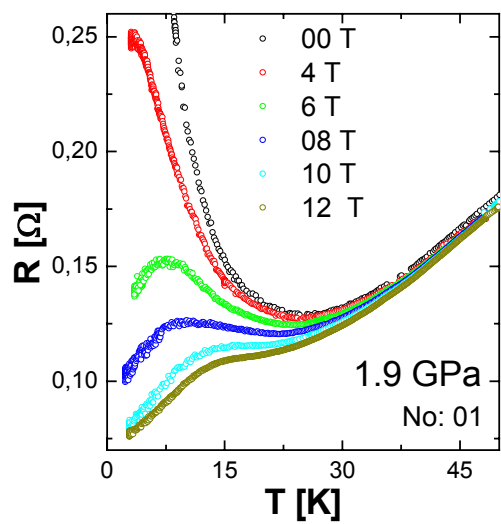
One of the most exploited features of BaVS<sub>3</sub>, during the course of this work, was its sensitivity to pressure. The most interesting area of the  $p$ - $T$  diagram is located at low temperatures (below 30 K), in the region close to the critical pressure ( $p_{\text{cr}} \sim 2$  GPa), where the MI phase boundary collapses. Because of the proximity of the Quantum Critical Point (QCP) in this region, the physical properties of the system can also be tuned by a magnetic field, disorder, or sulfur off-stoichiometry. In addition, it was shown in chapter 5 that the observed low-temperature behavior is strongly dependent on the magnetic properties of the system. Therefore, we present the results of ambient pressure susceptibility and high-pressure resistivity measurements, on several samples, in the form of a catalog. The aim in doing so is to enable a facile comparison of the quality of the different samples.

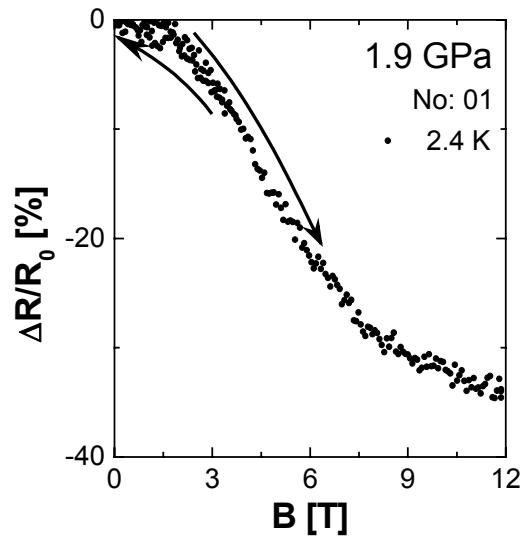
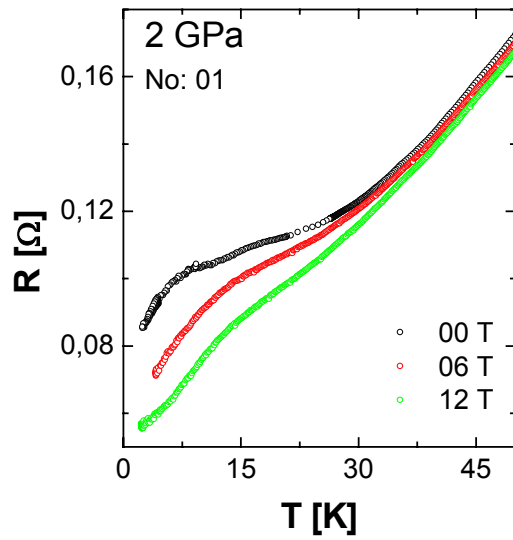
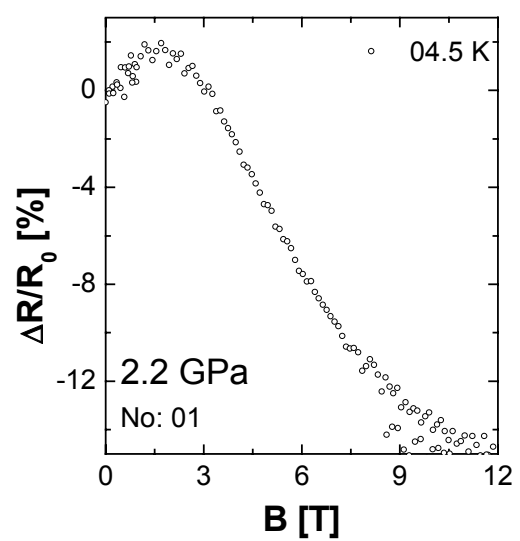
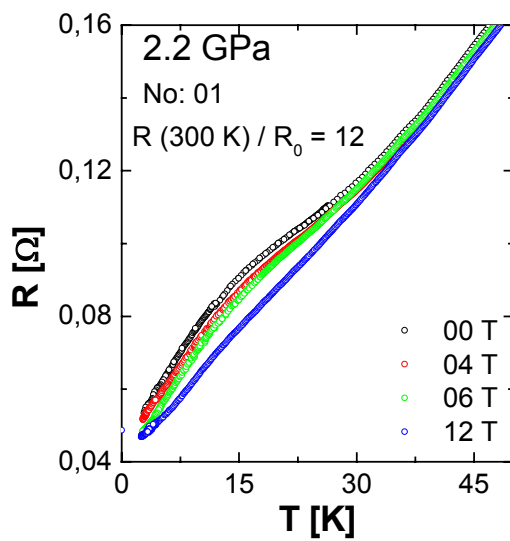
#### B.1.1 Sample No: 01

### 1.8 GPa

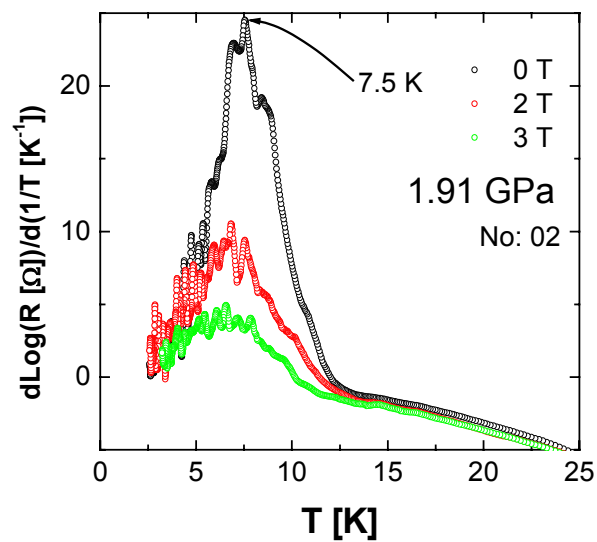
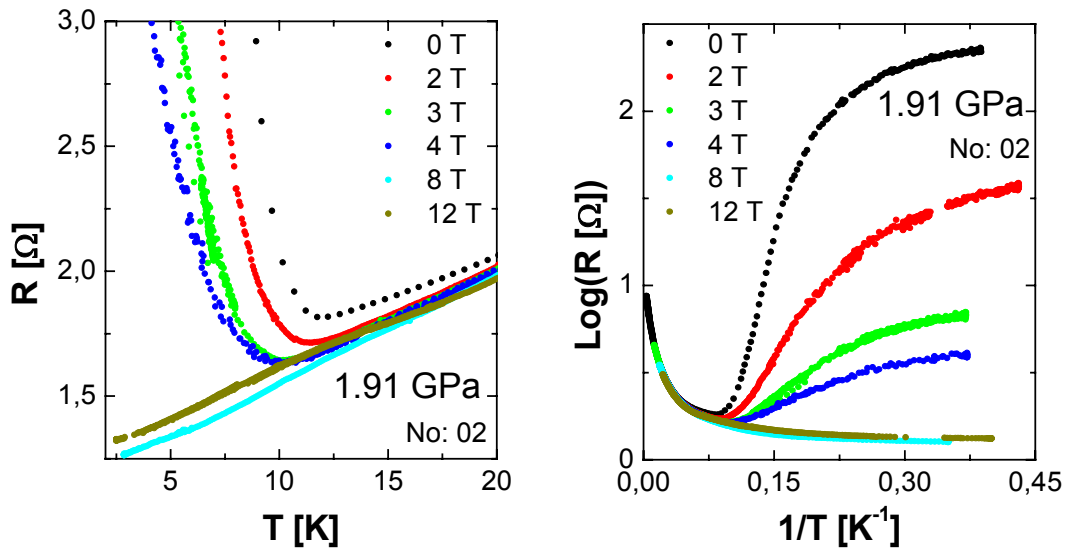


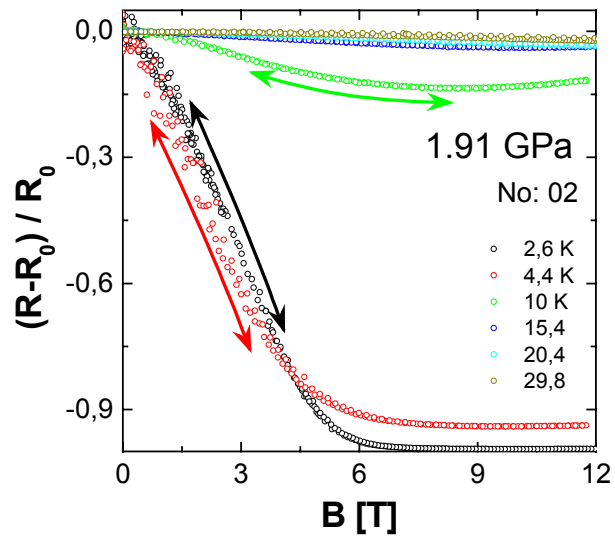
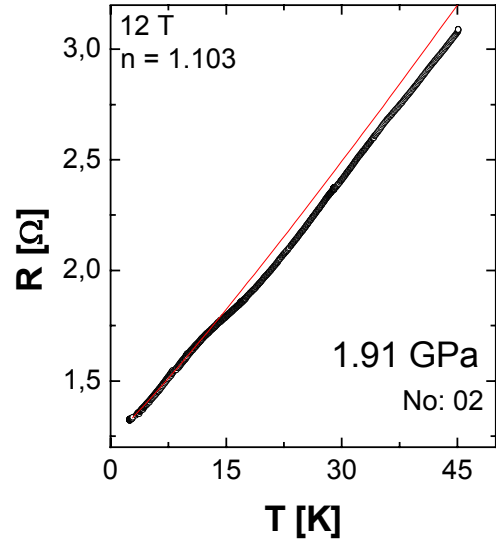
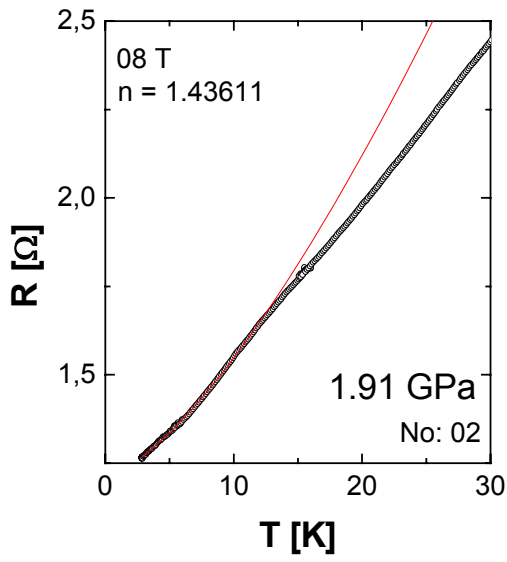
**1.8 GPa**

**1.9 GPa**

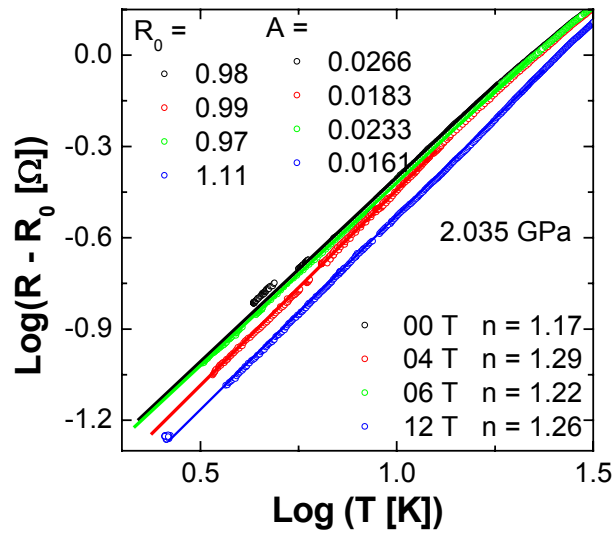
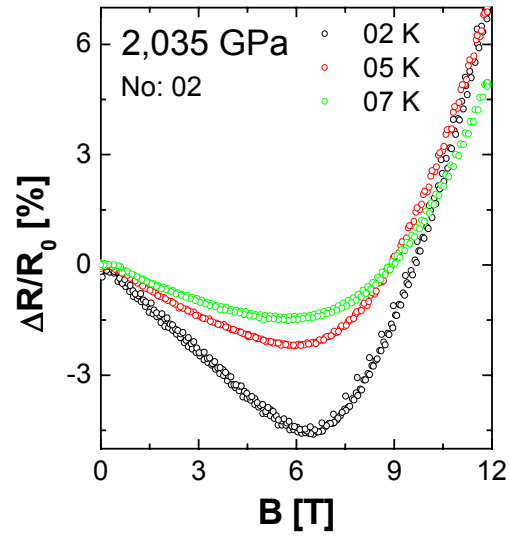
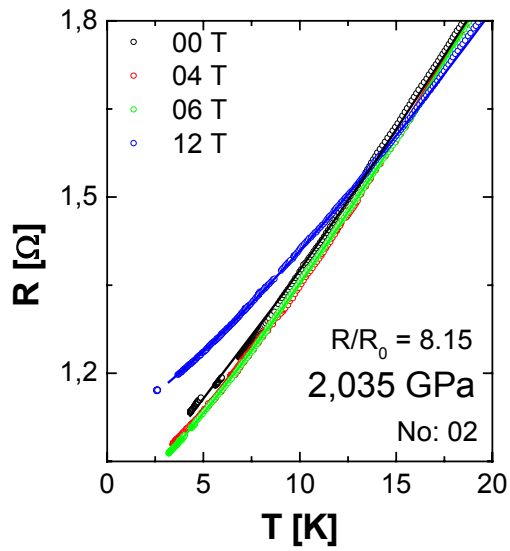
**2 GPa****2.2 GPa**

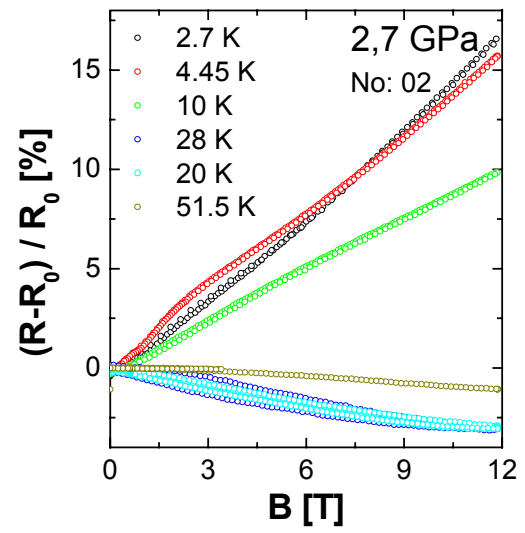
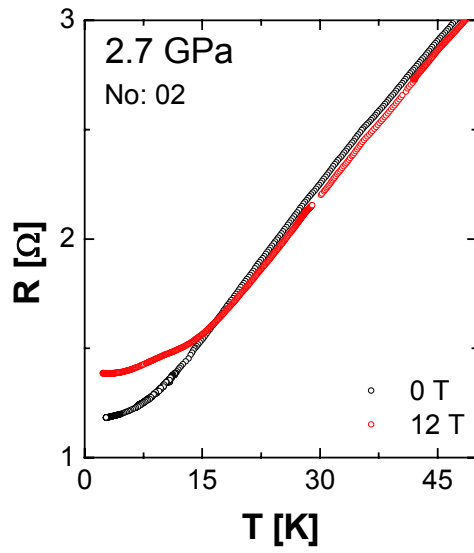
B.1.2 Sample No: 02

**1.91 GPa**

**1.91 GPa**

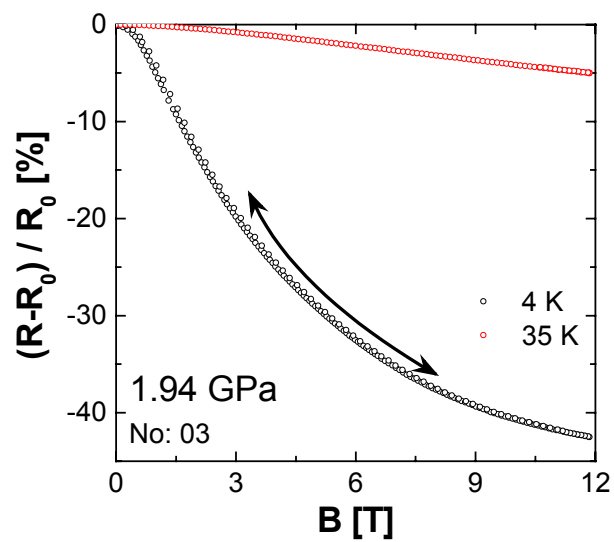
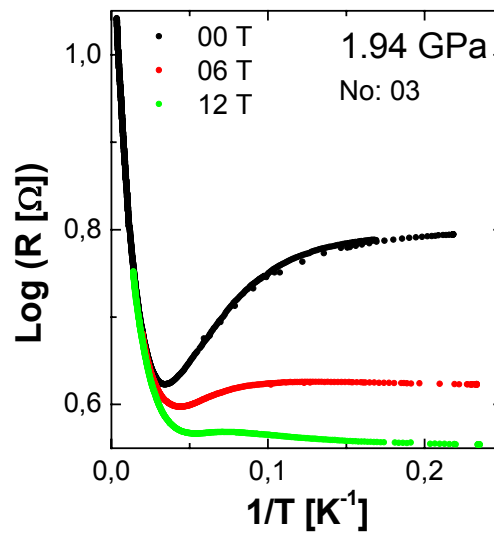
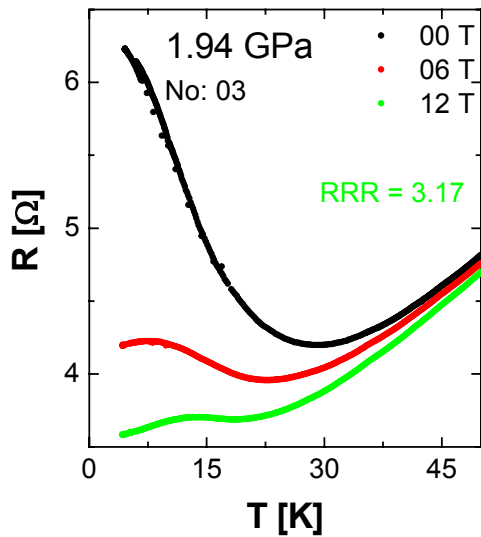
## 2.035 GPa

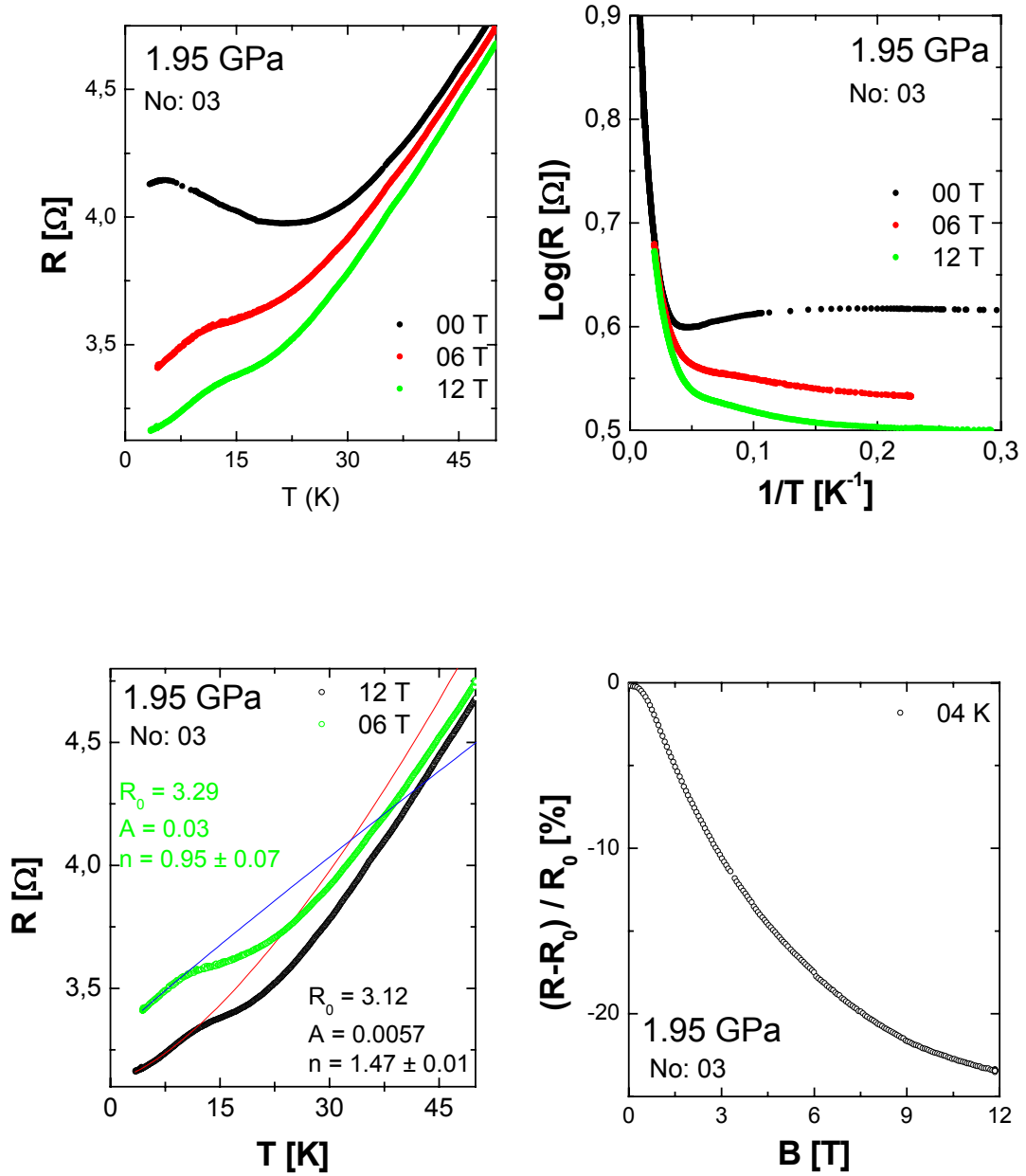


**2.7 GPa**

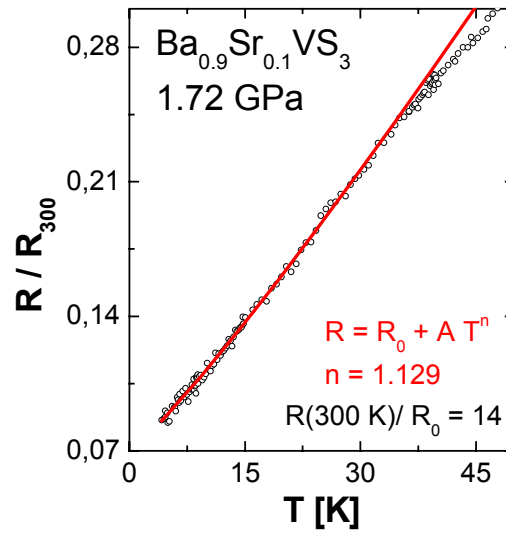
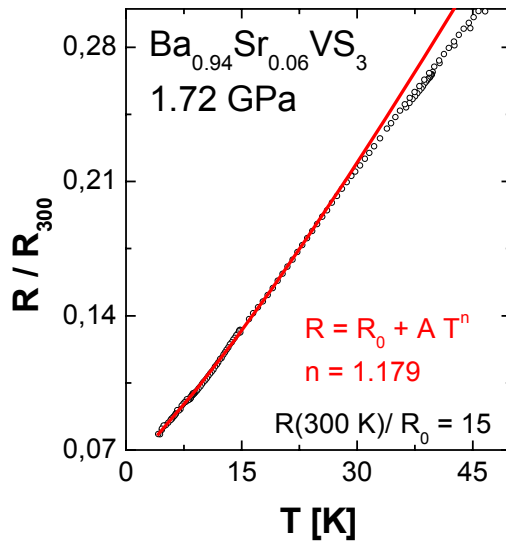
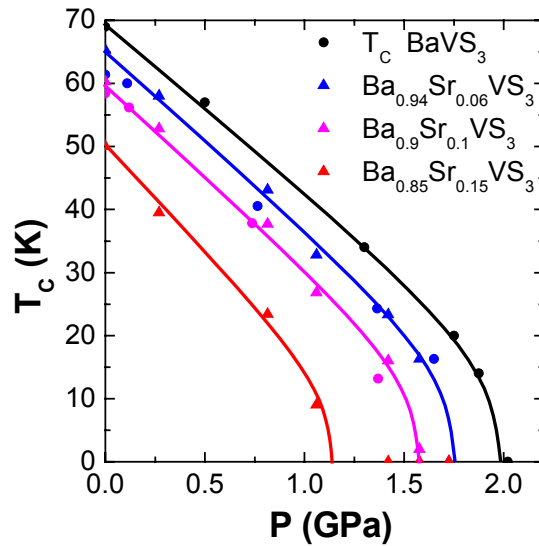


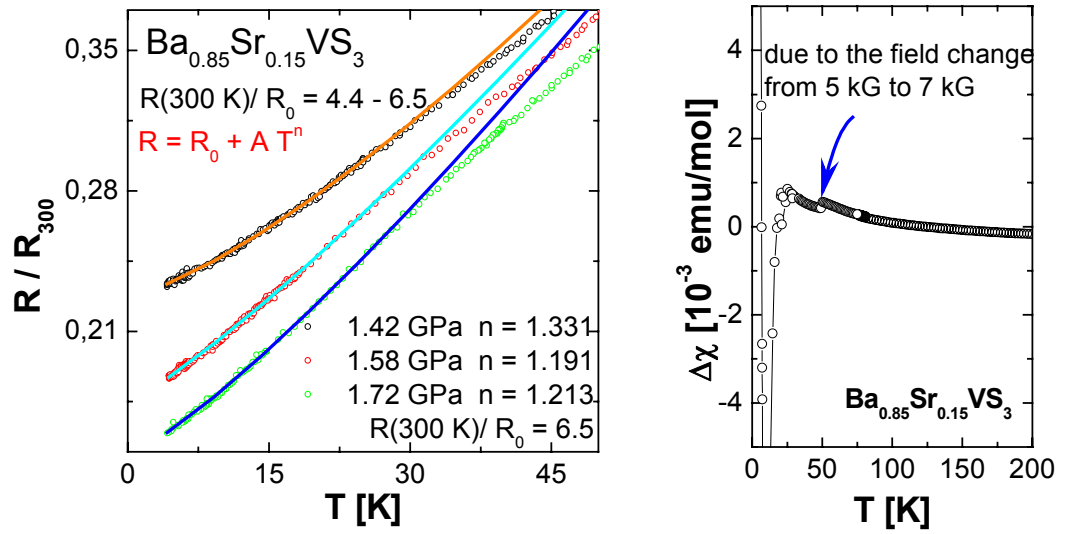
## B.1.3 Sample No: 03

**1.94 GPa**

**1.95 GPa**

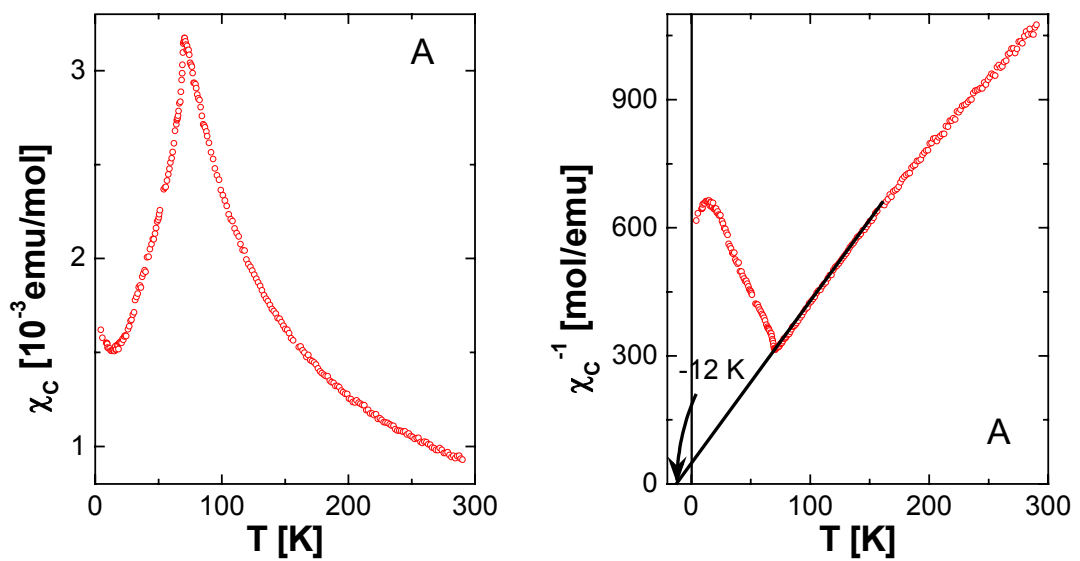
### B.2 Sr substituted samples

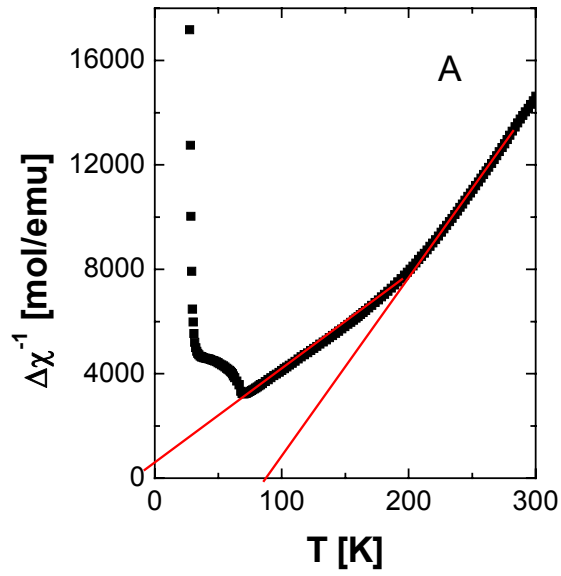
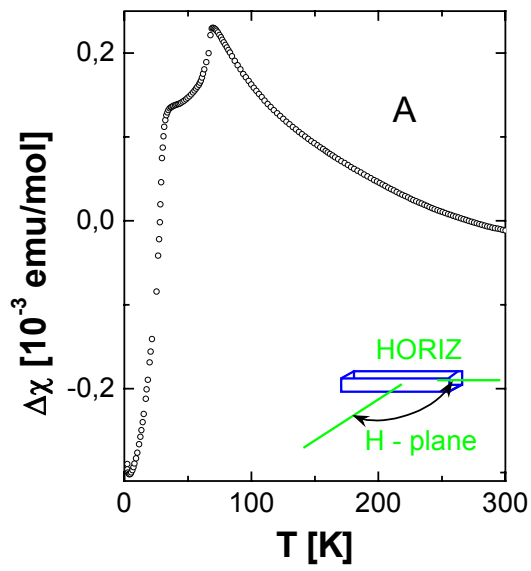




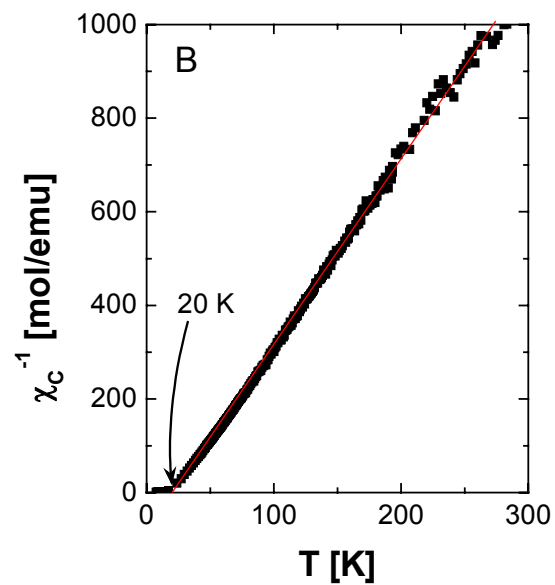
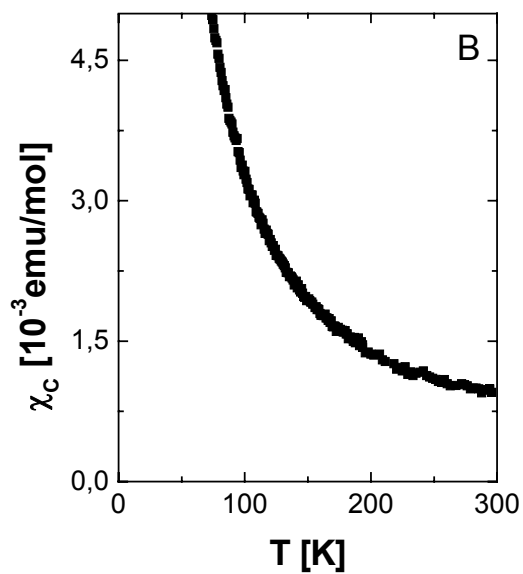
### B.3 Examples of magnetic susceptibility and its anisotropy

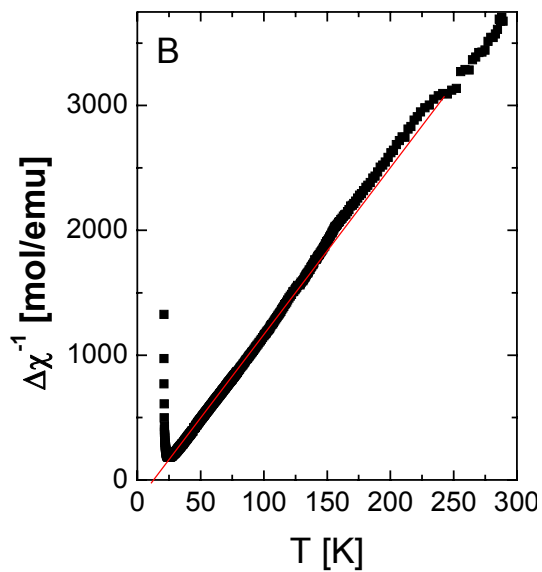
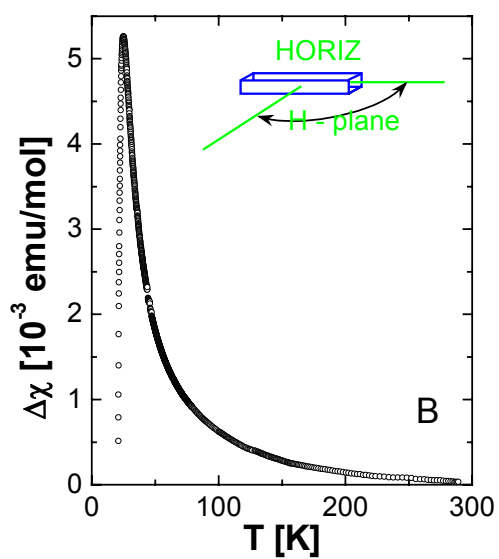
#### B.3.1 Sample A



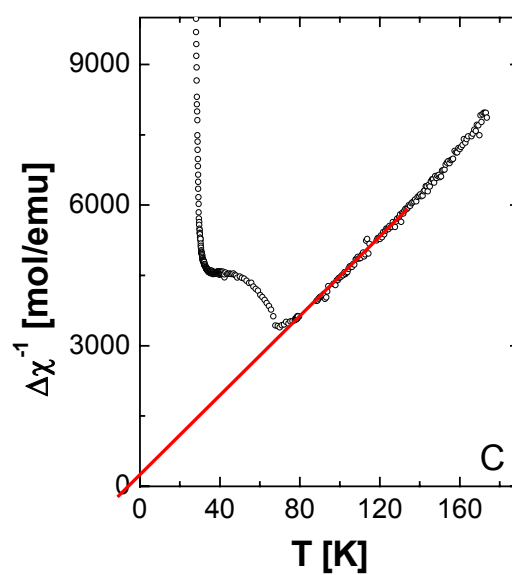
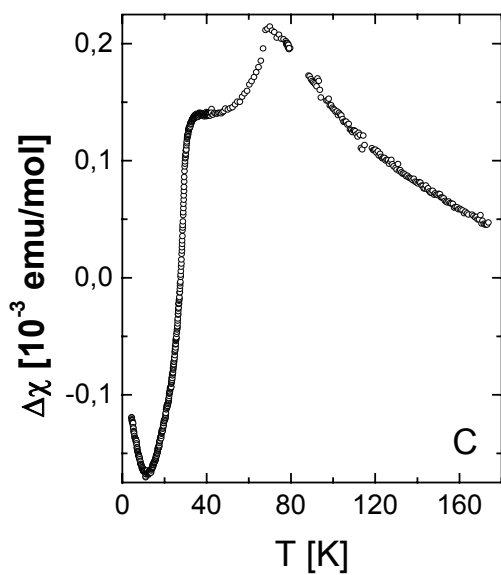


### B.3.2 Sample B

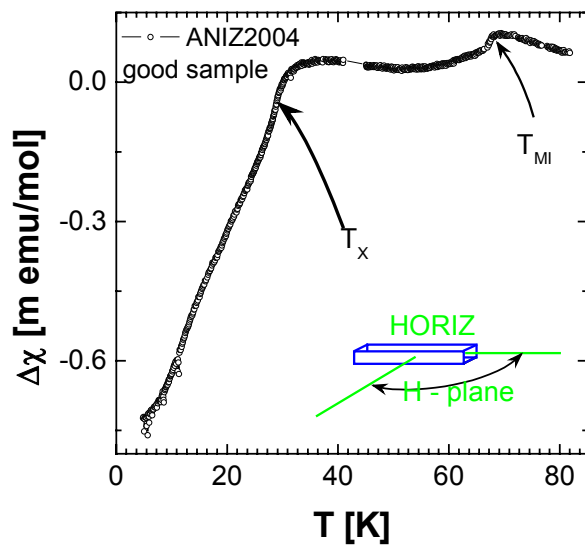




### B.3.3 *Sample C*



## B.3.4 Sample No: 00



## *List of abbreviations*

$a^*, b^*, c^*$	primitive vectors of the reciprocal lattice
$a', b', c'$	primitive vectors of the hexagonal unit cell
a, b, c	vectors of the orthorhombic unit cell
a.c.	alternating current
AFM	antiferromagnetic
ARPES	Angle Resolved Photoemission Spectroscopy
BCS	Bardeen, Cooper and Schrieffer
CDW	charge-density wave
d.c.	direct current
DMFT	dynamic mean field theory
DOS	density-of-states
$E_F$	The Fermi level
FC	field-cooling
FL	Fermi liquid
FM	ferromagnetic
ICFM	interchain-compensated FM
IRC	Ioffe-Regel criterion
JT	Jahn-Teller
$k_F$	Fermi wave vector
LAPW	linear augmented plane waves
LDA	Local density approximation
MI	metal-insulator transition
$n_F$	density of states at the Fermi level
NFL	non-Fermi liquid
NMR	Nuclear Magnetic Resonance
NQR	Nuclear Quadrupole Resonance
$p_{cr}$	critical pressure
QCP	quantum critical point
RF SQUID	radio frequency superconducting quantum interference device
RKKY	Ruderman-Kittel-Kasuya-Yosida
RRR	residual resistivity ratio
SDW	spin-density wave
TB	tight binding approximation
TEP	thermoelectric power
$T_{MI}$	metal-insulator transition temperature
$T_S$	critical temperature for a structural transition
$T_x$	long range magnetic ordering temperature
$U$	Hubbard $U$
ZFC	zero-field cooling





## Curriculum Vitae Neven Barišić

Institute of Physics of Complex Matter, FBS  
Swiss Federal Institute of Technology (EPFL),  
CH-1015 Lausanne Switzerland  
Tel: (+41)-21-693-4304, Fax: (+41)-21-693-4470.

Email: [neven.barisic@epfl.ch](mailto:neven.barisic@epfl.ch)

**Personal** Born: September 19, 1972 in Paris, France.

**Marital Status** Single.

**Citizenship** Croatian, French

### Education

2000 – 2004 PhD student in the Research Group of Professor László Forró at the Institute of Physics of Complex Matter, FBS, Swiss Federal Institute of Technology (EPFL), CH-1015 Lausanne Switzerland

1999 Diploma thesis in the subject of “Microwave Conductivity of  $\text{YBa}_2\text{Cu}_3\text{O}_{7-\delta}$  Thin Film in the Magnetic Field”  
Supervisor: Professor Antonije Dulčić

1990 – 1999 Physics Department of the University of Zagreb, Croatia, experimental and theoretical-state physics.

1990 Baccalaureate, MIOC (Mathematical and Informational Educational Centre) high school, Zagreb, Croatia

### Teaching experience

2001-2002 Teaching assistant-exercises, General Physics III and IV (Physique générale), EPFL (professor Libero Zuppiroli)

2002-2003 Teaching assistant-exercises, Solid State Physics I and II (Physique du solide), EPFL (professor László Forró)

2003-2004 Teaching assistant-exercises, General Physics III and IV (Physique générale), EPFL (professor László Forró)

**Oral presentations**

- 2004                      Invited: April, 22 2004 KFKI, Budapest, Electrical properties of the frustrated correlated  $d$ -electron system  $\text{BaVS}_3$ : studies under high pressure
- Contributed: Annual APS March Meeting 2004, March 22-26, 2004 Palais des Congres de Montreal, Montreal, Quebec, Canada, Magnetoresistance of  $\text{BaVS}_3$  under pressure
- 2003                      Contributed: 2003 Swiss Workshop on Materials with Novel Electronic Properties, Les Diablerets, September 29- October 1, 2003.  $\text{BaVS}_3$  a correlated  $d$ -electron system

**Publications**

- Barišić N., A. Dulčić, M Požek, D. Paar. 1999. Microwave conductivity of thin YBCO film in magnetic field. *Fizika A*, **8**(4), 245-52
- Barišić N., R. Gaál, I. Kézsmárki, G. Mihaly and L. Forró. 2002. Pressure dependence of the thermoelectric power of single-walled carbon nanotubes. *Phys. Rev. B*, **65**(24), 241403
- Barišić N., L. Forró, D. Mandrus, R. Jin, J. He and P. Fazekas. 2003. Electrical properties of  $\text{Cd}_2\text{Re}_2\text{O}_7$  under pressure. *Phys. Rev. B*, **67**(24), 245112
- Gauzzi A., F. Licci, N. Barišić, G. L. Calestani, F. Bolzoni, E. Gilioli, M. Marezio, A. Sanna, C. Franchini and L. Forró. 2003. Chemical pressure-induced ferromagnetism and stabilization of the metallic state in  $\text{Ba}_{1-x}\text{Sr}_x\text{VS}_3$ . *Int. J. Mod. Phys. B*, **17**(18-20), 3503-08
- Mikó C., M. Milas, J. W. Seo, E. Couteau, N. Barišić, R. Gaál and L. Forró. 2003. Effect of electron irradiation on the electrical properties of fibers of aligned single-walled carbon nanotubes. *Appl. Phys. Lett.*, **83**(22), 4622-24
- Mitrović S., L. Perfetti, C. Sondergaard, G. Margaritondo, M. Grioni, N. Barišić, L. Forró and L. Degiorgi. 2004. Electronic structure of a quasi-one-dimensional insulator: The molybdenum red bronze  $\text{K}_{0.33}\text{MoO}_3$ . *Phys. Rev. B*, **69**(3), 035102
- Perucchi A., C. Sondergaard, S. Mitrović, M. Grioni, N. Barišić, H. Berger, L. Forró and L. Degiorgi. 2004. Spectroscopic and dc-transport investigations of the electronic properties of  $\text{TaSe}_3$ . *Eur. Phys. J. B*, **39**(4), 433-40
- Caimi G, L, Degiorgi, H. Berger, N. Barišić, L. Forró and F. Bussy. 2004. Optical evidence for the proximity to a spin-density-wave metallic state in  $\text{Na}_{0.7}\text{CoO}_2$ . *Eur. Phys. J. B*, **40**(3), 231-234

Mitrović S., P. Fazekas, C. Sondergaard, D. Ariosa, N. Barišić, H. Berger, D. Cloetta, L. Forró, H. Höchst, I. Kupčić, D. Pavuna and G. Margaritondo. Experimental Electronic Structure and Interband Nesting in BaVS<sub>3</sub>. *Submitted to Phys. Rev.Lett.*

Kézsmárki I., G. Mihály, R. Gaál, N. Barišić, H. Berger, L. Forró, C. C. Homes and L. Mihály. Pressure induced suppression of the singlet insulator phase in BaVS<sub>3</sub>: infrared optical study. *Submitted to Phys. Rev.Lett.. cond-mat*, 0311335.

Kézsmárki I., C. Homes, L. Mihály, N. Barišić, L. Forró, P Fazekas and G. Mihály. Optical conductivity of BaVS<sub>3</sub>. *In preparation.*

N. Barišić, I. Kézsmárki, G. Mihály, H. Berger, P. Fazekas and L. Forró. Thermoelectric power of BaVS<sub>3</sub> under high pressure. *In preparation.*

N. Barišić, P. Fazekas, D. Mandrus, , R. Jin, J. He and L. Forró. The Kohler's rule for Cd<sub>2</sub>Re<sub>2</sub>O<sub>7</sub>. *In preparation.*

N. Barišić, P. Fazekas, I. Kézsmárki, G. Mihály, H. Berger and L. Forró. Pressure driven cross over from non-Fermi-liquid to Fermi-liquid of BaVS<sub>3</sub>. *In preparation.*

N. Barišić, A. Gauzzi, H. Berger, I. Kézsmárki, G. Mihály, P. Fazekas and L. Forró. Impurity dependence of non-Fermi-liquid exponent of BaVS<sub>3</sub>. *In preparation.*

N. Barišić, I. Kézsmárki, G. Mihály, P. Fazekas and L. Forró. Collapse of the metal-insulator transition of BaVS<sub>3</sub> in high magnetic field. *In preparation.*



## *Acknowledgments*

I extend my thanks to all the people who helped me in my professional, personal and any other life during my Doctorate degree. Many, however, warrant special mention:

Firstly, I would like to extend my sincerest thanks to my thesis advisor, Professor László Forró for the unconditional trust he has placed in me. His contagious passion for Physics and Science in general, his great ideas, and the beautiful working environment that he created in NN group, were my driving forces. His ability to recognize and provide the support and understanding, when I needed it the most, has left me with a feeling of being an extremely well-managed student.

Professor György Mihály and Dr. István Kézsmárki were there when I just started and they continued to give me substantial support along all these years. Their experiments were both the inspiration and the foundation of my start in the field of high-pressure transport experiments and materials with novel electronic properties. Equally unforgettable were the long days and nights spent at the Technical University of Budapest, which always provided a cheerful atmosphere and made my stays in Budapest much warmer.

I am very lucky to have had the privilege to work with Professor Patrik Fazekas and Dr. Ivan Kupčić. Although staying behind the scenes, they introduced me to the theory of correlated systems. Their sound advice and always immediate response to my constant questions were greatly appreciated.

I am indebted to Dr. Andrea Gauzzi and Helmuth Berger for providing me the fruitful discussions and precious, high-quality samples.

I have profited greatly from the support of Dr. Marko Miljak, Dr. László Mihály, Dr. Slobodan Mitrović and Dr. Richard Gaál.

Thanks are extended to past and present members of the NN group, for the collegial atmosphere, assistance and laughter which they provided in the day-to-day experience. Moments with Dr. Feher Titusz (Titi), Mirko Milas (Mimi) and Bertrand Vileno (Bert) will always be in my memories. I would also like to mention Ana Akrap, Dr. Arnaud Magrez (BG), Dr. Edina Couteau (Dina), Dr. Slaven Garaj, Csilla Mikó, Yanki Keles, Dr. Sylvia Jeney, Branimir Lukić and Camilo Guzman.

Many thanks to Monique Bettinger and Sigrid Lovato, who helped me a lot by their efficiency and smiles.

I am grateful to all the technicians of the IPMC workshop for their unconditional help and support over the years.

Particular words are also addressed to all the Forró family. I thank them for opening for me the door to the Hungarian culture, helping me not to feel so lonely in Switzerland, and giving me the impression of being welcome and at home.

With the warmth from my heart, I have to thank my mother and my father in the Bambian sense as well as all other members of my family for their unconditional love and support, wherever they are now, in Croatia, Russia, Germany, Australia or France.

Hvala svima. Merci beaucoup. Köszönöm. Спасибо. Thank you.





